UNIVERSITY OF OKLAHOMA

GRADUATE COLLEGE

In Vitro STUDY OF HISTATINS:

STUDIES OF THE FREE AND COPPER COMPLEXED BIOLIGAND'S

STRUCTURE AND CATALYTIC ACTIVITY.

A DISSERTATION

SUBMITTED TO THE GRADUATE FACULTY

in partial fulfillment of the requirements for the

Degree of

DOCTOR OF PHILOSOPHY

By

ERIC ALAN HOUGHTON

Norman, Oklahoma

2009

In Vitro STUDY OF HISTATINS:
STUDIES OF THE FREE AND COPPER COMPLEXED BIOLIGAND'S
STRUCTURE AND CATALYTIC ACTIVITY.

A DISSERTATION
APPROVED FOR THE
DEPARTMENT OF CHEMISTRY AND BIOCHEMISTRY

BY

_____
Dr. Kenneth M. Nicholas

_____
Dr. Ronald L. Halterman

_____
Dr. Paul F. Cook

_____
Dr. George B. Richter-Addo

_____
Dr. Lance L. Lobban

I wholeheartedly dedicate this work to my family; most of all my parents, Dennis and Betty. Their support and guidance throughout my life have made this work possible.

Acknowledgments

I would like to thank the members of my committee, Prof. Ken Nicholas, Prof. Lance Lobban, Prof. Paul Cook, Prof. Ron Halterman, and Prof. George Richter-Addo.

I would also like to thank Dr. Susan Nimmo and Prof. Susan Schroeder for their assistance and guidance in the realm of NMR.

Prof. Yashige Kotake was of great assistance in the EPR work.

I would like to acknowledge and thank current and past members of the Nicholas Research Lab.

I would like to thank my family and friends for their continuing support.

Members of the OU community also deserve recognition as they are the people who make the university function day to day.

Finally, the A.C.S. Petroleum Research Fund deserves thanks for their financial support of this project. The University of Oklahoma Graduate Student Senate also financially supported the presentation of parts of this work at various venues.

Table of Contents

List of Tables

List of Figures

Abstract

The ability of the histidine-rich peptides, histatin-5 (*Hst*-5) and -8 (*Hst*-8), to support the generation of reactive oxygen species (ROS) during the copper-catalyzed oxidation of ascorbate and cysteine has been evaluated. High levels of hydrogen peroxide (70-580 mol/mol Cu/hr) are produced by aqueous solutions containing Cu(II), *Hst*-8 or *Hst*-5, and a reductant, either ascorbate or cysteine, as determined by the post-reaction Amplex Red (AR) assay. When the reactions are conducted in the presence of superoxide dismutase (SOD), the total hydrogen peroxide produced is decreased, more so in the presence of the peptides (up to 50%), suggesting the intermediacy of superoxide in these reactions. On the other hand, the presence of sodium azide or sodium formate, traps for hydroxyl radicals, has no appreciable effect on the total hydrogen peroxide production for the Cu-*Hst* systems. Electron paramagnetic resonance (EPR) spectroscopy spin-trapping studies using CYPMPO (5-(2,2-dimethyl-1,3-propoxy cyclophosphoryl)-5-methyl-1-pyrroline N-oxide) in the cysteine/Cu(II) reactions reveal the formation of the CYPMO-hydroperoxyl and -hydroxyl radical adducts in the presence of *Hst-8*, whereas only the latter was observed with Cu alone.

As *in vitro* ROS production involved copper ions, the complex formation of the peptide-metal species was also of interest. The specific residues involved in coordinating the copper were investigated using nuclear magnetic resonance spectroscopy (NMR) experiments, specifically by ^{1}H-^{15}N

heteronuclear multiple bond correlation (HMBC), heteronuclear single quantum correlation (HSQC), and ^{1}H-^{13}C HSQCAD experiments. Protonation of *Hst*-8 and model poly-imidazole ligands resulted in distinct downfield shifts of proton, carbon and nitrogen resonances of the imidazolyl units. Tight binding metal complexes of model compounds were also observed to have downfield resonance shifts upon binding Cu(I). Unfortunately, *Hst*-8 does not bind copper tightly enough to permit observations of downfield shifted peaks. Peaks were instead observed to be broadened and in some cases absent. However, because these were localized to only certain residues, assignments were made on the basis of which resonances exhibited such behavior. This evidence in addition to computational results led to the conclusion that residues histidine 3, histidine 6, and histidine 7 are involved in the binding of Cu(I) in *Hst*-8 at a 1:1 Cu(I):*Hst*-8 ratio of concentration in DMSO.

The conformational structure of *Hst*-8 in DMSO, both in the presence and absence of a copper (I) ion, has also been investigated using NMR experiments. The Nuclear Overhauser Effect (NOE), which is a nuclear spin transfer through space, was used in experimental series to identify protons in nearby space. This was useful in determining the larger three dimensional picture of the peptide in solution when the identities of the proton resonances were identified via total correlation spectroscopy (TOCSY) and ^{1}H-^{13}C HSQC experiments. After the spatial contacts were identified, boundary restriction data was generated by MARDIGRAS and the restriction data was input into a

molecular dynamics (MD) simulator CNS, which output the structure. We found that *Hst*-8 did not have either beta strand or alpha helical secondary structural elements, in DMSO either as a free ligand or in the presence of Cu(I).

Chapter 1: Introduction

1.1: Histatins and Antimicrobial Peptides

The histatins (*Hst*) are a group of 30 structurally related histidine-rich cationic salivary peptides (15-30 μM in healthy people) that are important members of the non-immune defense system and are essential to good oral and dental health.[1-5] The entire family of *Hst* are encoded by only two genes[6, 7] and expressed in the salivary glands.[8, 9] Of the 30 known *Hst*, there are only two that are directly encoded, *Hst*-1 and *Hst*-3.[6, 7] Others are produced via an as yet undetermined proteolytic pathway or via distinct mRNA sequences.[10] Curiously enough *Hst*-1 is posttranslationally modified to be phosphorylated at Ser2 and have its tyrosine residues partially sulfated.[11, 12] Sulfation numbers of between 1 and 4 on *Hst*-1 occur only for *Hst*-1 produced in the submandibular salivary gland; *Hst*-1 produced in the paratoid and sublingual glands was not sulfonated.[11, 12] Most of the phosphorylation of *Hst*-1, on the other hand, occurs in the paratoid gland.[12] *Hst* are found only in old world apes and higher primates, including western gorillas, bonobos, chimpanzees, and humans.[9, 13] *Hst*-8 and *Hst*-5, which form the basis of this study, have in common a 12-residue, His_4-segment - Lys-Phe-His-Glu-Lys-His-His-Ser-His-Arg-Gly-Tyr (K-F-H-E-K-H-H-S-H-R-G-Y). Several studies have shown to be essential to their antimicrobial properties. The *Hst* have diverse antimicrobial activity, effectively killing a variety of fungal and yeast

species, including pathogenic *Candida albicans*[1-3] and *Candida dubliniensis*,[14] as well as several families of bacteria.[15]

Yeast cellular membranes have a negative charge on the exterior by virtue of the incorporation of phospholipids on their exterior lipid bilayers. This allows for an electrostatic attraction between evolved cationic antimicrobial peptides and their microbial targets. The mode of action that most cationic antimicrobial peptides operate by is membrane intercalation by individual peptide units followed by a conformational change to an alpha helix while immersed in the membrane. Then the individual alpha helices aggregate and form pores through which the cellular contents are subsequently leeched into extracellular environments. Given this mode of action secondary structure is very important in terms of effective antimicrobial function. Initially, these peptides need to lack alpha helical structural elements so that intercalation into the membrane is possible. Then given the change of solution conditions while in the membrane, an alpha helix must form.

Hst, however, do not operate in this fashion. Firstly, active transport across cell membranes is required to move histatins into the cellular matrix as opposed to passive introduction through the lipid bilayer. *Hst*-5 has been shown to bind to heat shock protein Ssa 1/2.[16, 17] Upon binding, the *Hst* is actively transported inside. Indeed, microbes that have reduced respiration capacity are not as susceptible to *Hst*. This provides greater support for the active transport hypothesis, in that organisms with less energy available will

not be as able to actively transport as much *Hst*-5 into the cytosolic environment as those of the wild type variety. *Hst*-5 and other histidine rich peptides have been shown to disrupt endosomes; this property allows for *Hst*-5 escape into the greater cellular environment.[18] Secondly, in terms of the mode of action for antimicrobial activity, histatins do not operate by pore formation. Indeed, only a few species exhibit an increased concentration in extracellular fluids, including potassium ions, chloride ions, ATP, and a few smaller nucleotides, like NADH.[19, 20] Pore formation would result in a leeching of all types of cellular material into the extracellular environment. A few studies have suggested that the selective leeching is due to *Hst* interaction with Trk1p, a potassium ion transporter.[21-23] However, this does not explain the chloride and ATP release.

Another line of inquiry has been made into the question of *Hst*-5 introduction into the cellular environment, membrane destabilization, and membrane pore formation using liposomes as model membrane systems.[24, 25] Liposomes are lipid bilayers vesicles that mimic cell membranes with no proteins. Translocation of species across liposomal membranes then would only occur via passive transport consisting of association with the membrane, intercalation into the membrane, and entry into the liposome. In both studies membrane association was observed.[24, 25] Also in the study that investigated membrane translocation, *Hst*-5 was observed to have very little capacity for membrane translocation and virtually no capacity for pore formation as determined by leeching experiments, which combined together, caused the

authors to conclude that either active transport was at work or some other intrinsic feature of cellular membranes enhanced *Hst*-5 membrane translocation.[24] Thus, pore formation as a mode of action by the *Hst* is further discounted. Internalization by active transport is further supported and more evidence provided that *Hst* can interact with negatively charged membranes, like those of *Candida* and mitochondria in general.

Hst has also been noted to cause marked changes in cell morphology. Cells and their organelles have been observed in the presence and absence of *Hst*-3 and *Hst*-5. By use of light microscopy, it was noted that cells in the presence of *Hst* had markedly decreased cell volumes, resembling deflated balls, which suggests either an alteration of cytoskeletal components or an osmotic imbalance.[26] Fluorescence microscopy revealed mitochondrial swelling, decreased mitochondrial charge potential, and atypical dye distributions.[26-28] As the mitochondria maintain structural integrity, as inferred by exclusion of fluorescent dye, pore formation in the mitochondria as a mode of action for the antimicrobial activity for the *Hst* is also excluded.[26, 27] Transmission electron microscopy (TEM) confirmed the observations of mitochondrial swelling and decreased cell volume, but it was also noted that most organelle structures were hardly identifiable, save for the nucleus, the slightly enlarged mitochondria, and the massively swelled vacuole.[26] The loss of organelle structures it would seem contributed to the atypical fluorescent dye uptake. High resolution scanning electron microscopy (HRSEM) revealed in addition to the markedly decreased cell volumes and

mitochondrial swelling, the cells had much smoother cellular membranes, a further indication of a change in the structural membrane makeup.[26] A subsequent study would show that using freeze fractionated TEM that there were areas of smooth membrane and areas of rough membrane; essentially incubation with *Hst*-5 resulted in aggregation of intramembranous particles.[28]

Once on the interior of the cell, *Hst* localizes primarily on the mitochondrial membranes.[27, 28] This localization has been inferred by observations made with fluorescence microscopy, light microscopy, TEM, and HRSEM.[26-28] It has also been inferred from the studies done with liposomes, which were negatively charged like the mitochondrial membrane, whereby depolarization as a result of association was argued.[24] Since the liposomes lack any external proteins, the cationic nature of the *Hst*-5 was sufficient to allow for association. Direct detection of FITC-labeled (fluorescein isothiocyanate) *Hst*-5 location has been done by means of labeling anti-FITC mouse antibodies with gold followed by observation with TEM.[28] Results here indicated that *Hst*-5 was internalized and had association with internal cellular structures, namely mitochondrial membranes and the internal cell membrane.[28] Though electrostatic attraction maybe one component of the association of *Hst*-5 to the mitochondrial membrane additional factors should not be ruled out.

Here, the respiratory chain is inhibited, ATP is released, and reactive oxygen species (ROS) are generated.[19, 20, 27, 29-32] Use of the non-specific ROS probe 2',7'-dichlorodihydrofluorescein diacetate (H_2-DCFDA) showed

that *Hst*-5 triples the total ROS levels in *Candida* cells.[32] Fluorescence microscopic imaging of *Hst*-3,5-treated *Candida albicans* cells showed mitochondrial ROS generation (with the non-specific ROS probe dihydrofluorescein diacetate (DHF)) and a decrease in mitochondrial potential (using the potential-sensitive probe tetramethylrhodamine methyl ester, TMRM).[27]

However, the validity of the central hypothesis of ROS production by *Hst* has been questioned.[20] Dihydroethidium (HEt), which was used as an ROS indicator in early trials, is oxidized to ethidium by ROS. Both HEt and ethidium are fluorescent, though ethidium fluoresces red and HEt fluoresces blue. Water can quench the fluorescent activity, while intercalation into DNA can effectively protect the ethidium from water and lead to greater fluorescent activity. ROS are produced at the mitochondria and its negatively charged membrane electrostatically attracts the oxidized ethidium cation to it. Mitochondrial membrane depolarization would have the effect of reducing positively charged ethidium at the surface of the mitochondria due to a reduction of electrostatic potential and allow for it to effectively spread throughout the cell. *Hst*-5 is certainly known to cause mitochondrial membrane depolarization.[24,27] Thus it is not inconceivable that the ethidium could be having secondary interaction with nuclear DNA resulting in enhanced fluorescence. Secondly, introduction of ROS scavenger TEMPO was observed not only to have no effect on the HEt / ethidium fluorescence, giving more support to the hypothesis that fluorescence increase is derived

from interaction with nuclear DNA as a result of membrane depolarization, but also TEMPO showed no effect on killing assays.[20] When TEMPO-AC was used as an ROS indicator, no ROS increase was observed and H_2-DCFDA was claimed to have a background reaction making it unsuitable for ROS detection studies.[20] This does not represent a deathblow to the ROS production hypothesis. Although, HEt may react with nuclear DNA, data from HEt assays used to detect ROS production in cell free environments, which was done in one study on isolated mitochondria with *Hst*-5, should be completely valid.[30] In this study, enhanced ROS production upon exposure to *Hst*-5 was supported.[30] In the case where H_2-DCFDA was used to detect ROS *in vivo*, the critique concerning its background reaction interfering is not well founded.[20] Appropriate control conditions can distinguish a real reaction from a background reaction, though the results may not be as solidly quantitative. Another issue, of course, is the nature of the ROS probes themselves, in that they are all primarily radical ROS detectors. If the ROS in question is hydrogen peroxide, these probes, in competition with other processes, such as cellular catalase, would not be the best choice. Also, though the ROS scavengers have been tested for their ability to permeate into the cytosol, mitochondrial membrane permeability has not been evaluated. Thus if ROS production inside the mitochondrial matrix is elevated then the scavengers might be ineffective.

Another problem with the ROS hypothesis has been the inability to detect cellular changes resulting from an increased ROS concentration level.

An increase in the intracellular ROS levels would be expected to result in oxidative damage to proteins; yet when *Candida albicans* were subjected to exogenous *Hst*-5 (31 µM 30 min) no increase in protein carbonylation was observed. However under identical conditions a tripling of intracellular ROS was observed[32]. Though when *Hst*-5 was expressed by *Candida albicans* mutants, protein carbonylation was found to be increased, even compared to a mutant control.[32]

Apoptosis is programmed cell death. Cells activate apoptotic pathways for a variety of reasons, but the reason most relevant to the ROS production argument for *Hst* microbicidal activity is extensive oxidative damage. The markers of apoptotic pathways such as chromosomal conformational changes, DNA fragmentation, and cytochrome *c* release from mitochondria were investigated. The DNA was analyzed by SDS-PAGE and was observed to be normal in the *Hst*-5 producing cells, cells subjected to exogenous *Hst*-5, and the two other controls.[32] Cytochrome *c* release was probed by SDS-PAGE analysis followed by immunoblotting of isolated mitochondria exposed to exogenous *Hst*-5 (31 µM 30 min) and no increase was observed.[32] Finally, the SOD mutants, sod1/SOD2, SOD1/sod2, and sod1/sod2 were prepared and subjected to exogenous *Hst*-5 (31 µM 1 hr). No statistically significant difference was found between the control and those incubated with *Hst*-5.[32] So, though ROS production is clearly enhanced, it may be ancillary to the antimicrobial mechanism as no clear link can be established between the enhanced ROS production and cellular

death. Though again, it bears repeating that in each of these cases the cytosolic area of the cell is being investigated. *Hst* may cause disruption in mitochondrial processes or enhanced ROS production inside the mitochondrial matrix, which results in cell death.

Osmotic balance is clearly affected upon exposure to *Hst*-5 as evidenced by the aforementioned microscopy studies which observed cellular volume reduction and mitochondrial swelling.[26-28] This has led to a hypothesis of antimicrobial activity derived from these observations. Potassium ions are a major species that are observed to have an increase in extracellular concentration as a result of *Hst* exposure. As potassium ion concentrations are also a major source of osmotic pressure due to bioaccumulation of potassium, it is of course reasonable to investigate this line of thinking. When *Candida albicans* cells are pretreated with anionic channel inhibitors, diisothiocyanatostilbene-2,2'-disulfonic acid (DIDS), niflumic acid, or 5-nitro-2-(3-phenylpropylamino) benzoic acid, prior to exposure to *Hst*-5, cellular volume disruption and cell cycle arrest are either prevented or attenuated.[33] Also deletion of the *TRK1* gene, which encodes for the major potassium ion uptake system in *Candida albicans,* resulted in near complete protection of cells from the antimicrobial effects of *Hst*-5.[21] Given the highly charged nature of *Hst*-5, the likelihood of *Hst*-5 interacting with both anion and cation transmembrane regulatory proteins is low. Generally, channels for cations are negatively charged to attract the cations and anion channels are positively charged to attract the anions. The *Hst*

being cationic would be electrostatically repelled by the positive charge. Consider, too, that the localization of *Hst*-5 in the interior of the cell was primarily the mitochondria.[27, 28] So although the hypothesis is reasonable; a conclusion drawn from the data concerning interaction with anion channels is somewhat unsatisfying. The explanation of osmotic regulation disruption is certainly better and more inclusive than either one of the independent hypotheses; one that invokes *Hst* interaction and disruption of Trk1p, a potassium channel, or the other that invokes *Hst* interaction and disruption of an anion channel.

To further investigate the antimicrobial mechanism of *Hst*-5, a study of gene expression profiles was done for the entire *Candida albicans* genome to observe which proteins exhibited different expression profiles upon *Hst*-5 exposure.[34] Upregulated genes included those involved in cellular stress (both oxidative and osmotic), cellular metabolism, and mitochondrial genes. The majority of cellular metabolism regulating genes that were upregulated were primarily involved with the production of glycerol, which is used to help mitigate the effects of osmotic stress. This combined with the evidence gathered in the down-regulation of genes used to create proteins involved in plasma membrane transport of amino acids, GAP2; ion homeostasis, CSA1; and monosaccharide transport, NAG1, and the down regulation of genes involved in aerobic respiration point to the possibility that interference with the osmotic regulation of the cell is the primary mode of action for *Hst*-5.[34] Glycerol is produced from anaerobic respiration. So the change in production

of proteins related reducing aerobic respiration can be explained on the basis of osmotic stress. Further, it provides an alternative explanation for the observation that aerobically stressed mutants were better able to protect themselves from Hst-5 antimicrobial activity.[35] Lastly, the work investigated how pretreatment of cells with various agents affected cell survival rates. In both radial diffusion assays and candicidial assays, *Hst*-5 pretreatment resulted in increased susceptibility to sorbitol, which is used as an osmotic stress inducing agent, but had no effect on cells treated with H_2O_2.[34]

Although most of the genes that were observed to have altered transcription regulation were involved in the HOG1 pathway, two notable exceptions that are observed to have increased production involved in oxidative stress responses are CAP1 and SOD2.[34] Both are HOG1 pathway independent.[34] It then remains possible that *Hst*-5 involves both ROS production and osmotic regulation interference.

1.2: Reactive Oxygen Species (ROS) and Metal Ions

ROS is a generic term referring to any oxygen species that is more reactive than triplet oxygen. The production of ROS; particularly hydrogen peroxide, superoxide, and hydroxyl radical, is widely associated with reactions of redox active metal ions, particularly Fe(II,III) and Cu(I,II) or their complexes, with hydrogen peroxide or oxygen with a reductant.[36-39] ROS in the cellular environment are very well controlled in viable cells. They can be produced intentionally as a direct means of fighting against other cells or for

other purposes like instigating lignin production for cell wall construction. ROS are often times also produced as unwanted byproducts of cellular respiration activities. ROS production is a source of oxidative stress, and a loss of ability to adequately control ROS results in oxidative damage. Oxidative stress has been associated with the cellular aging, aging process, and many diseases, including arteriosclerosis, neurodegenerative disorders, such as Alzheimer's and Parkinson's diseases, and cancer.[40-49] Oxidative damage can also induce apoptosis. As aforementioned, apoptosis is programmed cell death. Some of the major systems that life forms have developed to manage ROS include SOD and catalase (CAT) enzymes. SOD enzymes take two equivalents of superoxide and two protons and produce one equivalent of hydrogen peroxide and one equivalent of oxygen (equation 1.2.1). Life has evolved very efficient systems to control superoxide. SOD enzymes are usually rate limited by diffusion rates. CAT, then, can dismutate the hydrogen peroxide produced into water and oxygen (equation 1.2.2).

eqn. 1.2.1

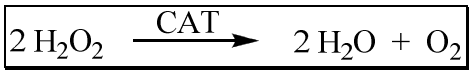

eqn. 1.2.2

In the system illustrated four equivalents of superoxide will have been used to generate two equivalents of oxygen and two equivalents of water. A potentially damaging ROS has been converted to materials required for aerobic survival, oxygen and water.

Although few quantitative comparisons have been made, it generally appears that metal ion coordination to a ligand, peptide, or protein can reduce or eliminate the metal ion's ROS-generating activity as well as alter the types of ROS produced.[50-52] Due to free copper and iron species ability to generate ROS combined with the need of cells to utilize both copper and iron in metalloproteins and elsewhere, cells have evolved systems to sequester and manage these biologically important yet dangerous metals. Some of the most notable iron containing metalloproteins includes hemoglobin and myoglobin, which are both involved in oxygen transport, here the iron is held as a heme unit. The enzyme cytochrome *c* oxidase (also known as complex IV) is one of many metalloenzymes involved in the respiration. Using its two heme iron moieties, Cu_B, and Cu_A centers, cytochrome *c* oxidase receives electrons and protons to reduce molecular oxygen to water via a series of one electron reductions.[53] ROS production by copper and/or iron containing metalloenzymes include the production of hydroperoxyl alkenes by the lipoxygenases, hydroxyl radical production by peroxidases, superoxide generation by xanthine oxidase, and of course oxygen radical production by horseradish peroxidase. As aforementioned; Cu, Zn SOD uses copper to help control both intentional and unintentionally generated ROS.[54-57] ROS production and handling by such complexes also can result in oxidative damage to the protein itself.[58-62]

Biomimetic complexes have also been created. These complexes also use transition metals and can also serve to mediate subsequent ROS transformations, e.g. superoxide disproportionation.[63-65]

A potential source for a transition metal in yeast could be a recently identified non-proteinaceous pool of copper.[66] This pool contains approximately 5 x 10^5 atoms in a soluble complex and acts as a copper buffer of sorts, responding to copper concentrations in the cytosol.[66] This then would allow for a source of copper ions by peptides like *Hst*, which contain metal binding motifs as well as metalloproteins synthesized by the organism.

1.3: Imidazole and Histidine

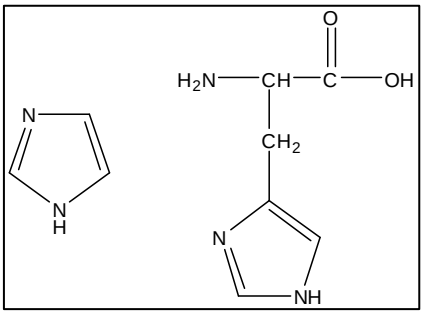

Figure 1.3.1. Illustration of structures; (left) imidazole and (right) histidine.

Imidazole is a well known ligand for transition metals. As illustrated in figure 1.3.1, nature has evolved an amino acid that incorporates the imidazole motif, histidine. Histidine is one of the least encoded amino acids. According to BLAST primary sequence data of the proteome, histidine

comprises a mere 1.8%-3% of all primary structure as calculated from a database of nonredundant proteins by R. F. Doolittle.[67] When histidine is found in the primary sequence of proteins, it is often involved in metal binding activities; Cu-Zn SOD, soybean lipoxygenase, and Auxin binding protein each use multiple histidine residues in their metal binding pockets. Certain sequences containing histidine have been shown to often be involved in metal binding interactions. Common Zinc binding motifs include His-X-His-X-His-X-X and His-His-Y-Z-His.[68] In addition to being a good zinc binding motif, the His-X-Y-Z-His sequence is also a good copper binding motif, particularly when X is a glutamate residue.[68] Though this list is far from complete, a final example of a metal binding primary sequence utilizing histidine is the amino terminal copper/nickel-binding motif (ACTUN) is Asp^{1}-X^{2}-His^{3}. This particular sequence has often been observed to be involved in metal binding.[69] The primary sequence of *Hst*-5, D-S-H-A-K-R-H-H-G-Y-K-R-K-F-H-E-K-H-H-S-H-R-G-Y, contains four of these types of motifs, an ACTUN and three variations of the histidine sequences. Furthermore, its primary sequence is 29% histidine. *Hst*-8, K-F-H-E-K-H-H-S-H-R-G-Y, contains variations of the metal binding histidine sequences and a histidine in the third position of the sequence which is a critical part of the ACTUN sequence. *Hst*-8 too is histidine rich; 25% of its primary structure is histidine.

1.4: Histatins, Metal Ions, and ROS

The respiratory inhibition and ROS generation induced by the histatins, their histidine-richness, their primary structures' similarity with metal-binding proteins, and relevant chemical studies suggest a possible link between the bioactivity of the histatins and metal ion binding.[70] Indeed, strong Zn^{2+}, Cu^{2+} and Fe^{2+} binding to *Hst*-5 (K_a ca. $2x10^7$ M^{-1} for Cu^{2+} and ca. 10^5 M^{-1} for Zn^{2+}) has been demonstrated using isothermal calorimetry (ITC).[71] In the study they found that there were three distinct binding events for *Hst*-5.[71] Cu^{2+} coordination to *Hst*-5 at the *N*-terminal D-S-H (Asp, Ser, His) domain was suggested by a later study based on NMR line broadening from added Cu^{2+}.[36, 37] As aforementioned this is an ACTUN region. ESI-MS studies have shown that 1-4 Cu^{2+}, 1-4 Ni^{2+} and 1-2 Zn^{2+} ions bind to *Hst*-3,-5.[38] The strong metal ion-binding histatins could potentially recruit Cu or Fe ions. The resulting metal/peptide complex could then activate molecular oxygen or hydrogen peroxide to produce damaging ROS.[39, 72-74]

The ITC, NMR, and MS studies together have added valuable information to the picture of metal binding by *Hst*. However, there are some gaps that remain to be filled in the knowledge base. The ITC work using the whole peptide does little to elucidate the precise binding motif involved in the binding events. Whereas the NMR study, in effect, proves what the researchers already knew. By utilizing only that fragment of *Hst*-5 that corresponds to the ACTUN region, the researchers were capable of proving metal binding to a known metal binding region. They neglected the potential

for competitive or synergistic interaction of the other type of known metal binding regions present in *Hst*-5, the His-X-Y-Z-His type regions. Another aspect of concern is that none of these studies addresses the issue of Cu(I) binding. The intracellular environment is a reducing environment, so copper species are likely to spend at least some of their time in a partially reduced state. This is an important point as the coordination environment of Cu(I) is different than that of Cu(II). Cu(I) generally prefers a tetrahedral environment whereas Cu(II) prefers a square planar geometry. Certainly there remains work to be done both in terms of identifying the metal binding moiety the full *Hst*-5 but also in those 19 other *Hst* fragments that do not possess an ACTUN region.[75]

Chemical reactivity studies too are similarly lacking in terms of their treatment of the peptide systems. *In vitro* work done on two synthetic analogues of *Hst*-5 indicated pro-oxidant activity.[76] However, here again they used first of all a fragment of *Hst*-5, and one that even lacks the potentially competing His-X-Y-Z-His motifs. The first peptide (DSHAKRAHGY) represented the first 10 residues of *Hst*-5 with an H7/A7 mutation the other (DSAAKRAHGY) was the first 10 residues of *Hst*-5 with H3/A3 and H7/A7 mutations.[76] The observation of ROS production by a copper bound in an ACTUN type environment is hardly surprising. Previous work has shown that such a complex can be involved in oxidative cleavage of DNA.[52, 77]

However, one should not be so quick to rule out the other binding sites for metal binding and ROS generation. Indeed *in vitro* studies have

demonstrated that *Hst*-8 copper complexes are capable of generating ROS at levels comparable to those of *Hst*-5 copper complexes.[70] Again, though *Hst*-5 maybe the most active in terms of antimicrobial activity, 19 of the *Hst* thus far identified have no *de facto* ACTUN motif.[75] Meanwhile many of those peptides discussed in the previous sections have active sites containing multiple histidine residues for metal ion binding purposes and are involved in handling ROS. Clearly scientific investigation into the possibility of multiple histidine residues binding copper ions in native *Hst* peptides is warranted.

1.5: Conformation and Bioactivity

Primary structure is only the beginning of the discussion of proteins. Since not all metal binding is done by residues in close proximity by virtue of sequence, a discussion of three-dimensional conformation is very important. Indeed, the conformation of proteins is so important that denaturation often results in loss of function. In addition misfolded proteins have been shown to be the cause of several diseases not the least of which are Kuru, Creutzfeldt-Jakob Disease, and others. Studies of *Hst*-5 and *Hst*-8 have been done in both water and lipid mimicking solvents such as DMSO and hexafluoroacetone (HFA). Though *Hst*-5 is lacks alpha helical or beta strand secondary structure in water, it adopts an alpha helical conformation in the membrane mimicking solvents DMSO as determined by NMR techniques coupled with *in silico* MD simulations.[78] *Hst*-8 has been determined to be a beta strand in pH 4.0 water and pH 4.0 DMSO, but alpha helical in an HFA

water solution by utilization of similar methodology.[79] Other techniques used to probe the conformation of *Hst* in solution include CD and FTIR.[80-82] Just as conformation can affect metal binding, so too can metal binding influence conformation. One of the best studied examples of such are the zinc fingers, which give rise to conformationally compact domains for DNA binding, as a consequence of binding a zinc ion. In addition to the aforementioned conformation studies, information can also be gathered on the metal and its local environment by NMR and EPR spectroscopies.

1.6: *In silico* modeling and studies

As computers become ever more powerful, chemists have been using them to solve ever more sophisticated problems. Peptides and proteins contain a large number of atoms and have traditionally been investigated using molecular mechanics (MM) and semi-empirical methods. Each of these methods has its own assets and liabilities as a result of assumptions made for that particular methodology. MM initially assumes that bonds of a given bond order have a set of properties, such as rotation and length, based upon the generally user specified bond order. Semi-empirical methods, such as PM3 and AM1 begin to treat bonding between atoms as a result of electron density. However, only the electrons involved in bonding are considered, and many of the parameters of the bonding electrons have been set by using parameters from real molecules. This is done for calculational simplicity. A limitation is that only molecules most similar in structure to those molecules

used to build the parameters will have the most accurate structures. *Ab initio* and density functional methods (DFT) once practical only for small molecules have increasingly been used for investigating larger systems up to and including short peptides. *Ab initio* methods are attractive in that bonds and bonding electrons are now treated as electron systems without external reference to other molecules. In effect, far fewer assumptions are made about the system as a whole, including treatment of core electrons. However, this accuracy comes at a price in terms of calculation size and time. For larger proteins and enzymes mixed methods, which use molecular mechanics and semi-empirical methods for the majority of the structure allow higher levels of theory to be applied directly to the active site.

1.7: Statement of Objectives

We have sought to add to the knowledge base of the antimicrobial *Hst* peptides in terms of meeting several project objectives. First, as there is still debate as to if ROS are implicated in the antimicrobial activity of the *Hst*, we sought to investigate the possibility in an *in vitro* system. In this way all external variables and possible side reactions would be eliminated and there would be definitive and quantifiable evidence for specific ROS production by *Hst* systems.

Another major gap identified in the scientific literature is the lack of conformational knowledge of the *Hst* when involved in metal binding. Many studies have already been done both on *Hst* conformation in the free state

and *Hst* metal binding activity, however, there has yet been no study that has integrated both metal binding and global conformation of the peptide.

Along the same lines, there has not yet been a definitive study on the metal binding environment of the peptides themselves. Many peptide analogues have been made and their metal binding activity studied. However as most of them delete histidine residues, and are very short in length, a comprehensive understanding of the metal binding environment has yet to be investigated.

Chapter 2: Study of Reactive Oxygen Species *in vitro*

2.1: Introduction

We sought to study specific ROS production by a copper metal complex in a reducing aerobic environment and quantify those species produced. Previous studies had used only general probes in quantification of ROS. Moreover, *in vivo* experiments make an absolute quantification of many ROS impossible, given the presence of enzymes, such as superoxide dismutase and catalase, as well as other ROS scavengers. In order to quantitatively identify specific ROS we conducted *in vitro* experiments, however, we took several steps to ensure that the results were as biologically relevant as possible. The cellular environment is a reducing environment, and many biologically relevant reductants exist, including ascorbate, cysteine, NADH, and GSH. Also given the *Hst* affinity for copper ions as well as a recently identified labile pool of copper in yeast,[66] we chose to utilize copper as our transition metal.

The system was buffered at pH 7.4. The pH was chosen due to its biorelevance. However, the buffer selection was one of the most difficult decisions to make. The ideal buffer should not interfere with metal ion binding of *Hst* to metal, not be oxidizable under the conditions of the experiment, not be capable of being used as a reductant nor interfere with the assay being utilized. Phosphate is often used as a buffer *in vitro* for several reasons. The buffering capacity occurs in the biologically relevant

range and humans use phosphate species as buffering agents. It is not oxidizable and is not utilized as a reducing agent. However phosphate is not suitable for our purposes, since it has been shown to form complexes with copper ions[83, 84] and perhaps most importantly has been shown to have adverse effect for study of ROS producing systems.[85] We selected morpholinopropylsulfate, MOPS, as our buffer after some initial work with phosphate buffered systems. Though MOPS is oxidizable,[85] we wanted to ensure that ROS generation was due exclusively to *Hst*-cupro complexes and not from free metal ion species as MOPS does not engage in copper ion binding.[84, 86, 87]

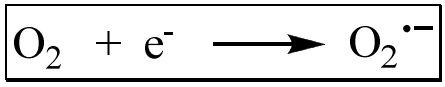
eqn. 2.1.1


eqn. 2.1.2

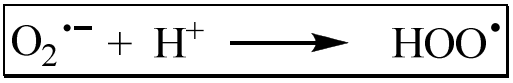
eqn. 2.1.3


eqn. 2.1.4

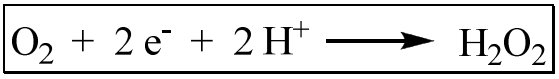
eqn. 2.1.5

The first ROS we sought to investigate was the formation hydrogen peroxide. As shown by the series of equations listed above (equations 2.1.1-2.1.5) there are a number of ways by which oxygen can be converted to hydrogen peroxide in a reducing environment. Equation 2.1.1 illustrates superoxide being generated by a single electron transfer, SET, to molecular

oxygen. Hydrogen peroxide can then be created from superoxide by a subsequent SET in the presence of protons according to equation 2.1.2. Another possibility exists utilizing the superoxide and adding a proton to obtain the hydroperoxyl radical (equation 2.1.3), which can then be further reduced in a separate step in the presence of a proton to get hydrogen peroxide (equation 2.1.4). Of course the most direct way to obtain the hydrogen peroxide from molecular oxygen is a two electron transfer in the presence of protons (equation 2.1.5). Addition of a transition metal catalyst to the system can complicate thing further because each of these steps could happen while substrate or product is bound to the metal or if it is free in solution. As described in the previous narrative, there is a distinct possibility that superoxide plays a role in the formation of hydrogen peroxide. Thus we sought to investigate the possibility of free superoxide's intermediacy in the formation of hydrogen peroxide, the first ROS we sought to investigate. These two major ROS provide the foundation of this study.

To assess the viability of metal-*Hst* complexes for ROS production, we report on our study of the Cu-*Hst*-promoted aerobic reactions with the bioreductants ascorbate and cysteine, which shows that hydrogen peroxide and superoxide are produced at high levels and catalytically by both Cu-*Hst*-5 and Cu-*Hst*-8 complexes. The major findings of this study have already been published.[70]

2.2: Amplex Red Assay

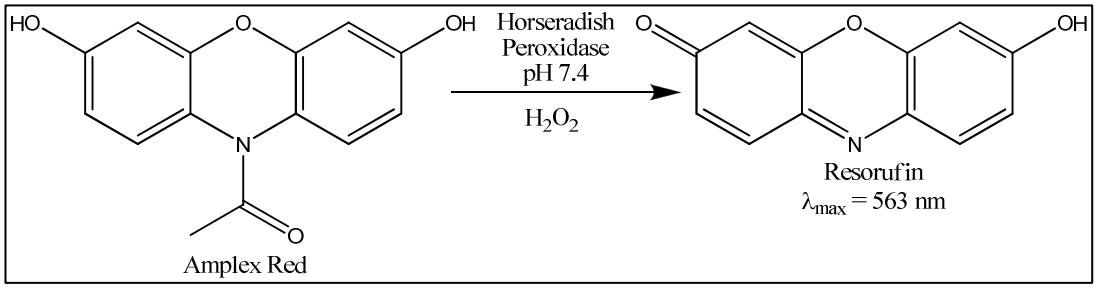

Figure 2.2.1. The transformation of Amplex Red to resorufin by horseradish peroxidase in the presence of hydrogen peroxide at pH 7.4.

As shown in figure 2.2.1, Amplex Red (AR) can be used to spectrophotometrically monitor hydrogen peroxide. Hydrogen peroxide produced can be determined by the horseradish peroxidase (HRP) catalyzed reaction with AR to give resorufin.[88-90]

$$AscH_2 + O_2 \xrightarrow{Hst\text{-}Cu} Asc_{(ox)} + H_2O_2 \quad \textbf{eqn. 2.2.1}$$

We initially chose to utilize ascorbic acid as the reducing agent as it is readily available in the cellular environment. Also, ascorbate had previously been shown to be able to reduce molecular oxygen to hydrogen peroxide at neutral pH both with[91-93] and without transition metal catalysts.[91, 94] The autooxidation of ascorbate to yield superoxide and hydrogen peroxide has been shown to proceed at a rate of $1x10^{-10}$ M^{-1} s^{-1}.[94] The reaction of interest is profiled in equation 2.2.1. Here the ascorbic acid and molecular oxygen are reacted together in the presence of the *Hst*-Cu complex to dehydroascorbate and hydrogen peroxide. Reactions conducted in the

presence of a transition metal exhibit a different kinetic profile and much greater activity than reactions carried out in the absence of a transition metal. This leads to the conclusion that though the autooxidation pathway exists as a potentially competitive reaction, the preferred reaction route involves the transition metal complex. Further, copper had been shown to catalyze this reaction and the rate of catalysis was dependent on the ligand set and coordination geometry.[92, 95] Experiments were done to ascertain what concentration of copper ion would be best for the system. These initial screenings were done in phosphate buffer without addition of ligands and an arbitrary concentration of hydrogen peroxide.

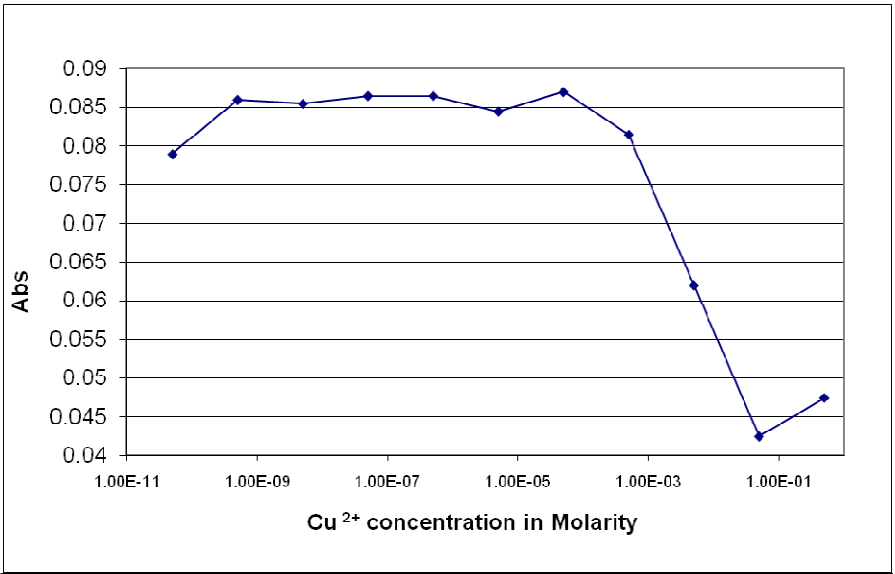

Figure 2.2.2. Illustration of the effects of addition of $CuCl_2$ to a solution of 50 µM hydrogen peroxide, which was then assayed with the Amplex Red assay.

Figure 2.2.2 is an illustration of the effects of addition of $CuCl_2$ to a solution of 50 µM hydrogen peroxide, which was then assayed with the

Amplex Red assay. It shows a test conducted with a constant amount of hydrogen peroxide and a variable amount of copper in a phosphate buffered system utilizing the AR assay for hydrogen peroxide. The expected result would be a constant level of absorbance across the continuum of the assay. However, due to interference of copper at high concentrations the assay is not suitable for millimolar concentrations of copper and higher. However, since we are primarily concerned with micromolar concentrations and lower, this interference should not pose a problem with our experiments. The micromolar range, which is the most bio-relevant, is certainly within the linear region. The drop in response is likely due to denaturation of the HRP, though Fenton chemistry cannot be ruled out. Fenton chemistry involves redox-active transition metals, usually iron or copper complexes, and produces hydroxyl radicals and hydroxide equivalents using hydrogen peroxide as a substrate as shown in equation 2.2.2.[96, 97]

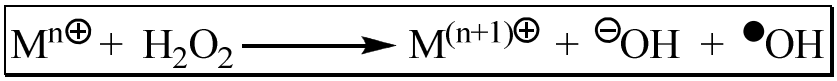
eqn. 2.2.2

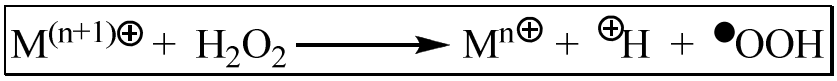
eqn. 2.2.3

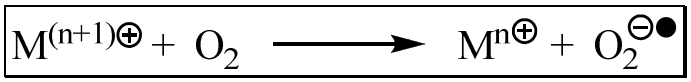
eqn. 2.2.4


eqn. 2.2.5

In order to regenerate the reduced metal species hydrogen peroxide again acts as a substrate as shown in equation 2.2.3. Alternatively, oxygen can be reduced to superoxide to regenerate the oxidized metal as shown in equation 2.2.4. This clearly then directly interferes with the ability to observe the hydrogen peroxide using the AR assay (figure 2.2.1 and equation 2.2.5).

We conducted some preliminary studies of systems with variable copper ion concentrations in constant concentrations of peptide (if present) and ascorbic acid in pH 7.4 phosphate buffer (data not shown). The wells were incubated for 1 hr and then developed with AR working solution. In these initial studies we observed *Hst*-8 copper systems produce ROS at a concentration similar to that of free copper similar to the systems discussed later. The *Hst*-5 copper system had fivefold greater activity However, as aforementioned phosphate buffer engages in complexing behavior with copper.[83, 84] This of course creates an issue with the identification of the compound responsible for ROS production. That is why we chose to focus on a buffer system that would not be engaging in complexation.

Our initial study focused on the production of hydrogen peroxide by Cu-*Hst* systems. In these experiments aerobic aqueous solutions (MOPS buffer, pH 7.4) containing Cu(II) (0.0 - 0.00125 mM), *Hst*-5, 0.0- 0.025 mM) or *Hst*-8, 0.0- 0.025 mM) and ascorbate as the stoichiometric reductant (1.25 mM) were incubated at room temperature for 60 min. As aforementioned, though MOPS is oxidizable,[85] we wanted to ensure that ROS generation was due exclusively to *Hst*-cupro complexes and not from free metal ion species

as MOPS does not engage in copper ion binding.[84, 86, 87] The hydrogen peroxide produced was then determined by its horseradish peroxide-catalyzed reaction with Amplex Red to give resorufin, monitored spectrophotometrically (570 nm).[88] Figure 2.2.3 illustrates the hydrogen peroxide production in the three ascorbate/oxygen systems: A) with Cu^{2+} only (as $CuCl_2$); B) with Cu^{2+}/*Hst*-8; and C) with Cu^{2+}/*Hst*-5 as a function of the copper concentration. The key findings are: 1) all three systems catalyze the efficient generation of hydrogen peroxide with similar activity, with turnover numbers (TON, mol H_2O_2/mol Cu) measured at 0.1875 nanomoles Cu present of up to 130 for *Hst*-5/Cu, 107 for *Hst*-8/Cu, and 140 for free Cu; 2) in the absence of added Cu^{2+}, hydrogen peroxide generation is negligible; and 3) hydrogen peroxide production increases approximately linearly with copper concentration in all three systems up to ca. 2:1 Cu/*Hst* for B,C.

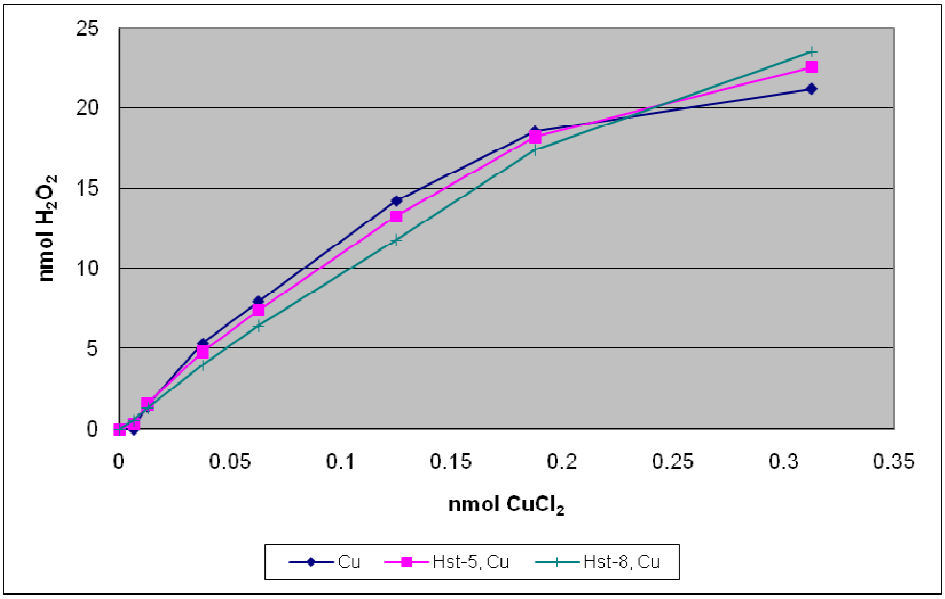

Figure 2.2.3. Copper(II)-dependent hydrogen peroxide generation with ascorbate. Reactions contain 62.5 nmol ascorbic acid, 0.0625 nmol peptide (if present), and a varied amount of copper (II) chloride in pH 7.4 MOPS buffer (background subtracted).

The similar catalytic activities of the oxidizing systems in the presence and absence of the Histatin peptides raises the possibility that much of the peroxide activity is derived from free copper ion catalysis.[98, 99] Since it has been shown that K_a for Cu(II) binding to *Hst*-5 is 10^7,[16] a set of reactions was conducted at a high (100:1) *Hst*/Cu ratio to ensure virtually complete *Hst*-5 binding to Cu^{2+} (> 99 % calculated). Under these conditions hydrogen peroxide is still produced at high levels with a TON up to 136 (figure 2.2.4). This TON is similar to that obtained in the lower *Hst*:Cu concentration ratio indicating that hydrogen peroxide formation in the Cu-*Hst* systems is derived primarily from peptide-bound copper species.

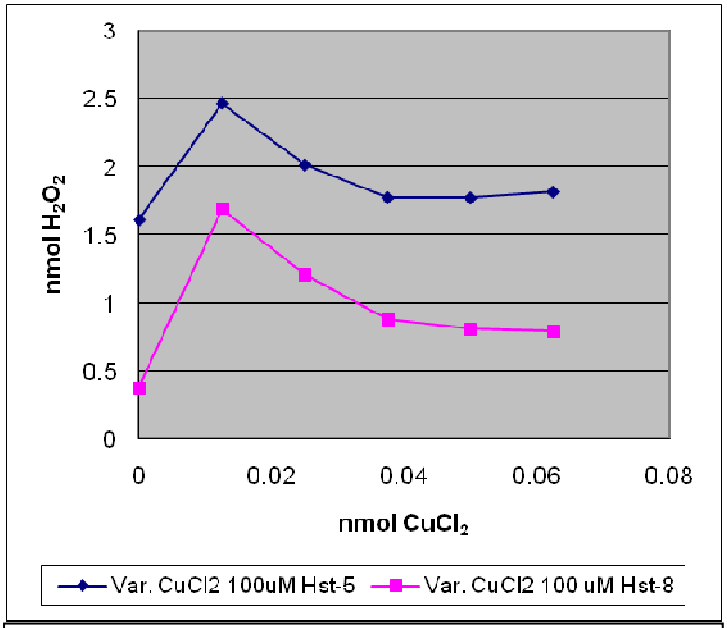

Figure 2.2.4. H_2O_2 production at high *Hst*/Cu(II) with ascorbate. 62.5 nmol ascorbic acid, 1.25 nmol *Hst* and 0-0.0625 nmol $CuCl_2$ in pH 7.4 MOPS.

Another bio-relevant reductant, cysteine, is also effective for the production of hydrogen peroxide by Cu-*Hst* catalyst systems. Figure 2.2.5 shows the Cu-dependent hydrogen peroxide production by aerobic cysteine solutions (MOPS, pH 7.4) after one hr using the Amplex Red assay. Key features include: 1) similar, high H_2O_2 activity for both the Cu-only and Cu-*Hst-8* systems with TONs of 300-500/hr; 2) hydrogen peroxide production increases approximately linearly with copper concentration up to ca. 1:1 Cu/*Hst*-8; and 3) hydrogen peroxide formation is negligible in the absence of copper.

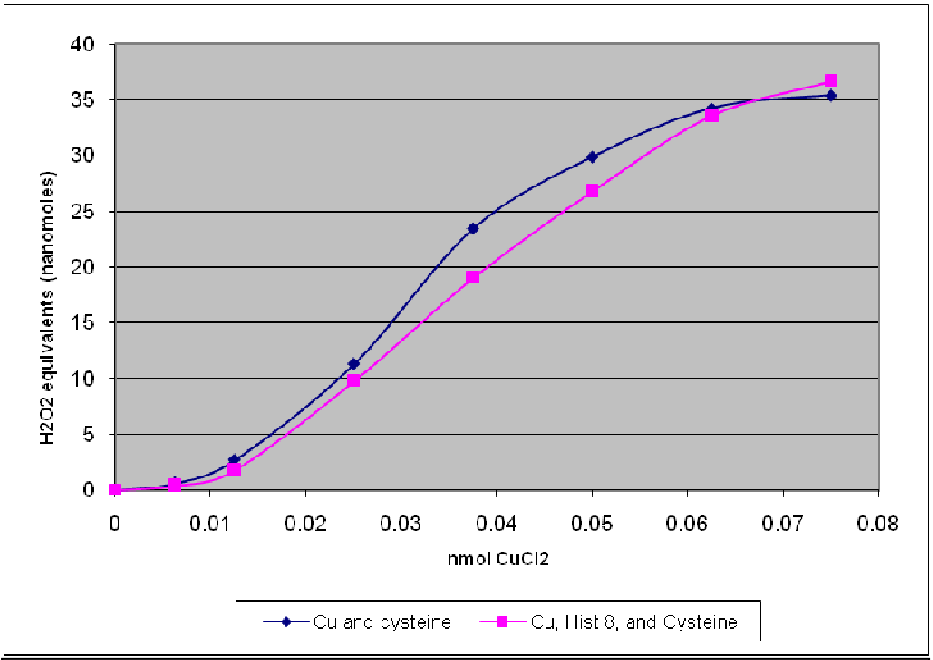

Figure 2.2.5. Copper (II) dependent H_2O_2 generation by cysteine. Reactions contain 62.5 nmol cysteine, 0.0875 nmol peptide (if present), and a varied amount of copper (II) chloride in pH 7.4 MOPS buffer (background subtracted).

We have shown that *in situ* generated copper/*Hst*-5 copper/*Hst*-8 complexes are capable of generating hydrogen peroxide at levels similar to that of free copper in reducing environments. Ligands can greatly affect the ability of copper to generate ROS. Some, like EDTA can completely inhibit the ability of copper to undergo such chemistry. However, even in systems with a high *Hst*:Cu ratio, we were still able to observe ROS production catalyzed by an *Hst*/Cu complex (figure 2.2.4).

However, given such a high concentration of *Hst* relative to Cu, it should be pointed out that the complex formed under such conditions may be different than one formed under lower concentration ratios. Specifically, there

exists a high probability that multiple peptides are associated with a single copper ion. Also one should not forget that *Hst*-5 has multiple binding sites. So a complex formed by utilization of multiple intrapeptide binding motifs would be disfavored at high *Hst*-5:Cu ratio.

It is also worth noting that we observe similar trends in activity using either cysteine (figure 2.2.5) or ascorbic acid (figure 2.2.3) at low *Hst*:Cu concentration ratios. Both of these external reductants are biorelevent. Ascorbic acid is of course vitamin C and cysteine is the reducing equivalent in the glutathione. In both cases ROS production for the peptide copper complexes was at a level similar to that of free copper.

2.3: Amplex Red with SOD Assay

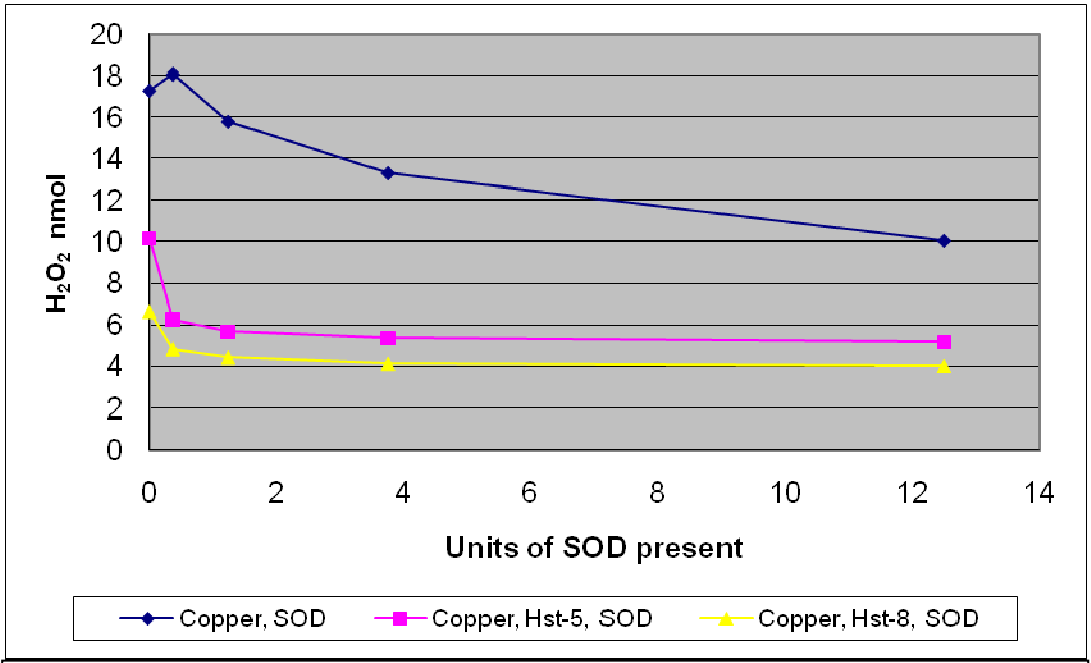

Figure 2.3.1. SOD effects on H_2O_2 production by an ascorbate system. 0.0625 nmol $CuCl_2$, 62.5 nmol ascorbic acid, and 0.188 nmol peptide (if present) in pH 7.4 MOPS.

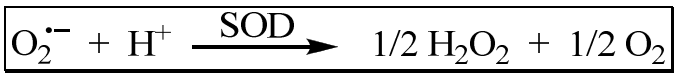

eqn. 2.3.1

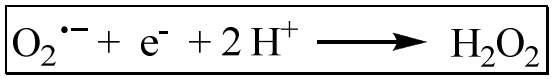

eqn. 2.3.2

eqn. 2.3.3

eqn. 2.3.4

To probe further the mechanism of hydrogen peroxide formation in the Cu-only and Cu-*Hst* catalyst systems, we investigated the effects of superoxide dismutase (SOD) on the ascorbate-oxygen reactions. A previous study had already established the ability of the SOD-Amplex Red-HRP linked assay system to detect superoxide.[89] To understand the observed SOD effects, it must be understood that hydrogen peroxide was quantified after a one hour reaction period. In one set of experiments no SOD is added and in the other, SOD is present from the initiation of the reaction. Since SOD catalyzes the conversion of superoxide to hydrogen peroxide and oxygen (equation 2.3.1), if superoxide is an intermediate in the formation of hydrogen peroxide according to equation 2.3.2, but is instead effectively trapped by SOD present during the reaction via equation 2.3.1, a decrease (up to half) in the total amount of H_2O_2 produced would be anticipated.

The reactions of ascorbate/oxygen with the Cu-only and Cu-*Hst* systems were conducted as previously *in the presence of 0.5-13 units of*

SOD and the H_2O_2 formed was again assayed *after the one hr reaction* via the AR/HRP method. Figure 2.3.1 compares the effects of SOD on the ascorbate oxidation by Cu alone, Cu-*Hst*-5 and Cu-*Hst*-8. Although the H_2O_2 production of all three reactions is decreased with increasing SOD, there are significant quantitative differences. The *Hst*-containing systems show a dramatic decrease in H_2O_2 production, up to ca. 50%, with only 1-4 units (8.64×10^{-2} – 3.46×10^{-1} nmol) of added SOD, whereas the free copper system requires over 10 units (8.64×10^{-1} nmol) of SOD for an approximate 40% decrease. As a control ascorbate in the presence of only SOD showed activity no greater than the ascorbate alone. These results indicate that while both the free Cu and *Hst*-Cu systems likely produce superoxide as an intermediate, there are differences in the extent to which superoxide contributes to the total hydrogen peroxide production in these systems, suggesting a difference in mechanisms of ROS generation in the presence and absence of the peptides. Due to the thiol oxidase activity of Cu/Zn-superoxide dismutase[55-57, 100, 101] (equations 2.3.3 and 2.3.4), it was not suitable for use with the cysteine reducing agent systems.

2.4: Amplex Red Assays with Hydroxyl Radical Traps

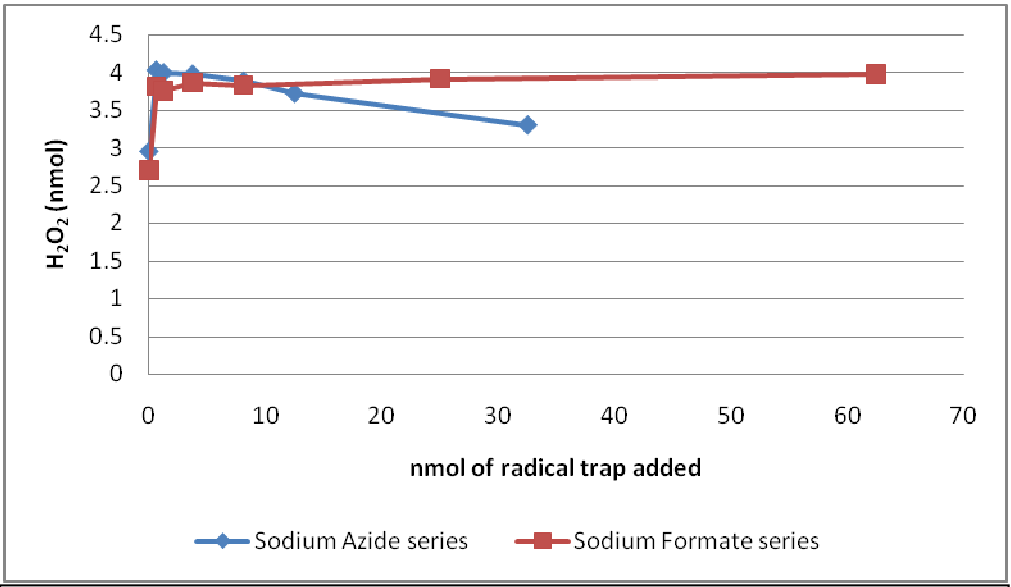

Figure 2.4.1. Effects of hydroxyl radical traps on hydrogen peroxide production by ascorbate systems.

Some aerobic copper/ascorbate systems have been reported to generate hydroxyl radical.[93] To assess the possible intermediacy of hydroxyl radicals and their contribution to hydrogen peroxide formation in the Cu/*Hst*-catalyzed reactions, the ascorbate oxidations were conducted in the presence of variable concentrations of the established hydroxyl radical traps,[54, 102-104] sodium formate and sodium azide, in separate trials, followed by determination of the hydrogen peroxide produced. It can be seen (figure 2.4.1) that they did not decrease H_2O_2 generation, even when in large excess. In fact we observe the opposite, observable hydrogen peroxide is increased. We conclude, therefore, that hydroxyl radical is not a major intermediate generated by the ascorbate-Cu systems in the presence of the

histatins.

Although we will observe that hydroxyl radical is generated by both peptide/Cu and free copper systems (Section 2.7), these are either generated by a competing pathway or the result of a decomposition of hydrogen peroxide or some form of hydroperoxyl adduct. As addition of these hydroxyl radical traps results in an increase in hydrogen peroxide assayed, they are protecting the formed hydrogen peroxide from a decomposition pathway, are protecting intermediate superoxide from a decomposition pathway, and/or are themselves used as an external reducing agent by the *Hst*/Cu system for hydrogen peroxide production. Such an investigation, however, would be a major undertaking, a project unto itself, and would serve to remove focus from the central ROS already identified, the hydrogen peroxide and superoxide.

2.5: Nitrotetrazolium Blue Assay

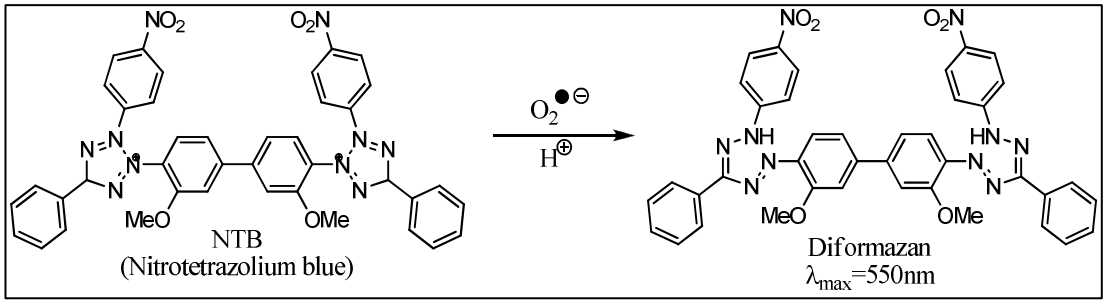

Figure 2.5.1. Production of diformazan from NTB by superoxide and protons.

Given the results obtained in the AR with SOD trials (section 2.3), we sought to further investigate the generation of superoxide by the peptide bound copper complexes. As shown in figure 2.5.1, nitrotetrazolium blue (NTB) has been shown in previous studies to be reduced by superoxide in the presence of protons to diformazan.[105, 106] This of course would be ideal for extending the experimental evidence for a difference in the mechanism and specific ROS produced by peptide bound and peptide free copper in a reducing environment. However, there exists some discrepancy in the literature concerning the compatibility of NTB with ascorbic acid. One study used ascorbic acid concentrations at 3 mM over a varying range of pH and claimed success in detecting superoxide with NTB.[107] To add support to their claim of superoxide detection in the presence of ascorbate, they added SOD and observed complete inhibition of the reduction of NTB to diformazan.[107] This is not to say that such a report of superoxide detection has been limited to only one report, in fact there exist several, Petyaev, I. and Weng, M. as well as references therein back such claims.[108, 109]

On the other hand NTB has been used to evaluate ascorbate oxidase activity of cell lysate fractions.[110] Cell lysate fractions were separated by SDS-PAGE. The resulting gels were washed in an ascorbic acid solution (25 µM) and then developed with an NTB solution. Fractions that were observed to have ascorbate oxidase activity were denoted by their lack of color. In effect they observed that NTB reacted with ascorbic acid to form the

diformazan because if ascorbic acid oxidase activity is present in the fraction no ascorbic acid is present to reduce the NTB.

Our studies suggest an incompatibility of NTB with ascorbic acid. We observed direct reduction of NTB by ascorbic acid (data not shown). The reaction was so fast at pH 7.4 in MOPS buffer that there was no real possibility for even subtraction of a background reaction. We observed during trials for potential backgrounds that the only variable that mattered was concentration and presence of ascorbic acid (data not shown). Thus we sought to uncover another bio-relevant reductant that would be compatible with the NTB. We ultimately found that thiols were compatible with NTB and produced superoxide in the presence of copper.

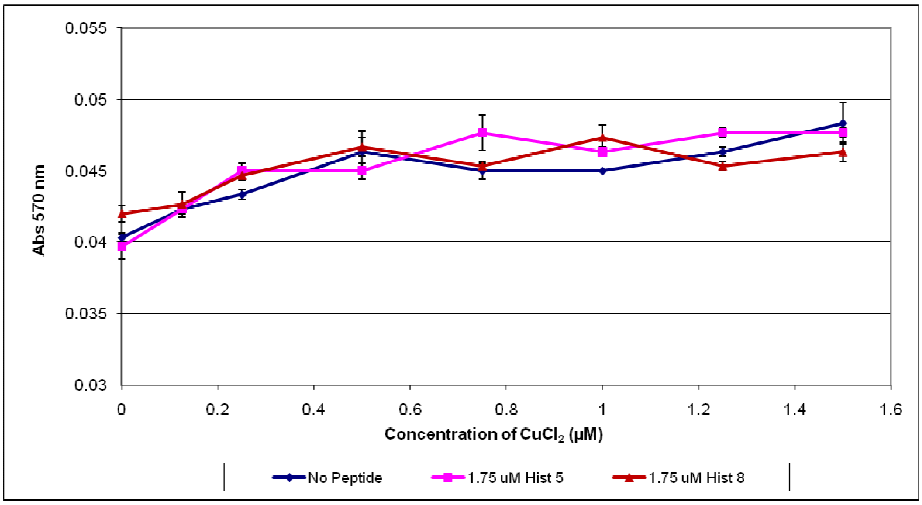

Figure 2.5.2. Effect of varying copper concentrations on superoxide production in systems containing 1.25 mM cysteine and 1.75 µM of peptide (if present) in pH 7.4 MOPS buffer as assayed by NTB assay.

Figure 2.5.2 illustrates the effects when we varied copper concentration on superoxide production by a system that utilizes cysteine as a reductant. The data indicates that there is increasing superoxide production with increasing copper concentrations. Though the system has a slightly increasing superoxide production in response to increasing copper concentration as shown in figure 2.2.5 there is a much larger effect for production of hydrogen peroxide in response to increasing copper concentrations. We can then conclude that the superoxide is rapidly converted to hydrogen peroxide in the presence of copper and that the rate at which it is converted to hydrogen peroxide by the copper or copper peptide complex is faster than the conversion of the NTB to the formazan.

2.6: NTB with SOD

Data for the NTB systems containing SOD is not shown because the SOD effectively quenched all superoxide that was produced when it was present at any level. Of course, an alternate explanation is that SOD was engaging in thiolase activity[55-57, 100, 101] and turning over the cysteine and N-acyl cysteine into hydrogen peroxide and the disulfide, neither of which is detectable using NTB. This was described earlier in equations 2.3.3 and 2.3.4. It had been reported that superoxide is generated by SOD engaging in thiolase activity as observed by diformazan produced by reduction of NTB.[55] However, we did not observe such activity. Our observations of systems containing cysteine and SOD showed no production of diformazan from NTB.

Given the results of the effective quenching of diformazan formation from NTB, the observation of formation of diformazan from NTB in the absence of SOD, as well as studies done with the spin trapping agent CYPMPO (Section 2.7), we feel confident in stating that *Hst*/Cu catalytic systems generate free superoxide when cysteine is utilized as an external reducing agent. Further, given the results obtained from the Amplex Red assay in presence of SOD, the *Hst*/Cu catalytic system also generates free superoxide. Taken together all of this points to the conclusion that the addition of *Hst* changes the nature of the ROS produced as an intermediate on the pathway toward hydrogen peroxide generation.

2.7: Spin Trapping ROS with CYPMPO

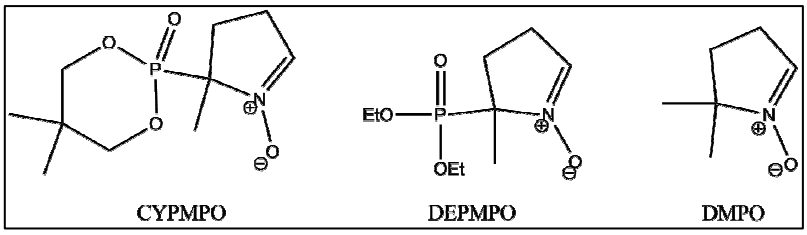

Figure 2.7.1. Structures of the spin traps CYPMPO, DEPMPO, and DMPO.

Spin trapping of reactive oxygen species is often utilized to indicate the types of species formed.[111] Figure 2.7.1 illustrates the structures of three compounds used in radical spin trapping studies. CYPMPO (5-(2,2-dimethyl-1,3-propoxy cyclophosphoryl)-5-methyl-1-pyrroline N-oxide) is structurally similar to DEPMPO, 5-(diethoxyphosphoryl)-5-methyl-1-pyrroline N-oxide,

and they both derive from the DMPO (5-dimethyl-1-pyrroline N-oxide).[112] The spectral signatures and hydroperoxyl adduct stabilities of CYPMPO and DEPMPO are very similar. However, the slight structural difference between the two compounds leads to greater stability of the CYPMPO.[112, 113] The phosphoryl unit is very important for hydroperoxyl adduct stability. Both CYPMPO and DEPMPO have hydroperoxyl adducts that are more than two orders of magnitude more stable than the DMPO hydroperoxyl adduct. [112, 113]

We have already seen that Cu-*Hst*-5,8 complexes can produce hydrogen peroxide and have very strong evidence for free superoxide being an intermediate on the pathway. In an effort to further establish the intermediacy of superoxide in the Cu-histatin (*Hst*) systems we undertook spin-trapping studies with CYPMPO.[112] As aforementioned, CYPMPO is a derivative of the common radical trap DEPMPO.[112] Both of these compounds are superior to the older DMPO (5,5-dimethyl-1-pyrroline N-oxide) in terms of their ability to capture and form long-lived adducts with superoxide and hydroxyl radicals.[112, 114] Due to EPR interference by the ascorbyl radical[115] in the ascorbate oxidations, only cysteine was a suitable reducing agent for the CYPMPO/Cu/*Hst*-systems.

Figure 2.7.2 shows EPR spectra of the CYPMPO-hydroxyl radical adduct generated under various conditions. The top spectrum is of a 1% hydrogen peroxide solution irradiated in the presence of CYPMPO, established conditions for generation of hydroxyl radical and its CYPMPO adduct,[112] the middle EPR spectrum was obtained from aerobic cysteine

oxidation in the presence of CYPMPO by Cu(II) alone; and the bottom spectrum is a simulated spectrum of the CYPMPO-hydroxyl radical adduct.

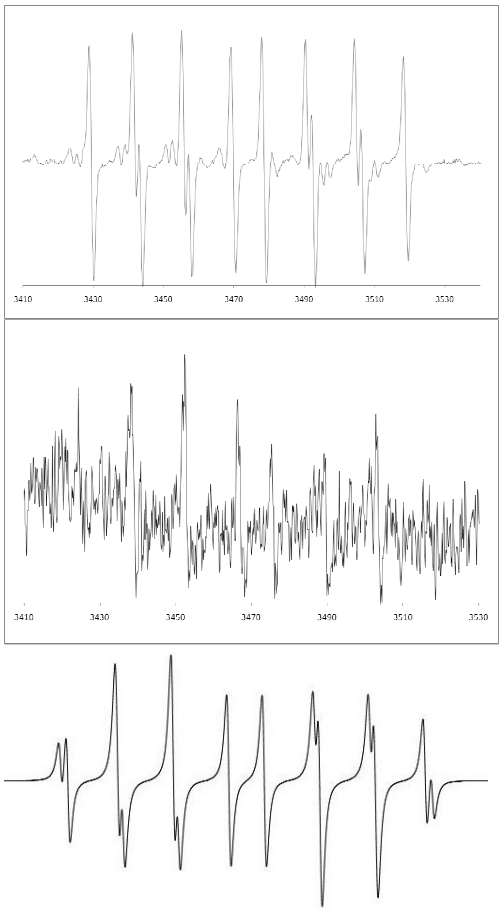

Figure 2.7.2. (top) EPR spectrum from irradiation of a solution of 0.326 M H_2O_2 with 10 mM CYPMPO, the CYPMPO hydroxyl radical adduct; (middle) EPR spectrum of solution with 3.33 µM copper (II), 26.67 mM CYPMPO, and 1.67 mM cysteine in MOPS buffer (pH 7.4); (bottom) simulated EPR spectrum of the hydroxyl-CYPMPO adduct.

The spectra contained in figure 2.7.2 clearly show that our conditions could easily detect CYPMPO-OH. This is demonstrated in the top spectrum where using standard conditions we detected the CYPMPO-OH. Further, we clearly show that CYPMPO-OH is produced by the free copper system using cysteine as a reductant.

Figure 2.7.3 shows the EPR spectra of the CYPMPO-hydroperoxyl radical adduct generated experimentally for reference and simulated. The top spectrum was obtained via UV irradiation of a 10% solution of hydrogen

peroxide in the presence of CYPMPO.[112] The bottom spectrum is the simulated spectrum of the CYPMPO-hydroperoxyl radical adduct.

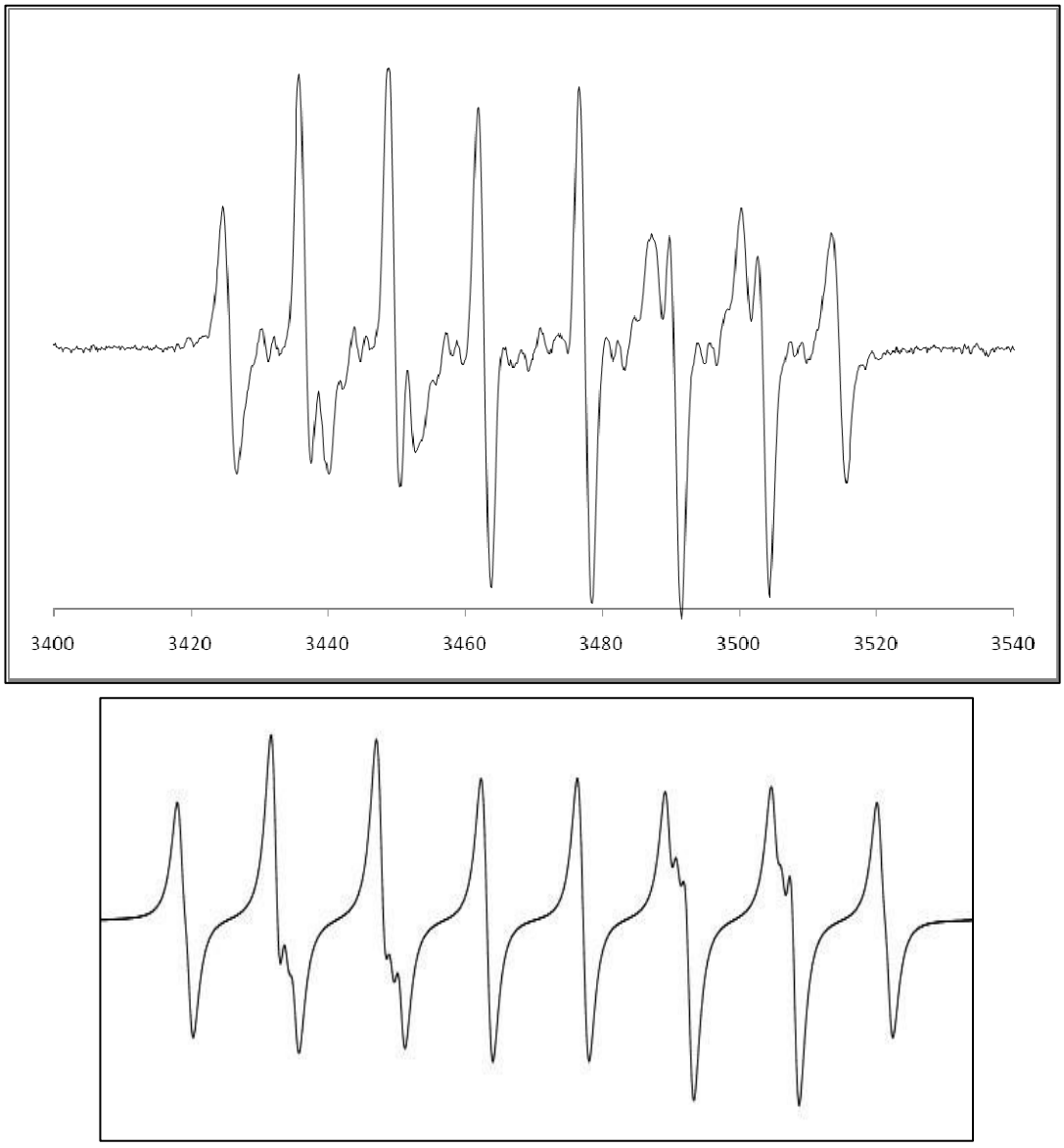

Figure 2.7.3. (top) EPR spectrum after irradiation of a solution that is 3.26 M H_2O_2 and 10 mM CYPMPO, primarily CYPMPO-OOH; (bottom) simulated EPR spectrum of the hydroperoxyl-CYPMPO adduct.

Clearly our experimental conditions were also suitable for observation of the hydroperoxyl adduct, CYPMPO-OOH (figure 2.7.3), as well as CYPMPO-OH (figure 2.7.2). This is demonstrated by the comparison of the CYPMPO-OOH adduct and CYPMPO-OH under standard conditions compared to their respective simulations. In addition to the excellent agreement to their simulated spectra, there is also excellent agreement with their respective literature values.[112]

Finally, the spectra in figure 2.7.4 indicate the combined presence of CYPMPO-hydroperoxyl and –hydroxyl radical adducts. The top spectrum was obtained from the system of *Hst*-8, $CuCl_2$, cysteine, and CYPMPO. The bottom spectrum is a combination of the two simulated spectra figure 2.7.2 bottom and figure 2.7.3 bottom. The intensity of the simulated CYPMPO-hydroperoxyl adduct (figure 2.7.3 bottom) contribution set at three tenths that of the simulated CYPMPO-hydroxyl adduct (figure 2.7.2 bottom). A comparison of the simulated spectrum of mixed CYPMPO-radical adducts to the experimentally obtained spectrum from the Cu-*Hst*-8 system (figure 2.7.4) shows good agreement, indicating the presence of both CYPMPO-hydroxyl and –hydroperoxyl adducts. This contrasts with the nearly exclusive detection of the CYPMPO-OH adduct in the absence of the peptide, i.e. cysteine/Cu(II) and CYPMPO only (figure 2.7.2).

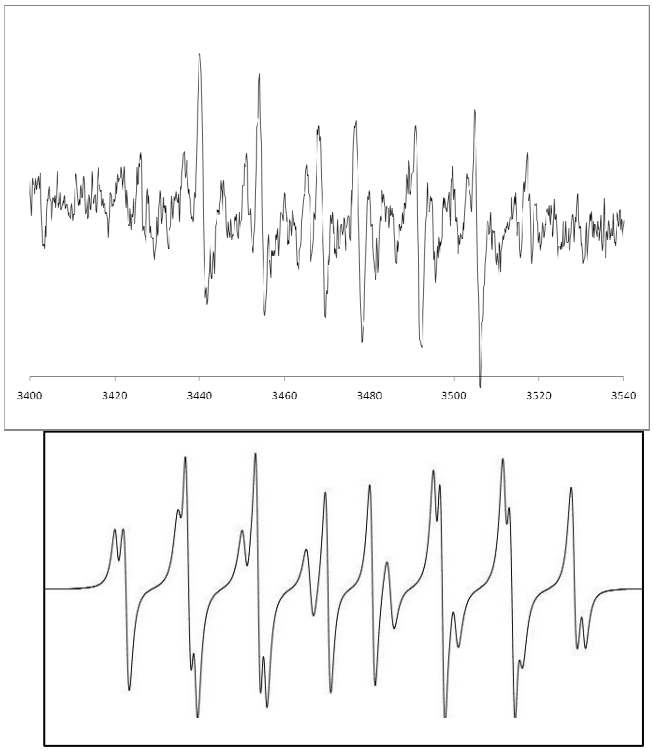

Figure 2.7.4. (top) EPR spectrum of a solution with 3.33 µM copper(II), 4.44 µM *Hst*-8, 26.7 mM CYPMPO, and 1.67 mM cysteine; (bottom) simulated EPR spectrum from combination of the two simulated spectra (figure. 2.7.2 bottom and figure 2.7.3 bottom) with the hydroperoxyl adduct being three tenths the intensity of the hydroxyl radical adduct. See experimental section for simulation parameters.

2.8: Conclusion

From our study on the catalytic production of ROS by an *Hst*/Cu system we have reached several conclusions. First, we have found that the *Hst*/Cu systems produce hydrogen peroxide at approximately the same rate as free copper. This is true whether the *Hst*:Cu concentration ratio is less than 1:1 or 100:1. The similarity in activity is observed in systems utilizing either ascorbic acid or cysteine as a biorelevant external reducing agent. These observations were made using our Amplex Red assay.

However, though the rate of hydrogen peroxide production may be similar, we have conclusively demonstrated that the pathway to generate the hydrogen peroxide by the *Hst*/Cu system differs from the pathway that the free copper ion catalyzed system uses. As demonstrated by the Amplex Red assay in the presence of SOD, the *Hst*/Cu utilizes free superoxide as an intermediate to hydrogen peroxide generation whereas free copper systems do not. This conclusion is evidenced by the near halving of hydrogen peroxide assayed by AR in the presence of SOD with the *Hst*/Cu systems. Free copper systems did not exhibit similar sensitivity to the presence of SOD. The intermediacy of free superoxide was further established by our spin trapping studies with CYPMPO. A CYPMPO-OOH adduct was clearly detected in *Hst*-8/Cu systems using cysteine as a reductant, but were absent when *Hst*-8 was not present.

2.9: Experimental Section

2.9.1: General Materials/Methods

Commercial materials were obtained as follows: Amplex Red (AR) from Molecular Probes; nitrotetrazolium blue chloride (nitro blue tetrazolium, NTB), N-acetyl-L-cysteine (Sigma grade ≥99%), and Superoxide dismutase (SOD, Bovine Erythrocytes, 98% 4470 U/mg) from Sigma; Peroxidase (from Horseradish roots, EIA Grade, purified, single basic isozyme 500U/mg) from Worthington. L-Ascorbic acid (99+% A.C.S. reagent) was obtained from

Aldrich. Hydrogen peroxide (30% aqueous solution) was obtained from EMD. Sodium phosphate dibasic (A.C.S. reagent grade anhydrous), sodium phosphate monobasic (USP/NF grade anhydrous), sodium hydroxide (A.C.S. reagent grade), and Becton Dickinson Microtest 96, tissue culture treated by vacuum gas plasma, polystyrene, sterile, individually packaged, 96 well plates were obtained from Fisher. Zinc chloride hexahydrate (analytical reagent) and copper chloride hexahydrate (analytical reagent) from Mallinkrodt, MOPS from Research Organics Inc. and L-cysteine from Sigma both generous gifts from Prof. Paul Cook's Lab. CYPMPO, (5-(2,2-dimethyl-1,3-propoxy cyclophosphoryl)-5-methyl-1-pyrroline N-oxide) was the generous gift of Dr. Yashige Kotake and may be obtained commercially from Cayman Chemicals or Radical Research Inc.

A 0.05 M pH 7.4 MOPS buffer solution was produced by dissolving MOPS in Chelex-treated double distilled DI water. This was then adjusted to pH 7.4 by addition of 0.1 M NaOH with Chelex resin present throughout the addition process. The solution was then diluted to 10 mL in a volumetric flask by addition of DD DI water.

Amplex Red solutions were prepared by dissolving 5.0 mg of AR in 1948 µL DMSO. This solution was divided into 60 µL aliquots which were frozen in amber vials in a blacked out dessicator until used. The Amplex Red working (assay) solution was created by mixing 4850 µL MOPS buffer with 100 µL of 10 U/mL HRP and 50 µL of the Amplex Red in the DMSO aliquot above.

A SOD stock solution was produced by dissolving the contents of the 15,000 unit vial in 1.0 mL DI H_2O; a serial dilution series was created from that and the remainder of the SOD stock solution was frozen until needed.

An NTB stock solution was prepared by dissolving 50 mg of NTB into 611 µL DI H_2O. This is then divided into 45 µL aliquots. These were stored frozen in amber vials in a blacked out dessicator. NTB working solution was created by dissolving a 45 µL aliquot of NTB stock solution in 4955 µL pH 7.4 MOPS buffer solution.

Hydrogen peroxide stock solutions were standardized spectrophotometrically (Perkin-Elmer Lambda 3 UV/Vis Spectrophotometer) from its absorbance at 240 nm with $\varepsilon = 40\ M^{-1}\ cm^{-1}$.

Histatin-8 was purchased as a crude solid phase preparation product (55-60% purity depending on batch) from the Molecular Biology Proteomics Facility of the University of Oklahoma Health Sciences Center. It was isolated and purified by HPLC by dissolving the sample in a small volume of 0.1% TFA/water followed by injection onto a C18 RP-Prep-HPLC column (Biorad BioLogic). Elution with a linear solvent gradient from 100% water (0.1% TFA) to 60% H_2O (0.1% TFA) / 40% 4:1 acetonitrile:H_2O (0.1% TFA) (4 mL/min) over 74 min afforded *Hst*-8 with a typical retention time of 9 min. The *Hst*-8 fraction was determined by ESI-MS.

Histatin-5 was obtained from stimulated human saliva.[116] Whole human saliva was collected, chilled and kept at 4 ℃. This was then centrifuged to remove high molecular weight proteins in a Centricon Plus 70

35 Kdal cutoff (Millipore). The filtrate was then adjusted to 500 µM $ZnCl_2$ by addition of $ZnCl_2$ hexahydrate. This solution was adjusted to pH 9 using 0.01 M NaOH and centrifuged at 25000 G to precipitate and isolate the Zn-bound peptides. After decantation of the supernatant solution, the precipitate was dissolved in a small volume of 0.1% TFA/water and followed by injection onto a C18 RP-Prep-HPLC column (Biorad BioLogic). Elution with a linear solvent gradient (4 mL/ min) from 100% water (0.1% TFA) to 60% H_2O (0.1% TFA) 40% 4:1 acetonitrile:H_2O (0.1% TFA) over 74 min afforded *Hst*-5 with a typical retention time of 30 min. The identity of the *Hst*-5 fraction was established by ESI-MS.

2.9.2: Hydrogen Peroxide Generation by Ascorbate- or Cysteine-Copper-Histatin Solutions

In a typical set of experiments using a 96-well microtiter plate 12.5 µL of 0-0.1 mM peptide stock solution was first added to a well, followed by 12.5 µL of 0-0.005 mM copper chloride hydrate solution, and then 12.5 µL of Chelexed DD DI water (or SOD). To start the reaction 12.5 µL of 5 mM ascorbate (or 5 mM cysteine) solution in MOPS buffer was added. The mixture was allowed to incubate at room temperature (20-22 ℃) for 60 min. After this time the reaction was quenched by adding 50 µL of Amplex Red working solution to the well. The absorbance of the well(s) was then measured at 570 nm with a Molecular Devices Thermomax UVT-07092 Microplate Reader (96 well UV/Vis plate reader-spectrophotometer) with

Softmax software version 2.35. The hydrogen peroxide concentration was then determined by comparison of the absorbance readout with the working curve produced from standardized hydrogen peroxide solutions and the HRP-Amplex reagent.[88]

2.9.3: SOD Effects on Hydrogen Peroxide Generation by Ascorbate-Copper-Histatin Solutions

In a typical set of experiments using a 96-well microtiter plate 12.5 µL of 0.007 mM peptide stock solution was first added to a well, followed by 12.5 µL of 0.005 mM copper chloride hydrate solution, and then 12.5 µL of 0-3000 U/mL concentrated SOD solution. To start the reaction 12.5 µL of 5 mM ascorbate solution in MOPS buffer was added. The mixture was allowed to incubate at room temperature (20-22 ℃) for 60 min. After this time the reaction was quenched by adding 50 µL of Amplex Red working solution to the well. The absorbance of the well(s) was then measured at 570 nm with a microplate reader as above. The H_2O_2 concentration was then determined by comparison of the absorbance readout with the working curve produced from standardized H_2O_2 solutions and the HRP-Amplex reagent.[88]

2.9.4: Effects of Hydroxyl Radical Traps on Hydrogen Peroxide Generation by Ascorbate-Copper-Histatin Solutions

In a typical set of experiments using a 96-well microtiter plate 12.5 µL of 0.007 mM peptide stock solution was first added to a well, followed by 12.5

µL of 0.005 mM copper chloride hydrate solution, and then 12.5 µL of the hydroxyl radical trap solution (either sodium azide or sodium formate) was added. To start the reaction 12.5 µL of 5 mM ascorbate solution in MOPS buffer was added. The mixture was allowed to incubate at room temperature (20-22 ℃) for 60 min. After this time the reaction was quenched by adding 50 µL of Amplex Red working solution to the well. The absorbance of the well(s) was then measured at 570 nm as above with a microplate reader. The hydrogen peroxide concentration was then determined by comparison of the absorbance readout with the working curve produced from standardized hydrogen peroxide solutions and the HRP-Amplex Red reagent.[88]

2.9.5: Superoxide Generation by Cysteine- and N-Acylcysteine-Copper-Peptide Systems

In a typical set of experiments using a 96-well microtiter plate 12.5 µL of 0-0.1 mM peptide stock solution was first added to a well, followed by 12.5 µL of 0-0.005 mM copper chloride hydrate solution, and then 12.5 µL of Chelexed DD DI water (or SOD). 50 µL of NTB working solution was next added. To start the reaction 12.5 µL of 5 mM N-acylcysteine (or 5 mM cysteine) solution in MOPS buffer was added. The mixture was allowed to incubate at room temperature (20-22 ℃) for 60 min. The absorbance of the well(s) was then measured at 570 nm with a Molecular Devices Thermomax UVT-07092 Microplate Reader (96 well UV/Vis plate reader-spectrophotometer) with Softmax software version 2.35.

2.9.6: EPR Spin Trapping Studies

In a typical experiment the reactants were mixed in an Eppendorf tube with an order of addition of peptide, metal ion, CYPMPO, water, and reducing agent. These were then immediately drawn into a quartz flat cell and placed in the microwave cavity. The instrument was a Bruker EMX EPR system using an ER041XG X-band microwave bridge and an ER4102ST microwave cavity. Spectra were collected using the 32-bit WinEPR ver. 4.32 Rev. 10 software from Bruker. Typical spectral acquisition parameters for the experiment were modulation frequency 100 kHz; modulation amplitude 1.0 G; microwave power 10 mW; amplifier time constant 0.1 s; and filed sweep rate 150 G / 80 s. The static field was set at 3480 G. Generally, 16 scans were collected per spectra.

2.9.7: Irradiation of EPR Samples

A Rayonet Srinivasan-Griffin Photochemical reactor (Southern New England Ultraviolet Company, RPR-100) was used for irradiation of hydrogen peroxide-CYPMPO samples to produce the CYPMPO-OH and CYPMPO-OOH adducts. Samples were irradiated for between 0.5 and 2 min while in the quartz flat cell.

2.9.8: EPR Simulation Parameters

WinRad ESR simulation program (Radical Research Inc, Hino Tokyo Japan) was used to simulate the desired spectra. The CYPMPO-OOH spectrum was simulated using the following parameters (1 mT = 10 G): diastereomer 1: A_H = 1.11 mT, A_N = 1.26 mT, A_P = 5.25 mT, LW = 0.13 mT, relative conc. = 1; diastereomer 2: A_H = 1.04 mT, A_N = 1.27 mT, A_P = 5.1 mT, LW = 0.13 mT, relative conc. = 1. The CYPMPO-OH spectrum was simulated using the following parameters: diastereomer 1: A_H = 1.37 mT, A_N = 1.37 mT, A_P = 4.98 mT, LW = 0.11 mT, relative conc. = 1; diastereomer 2: A_H = 1.23 mT, A_N = 1.35 mT, A_P = 4.8 mT, LW = 0.11 mT, relative conc. = 1. Assignments of these spectra were based on Kamibayashi et al.[112] The combination spectra were generated by combining the spectra that were the resultant of the previous simulations in a 1:0.3 CYPMPO-OH:CYPMPO-OOH ratio.

Chapter 3: Metal Binding Studies

3.1: Introduction

Uncovering the ligand environment of the copper ion in the Cu/*Hst* complexes of *Hst*-5, D-S-H-A-K-R-H-H-G-Y-K-R-K-F-H-E-K-H-H-S-H-R-G-Y, and *Hst*-8, K-F-H-E-K-H-H-S-H-R-G-Y, is of interest. It has already been shown that different ligand environments give rise to different ROS both in my own work and in other literature examples.[50-52, 70, 91, 95] Most notably, we were able to observe production of a free superoxide intermediate on the pathway to produce hydrogen peroxide in both *Hst*-5 and *Hst*-8 containing systems.[70] Thus it is of interest to investigate the metal binding environment to add to the knowledge base information correlating specific ROS production to ligand environment. Unlike *Hst*-5, *Hst*-8 has no ACTUN environment, amino terminal copper/nickel-binding motif (Asp^1-X^2-His^3). Yet, *Hst*-8/Cu systems produce ROS at a rate similar to that of both free copper and *Hst*-5/Cu systems. We chose to use several different techniques to investigate the possible structures for both *Hst*-8 and associated model complexes, among them were NMR, EPR, and computational study.

Hst-5, D-S-H-A-K-R-H-H-G-Y-K-R-K-F-H-E-K-H-H-S-H-R-G-Y
Hst-8 K-F-H-E-K-H-H-S-H-R-G-Y

Figure 3.1.1. Primary structures of *Hst*-8 and *Hst*-5.

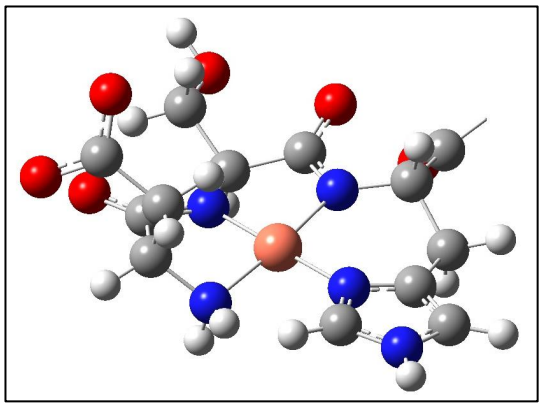

Figure 3.1.2. ACTUN fragment of *Hst*-5 coordinating copper.

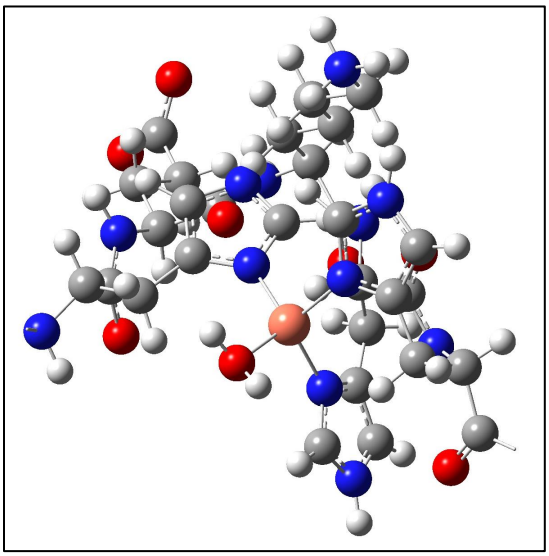

Figure 3.1.3. H-E-K-H-H fragment (common to both *Hst*-5 and *Hst*-8) coordinating copper as a tridentate ligand.

As discussed in the introductory chapter, imidazolyl motifs are commonly used as metal ligands. *Hst*-5 and *Hst*-8 contain these imidazolyl units by virtue of inclusion of the histidine residues. Several different types of coordination modes can be imagined, though there are a few motifs that are most likely to be involved. The ACTUN motif illustrated in figure 3.1.2 is the one present in *Hst*-5 shown coordinating copper. All ACTUN motifs use the terminal amine nitrogen, the amide nitrogen atoms that connect the first three residues together, and the imidazolyl unit of the histidine, which must be the third residue to coordinate the metal ion. Although, classically ACTUN regions have an aspartic acid residue as the first residue, it is not requisite to engage in metal binding. *Hst*-5 has a classical ACTUN motif as illustrated in its primary structure, figure 3.1.1 and figure 3.1.2. *Hst*-8 though lacking the

aspartic acid has a histidine as the third residue. The other commonly observed metal complexing motifs are those that of the His-X-Y-Z-His and the His-X-Y-His-His motifs. Figure 3.1.3 illustrates tridentate metal binding of a His-Glu-Lys-His-His sequence to copper. The sequence illustrated is common to both *Hst*-5 and *Hst*-8. Another possible mode of binding would be bidentate coordination though it is not shown. Imidazolyl units are each involved in these common binding motifs, thus for our studies in the metal binding activity we focused on not only the aforementioned motifs, but also the imidazolyl units.

NMR spectroscopy is an excellent technique to probe the ligand environment. Protons are very sensitive to their environments and changes to that environment are easily observed given the relative abundance of ^{1}H nuclei and their sensitivity to radio frequencies. Other atomic nuclei can also be used; however, results often take substantially longer to obtain due to lower concentrations of heteronuclear atoms that have spin at natural abundance and their comparatively lower sensitivities. To overcome the challenge posed by investigation of the heteronuclear environments, two dimensional proton coupled heteronuclear experiments are utilized. In these experiments we are able to utilize the high natural abundance and sensitivity of protons to indirectly observe those nuclei that have much lower natural abundance and sensitivity. In this way we can observe the chemical shift differences in the free and metal bound peptide of the nuclei involved in the metal binding. As suggested by studies on ACTUN type complexes and

indeed the host of other material, nitrogen nuclei, particularly those on imidazolyl motifs are often involved with metal ion binding. ^{1}H-^{15}N HSQC and ^{1}H-^{15}N HMBC experiments are therefore likely to give very good information about metal binding activities.

In addition to the two dimensional experiments we can also get information about where metals bind by observing the one dimensional proton spectrum. Changes in chemical shift and line broadening are often observed for protons located in the vicinity of metal binding. Further, if the complex is engaging in ACTUN type binding as illustrated in figure 3.1.2, the displacement of the amide protons will be observed.

Although many NMR studies that involve metal binding studies use Cd due to its own NMR activity,[117, 118] we decided that Cu was a better choice. Indeed Cu(II) has been used in metal ion binding studies done by NMR.[105, 119, 120] It was observed to quench the NMR signal when it was added in sub-stoichiometric quantities. This loss of signal was due to paramagnetic relaxation alteration and could easily result in a complete loss of signal for the entire peptide in a protein as small as *Hst*-8. Thus Cu(I) was selected to be the metal ion used for binding studies.

Cu(I) has been successfully used in a great number of studies, studied both directly and indirectly by NMR.[121-124] As with other metal complexation studies done with NMR, copper complexation results in downfield shifts of the imidazolyl unit's and other proton resonances of residues involved in metal binding.[121, 123] It was also noted that those resonances of adjacent

residues were sometimes shifted, though distant resonances had little if any chemical shift differences.[121, 123]

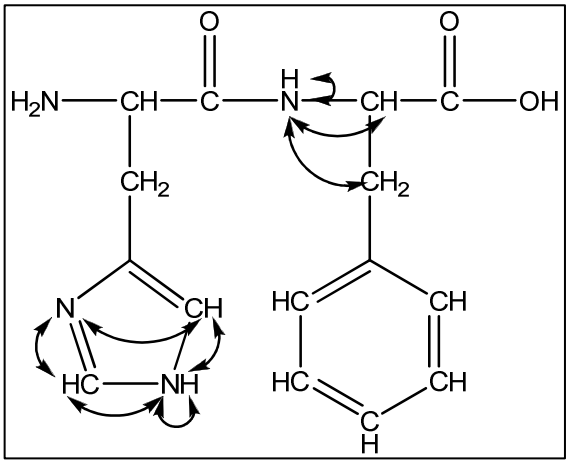

Figure 3.1.4. ^{1}H-^{15}N HMBC correlations in a his-phe dipeptide.

Figure 3.1.4 illustrates some of the correlations that would be possible to observe in a ^{1}H-^{15}N HMBC experiment. These indirect detection experiments allow for much easier observation of nitrogen nuclei. As we hypothesize that the nitrogen nuclei are most likely involved in metal binding observation of their chemical shift resonances is important. Combined with a ^{1}H-^{15}N HSQC experiment, which illustrates only single bond correlations, the two or three bond correlations of the ^{1}H-^{15}N HMBC become apparent. Using this methodology one can uncover which nitrogen nuclei, whether they are part of an amide or imidazole, are involved in metal ion binding. Carbon nuclei adjacent to metal ion binding sights also have been observed to undergo changes in chemical shift. These too have been investigated using similar techniques.

EPR spectroscopy, unlike NMR spectroscopy, requires the presence of an unpaired electron spin to work. Thus the Cu(II) system was investigated utilizing EPR spectroscopy. Though we had to look at the Cu(I) and Cu(II) systems independently with different techniques, both oxidation states are important in terms of investigation of the ROS production. Considering that the generation of superoxide from molecular oxygen involves a single electron transfer, the cycling of Cu(I) to Cu(II) is of considerable importance. Though a given oxidation state of the metal may be transitory in the overall catalytic reaction, it none the less plays an important role. We sought to investigate the ligand binding environment by investigation of the hyperfine coupling constant (hfcc). Here the unpaired electron spin on the copper is split by the spin state of nuclei of adjacent atoms. This would then allow for a diagnostic splitting pattern that would allow for inference of atoms and by extension moieties involved in binding the metal ion.

Finally computational models of various complexes were created and evaluated to explore binding of the *Hst*-8 to metal ions.

3.2: ^{1}H-^{15}N HSQC and ^{1}H-^{15}N HMBC

Before investigating complicated peptide systems, model complexes were initially investigated. A major factor contributing to the complexity of the peptide systems was their relatively large size. Another factor was the proton exchange that occurs on the imidazolyl unit. The proton exchange illustrated in figure 3.2.1 occurs between the nitrogen atoms on the imidazolyl unit.

Distinct isomers are formed as a result of this proton exchange. The figure on the left of the equilibrium arrows has its imidazolyl unit attached at the C_4 position, whereas the structure on the right of the arrows has its imidazolyl unit attached at the C_5.

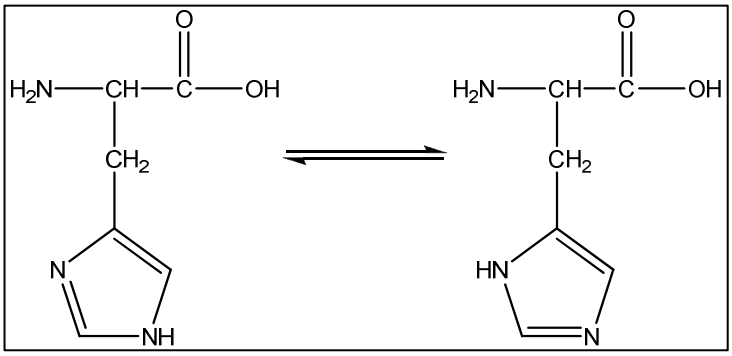

Figure 3.2.1. The proton exchange results in 4(5) isomerism of histidine.

Though we would like to use an HSQC experiment to observe the chemical shifts of the nitrogen atoms indirectly, the exchange illustrated in figure 3.2.1 and the exchange of the proton with others available in solution prohibit our use of this particular experiment. An HSCQ experiment is clearly more desirable than an HMBC in terms of sensitivity. The N-H *J* value for an HSQC experiment is 93 Hz which is an order of magnitude greater for the multibond *J* value used for HMBC experiments of 3-8 Hz. Though less sensitive than an HSQC experiment, the HMBC experiments hold promise to observe the nitrogen nuclei's resonances. Though the nitrogen atoms themselves are engaged in a proton exchange, the C_2 position remains the C_2 position regardless of which nitrogen contains the proton. So though the

nitrogen nuclei are likely to be a single signal averaged resonance as a result of the exchange, at least we will be able to observe them.

Other possibilities remain for use of HSQC experiments to monitor nitrogen resonances. In systems where the imidazolyl units of histidine and model complexes have been exhaustively protonated, the exchange maybe prevented. Also when the imidazolyl units are involved in complexation of a metal exchange of the proton on and off the nitrogen not involved in metal binding may be prevented. In both of these systems HSQC experiments have some probability for success.

We started out with simple histidine systems utilizing just one dimensional proton and two dimensional ^{1}H-^{15}N HMBC for the purposes of investigating instrument parameters and collection times. Though we were able to obtain good one dimensional data, despite our best efforts we were unable to obtain satisfactory two dimensional data using natural abundance histidine and histamine samples within reasonable experimental times. The one dimensional data essentially was a ^{1}H NMR spectrum that only had protons present that had a coupling to nitrogen nuclei. So though we could see the proton chemical shifts in the one dimensional ^{1}H-^{15}N HMBC, we could not observe any nitrogen chemical shifts.

Thinking that N_1-N_3 proton exchange may be at the cause of our problem in obtaining good two dimensional ^{1}H-^{15}N HMBC spectra, we then decided attempt ^{1}H-^{15}N HMBC experiments with the completely protonated histidine methyl ester dihydrochloride. This molecule will no longer engage in

exchange since both nitrogen atoms on the imidazolyl unit will be protonated as well as the amino terminus.

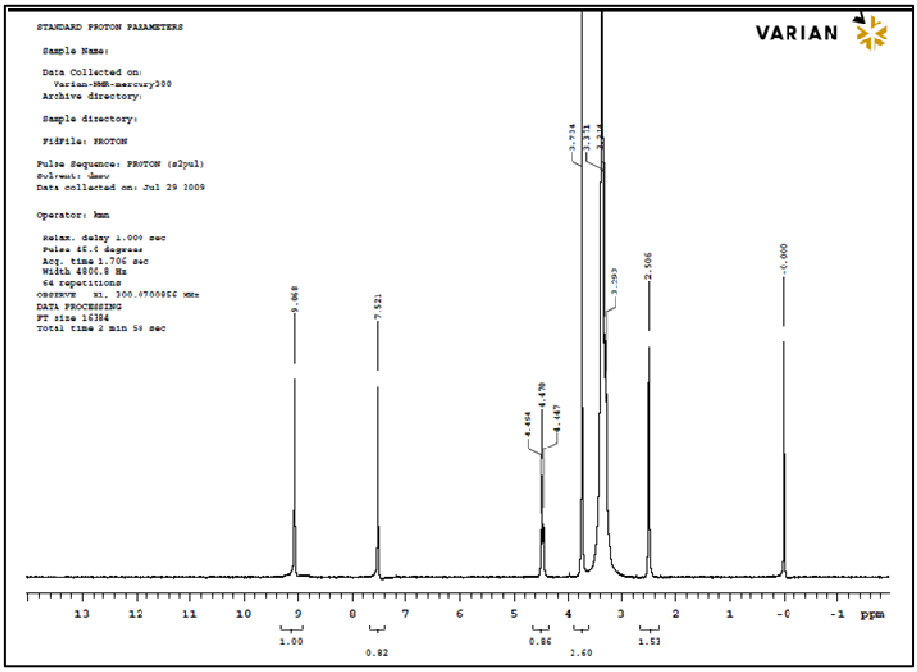

Figure 3.2.2. ^{1}H NMR spectrum of histidine methyl ester dihydrochloride.

Figure 3.2.2 is the ^{1}H NMR spectrum of histidine methyl ester dihydrochloride. We can see the H_{C2} peak at 9.01 ppm, the H_{C5} peak at 7.52 ppm, the H_{α} peak at 4.74 ppm, the H_{methyl} peak at 3.73 ppm and the H_{β} peak at 2.5 ppm. The integrations fit nicely at a 1:1:1:3:2 ratio.

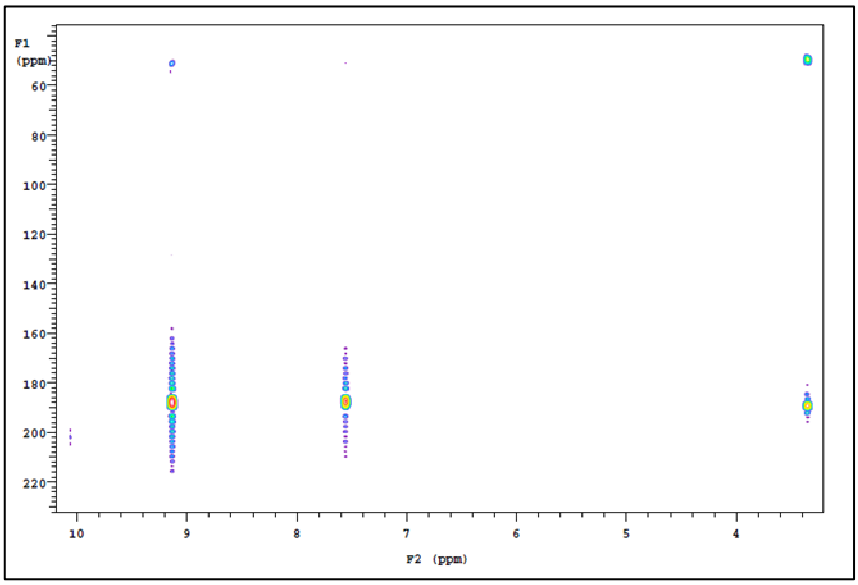

Figure 3.2.3. ^{1}H-^{15}N HMBC spectrum of histidine methyl ester dihydrochloride.

Figure 3.2.3 is the ^{1}H-^{15}N HMBC spectrum of histidine methyl ester dihydrochloride. The F1 axis is the chemical shift of the nitrogen nuclei and the F2 axis is the chemical shift of the hydrogen nuclei. There are two separate and distinct nitrogen absorptions. One is at 190 ppm and is a bit streaked due to some lingering N_1-N_3 exchange. However, very strong correlations are observed to the C_2 proton (9.2 ppm) and C_5 proton (7.6 ppm) on the imidazolyl ring. Also, substantially weaker correlation to the water dissolved in DMSO (3.4 ppm) is observed. We noted that the ammonium nitrogen at 50 ppm has a correlation to the water dissolved in DMSO (3.4 ppm) and a weak correlation to the C_2 proton (9.2 ppm). Again, the correlation to the water dissolved in the DMSO is the result of proton exchange.

This experiment gave us a point to compare with the standard ^{1}H NMR of histidine (data not shown). The H_{C2} of histidine is at 7.79 ppm and the H_{C5} is at 7.05 ppm. The completely protonated histidine methyl ester dihydrochloride has peaks that are substantially downfield shifted. This of course is expected as the electron poor proton withdraws electron density from the aromatic imidazolyl unit. The result being that the H_{C2} and H_{C5} of the histidine methyl ester dihydrochloride are both deshielded and their resonances appear farther downfield, 9.2 ppm and 7.6 ppm respectively. With these results we then went forward to another simple imidazolyl system, one which would allow us to get resonances for the nitrogen nuclei of uncomplexed or unprotonated imidazolyl units.

2-Tris(N-methylimidazolyl)carbinol (2-TMIC) is readily synthesized and has been used as a metalloenzyme's metal binding active site mimic.[36] It has a NMR spectrum that is simpler than histidine in that there is no exchange possible of protons on the imidazolyl portion. This then should allow for us to obtain ^{1}H-^{15}N HMBC spectra of both the free ligand and copper complex.

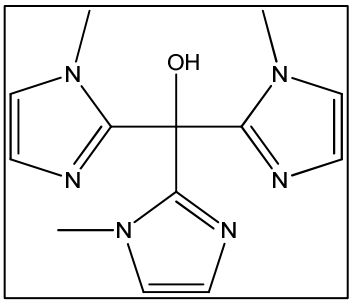

Figure 3.2.4. 2-Tris(N-methylimidazolyl)carbinol (2-TMIC).

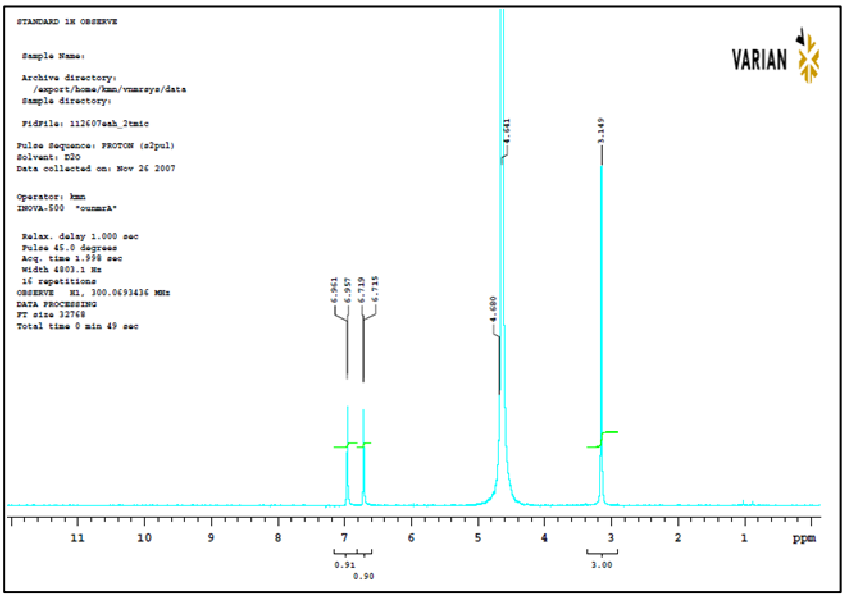

Figure 3.2.5. ^{1}H NMR spectrum of 2-tris(N-methylimidazoyl)carbinol (2-TMIC).

The 2-TMIC ^{1}H NMR spectrum in figure 3.2.5 clearly shows the C_4 protons at 6.7 ppm which are clean doublets coupling to the C_5 protons at 6.96 ppm which are of course also doublets. We obtained the expected integration of 3:1:1 for the methyl unit, the C_4 proton, and the C_5 proton.

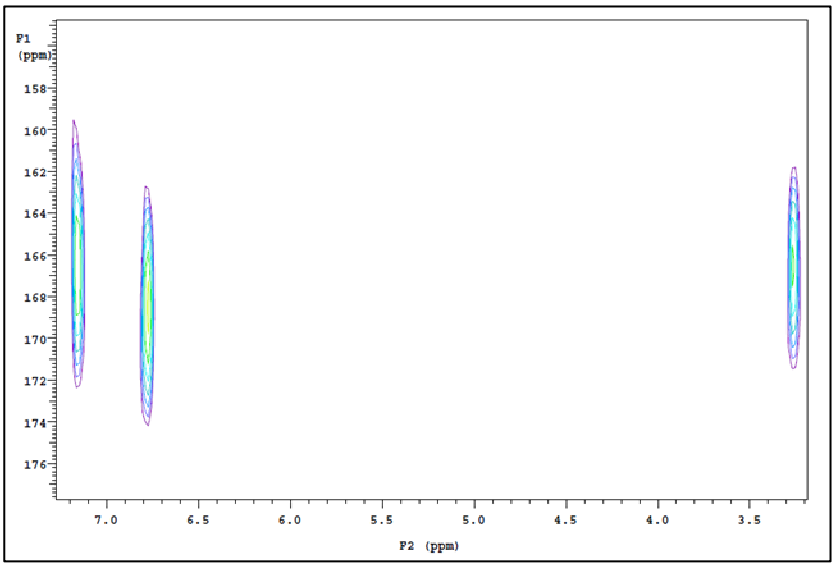

Figure 3.2.6. ^{1}H-^{15}N HMBC spectrum of 2-TMIC.

In figure 3.2.6, which illustrates the ^{1}H-^{15}N HMBC spectrum of 2-TMIC, we can observe two nitrogen nuclei very distinctly. The N_1 (166.8 ppm) has a strong correlation to the methyl moiety (3.25 ppm) and a strong correlation to the C_5 proton at 7.15 ppm. Whereas the N_3 (168.4 ppm) has the strongest correlation to the C_4 proton at 6.78 ppm. There may be weak correlations of the N_1 to the C_4 proton and the N_3 to the C_5 proton, but they would be underneath the stronger correlations already identified. Note that the difference in the chemical shifts of the protons from figure 3.2.5 and figure 3.2.6 are due to the referencing. For figure 3.2.5 the reference used was the solvent, D_2O, and the reference for figure 3.2.6 was TMS.

We were able to observe distinct nitrogen chemical shifts for each of the two nitrogen atoms in the imidazolyl unit in 2-TMIC. In previous experiments using histidine and histamine had been unable to observe any

nitrogen resonances. Using the histidine methyl ester dihydrochloride, we had been able to observe the chemical shifts of an imidazolium species. However, due to the protonation of the imidazolyl motif of the histidine methyl ester dihydrochloride the proton and nitrogen chemical shifts were substantially downfield shifted. Covalent attachment of a methyl unit to the N_1 allowed us to overcome the problems that arose from the proton exchange and allowed us to visualize the 2-TMIC free ligand.

Given our success in visualizing 2-TMIC as a free ligand, we then proceeded to add one equivalent of Cu^{+} in the form of copper tetrakis(acetonitrile) hexafluorophosphate, $Cu(CH_3CN)_4PF_6$. Hopefully we would be able then to visualize a downfield shift of both the proton and nitrogen resonances as a result of metal binding.

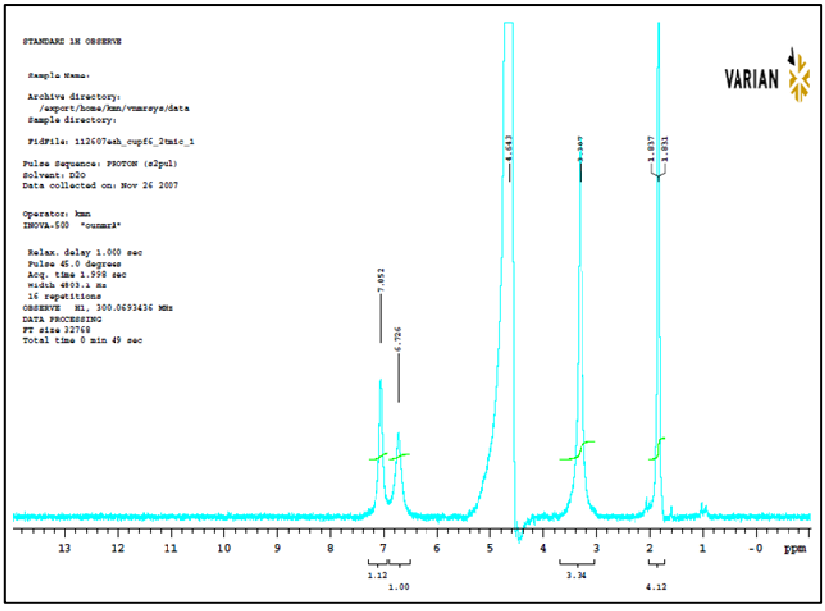

Figure 3.2.7. ^{1}H NMR spectrum of 2-TMIC with $Cu(CH_3CN)_4PF_6$.

As shown in figure 3.2.7, the ^{1}H NMR spectrum of 2-TMIC with $Cu(CH_3CN)_4PF_6$, we see the C_5 protons at 7.05 ppm, the C_4 protons at 6.73 ppm, and the methyl protons at 3.31 ppm. Also present are the acetonitrile protons at 1.83 ppm. Notice that the peaks are clearly broader than that of the free ligand, and also the coupling information of the imidazolyl protons is lost. However, the integration is 1:1:3:4 (3:3:9:12) for the H_{C4}: H_{C5}: H_{methyl}: $H_{acetonitrile}$.

Curiously, the proton shifts of 2-TMIC are not substantially shifted downfield as a result of copper complexation. However, we were able to observe line broadening in the one dimensional proton spectrum, which would seem to indicate binding as some of the copper may be present as Cu(II), which would result in paramagnetic line-broadening or it could result from the averaging of signal resulting from the equilibrium exchange of the ligand on and off the metal. The strong signal obtained from the acetonitrile in the ^{1}H-^{15}N HMBC (not shown) forced a reduction in the gain. This in turn led to unsatisfactory results in that we were unable to observe the nitrogen nuclei of interest within a reasonable timeframe. Another possible explanation for the inability to observe the nitrogen peaks in the ^{1}H-^{15}N HMBC was discussed at length by H. Fujii *et. al*. He noticed that when performing NMR experiments on ^{63}Cu and ^{13}C that when weakly binding ligands were used, they were unable to observe signal for either the ^{63}Cu or the ^{13}C in the ligand binding the copper.[124] By switching to a stronger ligand (from acetonitrile to carbon monoxide), they were able to once again observe

both ^{63}Cu and ^{13}C signal.[124] Both hexafluorophosphate and acetonitrile are weak ligands, so it remains a possibility that this was a cause for our inability to observe signal in the two dimensional ^{1}H-^{15}N HMBC spectrum.

So we moved to a different source of Cu(I) for investigation of imidazolyl motif complex behavior. Copper was added as $CuCl_2$ and then reduced *in situ* by addition of ascorbate. Figure 3.2.8 illustrates the probable products of the reduction of a 2-TMIC-$CuCl_2$ complex by ascorbic acid, which are the ascorbyl radical, 2-TMIC-CuCl, and an equivalent of hydrochloric acid. The results are illustrated in figure 3.2.13, which will be discussed later. However, since we are adding another component to the system, we include the initial structure (figure 3.2.9) and the ^{1}H NMR spectrum (figure 3.2.10) of ascorbic acid.

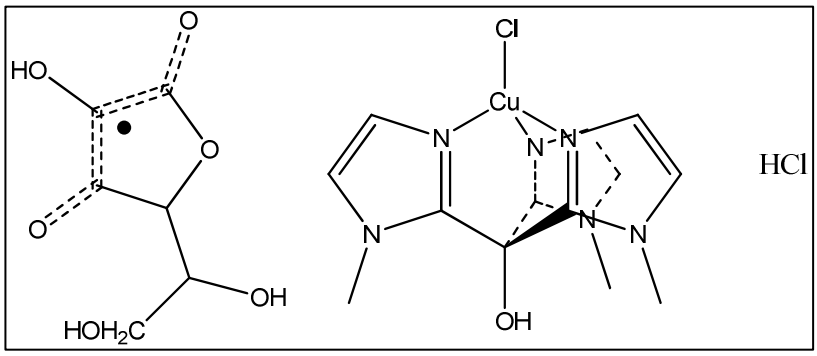

Figure 3.2.8. Structure of probable products from 2-TMIC-$CuCl_2$ reduction by ascorbate. (from left) Ascorbyl radical, 2-TMIC-Cu(I) chloride, and 1 equivalent of hydrochloric acid.

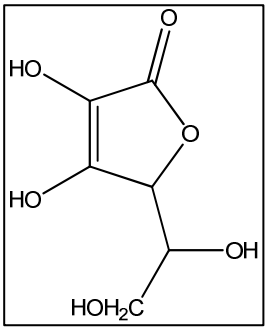

Figure 3.2.9. Structure of ascorbic acid.

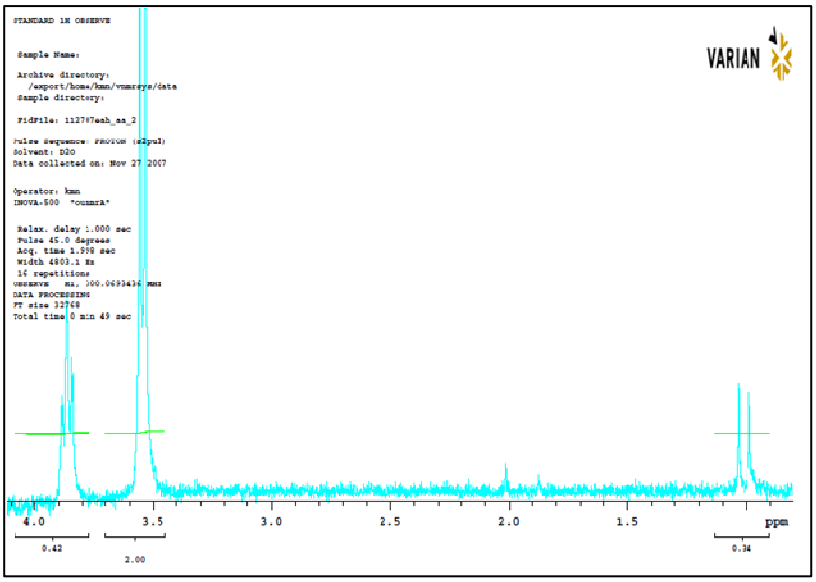

Figure 3.2.10. ^{1}H NMR spectrum of ascorbic acid.

The ^{1}H NMR spectrum (figure 3.2.10) is not very clear, though the peaks are quite apparently a triplet at 3.9 ppm, a doublet at 3.55 ppm, and a doublet at 1.0 ppm. The diastereotopic protons on the C_{ε} (3.55 ppm) are set at two and appear in the expected position. The C_{δ} proton though in the correct position (3.9 ppm) integrates to only half of its expected value. The C_{γ} proton was obscured by solvent so was thus unobserved, though we would

have expected to observe it at around 4.5 ppm. It is unclear what the upfield doublet at 1.0 ppm is. Also, the upfield doublet and the downfield triplet are significantly less than one.

Regardless, in a system composed solely of 2-TMIC and ascorbic acid (figure 3.2.11), we do not see a significant downfield shift of the imidazolyl protons. Here we see the H_{C4} peak at 6.94 ppm and the H_{C5} peak at 7.13 ppm compared to the corresponding resonances in the free ligand (figure 3.2.6) at 6.78 ppm and 7.15 ppm respectively. The N-methyl remains at 3.28 ppm. The integration again is in good agreement 1:1:3 for the 2-TMIC portion of the spectrum. The contribution of ascorbic acid to the spectrum is in good agreement too. The C_δ proton is in the correct position (3.83 ppm) along with the C_ε protons at (3.52 ppm). The C_γ proton was again obscured by solvent. This time the integration of the C_δ proton to C_ε protons is the expected 1:2 and we observe only a slight contribution of the contaminant at 1.0 ppm.

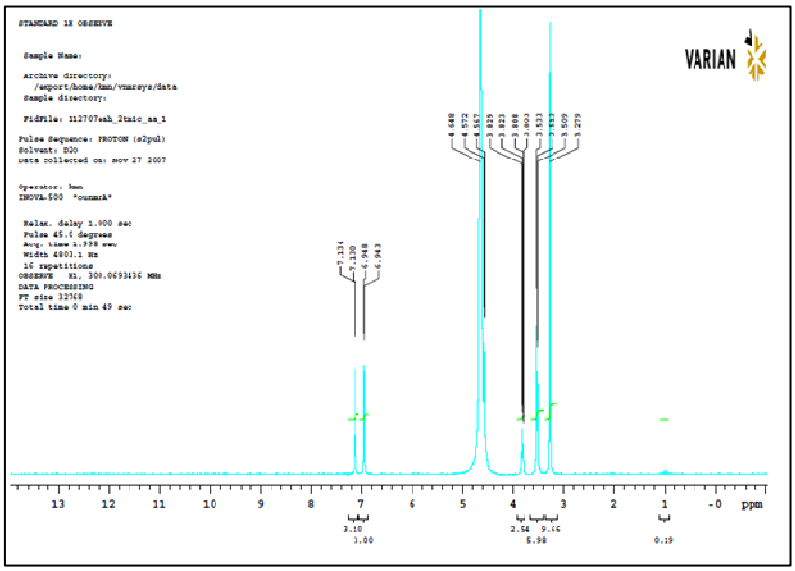

Figure 3.2.11. ^{1}H NMR spectrum of 2-TMIC and ascorbic acid.

Once copper (II) chloride is added to the 2-TMIC and ascorbic acid solution in DMSO (figures 3.2.12 and 3.2.13), a dramatic downfield shift of the imidazolyl protons is observed; the H_{C4} peak is found at 7.2 ppm and the H_{C5} peak is found at 7.5 ppm compared to the corresponding resonances in the free ligand (figure 3.2.6) at 6.78 ppm and 7.15 ppm respectively. We chose to focus solely on the chemical shifts of the imidazolyl protons, because we did not have standard spectra for ascorbyl radical, which is expected to be the result of the reduction of Cu(II) to Cu(I) by ascorbic acid. The integration of peaks in figure 3.2.12 is no longer meaningful as a result of the complexation to the copper. The influence of the quadrupolar nucleus of the Cu, is known to affect relaxation times. Also as a result of complexation of the 2-TMIC to the Cu(I), the coupling of the imidazolyl protons to each other was lost.

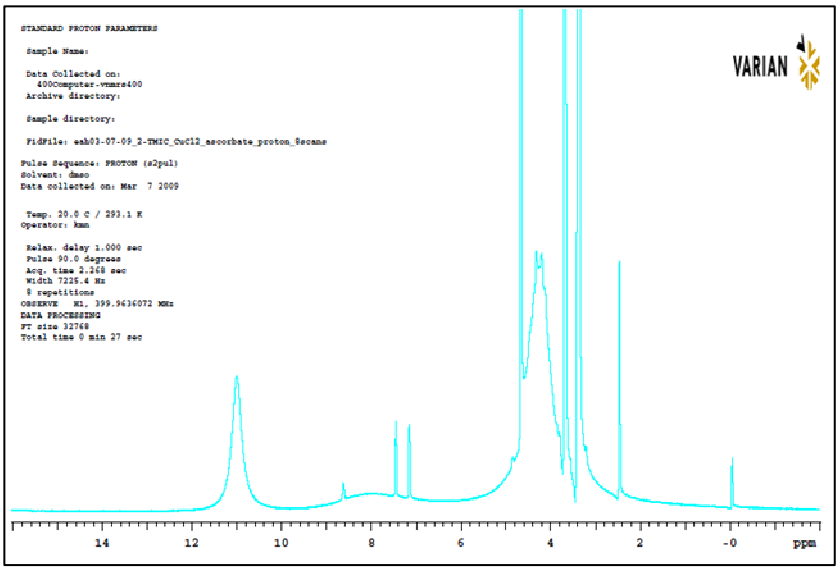

Figure 3.2.12. ^{1}H NMR spectrum of 2-TMIC, $CuCl_2$, and ascorbic acid.

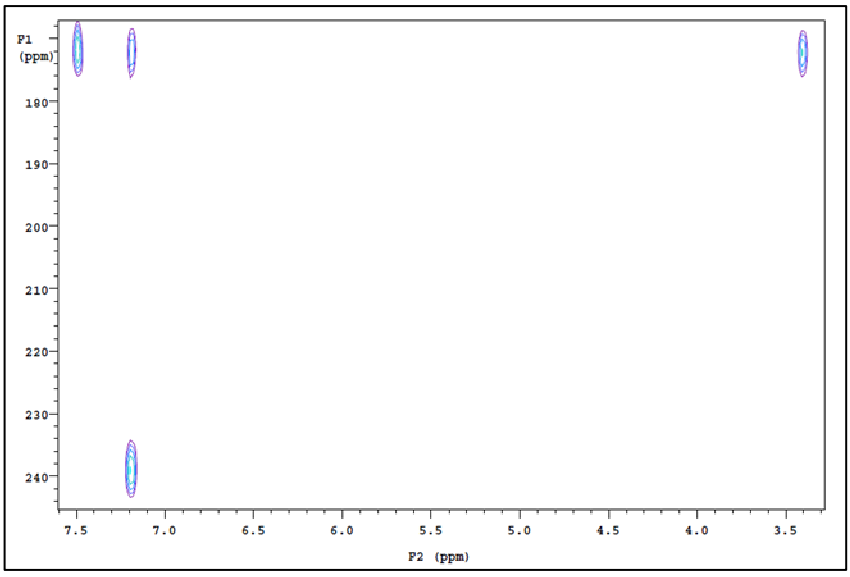

Figure 3.2.13. ^{1}H-^{15}N HMBC spectrum of 2-TMIC with $CuCl_2$ and ascorbic acid.

In terms of the ^{1}H-^{15}N HMBC spectrum of the complex (figure 3.3.13), the N_1 signal remains in the same region as the free ligand at 172 ppm and strong correlations are observed to the C_5 proton at 7.5 ppm and the methyl

protons at 3.4 along with a slightly weaker correlation with the C_4 proton at 7.2 ppm. The N_3, which is involved in copper coordination, has been substantially shifted downfield to 240 ppm and from 168.4 in the free ligand. Also it has only one correlation to the C_4 proton at 7.2 ppm.

Table 3.2.1. Summary of chemical shifts of histidine methyl ester dihydrochloride and 2-TMIC NMR studies in ppm. (N.P. - not present)

	H_{C2}	H_{C4}	H_{C5}	N_1	N_3
histidine methyl ester dihydrocholoride	9.2		7.6	~190	~190
2-TMIC		6.78	7.15	166.8	168.4
2-TMIC with $Cu(CH_3CN)_4PF_6$		6.73	7.05	N.P.	N.P.
2-TMIC with ascorbic acid		6.78	7.15	N.P.	N.P.
2-TMIC, $CuCl_2$, and ascorbic acid		7.2	7.5	172	240

As summarized in table 3.2.1, one can clearly see downfield shifting of resonances of imidazolyl peaks as a result of binding interactions and protonation with one exception. The 2-TMIC free ligand has an H_{C5} peak at 7.15 ppm. The H_{C5} peak remains in the same place in the presence of ascorbic acid. Although the peak would seem to be upfield shifted when $Cu(CH_3CN)_4PF_6$ is added to the free ligand this is merely the result of referencing differences. I should note that the H_{C5} peak at 6.73 ppm and H_{C4} peak at 7.05 ppm of the 2-TMIC with $Cu(CH_3CN)_4PF_6$ are in nearly the same places as that of the 2-TMIC (figure 3.2.5), which was referenced to solvent rather that TMS, showing a H_{C5} peak at 6.7 ppm and a H_{C4} peak at 6.96 ppm. It has been noted in previous studies that ligand field is very important in NMR investigations of ^{63}Cu and ^{13}C of Cu(I) species.[124] It was noted that both copper and carbon signals were not present when weakly coordinating

ligands were used, even if it was at only one of the four coordination sites. Merely changing the fourth weakly coordinating ligand to a stronger ligand resulted in NMR spectra with observable signal for carbon and copper nuclei. The 2-TMIC, $CuCl_2$, and ascorbic acid sample has very clear downfield shifts of all peaks as a result of complexation compared to the free ligand or even the ligand with ascorbic acid. Although all peaks are downfield shifted, perhaps the most dramatically different is the N_3 peak, which would be the peak involved in coordination of the copper ion. It moved from 168.4 ppm in the free ligand to 240 ppm in the 2-TMIC, $CuCl_2$, and ascorbic acid system. The H_{C5} peak at 7.5 ppm approaches the 7.6 ppm peak of the histidine methyl ester dihydrochloride. This evidence points to the conclusion that in the 2-TMIC, $CuCl_2$, and ascorbic acid system, a stable 2-TMIC-Cu(I) complex is formed. As the hexafluorophosphate ligand is known to be a comparatively much weaker than chloride in terms of its coordination strength, this may help to explain why we were able to observe a downfield shift in the 2-TMIC, $CuCl_2$, and ascorbic acid system and not in the simple 2-TMIC with $Cu(CH_3CN)_4PF_6$.

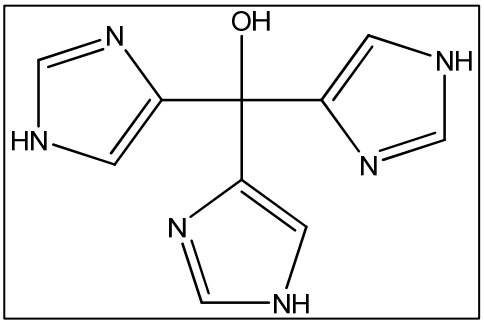

Figure 3.2.14. 4-Trisimidazoylcarbinol (4-TIC).

Given our success with 2-TMIC, namely our ability to observe downfield shifts of proton and nitrogen resonances of the imidazolyl units when binding Lewis acids, we next moved to a 4-trisimidazolylcarbinol (4-TIC). 4-TIC is related to 2-TMIC, but incorporates many of the features that histidine has, which is illustrated in figure 3.2.14. The attachment at the four position of the imidazolyl unit and the possibility of isomerism brought about by proton exchange makes this compound much more similar to histidine than the 2-TMIC. The ^{1}H NMR spectrum of 4-TIC, as illustrated in figure 3.2.15, was already very complex as a result of the aforementioned issues of exchange and isomerism. One can clearly distinguish three separate peaks in the imidazolyl region for each of the protons in the $C_{5(4)}$ and C_2 positions. The ^{1}H-^{15}N HMBC and HSQC experiments turned out to be of little use as no meaningful results were obtained (data not shown) as no peaks were observed. This is again due to the isomerism that arises from the N_1-N_3 proton exchange. We also attempted to use CPMG-HSQC pulse sequences, which often help to observe exchangeable protons. Although we were able to

see something, a streaked proton resonance at 11.2 ppm, the most intense correlation to a nitrogen resonance at 155 ppm was barely greater than the noise and thus barely meaningful. The nitrogen peak was in the expected place, but the experiment did not seem worth pursuing given the noise level that persisted in the spectrum (data not shown). This is likely due to the proton exchange of the imidazolyl nitrogen atoms that results in the 4(5) isomerism, which occurs on the NMR timescale.

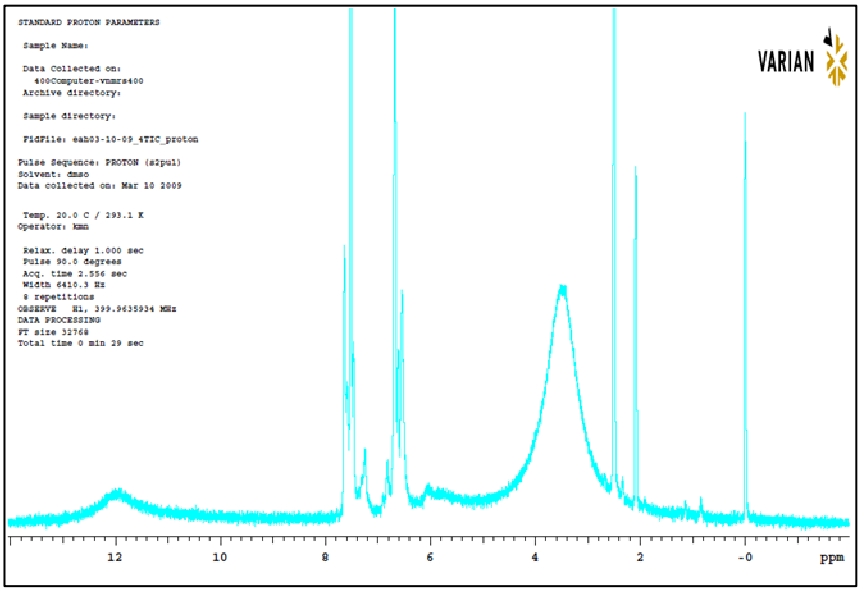

Figure 3.2.15. ^{1}H NMR spectrum of 4-trisimidazolylcarbinol (4-TIC).

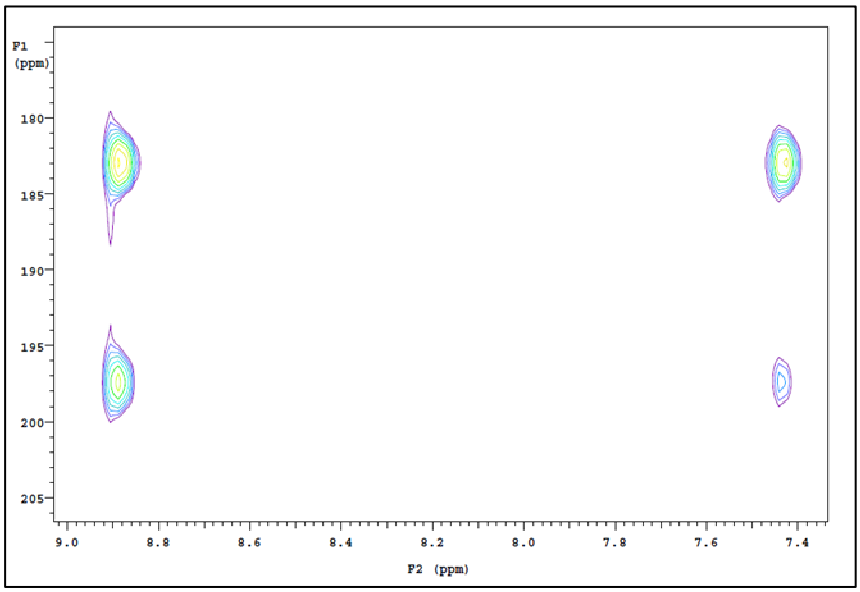

Figure 3.2.16. ^{1}H-^{15}N HMBC spectrum of 4-TIC and 3 eq. TFA.

As seen with histidine in previous experiments, exhaustive protonation proved to yield data concerning the chemical shifts of the nitrogen atoms in the imidazolyl unit as illustrated in figure 3.2.16, which is a ^{1}H-^{15}N HMBC spectrum of 4-TIC and 3 eq. TFA. We clearly observed a downfield shift of the C_2 proton to 8.9 ppm and the $C_{5(4)}$ proton to 7.42 ppm. Both nitrogen peaks are in the same general area N_3 is at 197.5 ppm and N_1 is at 183 ppm. These assignments are made as a result of the intensity of the correlation observed to the $C_{5(4)}$ proton. The N_1, having only three bonds between the C_5 proton has a much stronger correlation than the N_3, which has 4 bonds between the interacting nuclei.

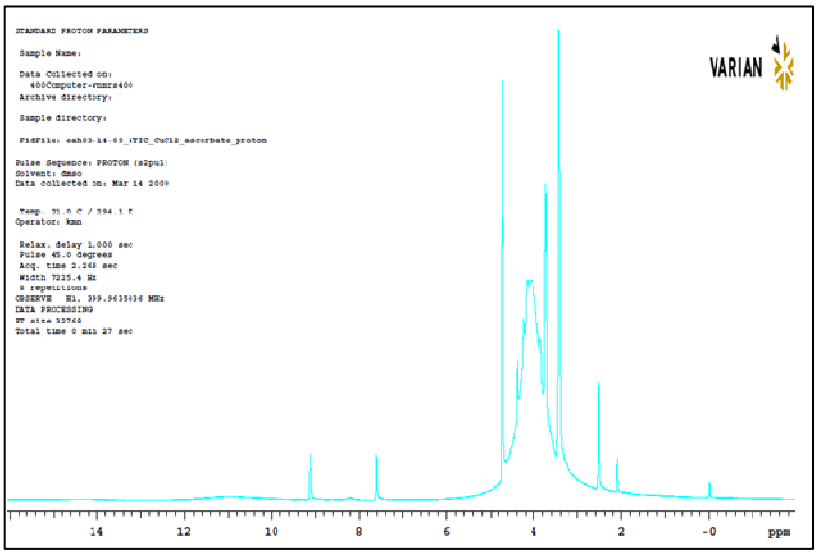

Figure 3.2.17. ^{1}H NMR spectrum of 4-TIC, $CuCl_2$, and ascorbic acid.

Given our ability to obtain clear distinct and interpretable data of the NMR experiments when 4-TIC was protonated, we decided to move to metal complexation. Again, Cu(II) was reduced *in situ* with ascorbic acid to produce a Cu(I) species. Notice in the ^{1}H NMR spectrum of the complex in figure 3.2.17, the C_2 (9.2 ppm) and C_5 (7.5 ppm) protons are now simplified as there is no longer any exchange and the ligand is in one form, attached at the C_4 position to the central carbon. Also the protons have been substantially shifted downfield as a result of complexation compared to the free ligand (figure 3.2.15).

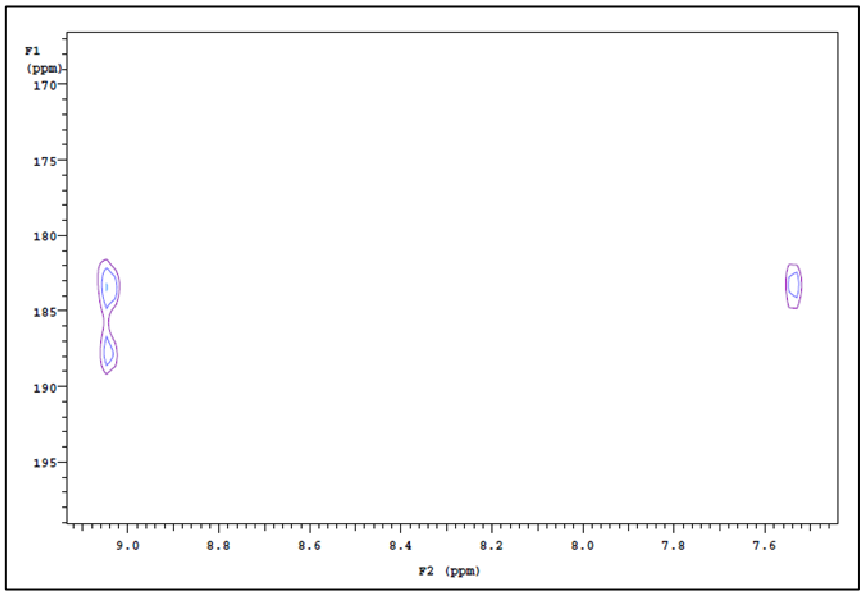

Figure 3.2.18. ^{1}H-^{15}N HMBC spectrum of 4-TIC, $CuCl_2$, and ascorbic acid.

In figure 3.2.18 we show the ^{1}H-^{15}N HMBC spectrum of the solution mixture of 4-TIC, $CuCl_2$, and ascorbic acid. The N_1 (183 ppm) has an intense correlation peak with the C_2 proton and a weaker peak with the C_5 proton. The N_3 peak (188 ppm), on the other hand, only correlates to the C_2 proton. Curiously, the N_3 peak is not shifted as far downfield when coordinating the copper (figure 3.3.18) as it is when protonated by the TFA (figure 3.2.16). For the sake of completeness we sought to obtain an ^{1}H-^{15}N HMBC or ^{1}H-^{15}N HSQC of the free 4-TIC, so that we might be able to make a statement as to how far the nitrogen nuclear resonances shifted. Despite experiments that involved changing solvents and sometimes adding base, we were unable to obtain acceptable spectra. Even changing to a ^{1}H-^{15}N CPMG-HSQC experiment we were unable to get anything other than streaked peak at 11.2

ppm across the nitrogen range indicating exchange (not shown). However, this was better than previous ^{1}H-^{15}N HSQC, which had no meaningful data.

Table 3.2.2. Summary of chemical shifts of various nuclei in ppm. (N.P. - not present)

	H_{C2}	H_{C5}	N_1	N_3
histidine methyl ester dihydrocholoride	9.2	7.6	~190	~190
4-TIC	7.5	6.6	N.P.	N.P.
4-TIC, 3 eq. TFA	8.9	7.42	183	197.5
4-TIC, $CuCl_2$, and ascorbic acid	9.2	7.5	183	188

As summarized in table 3.2.2, we can clearly observe a downfield shift of resonances in 4-TIC as a result of complexation or protonation. Histidine methyl ester dihydrochloride is included as a reference point. With the exception of the free 4-TIC all of the species have chemical shifts of their respective resonances in the same region. This is expected because each of those species except the free ligand is donating electron density from the N_3 to a relatively electron poor species, whether that be a proton or a Cu(I). Figure 3.2.19 is an illustration of the probable complex resulting from 4-TIC, $CuCl_2$, and ascorbic acid solution. The downfield shifts of the proton resonances compared to that of the free ligand are indicative of binding activity. This has been established in both our protonation studies of 4-TIC as well as other model complexes (2-TMIC and histidine methyl ester dihydrochloride). In addition the metal binding of 2-TMIC with Cu(I) followed the same trend.

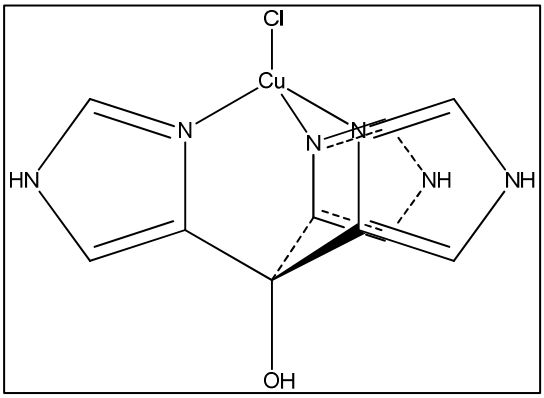

Figure 3.2.19. Probable complex resulting from 4-TIC, $CuCl_2$, and ascorbic acid solution.

We now decided to move to examine *Hst*-8 using these and some other NMR experiments. We wished to establish that an *Hst*/Cu complex forms *in situ*. This would add to the evidence already gathered that an *Hst*/Cu complex is responsible for ROS production. As with our model complexes, we first attempted a ^{1}H-^{15}N HSQC experiment. Unlike, our model complexes we were able to visualize some resonances. Although, as with previous ^{1}H-^{15}N HSQC experiments on the model complexes, we failed to observe any signals originating from nitrogen hydrogen correlations in imidazolyl units. We were however able to observe the amido resonances (data not shown).

We attempted to visualize the imidazolyl protons by protonation with TFA. The proton NMR spectra exhibited a marked sharpening as shown in figures 3.2.20 and 3.2.21 after 9 equivalents of TFA were added, thus leading us to hope for promising results from the ^{1}H-^{15}N HMBC and possibly even the ^{1}H-^{15}N HSQC experiments.

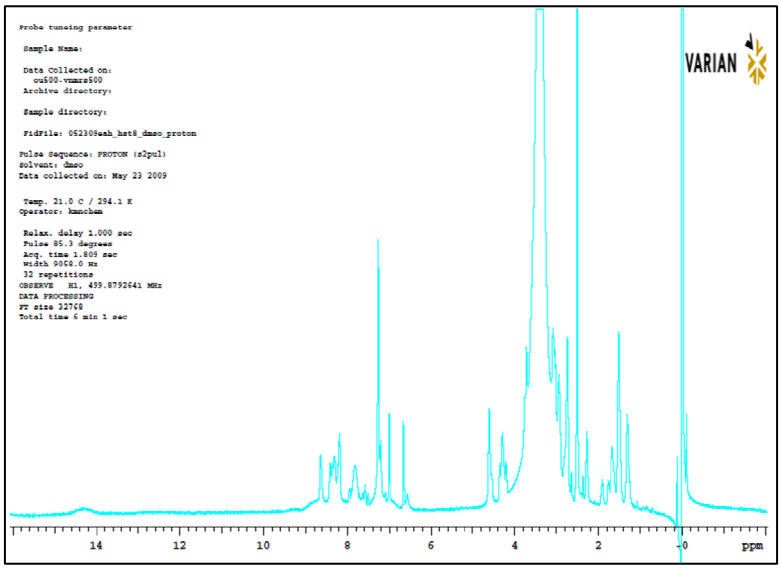

Figure 3.2.20. ^{1}H NMR spectrum of *Hst*-8 in DMSO.

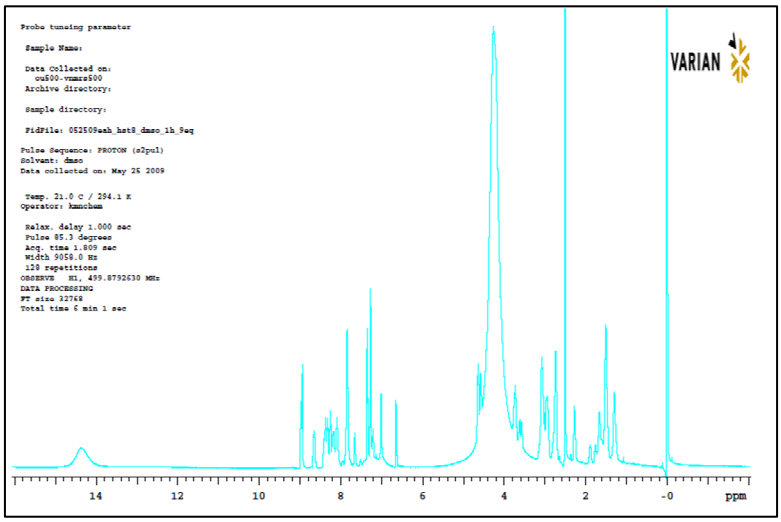

Figure 3.2.21. ^{1}H NMR spectrum of *Hst*-8 + 9 eq. TFA in DMSO.

Even after addition of 9 equivalents of TFA, we were still unable to visualize the imidazolyl proton signals by ^{1}H-^{15}N HSQC, though the amido resonances remained unchanged (data not shown). Again we are able to observe imidazolyl C_2 and $C_{5(4)}$ protons correlating to imidazolyl nitrogen

atoms by means of an ^{1}H-^{15}N HMBC experiment as demonstrated in figure 3.2.22. H_{C2} is at 8.98 ppm and the $H_{C5(4)}$ is at 7.35 ppm. Those protons both correlate to an imidazolyl nitrogen at 186 ppm. The result is consistent with the results obtained from our model complex, histidine methyl ester dihydrochloride (figure 3.2.3). For histidine methyl ester dihydrochloride we had observed H_{C2} at 9.2 ppm and $H_{C5(4)}$ at 7.6 ppm both correlate to a single imidazolyl nitrogen at 190 ppm. Although we did not visualize resonances that correlate to individual imidazolyl units of the four histidine residues it is highly likely that they are overlapping. Another possibility is that despite addition of 9 equivalents of TFA, not all of the imidazolyl units are protonated. As *Hst*-8 would become more highly charged as a result of TFA addition, it becomes more difficult to protonate the various basic sites. So this may mean that there are still histidine residues engaging in proton exchange, which as we have seen do not appear in ^{1}H-^{15}N HMBC or ^{1}H-^{15}N HSQC experiments.

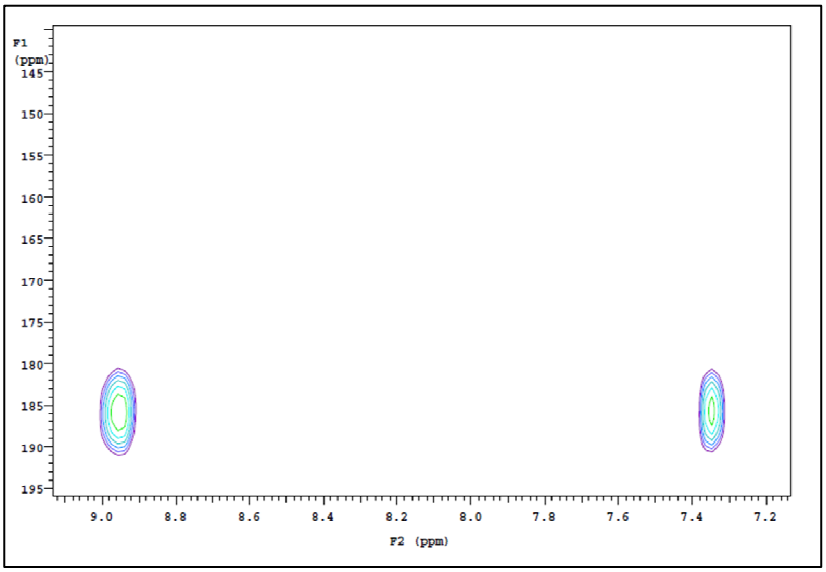

Figure 3.2.22. ^{1}H-^{15}N HMBC spectrum of *Hst*-8 with 9 eq. TFA in DMSO.

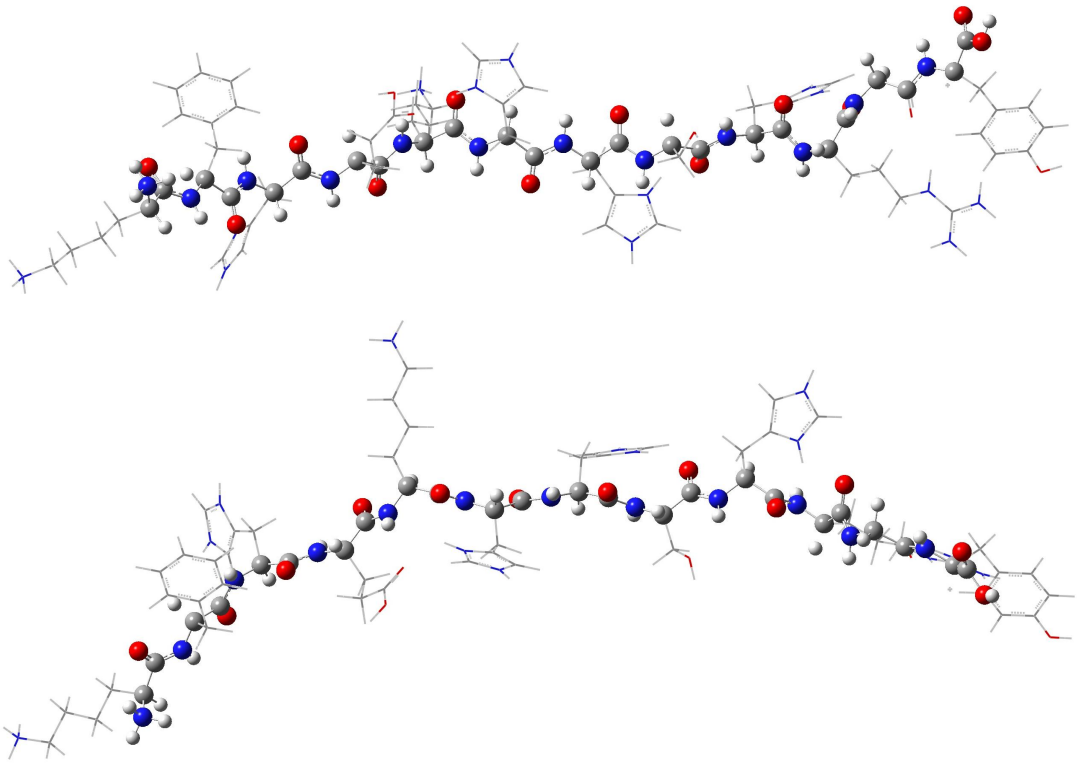

Figure 3.2.23. Two views of *Hst*-8 completely protonated structure calculated at the AM1 semi-empirical level of theory (gas phase). The back bone has been put in ball and stick, the side chains are wireframe. (Colorcode: white – hydrogen, gray – carbon, blue – nitrogen, and red – oxygen)

Figure 3.2.23 illustrates a calculated structure of *Hst*-8 that is completely protonated. It has been calculated using the semi-empirical AM1 level of theory. With a total charge of 8^+ it is hardly surprising that the charged moieties are as distant from each other as possible. The AM1 calculated structure has adopted a beta sheet. Although this is a calculated structure, done for gas phase conditions, the results are consistent with our expectations for the solvated structure. Again, the positively charged moieties are going to be as distant from each other as possible due to

electrostatic repulsion. A beta strand is a structure that would certainly move charge residues away from each other. The backbone from H3-S8 is fairly regular in terms of a beta strand conformation, though it should be noted that there is random coil outside this area. We noted in particular the twisting of the amide linkages at the N and C terminus ends of the structure.

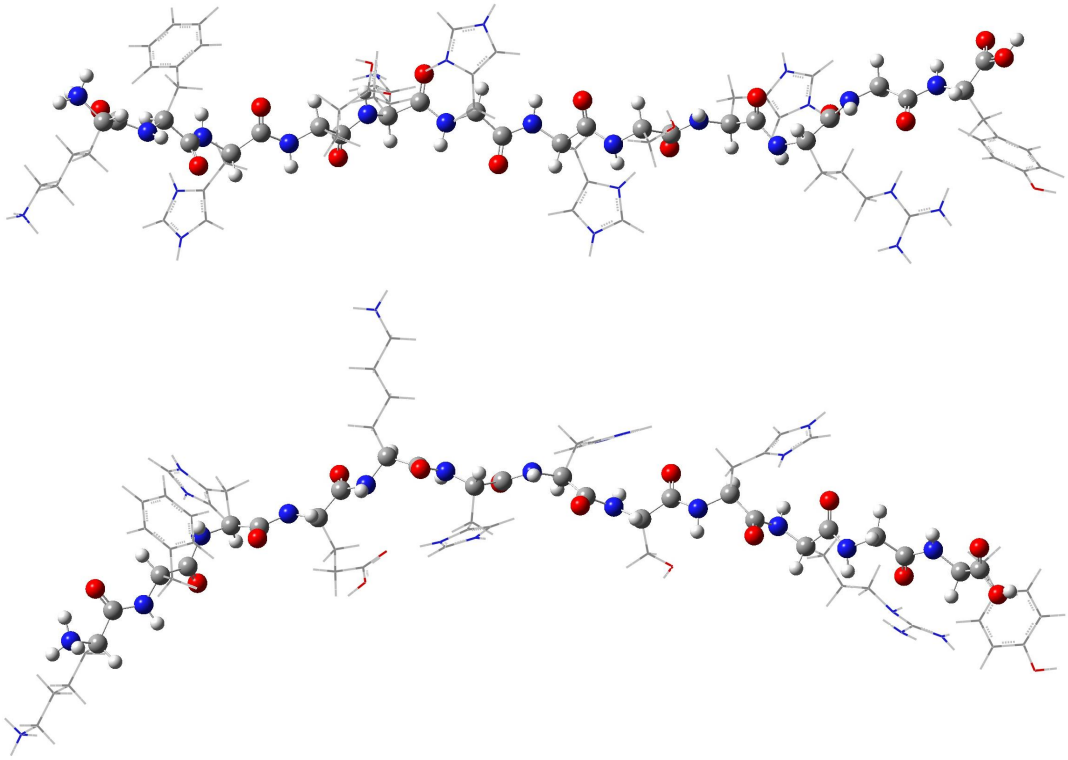

Figure 3.2.24. Two views of *Hst*-8 completely protonated structure calculated at the PM3 semi-empirical level of theory (gas phase). The back bone has been put in ball and stick, the side chains are wireframe. (Colorcode: white – hydrogen, gray – carbon, blue – nitrogen, and red – oxygen)

However, PM3 (figure 3.2.5) and PM3MM (not shown) levels of theory were used to generate structures of *Hst*-8 in its completely protonated form as well. However, as illustrated in figure 3.2.24 which illustrates the structure

of completely protonated *Hst*-8 as calculated by PM3 semi-empirical level of theory, though the protonated moieties have again remained distant from each other, there is significantly more twisting of the mostly beta sheet structure. Here the beta structure exists only in short stretches, from H3-K5 and then due to a twisting at K5, another stretch from K5-S8. As in the AM1 calculated structure we again observe significant disorder at the terminal ends of the peptide. That there is general of agreement between the AM1 PM3 and PM3MM levels of theory in the geometry optimization of *Hst*-8 points to the conclusion that either a beta sheet or random coil structure exists in the gas phase. Note that the PM3 and PM3MM had only very short runs of regular structure and AM1 may weight the beta conformation greatly. Calculations at AM1, PM3, and PM3MM were also attempted starting from an alpha helix. They were unable to complete as a self consistent field was never reached.

At this point we felt ready to pursue Cu(I)-bound *Hst*-8. By removing protons that would potentially compete for binding with the metal at the histidine residues, we believed that metal binding would be made more favorable. To this end, we raised the pH to 9 by addition of sodium hydroxide, monitored by a pH probe. We then lyophilized the sample and dissolved it in DMSO. In the 1-D proton spectrum, figure 3.2.25, we observed several broad resonances in the 8-9 ppm region. Such a phenomenon is generally indicative of an exchange. This is likely due to imidazolyl units undergoing a proton exchange / isomerization. We also noted that despite

lyophilization after the pH adjustment, a large quantity of either water or hydroxide persists in solution as inferred from large broad peak at 3.4 ppm, though we have observed this in prior peptide samples as well.

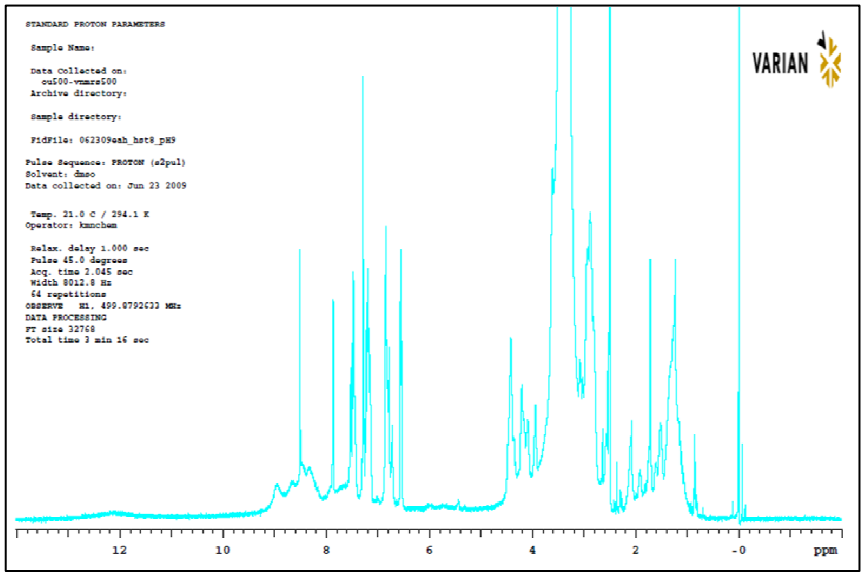

Figure 3.2.25. ^{1}H NMR spectrum of *Hst*-8 adjusted to pH 9 then lyophilized and dissolved in DMSO.

The ^{1}H-^{15}N HMBC spectrum was acquired, but though it had peaks in the imidazole region, they were indistinguishable from noise and we again observed streaking (data not shown). The ^{1}H-^{15}N HSQC of the *Hst*-8 which was adjusted to pH 9 and then dissolved in DMSO, as in previous samples, had no resonances in the imidazolyl region. However, as the ^{1}H NMR spectrum (figure 3.2.25) suggested with its broad peaks, none were expected as they were undergoing proton exchange on the NMR time scale (data not shown). At this point, Cu(I) was added as $Cu(CH_3CN)_4PF_6$ to the sample. As illustrated in figure 3.2.26, there was a generalized line broadening throughout the ^{1}H NMR spectrum.

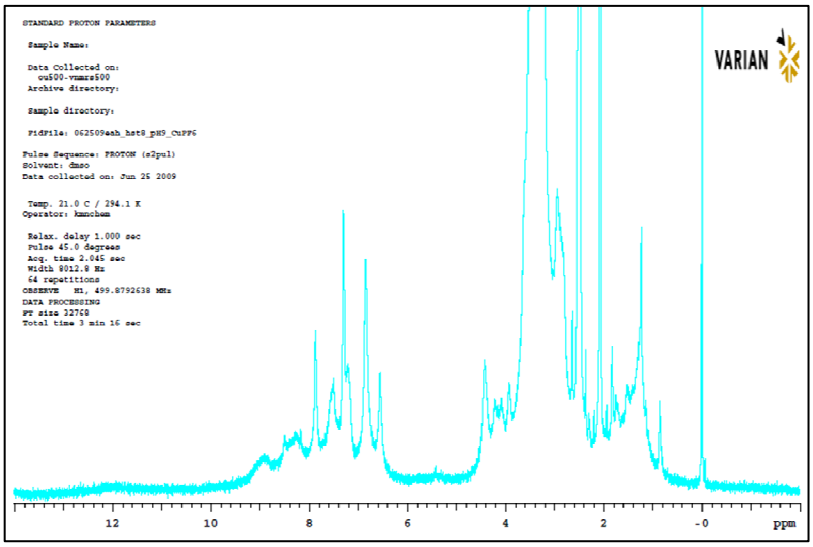

Figure 3.2.26. ^{1}H NMR spectrum of $Cu(CH_3CN)_4PF_6$ and *Hst*-8 which had been adjusted to pH 9 prior to dissolution in DMSO.

The ^{1}H-^{15}N HSQC and ^{1}H-^{15}N HMBC experiments fared little better. The ^{1}H-^{15}N HMBC again had streaking in the imidazolyl region. It also had streaking at 3.38 ppm, 2.6 ppm and 2.1 ppm, which is likely due to exchanging protons interacting with water in DMSO, DMSO, and acetonitrile respectively (data not shown). Thus we were unable to obtain definitive data concerning the complexation of Cu(I) to *Hst*-8 that had been adjusted to pH 9. However, we can infer binding due to the broadening of imidazolyl related signals.

Table 3.2.3. Summary of chemical shift data from ^{1}H NMR and ^{1}H-^{15}N HMBC spectra. (N.P. – not present; N.D. – experiment not done)

	H_{C2}	H_{C4}	H_{C5}	N_1	N_3
histidine methyl ester dihydrocholoride	9.2		7.6	~190	~190
2-TMIC		6.78	7.15	166.8	168
2-TMIC with $Cu(CH_3CN)_4PF_6$		6.73	7.05	N.P.	N.P.
2-TMIC with ascorbic acid		6.78	7.15	N.D.	N.D.
2-TMIC, $CuCl_2$, and ascorbic acid		7.2	7.5	172	240
4-TIC	7.5		6.6	N.P.	N.P.
4-TIC, 3 eq. TFA	8.9		7.42	183	198
4-TIC, $CuCl_2$, and ascorbic acid	9.2		7.5	183	188
Hst-8 and 9 eq. TFA	8.98		7.35	186	186

Table 3.2.3 is a summary of data obtained from ^{1}H NMR and ^{1}H-^{15}N HMBC spectra of *Hst*-8 and other model complexes in a variety of environments. We can see that upon protonation or complexation (with the exception of the 2-TMIC with $Cu(CH_3CN)_4PF_6$) that proton and nitrogen resonances shift downfield. Upon complexation or protonation, C_2 protons (if present) shift to the 9.0 ppm region from the 7.5 ppm region and C_4 protons (if present) shift to the 7.2 ppm region from the 6.7 ppm region. The C_5 protons too show diagnostic shifts upon complexation or protonation. In 4-TIC they appear at 6.6 ppm yet shift to the 7.5 ppm region upon protonation with TFA or complexation with Cu(I) from a $CuCl_2$ and ascorbic acid system. In the free 2-TMIC ligand they start at 7.15 ppm and after complexion with Cu(I) from a $CuCl_2$ and ascorbic acid system they are shifted downfield to 7.5 ppm. The nitrogen nuclei also demonstrate a similar trend, that of downfield shifting as a result of complexation or protonation. However, since we were

ultimately unable to see the expected downfield shift of imidazolyl nitrogen resonances as a result of coordination of Cu(I) to *Hst*-8, we decided to change to an indirect NMR method for investigation of metal ion coordination to *Hst*-8.

3.3: ^{1}H-^{13}C HSQC

As has already been demonstrated in the previous section's work with ^{1}H-^{15}N HMBC, the protons attached to the carbons on the imidazolyl ring can be monitored for evidence of metal ion binding and protonation of the imidazolyl motif as demonstrated in the series of figures 3.2.15-3.2.18 in the previous section. 4-TIC, which was the subject of study in the aforementioned figures, is very similar to the histidine residue. It creates isomers simply on the basis of proton exchange and it has attachment at the 4(5) position. 4-TIC has substantial downfield shifts of both imidazolyl proton resonances, particularly that of H_{C2}. As illustrated in figures 3.2.5-3.2.7 2-TMIC exhibited a marked downfield shift in the nitrogen resonance upon binding to Cu(I) as well as movement of the H_{C4} and H_{C5} proton resonances. Though it would seem it does not complex well with the $Cu(CH_3CN)_4PF_6$, it does complex well with Cu(I) which was formed by the *in situ* reduction of $CuCl_2$ by ascorbic acid. Also, as illustrated in figures 3.2.21, 3.2.24, and 3.2.25, we observed distinct differences in the ^{1}H NMR spectra of *Hst*-8 due to the differing pH and the presence of metal ion. However, though, by inference imidazolyl units are involved in metal binding, we sought more

definitive evidence for such an interaction by investigating the carbon resonances of the imidazolyl units.

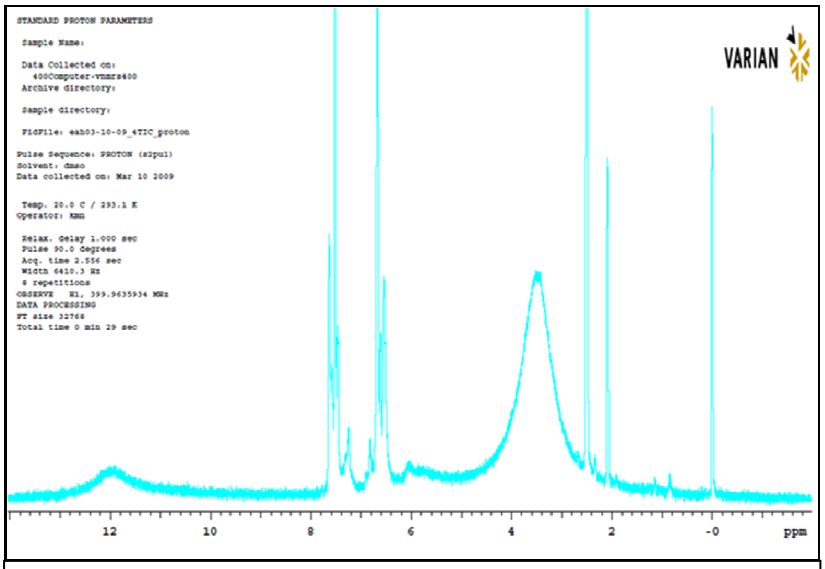

Figure 3.3.1. ^{1}H NMR spectrum of 4-TIC.

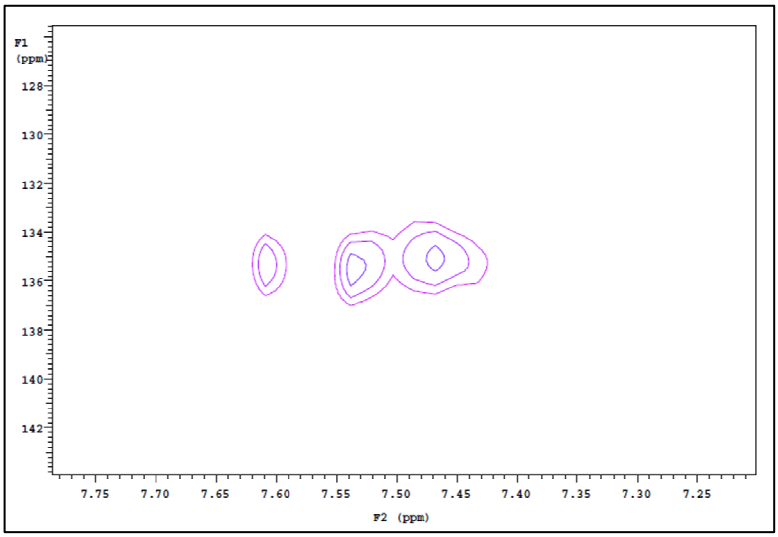

Figure 3.3.2. ^{1}H-^{13}C HSQCAD spectrum of 4-TIC.

The ^{1}H NMR spectrum of the 4-TIC is reproduced above in figure 3.3.1 to reiterate the point of multiple species being present in the free ligand

system. As illustrated in the ^{1}H-^{13}C HSQCAD spectrum of 4-TIC, figure 3.2.2, the C_2 carbon has multiple resonances all in the 135 ppm region. The H_{C2} proton resonances are at 7.60 ppm, 7.54 ppm, and 7.46 ppm. The correlations of the $C_{5(4)}$ to the $H_{C5(4)}$ were not able to be observed in this experiment. We had expected to observe them in the 6.6 ppm region on the basis of the data from the ^{1}H NMR spectrum of 4-TIC (figure 3.3.1). The likely reason for being unable to observe them in this experiment is that as this 2D experiment is longer than the 1D proton experiment we are losing them in the isomerism brought about by proton exchange.

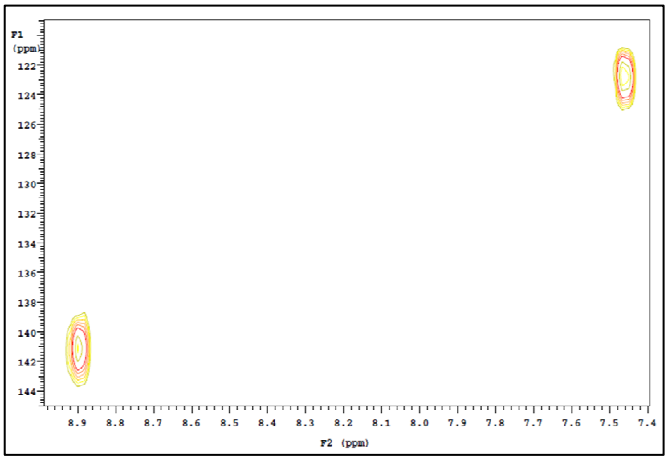

Figure 3.3.3. ^{1}H-^{13}C HSQCAD spectrum of 4-TIC + 3 eq. TFA.

In the ^{1}H-^{13}C HSQCAD spectrum of 4-TIC + 3 eq. TFA (figure 3.3.3), we observe a slight downfield shift of the C_2 resonance to 141 ppm and its associated proton to 8.9 ppm from the free 4-TIC resonances of the C_2 at 135 ppm and the H_{C2} at 7.60 ppm, 7.54 ppm, and 7.46 ppm as a result of addition of 3 equivalents of TFA. Clearly, protonation resulted in the

resolution of the various forms of 4-TIC (whether they be rotamers or isomers) to one form. This downfield shift was of course was expected as we had seen similar behavior in previous ^{1}H-^{15}N HMBC experiments (see previous section). Now we are able to observe the C_5 resonance at 122 ppm. Its associated proton moves downfield to the 7.45 ppm region from the 6.6 ppm region where it was in the free ligand. These assignments are further supported by the data shown in figure 3.2.15 which illustrated a strong ^{1}H-^{15}N HMBC correlation of the H_{C2} position to both nitrogen nuclei, but one strong and one weak correlation of the H_{C5} to the individual nitrogen nuclei.

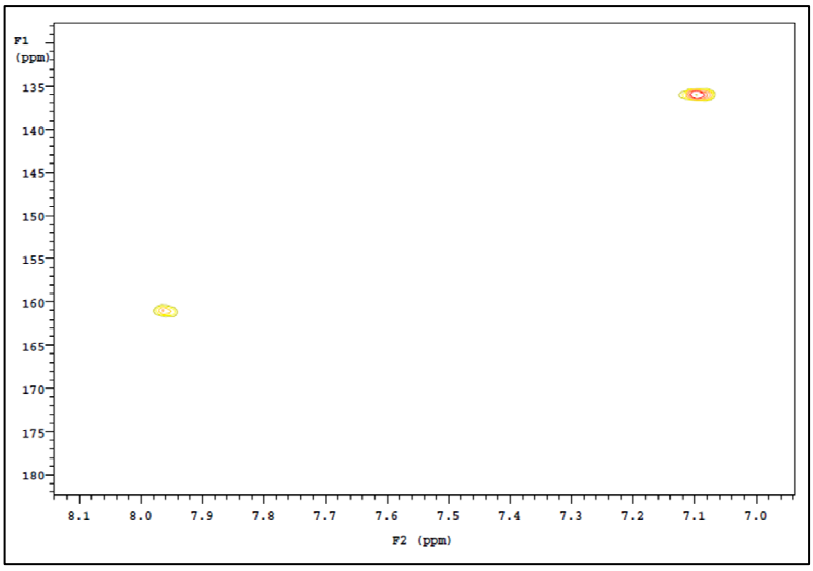

Figure 3.3.4. ^{1}H-^{13}C HSQCAD spectrum of 4-TIC + $Cu(CH_3CN)_4PF_6$ + ascorbic acid.

Although we were unable to obtain a satisfactory ^{1}H-^{13}C HSQCAD spectrum of a $Cu(CH_3CN)_4PF_6$ plus 4-TIC sample, as no peaks were present, addition of ascorbate to the $Cu(CH_3CN)_4PF_6$ and 4-TIC solution resolves the issue entirely as illustrated in figure 3.3.4. There are two

correlations. The H_{C2} peak at 7.96 ppm correlates to the C_2 peak at 161 ppm; the $H_{C5(4)}$ peak at 7.1 ppm correlates to the $C_{5(4)}$ one at 135 ppm. The C_2 and its associated proton now on an imidazolyl unit clearly involved in metal binding are now farther downfield (figure 3.3.4) than the protonated 4-TIC (figure 3.3.3). Though the $C_{5(4)}$ peak has shifted farther downfield to 135 ppm upon metal binding compared to the 122 ppm observed for protonation, the $H_{C5(4)}$ peak for the metal bound is upfield (7.1 ppm) of the protonated $H_{C5(4)}$ (7.45 ppm). We hypothesize that the addition of ascorbate brought about these changes as a consequence of it being a stronger ligand for the *Hst*/Cu complex than either the hexafluorophosphate or the acetonitrile. As had been observed in model complexes and discussed in the literature, the use of a stronger ligand with copper complexes can result in a restoration of signal lost as a result of the effects of copper's quadrupolar nucleus.

Table 3.3.1. Summary of 4-TIC NMR chemical shift data in ppm. (N.D. – experiment not done; N.P. – not present)

	H_{C2}	H_{C5}	C_2	C_5
4-TIC	7.5	6.6	135	N.P.
4-TIC, 3 eq. TFA	8.9	7.42	141	122
4-TIC, $CuCl_2$, and ascorbic acid	9.2	7.5	N.D.	N.D.
4-TIC, $Cu(CH_3CN)_4PF_6$, and ascorbic acid	7.96	7.1	161	135

Table 3.3.1 presents a summary of NMR data obtained for 4-TIC in a variety of environments; as a free ligand, in protonated form, and as a ligand to Cu(I). Clearly upon complexation and protonation chemical shifts of protons and their corresponding carbons are shifted downfield. This is of

course reasonable as one would expect the electron rich imidazolyl unit to donate electron density to the Lewis acidic protons or copper ion. This then in turn removes electron density from the imidazolyl unit pushing the resonances downfield. What is most curious though is that the 4-TIC, $Cu(CH_3CN)_4PF_6$, and ascorbic acid system has a much smaller shift of proton resonances downfield compared to the 4-TIC with TFA and 4-TIC with $CuCl_2$ and ascorbic acid, but the carbons are downfield shifted more. A few possible explanations exist for this phenomenon. The 4-TIC is likely involved in occupying three coordination sites of the Cu(I). There exists then a site open for coordination. In the case of the system utilizing $CuCl_2$, a chloride is available for coordination. A chloride is a much stronger ligand than either acetonitrile or hexafluorophosphate. Previous NMR studies of copper complexes have shown that strong ligands are essential for obtaining good specta.[124] They noted a loss of carbon and copper signal when weak ligands were used. Thus the 4-TIC/Cu(I) complex formed by the $Cu(CH_3CN)_4PF_6$ alone had no peaks due to there being no available strong ligand. When ascorbate was added a stronger ligand was present which enabled a partial visualization of the signal from the 4-TIC/Cu(I) complex. However the ascorbate ligand is still not as strongly coordinating as others. So there exists the possibility that the signal obtained in the 4-TIC, $Cu(CH_3CN)_4PF_6$, and ascorbate system was actually an averaged signal. The 4-TIC/Cu(I) complex with the ascorbate as a ligand, which has a downfield shifted signal as a result of the copper coordination, is averaged with 4-TIC/Cu(I) complex which

does not have the ascorbate ligand and no signal. The other possibility is that the 4-TIC/Cu(I)/ascorbate complex simply does not have a very far downfield shift of its imidazolyl carbon and hydrogen resonances.

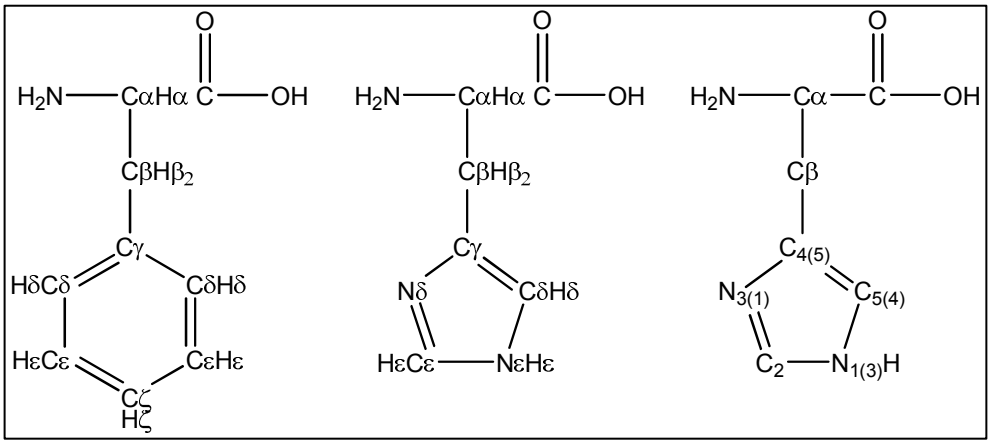

Figure 3.3.5. Naming of amino acids. (left) Phenylalanine with Greek letters, (middle) histidine with Greek letters, and (right) histidine with Greek letters and numbers for imidazolyl motif.

Since we had obtained good results that indicated binding of Cu(I) and protonation in the 4-TIC model complex using ^{1}H-^{13}C HSQCAD experiments, we next looked to investigate the behavior of *Hst*-8 in similar systems. Prior to examining the work done with *Hst*-8, it is worthwhile to again be reminded of how various atoms are identified. Figure 3.3.5 is an illustration of how to identify the protons and carbons of amino acids. On the left is phenylalanine labeled with its Greek lettering notation. Another aromatic residue that will be discussed is tyrosine. Of course, it has similar notation except that a hydroxyl unit substitutes for hydrogen at the ζ (zeta) position. The histidine in the

middle is labeled using Greek letters. However, in this section we have chosen to use the notation on the right, which incorporates the classical Greek lettering notation and the organic chemistry numbering approach. The reason for this is that the classical Greek lettering is good for static systems, but as we have seen already in model system studies the imidazolyl unit undergoes proton exchange and the organic chemistry approach to numbering the imidazolyl motif acknowledges this phenomenon and allows for easier discussion of the system.

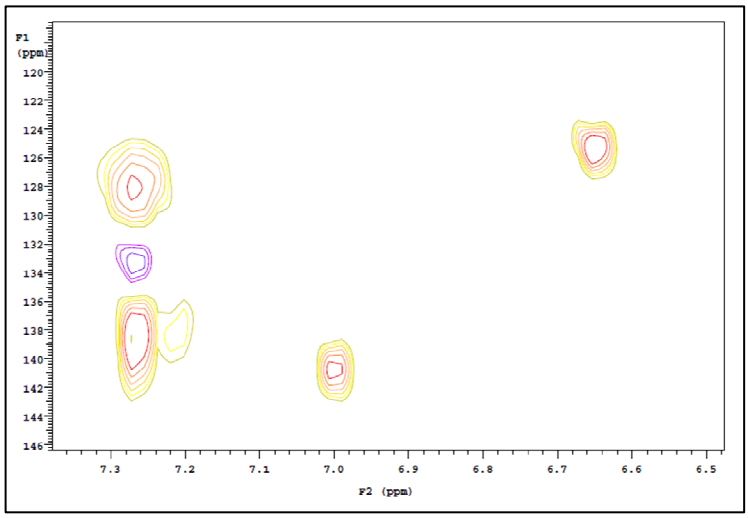

Figure 3.3.6. ^{1}H-^{13}C HSQCAD spectrum of *Hst*-8 in DMSO.

As we had been able to observe the carbon attached imidazolyl proton in our model complex, 4-TIC, using ^{1}H-^{13}C HSQCAD, we attempted the same experiment on *Hst*-8. Figure 3.3.6 illustrates the ^{1}H-^{13}C HSQCAD of *Hst*-8 in deuterated DMSO. We primarily observe the resonances for the protons attached to phenylalanine and tyrosine aromatic motifs. The tyrosine

resonances are the C_{δ} at 141 ppm and its H_{δ} at 7.0 ppm and the C_{ε} at 125 ppm and H_{ε} at 6.64 ppm. Whereas the C_{ζ} of the phenylalanine is at 138 ppm with the corresponding H_{ζ} is at 7.22 ppm. I am unfortunately not able to definitely assign the δ and ε positions in the phenylalanine because of the similarity of their proton resonances 7.26 ppm and 7.27 ppm makes it difficult to distinguish within reasonable experimental times in a sample at natural abundance. Moreover, as we are not particularly interested in those positions anyway, it makes little sense to pursue such a line of inquiry. The correlation observed between the 128 ppm and 7.26 ppm peaks may be ascribable to either the phenylalanine residue or the $C_{5(4)}$ and $H_{C5(4)}$ of the imidazolyl units of the histidine residues. Given its movement and disappearance in subsequent experiments as well as correlations observed in previous experimental series (see previous section), assignment of it as the $C_{5(4)}$ and $H_{C5(4)}$ of the imidazolyl unit is most likely.

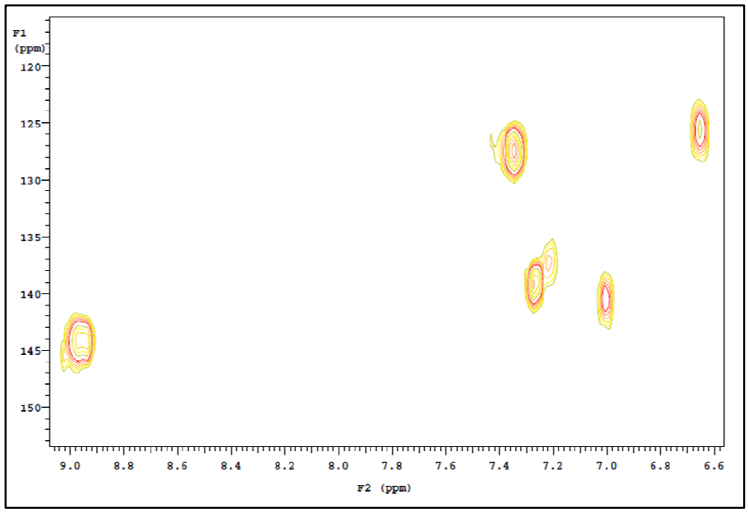

Figure 3.3.7. ^{1}H-^{13}C HSQCAD of *Hst*-8 in DMSO + 9 eq TFA.

Considering the success of the prior exhaustive protonation experiments, we sought to utilize similar methodology with our *Hst*-8 sample. Figure 3.3.7 is the ^{1}H-^{13}C HSQCAD of *Hst*-8 in DMSO with 9 equiv of added TFA. We observe the emergence of the C_2 resonance of the imidazolyl motif at 144 ppm along with its corresponding H_{C2} at 8.98 ppm. Given the intensity it is likely that there are several histidine residues represented by this peak, though we are unable to say for certain which ones. Also, we see that the tyrosine and phenylalanine resonances have remained unchanged. Just as before, the tyrosine resonances are the C_δ at 141 ppm and its H_δ at 7.0 ppm and the C_ε at 125 ppm and H_ε at 6.64 ppm; the C_ζ of the phenylalanine is at 138 ppm with the corresponding H_ζ is 7.22 ppm. Again, I am unfortunately not able to definitely assign the δ and ε positions in the phenylalanine as the similarity of their proton resonances 7.26 ppm and 7.27 ppm makes it difficult

to distinguish within reasonable experimental times with a natural abundance ^{13}C sample. Obviously what is missing is the $C_{5(4)}$ and its proton. Given the odd peak shape of the 127 ppm by 7.26 ppm peak, as well as the results of the ^{1}H-^{15}N HMBC experiment (figure 3.3.8) of the same sample, which indicates a correlation to that particular resonance, it is almost certain this is the imidazolyl 5(4) peak of possibly several histidine residues.

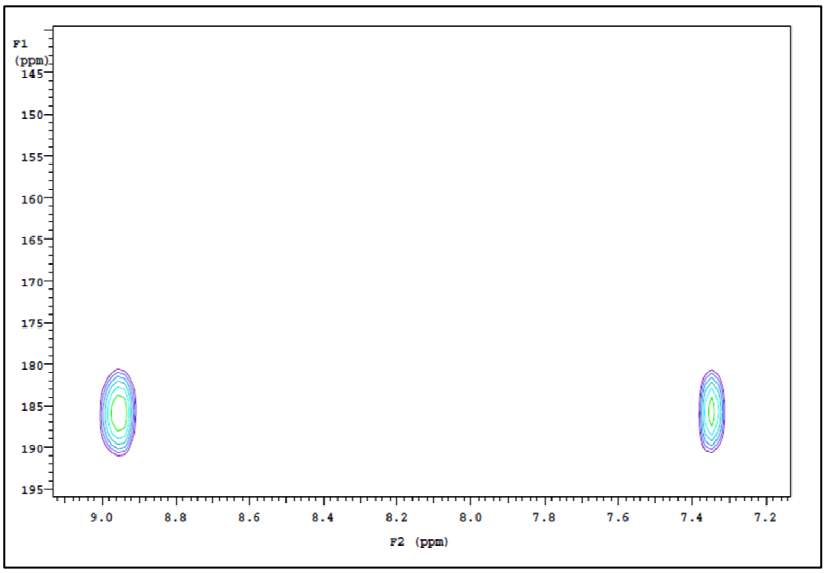

Figure 3.3.8. ^{1}H-^{15}N HMBC spectrum of *Hst*-8 with 9 eq. TFA in DMSO.

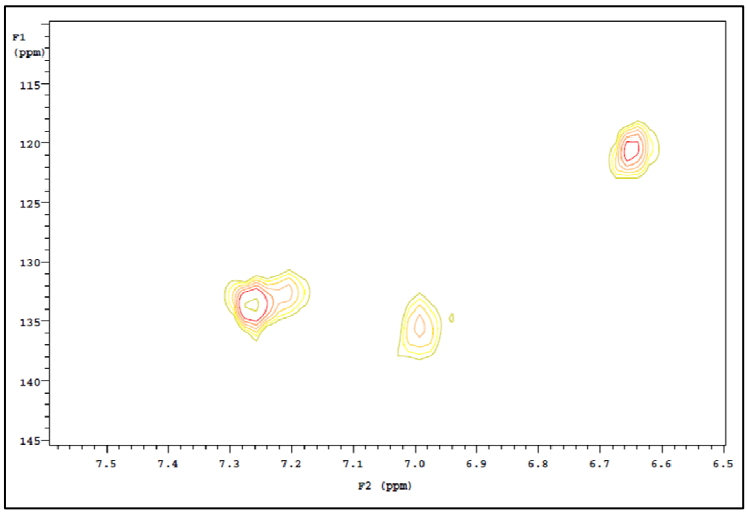

Figure 3.3.9. ^{1}H-^{13}C HSQCAD spectrum of *Hst*-8 + $Cu(CH_3CN)_4PF_6$ in DMSO.

If instead of adding TFA, one equivalent of $Cu(CH_3CN)_4PF_6$ is added to *Hst*-8 in DMSO the ^{1}H-^{13}C HSQCAD spectrum shown in figure 3.3.9 was obtained. We again can only distinguish peaks from phenylalanine and tyrosine. The δ resonances of the tyrosine (135 ppm by 7.0 ppm) are observed to decrease in intensity unlike the peak of correlation for the C_ε to H_ε at 120 ppm by 6.66 ppm. In addition, it would seem that one of the peaks, which is ascribable to the histidine residues has disappeared. However, we clearly observe phenylalanine peaks at 134 ppm and 7.28 ppm and 133 ppm and 7.21 ppm. Since we cannot see any of the 5(4) position, it is likely that all of the histidine residues are involved with Cu(I) binding in some way. The quenching could result from one or a combination of several factors. First, any copper present in a Cu(II) form would result in paramagnetic quenching of signal, as no external reductant was added to this sample it remains

possible that Cu(II) could be present. However, it is far more likely that the quenching of signal is the result of exchange. A histidine exchanging with another histidine on the peptide would result in a loss of signal if it occurred on the NMR timescale. Also, there are protons in the system that compete for the basic imidazolyl units with the Cu(I). *Hst*-8 in this system is already likely to have some of its imidazolyl units protonated. In mass spectroscopy samples analyzed using MALDI-TOF after isolation on HPLC using conditions identical to ours the major protonation state of *Hst*-8 is +1, however, some exists in a +2 state.[125] Considering the four imidazolyl units competing for the metal just on one peptide strand as well as the possibility of inter-strand histidine competition and proton competition with the metal, there exist a wide range of exchange possibilities.

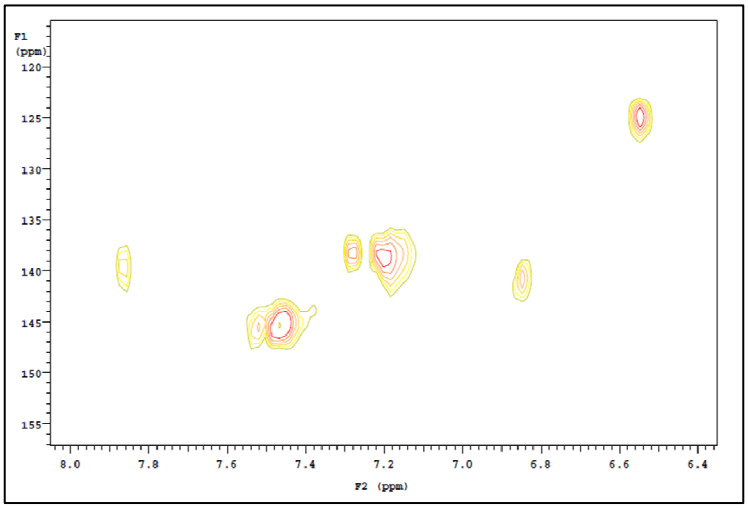

Figure 3.3.10. ^{1}H-^{13}C HSQCAD spectrum of *Hst*-8 adjusted to pH 9 then dissolved in DMSO.

Figure 3.3.10 is the ^{1}H-^{13}C HSQCAD spectrum of *Hst*-8 adjusted to pH 9 then dissolved in DMSO. Again we clearly can observe those correlations for the tyrosine residue; the C_{δ} at 141 ppm and its H_{δ} at 6.88 ppm and the C_{ε} at 124 ppm and H_{ε} at 6.58 ppm. We cannot observe the phenylalanine correlations due to overlap of the imidazolyl resonances. Given the streaking observed in the ^{1}H-^{15}N HMBC of the *Hst*-8 adjusted to pH 9 then dissolved in DMSO sample (data not shown), the peak for the correlation of 7.86 ppm to 139 ppm is the 2 position of the imidazolyl motifs of the histidine residues. We can also see $C_{5(4)}$ and $H_{C5(4)}$ of imidazolyl units at 138 ppm with 7.2 ppm and 7.28 ppm and at 145 ppm correlating with 7.45 ppm and 7.52 ppm. As we observed streaking in the ^{1}H-^{15}N HMBC spectrum it is likely then there remains some exchange.

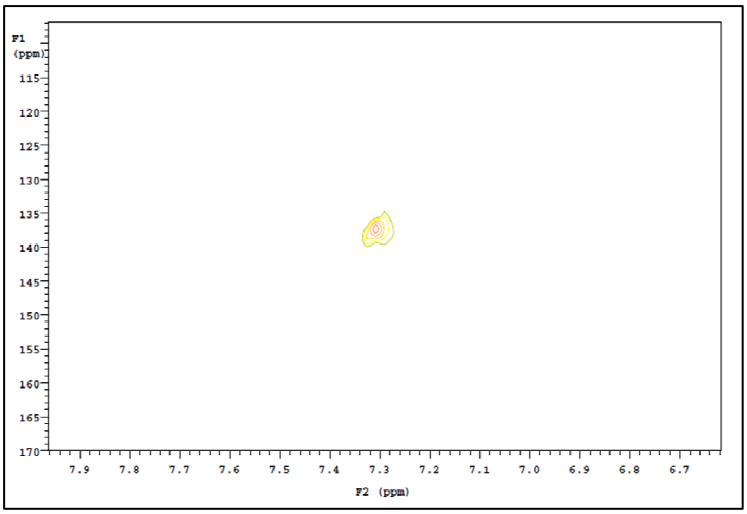

Figure 3.3.11. ^{1}H-^{13}C HSQCAD spectrum of *Hst*-8 adjusted to pH 9 then dissolved in DMSO + $Cu(CH_3CN)_4PF_6$.

Considering the shape of the correlation peak observed in the ^{1}H-^{13}C HSQCAD spectrum of *Hst*-8 adjusted to pH 9 then dissolved in DMSO plus $Cu(CH_3CN)_4PF_6$ (figure 3.3.11), it is likely that there are multiple overlapping resonances present. Also given the chemical shifts of the resonances as well as the fact that metal ion complexation is not likely to involve the aromatic motif of the phenylalanine residue, I would assign this to be phenylalanine. The tyrosine resonances have disappeared as a result of the combination of the high pH and the copper addition. Recall that in the non pH adjusted *Hst*-8 sample with copper (I) (figure 3.3.9), the tyrosine resonances persisted. In all likelihood, the high pH resulted in a deprotonated phenol unit of the tyrosine which allowed for interaction with the copper ion. This in turn resulted in signal quenching. Note also, that there are no imidazolyl resonances present. It is therefore likely that the histidine residues too are involved with complexing the copper (I) ion and are also quenched.

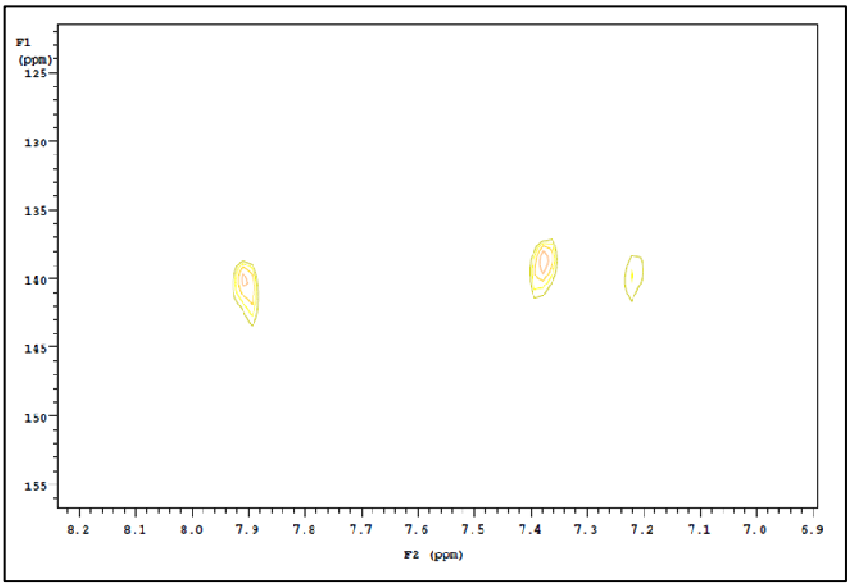

Figure 3.3.12. ^{1}H-^{13}C HSQCAD spectrum of *Hst*-8 adjusted to pH 9 then dissolved in DMSO + $Cu(CH_3CN)_4PF_6$ + ascorbic acid.

We had observed a reemergence of signal in previous trials upon addition of ascorbic acid to the system, so we tried such an approach here. It worked very well as illustrated in figure 3.3.12. The correspondence peak at 140 ppm and 7.9 ppm results from a C_2–H_{C2} on the imidazolyl unit of a histidine involved in complexation. The phenylalanine peaks remain, though they have been slightly moved to 138.5 ppm at 7.39 ppm and 139 ppm at 7.22 ppm. Unfortunately, these may also be imidazolyl peaks, however since ^{1}H-^{15}N HMBC experiments to investigate if they were imidazolyl and ^{1}H-^{13}C HMBC experiments to investigate if they were phenylalanine did not provide a definitive answer, the assignment is unclear. Again we observe that the tyrosine residues peaks have completely disappeared. Although the ^{1}H-^{13}C HMBC did not have any data save for that of the solvents, DMSO and

acetonitrile (data not shown), the ^{1}H-^{15}N HMBC (streaked, data not shown), indicates that the 7.9 ppm hydrogen resonance is part of an imidazolyl unit.

Table 3.3.2. Summary of histidine chemical shifts (in ppm) of *Hst*-8 under a variety of conditions. (N.P. – not present; Am. – ambiguous)

	H-H_{C2}	H-H_{C5}	H-C_2	H-C_5
Hst-8	Am.	7.3	Am.	128
Hst-8 and 9 eq. TFA	8.98	7.3	144	127
Hst-8 with $Cu(CH_3CN)_4PF_6$	N.P.	N.P.	N.P.	N.P.
Hst-8 adjusted to pH 9	7.86	7.2	139	138
		7.28		138
		7.45		145
		7.52		145
Hst-8 pH 9 with $Cu(CH_3CN)_4PF_6$	N.P.	N.P.	N.P.	N.P.
Hst-8 pH 9 with $Cu(CH_3CN)_4PF_6$ with ascorbic acid	7.9	Am.	140	Am.

As illustrated in table 3.3.2, which summarizes the histidine chemical shifts (in ppm) of *Hst*-8 under a variety of conditions, we still encountered a great deal of difficulty in probing the imidazolyl units of *Hst*-8. In +1 to +2 charged *Hst*-8 we were unable to detect individual imidazolyl residues; the 5 position of perhaps an averaged histidine was all that was observable. Although the chemical shift of the hydrogen seems to be rather downfield, when compared to the free 4-TIC, the upfield chemical shift of the carbon combined with the NOESY data in the previous section, as well as other published literature[79] indicate that this is in fact a 5 position of a histidine imidazolyl unit. In all likelihood this is of a protonated histidine, as the chemical shifts are similar to that of the *Hst*-8 with 9 eq. of TFA and the 4-TIC with 3 eq. of TFA. Unfortunately, we were unable to detect the 2 position of

any imidazolyl unit in free *Hst*-8. However, we were able to visualize it, as well as the 5 position, in the *Hst*-8 with 9eq. of TFA solution. Here the chemical shifts match up nicely to those of our model 4-TIC with 3 eq. TFA.

We were unable to detect any relevant resonances when we added $Cu(CH_3CN)_4PF_6$ to *Hst*-8. When the *Hst*-8 was adjusted to pH 9, several new resonances were observed. Given the correlations of two protons to one carbon in the ^{1}H-^{13}C HSQCAD spectrum, the assignment is made to the 5(4) positions. This was observed in prior experiments illustrated in the spectra of 4-TIC (figures 3.3.1 and 3.3.2). As previously mentioned, 4-TIC, like histidine residues, can undergo facile isomerization by proton exchange between the nitrogen on the imidazolyl unit. An alternative explanation is that these are in fact unique resonances of the 5 positions of the four histidine residues of *Hst*-8. Nonetheless, we were also able to observe the C_2 and the H_{C2} of a histidine's imidazolyl unit at 139 ppm and 7.86 ppm respectively. Despite our success with the pH 9 adjusted *Hst*-8 sample, we were unable to visualize any imidazolyl resonances when $Cu(CH_3CN)_4PF_6$ was added to *Hst*-8, which had been adjusted to pH 9. When ascorbic acid was added to the *Hst*-8, which had been adjusted to pH 9, / $Cu(CH_3CN)_4PF_6$ sample, we were able to observe an imidazolyl C_2-H_{C2} correlation at 140 ppm and 7.9 ppm. Although the ascorbic acid addition to the *Hst*-8 pH 9 with $Cu(CH_3CN)_4PF_6$ undoubtedly added protons to the system, it did not adjust the pH enough to return the *Hst*-8 to the monocationic state of the initial sample because we were clearly unable to visualize the tyrosine's phenolic protons like we were

able to in the *Hst*-8 with $Cu(CH_3CN)_4PF_6$ in DMSO sample. It is likely that the additional proton equivalent became involved with the amino-ammonium equilibrium.

Table 3.3.3. Summary of NMR data in ppm of the tyrosine residue in *Hst*-8 under a variety of conditions. (N.P. – not present)

	Y-C_δ	Y-H_δ	Y-C_ε	Y-H_ε
Hst-8	141	7	125	6.6
Hst-8 and 9 eq. TFA	141	7	125	6.6
Hst-8 with $Cu(CH_3CN)_4PF_6$	135	7	120	6.7
Hst-8 adjusted to pH 9	141	6.9	124	6.6
Hst-8 pH 9 with $Cu(CH_3CN)_4PF_6$	N.P.	N.P.	N.P.	N.P.
Hst-8 pH 9 with $Cu(CH_3CN)_4PF_6$ with ascorbic acid	N.P.	N.P.	N.P.	N.P.

Although histidine residues of *Hst*-8 seem to have the most dynamic role in the environments examined for metal complexation and protonation, we noted over the course of our studies that the tyrosine residue also seems to play a role in metal complexation as the data in table 3.3.3 suggests. We found the tyrosine to be insensitive to the various pH environments tested except under conditions of high pH with copper. Note that the +1 / +2 charged *Hst*-8, the *Hst*-8 with 9 eq. of TFA, and *Hst*-8 that was adjusted to pH 9 all had C_δ, H_δ, C_ε, and H_ε at 141 ppm, 7 ppm, 125 ppm, and 6.6 ppm respectively. However, addition of $Cu(CH_3CN)_4PF_6$ to *Hst*-8 results in an upfield shift of the carbon resonances, the C_δ moved from 141 ppm to 135 ppm and the C_ε moved from 125 ppm to 120 ppm. Curiously though, the protons proved to be mostly insensitive to the addition. However, in the high

pH environments the data, or rather the lack of data allows for interpretation. As none of the resonances were observed, this leads us to the conclusion that the tyrosine residue is deprotonated and involved with copper ion coordination in the two samples that have both high pH and copper ion.

Table 3.3.4. Summary of resonances of protons in *Hst*-8 with 1 eq. $Cu(CH_3CN)_4PF_6$ in DMSO compared to *Hst*-8 in DMSO. (N.M. - not meaningful; Am. – ambiguous; N.P. - not present)

Group	Proton	Shift for 1 eq. Cu(I)	Shift for 0 eq. Cu(I)	difference
K1	α	3.72	3.71	-0.01
K1	β	Am.	1.65	N.M.
K1	γ	Am.	1.46	N.M.
K1	δ	Am.	2.73	N.M.
K1	ε	Am.	1.29	N.M.
F2	N	8.63	8.62	0.00
F2	α	4.58	4.57	-0.02
F2	β1	2.80	2.80	-0.01
F2	β2	3.01	3.01	0.00
F2	2,6H	7.27	N.P.	N.M.
H3	N	N.P.	8.63	N.M.
H3	α	N.P.	4.63	N.M.
H3	β1	Am.	2.96	N.M.
H3	β2	Am.	3.06	N.M.
E4	N	8.19	8.22	0.03
E4	α	4.28	4.29	0.00
E4	β1	1.75	1.75	0.00
E4	β2	1.89	1.89	0.00
E4	γ	2.26	2.26	0.00
K5	N	N.P.	8.24	N.M.
K5	α	N.P.	4.20	N.M.
K5	β1	Am.	1.59	N.M.

K5	δ	Am.	1.50	N.M.
K5	ε	N.P.	2.74	N.M.
H6	N	8.34	8.33	-0.01
H6	α	N.P.	4.57	N.M.
H6	β1	2.96	2.95	-0.01
H6	β2	Am.	3.04	N.M.
H6	4H	Am.	7.33	N.M.
H7	N	N.P.	8.32	N.M.
H7	α	N.P.	4.63	N.M.
H7	β1	N.P.	2.95	N.M.
H7	β2	N.P.	3.06	N.M.
S8	N	8.26	8.29	0.03
S8	α	4.31	4.30	0.00
S8	β1	N.P.	3.61	N.M.
S8	β2	3.57	3.56	-0.02
H9	N	8.38	8.39	0.01
H9	α	4.62	4.63	0.01
H9	β1	2.97	2.98	0.02
H9	β2	3.10	3.11	0.01
R10	N	8.19	8.16	-0.02
R10	α	4.27	4.26	-0.01
R10	β1	1.68	1.67	-0.01
R10	β2	3.07	3.07	0.00
R10	γ	1.50	1.49	-0.01
R10	NH1	7.56	7.61	0.06
G11	N	8.29	8.31	0.02
G11	α	3.74	3.73	0.00
Y12	N	8.21	8.22	0.00
Y12	α	4.34	4.35	0.00
Y12	β1	2.75	2.75	0.00
Y12	β2	2.91	2.90	0.00
Y12	2,6H	6.99	6.99	0.00
Y12	3,5H	6.64	6.64	0.00

Table 3.3.4 was drawn from the conformational studies of *Hst*-8 by NOESY, ROESY, and TOCSY experiments and will be discussed in chapter 4.3 in greater detail. However, it does contain data, which is important in the metal binding studies. Firstly one can notice that we observe chemical shifts for the phenylalanine amide proton ($F2H_N$) in the *Hst*-8 sample with the Cu(I). Such an observation necessarily precludes ACTUN like binding on the part of *Hst*-8. Recall that ACTUN like binding would involve the amino terminus, the nitrogen atoms of the first two amide linkages of the peptide and the imidazolyl unit of the histidine residue in the third position. In the classical ACTUN model the first residue is an aspartic acid. Other data to note is that the chemical shifts of the vast majority of *Hst*-8 are not affected very much at all as a result of metal binding. The obvious conclusion is that those particular residues that are not dramatically shifted are not involved in metal ion binding. Also those resonances that disappear are likely involved in metal ion binding. Though one would initially expect a mere downfield shift in residues involved in metal ion binding, a loss of signal points to a different conclusion. Namely that metal ion binding is not very tight and an equilibrium on and off the metal is occurring on the NMR time frame. The data with respect to which residues are involved in metal ion binding fit with our hypothesis as to where the metal likely binds: the histidine residues in the 3, 6, and 7 positions. The equilibrium exchange on and off the metal not only affects the chemical shifts of the imidazolyl units of the residues, but also the beta, alpha, and amide protons as a consequence of the conformational

changes occurring resulting from the metal binding equilibrium. Granted this is not conclusive evidence, but the data certainly fits the hypothesis.

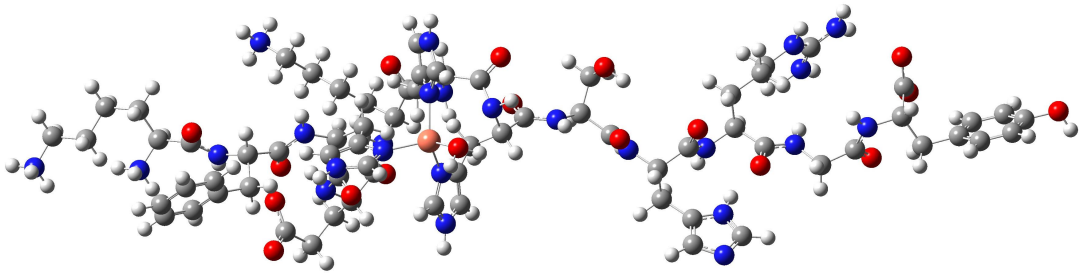

Figure 3.3.13. Structure of *Hst*-8/Cu complex and a water ligand. Minimized with UFF MM (gas phase). The *Hst*-8 was initially a beta sheet. (Colorcode: white – hydrogen, gray – carbon, blue – nitrogen, red – oxygen, and peach - copper)

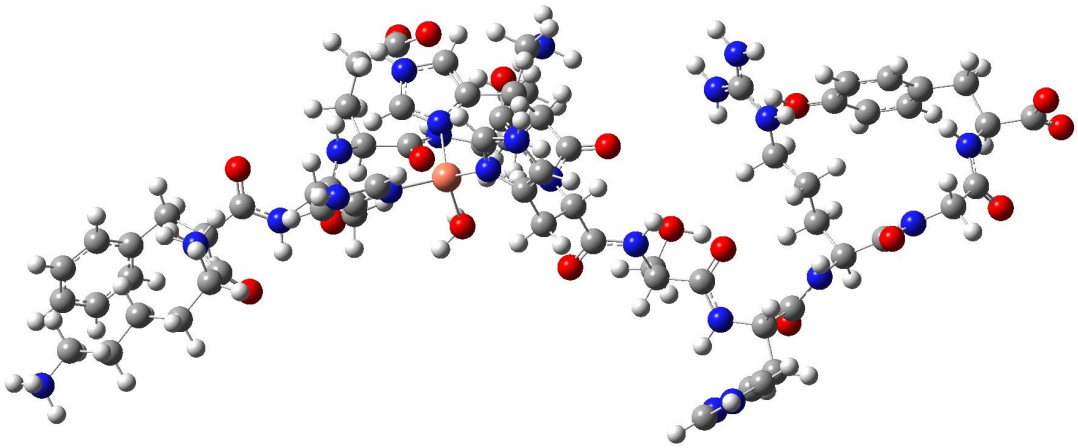

Figure 3.3.14. Structure of *Hst*-8/Cu complex and a water ligand. Minimized with UFF MM (gas phase). The *Hst*-8 was initially an alpha helix. (Colorcode: white – hydrogen, gray – carbon, blue – nitrogen, red – oxygen, and peach - copper)

Presented in figures 3.3.13 and 3.3.14 are molecular mechanics minimized structures of *Hst*-8 complexed to copper via its H3, H6, and H7 residues. The copper's fourth ligand is water. The difference between the two

structures is the starting points of the minimization. For figure 3.3.13, the starting point was *Hst*-8 in a beta strand. *Hst*-8 initially was in an alpha helix for the result of the calculation illustrated in figure 3.3.14. Unfortunately, we were unable to obtain a final minimized structure at PM3 level of theory for either starting point. Figure 3.3.13 is obviously unstructured; meaning that there are no beta strand or alpha helical secondary structures. In the first part of the structure the complexing histidine residues are a tight turn. The beta strand structure in the last half as well has been disrupted. Notice that the amide functionalities on the H9 residue are clearly not that of either a beta strand or alpha helix. Similarly, the secondary structural elements of the structure illustrated in 3.3.14 have been disrupted. Beta strand elements can be observed between H7-H9.

The unstructured nature of the *Hst*-8 when bound with copper as determined by computational chemistry methods is certainly in line with our interpretation of figure 4.3.1 (Part of the NOESY spectrum of *Hst*-8 and Cu(I) in DMSO illustrating amide alpha and amide beta interactions) and the rest of the conformational data. We found in our analysis of the conformational data, Chapter 4, that *Hst*-8 is unstructured when it is complexed with copper. Also supporting the idea of exchange, that of multiple conformations, was the interpretation of figure 4.3.1. The lack of peaks in the alpha amide region for the H3-H7 region, as summarized in table 3.3.4, is the result of exchange of the ligating histidine residues on and off the metal. When copper (I) is tightly bound such as in prior studies[121-123] and our studies on model complexes the

imidazolyl resonances were downfield shifted. We also observed downfield shifts of proton, nitrogen, and carbon resonances of imidazolyl units when those units were protonated.

Exchange can result in many types of spectral changes. Amino proton peaks are broad and often not observed as a result of proton exchange. Conformational exchange often results in signal averaging and the averaged signal is also often broad. A common solution to this problem is lowering the temperature of sample. This technique results in the separation of the averaged peak into two distinct separate peaks. However, as our sample was already at 20ºC, the hopes of freezing out two conformations as close to the DMSO freezing point, 18.5ºC, was unlikely. Nonetheless, such examples demonstrate the effects of exchange upon NMR spectra. Such illustrative examples of exchange then help to rationalize our conclusions as to the location and nature of ligation of the *Hst*-8 to the copper.

3.4: EPR Studies on Copper(II)-*Hst*-8

As aforementioned, EPR studies have been used to investigate metal ligand environments.[119, 126, 127] We sought to utilize this tool to investigate the metal binding environment of Cu(II) with *Hst*-8. As before, we used model complexes to test our experimental techniques and setup. Although we can clearly see the EPR signal for the unpaired electron in the copper, there is no discernable hyperfine coupling (hfc) in the 2900-3100 g region.

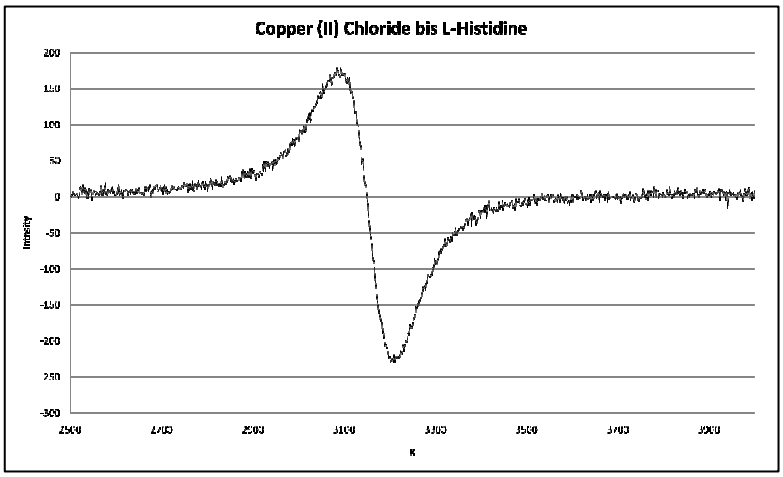

Figure 3.4.1. EPR spectrum of Cu(II) bis L-histidine complex.

Similar results were also obtained for a Cu(II)-2-TMIC complex in that no hfc was discernable (data not shown). We had undertaken many different attempts to improve resolution and adapt our experiments to the equipment. The apparatus used was a liquid nitrogen dewar, which due to boil off, shifted the sample inside the microwave cavity which resulted in noise. Also as bumping was a problem scan times were shortened. Multiple scans were taken and averaged to improve signal to noise. We also attempted less conventional measures such as smaller samples, which we considered, as water (the solvent) may be absorbing radiation and resulting in a loss of sensitivity. Despite our many attempts to visualize an hfc in copper complexes, we were unable to obtain satisfactory results and this line of inquiry was abandoned.

3.5: Experimental Section

3.5.1: General NMR Procedure, Materials, and Methods

A Varian Unity/Inova 400 MHz system upgraded to VNMRS with an auto-tunable Dual Broadband ^{15}N-^{31}P $\{^{1}H\}$ PFG probe utilizing the VNMRJ software suite for collection and processing or a Varian VXR 500 MHz system upgraded to VNMRS with a triplet resonance $^{1}H\{^{13}C/^{15}N\}$ PFG probe utilizing VNMRJ software suite for collection and processing was employed. Samples were maintained at 20ºC for the duration of the experiment. Prior to collection of 2D homonuclear or heteronuclear experiments each sample had its 90º pulsewidth (PW90) determined, which then was input as a parameter into subsequent experiments.

For experiments involving air and moisture sensitive copper(I) species, including those species that were reduced *in situ*, samples were placed in a J. Young NMR tube (600 MHz glass, Wilmad Labglass). This allowed the sample to be maintained under inert atmospheric conditions (either argon or nitrogen). Also manipulation of $Cu(CH_3CN)_4PF_6$ was done in a glovebox (VAC model MO-M).

Histatin-8 was purchased as a crude solid phase preparation product (55-60% purity depending on batch) from the Molecular Biology Proteomics Facility of the University of Oklahoma Health Sciences Center. It was isolated and purified by HPLC by dissolving the sample in a small volume of 0.1% TFA/water and injection onto a C18 RP-Prep-HPLC column (Biorad

BioLogic). Elution with a linear solvent gradient from 100% water (0.1% TFA) to 60% H_2O (0.1% TFA) / 40% 4:1 acetonitrile:H_2O (0.1%TFA) (4 mL/min) over 74 min afforded *Hst*-8 with a typical retention time of 9 min. The *Hst*-8 fraction was determined by ESI-MS.

L-Ascorbic acid (99+% A.C.S. reagent), tetrakis(acetonitrile)copper(I)hexafluorophosphate, and L-histidine methyl ester dihydrochloride (97%) were obtained from Aldrich. Copper chloride hexahydrate (analytical reagent) from Mallinkrodt. L-Histidine was obtained from Matheson, Coleman, & Bell. Sodium hydroxide (ACS grade pellets) was obtained from EMD. Trifluoroacetic acid (99% extra pure) was obtained from Acros. Dimethylsulfoxide-D6 (D 99.9%) was obtained from Cambridge Isotope Laboratories.

4-Trisimidazoylcarbinol (4-TIC) was the generous gift of Jerome Volkman who synthesized it by a published procedure.[128]

2-Tris(N-methylimidazoyl)carbinol (2-TMIC) was synthesized via literature procedure.[36]

For experiments involving adjustment to pH 9 prior to dissolution in DMSO, first a solution of dilute sodium hydroxide was made that was approximately 0.01 M. The sample was dissolved in DD/DI water and the pH of the solution was monitored by pH meter. The NaOH solution was added drop wise until pH 9.0 was obtained. The sample was then lyophilized and dissolved in DMSO.

3.5.2: ^{1}H-^{15}N HMBC

A 3 Hz *J* was input and the experimentally obtained PW90 was input as parameters for collection. For observing imidazolyl motif nitrogen nuclei a decoupler offset frequency (dof) was routinely set at 120 ppm (on the 400 MHz instrument in DMSO d_6 this corresponds 695.4 Hz).

3.5.3: ^{1}H-^{15}N HSQC

Here a *J* value of 93 Hz was used as well as the experimentally collected PW90 parameter. The dof was again routinely set at 120 ppm.

3.5.4: ^{1}H-^{13}C HSQCAD

For these experiments a *J* value of 200 Hz was used as well as the experimentally collected PW90 parameter. The dof was not altered from the standard experimental settings.

3.5.5: EPR Studies

In a typical experiment the reactants were mixed in an Eppendorf tube. These were then transferred to a quartz 4mm tube cell and placed in a dewar containing liquid nitrogen in the microwave cavity. The instrument was a Bruker EMX EPR system using an ER041XG X-band microwave bridge and an ER4102ST microwave cavity. Spectra were collected using the 32-bit WinEPR ver. 4.32 Rev. 10 software from Bruker. Typical spectral acquisition

parameters for the experiment were modulation frequency 100 kHz; modulation amplitude 1.0 G; microwave power 10 mW; amplifier time constant 0.1 s; and filed sweep rate 1500 G / 80 s. The static field was set at 3480 G and the center of the field set at 3250 G. Generally, 1 scan was collected and then the data was exported to Microsoft Excel where it was averaged and combined to generate spectra. The concentration of the copper species was generally 5 mM in the sample.

3.5.6: Computational Chemistry Methods

ArgusLab (ArgusLab 4.0.1 written by Mark A. Thompson of Planaria Software LLC, Seattle, WA (http://www.arguslab.com)) was used for molecular mechanics calculations, PM3 calculations that involved metals, and AM1 calculations that involved metals.

For PM3 and AM1 calculations, as well as PM3MM and higher levels of theory Gaussian 03 was used.[129]

Results from both computational suites were visualized and exported to JPEG files using Gaussview (Gaussian, Inc., Wallingford CT http://www.gaussian.com) or ArgusLab.

Chapter 4: Conformation Studies

4-1: Introduction

The conformation of the *Hst* is of interest because as aforementioned in the introductory chapter many proteins's activity depends greatly on its conformation. *Hst*'s mode of action of antimicrobial activity on the basis of pore formation was ruled out. This was done not only on the basis of the studies with lysomes,[24, 25] the observation that active transport is required for uptake[16, 17] and the observation that only a few intracellular species are observed to have an increase in extracellular fluids upon *Hst* exposure,[19, 20] but also in part due to the conformational studies already done on both *Hst*-5[78] and *Hst*-8.[79]

As we have shown in previous work a *Hst*-copper complex can in a reducing environment produce ROS.[70] As has been illustrated with the previous NMR and CD work on *Hst,* the ability for *Hst* to adopt a helical conformation in membrane mimicking solvents has been positively correlated to its antimicrobial activity. Given the labile pool of copper in the cellular environment that *Hst* could potentially recruit a copper ion from, as well as a gap in the scientific literature about the conformation of *Hst* in the presence of metal ion; we sought to undertake such a study. Of course the conformation of peptides has been studied by X-ray crystallography, NMR, CD, and even vibrational spectroscopies. Each of these techniques has its own strengths and weaknesses. We choose to use NMR as it would give us

a solution state structure that was highly detailed. CD can only indicate the presence or absence of helical structures and X-ray characterization requires a crystal. Histatin's high solubility as well as the potential for peptide aggregation precluded such an investigation.

Hst-5: Asp-Ser-His-Ala-Lys-Arg-His-His-Gly-Tyr-Lys-Arg-Lys-Phe-His-Glu-Lys-His-His-Ser-His-Arg-Gly-Tyr

Hst-8: Lys-Phe-His-Glu-Lys-His-His-Ser-His-Arg-Gly-Tyr

Figure 4.1.1. Primary structures of *Hst*-5 and *Hst*-8.

Hst-5 has had its conformation studied in a number of solvents by different methods. In aqueous systems as investigated by circular dichroism, CD, *Hst*-5 was observed to be unstructured (random coil) over a pH range of 3.8 to 8.3.[81] Similar results were also obtained using NMR, though they restricted their measurements to pH 3.8.[78] It has also been determined that in DMSO *Hst*-5 adopts an alpha helical conformation both by CD and NMR.[78, 81] Chain length and composition has been shown to be influential in this behavior of transitioning between unstructured in aqueous environments and alpha helical in DMSO. As chain length and composition have also been shown to affect the antimicrobial activity of histatins and various histatin-like derivatives, a study was done that correlates these factors to the ability to undergo a conformational transition from unstructured in an aqueous system to alpha helical in DMSO. The study using CD found that those derivatives and analogues that underwent transition similar to that of *Hst*-5 were more active than those that did not.[80, 81, 130] These findings then support the idea

that the ability to adopt an alpha helical structure may be important in the functioning of *Hst*-5 as an antimicrobial agent.

Just as *Hst*-5 has been shown to undergo a conformational transition, *Hst*-8 has also been shown by NMR to undergo a conformational transition from a beta-pleated structure in an aqueous environment to an alpha helix in a less polar solvent system.[79] In this study *Hst*-8 was adjusted to pH 4.0 and then either used directly as an aqueous NMR sample or else freeze dried and then dissolved in the desired solvent. Just as with *Hst*-5, they observed that *Hst*-8 did not adopt an alpha helix in a simple aqueous environment. However, unlike *Hst*-5, *Hst*-8 did not adopt an alpha helical conformation in DMSO. *Hst*-8 did adopt an alpha helical conformation in a solvent system containing 40% hexafluoroacetone (HFA), 55% H_2O and 5% D_2O. A major difference between DMSO and HFA is the dielectric constant of the solvents. DMSO has a dielectric constant of 47.2 and a dipole moment of 3.96. HFA is significantly less polar with a dielectric constant reported between 2.4 and 1.9 and a dipole moment of between 0.61 and 0.64.[131] Of course, HFA will react with water to form the corresponding gem-diol,[132] so the actual nature of the 40% HFA / 60% aqueous solvent system used in the NMR study is not such a clear system to interpret. This is especially true given that formation of the gem-diol results in the release of one equivalent of proton. So the pH adjustment to 4.0 prior to addition of this solvent system is fairly meaningless as the solvent system itself is highly acidic. Nonetheless they were able to observe a conformational transition to an alpha helix on the basis of

alteration of the solvent environment.

The *Hst* conformation is likely to play a role in its ability to recruit and complex metal ions. As a beta strand or simply unstructured, the residue side chains capable of engaging in metal binding activities are far apart. Thus such a conformation would preclude chelation as other ligating moieties are distant. However, a change in conformation could bring metal ligating moieties in close proximity, which would favor chelation. An alpha helical conformation would certainly be a structure that would favor metal ion chelating activities. Shown in figure 4.1.2 is monocationic *Hst*-8 in a beta strand. Notice that the histidine residues' imidazolyl units are distant from one another. The only possibility for chelation to occur is with the H7 and H9 residues. The H6 residue is on the other side of the molecule and H3 is quite distant. However, that same monocationic *Hst*-8 in an alpha helical conformation has three histidine residues in close proximity.

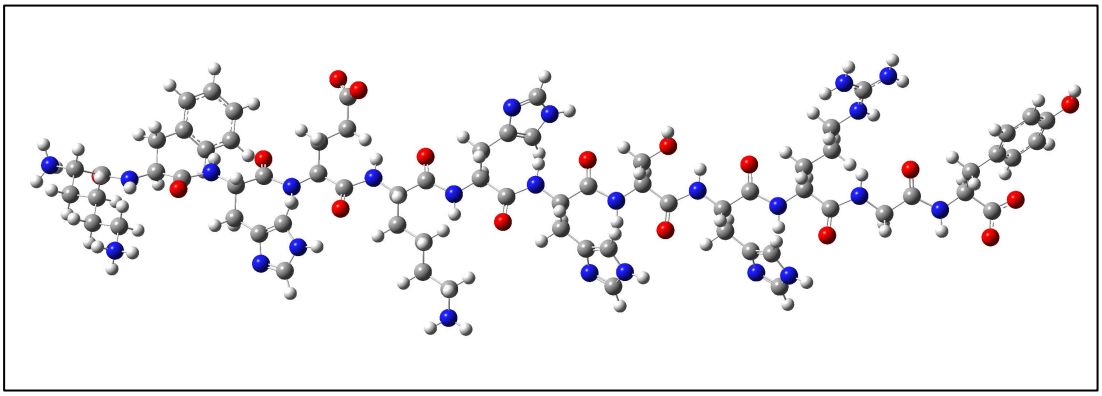

Figure 4.1.2. Monocationic *Hst*-8 in a beta strand. (Colorcode: white – hydrogen, gray – carbon, blue – nitrogen, and red – oxygen)

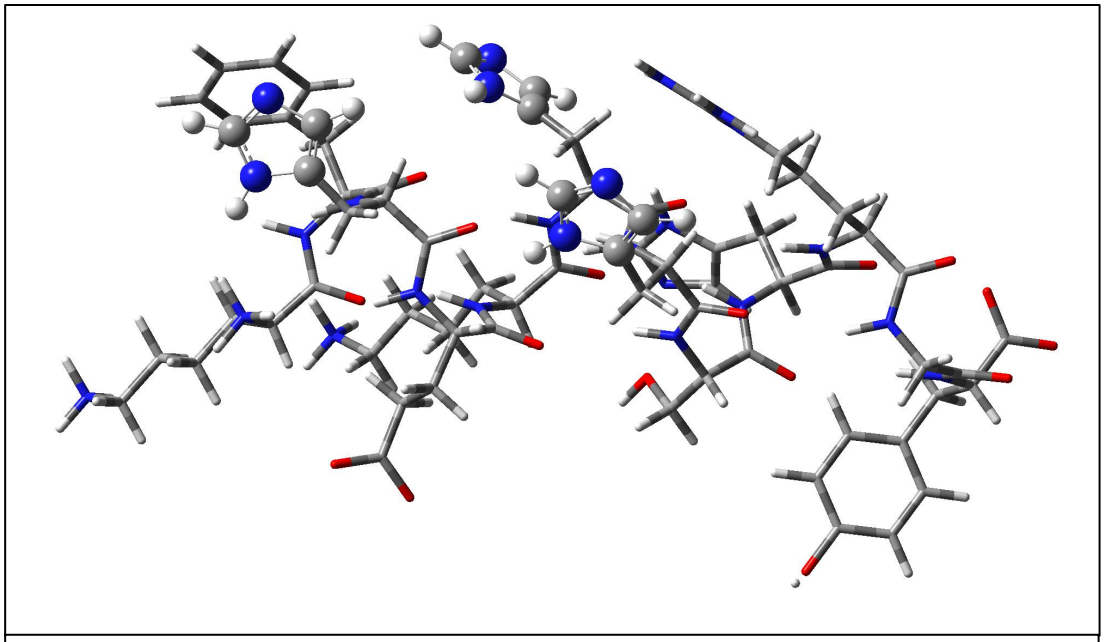

Figure 4.1.3. Monocationic *Hst*-8 in an alpha helical form. Imidazolyl units of histidine residues 3, 6, and 7 are in ball and bond display form the remainder is in tube display form. (Colorcode: white – hydrogen, gray – carbon, blue – nitrogen, and red – oxygen)

Figure 4.1.3 illustrates one view of monocationic *Hst*-8 where the helical axis is in the plane of the page. The majority of the molecule is in tube display form. However, to clearly indicate the imidazolyl units and highlight their proximity, they have been displayed in ball and bond form. Figure 4.1.4 illustrates another view of monocationic *Hst*-8 where the view is down the helical axis. The majority of the molecule is in tube display form. However, to clearly indicate the imidazolyl units and highlight their proximity, they have been displayed in ball and bond form.

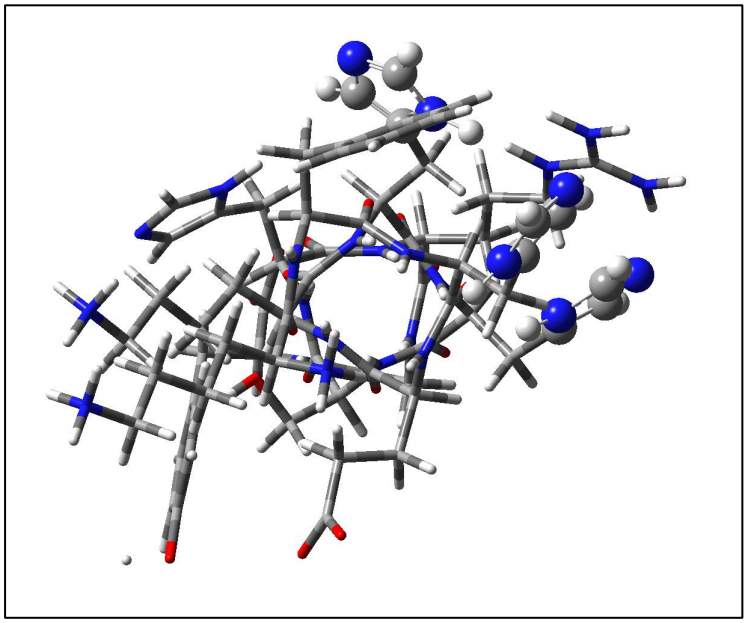

Figure 4.1.4. Monocationic *Hst*-8 in an alpha helical form looking down the helical axis. Imidazolyl units of histidine residues 3, 6, and 7 are in ball and bond display form the remainder is in tube display form. (Colorcode: white – hydrogen, gray – carbon, blue – nitrogen, and red – oxygen)

Metal ion interaction itself could potentially drive the conformational change from random coil or beta sheet to alpha helix. The increase in entropy by displacement of ligands to the copper could offset the entropy lost by reduction of the degrees of freedom available to the peptide in addition to enthalpy gains. This is not to say that histidine coordination in an alpha helical peptide to metal ions is the only possibility for the conformation of the peptide that results from the metal ion binding. As discussed in the introductory section, a histidine residue in the 3 position along with amide nitrogen atoms can interact with metal ions at the N terminus. This mode of biding is known as ACTUN type binding In addition nitrogen residues on lysine and arginine as well as carboxylate units can interact with cationic

species.

NMR has a host of techniques for the purposes of studying conformation in solution.[78, 79, 133] Many are based around the Nuclear Overhauser Effect, or NOE. Key to the technique is the observed phenomenon of nuclear spin transfer through space. This spatial transfer of spin occurs only across short distances of about 5 Å or less. Additionally the intensity and time required for spin transfer are both proportional to the distance through space. Thus protons that are in closer proximity will transfer spin faster and the intensity of the spin transferred will be of greater compared to protons that are more remote. In addition protons that will have a greater average time spent in close proximity will demonstrate a greater NOE compared to those that can more freely move away. NOESY experiments then can investigate the spatial relationship of protons by observation of NOE signals and assignments can be made of relative positions be variation of the mixing times when spin transfer is allowed to occur. A similar technique, which takes advantage of the same phenomenon, is ROESY. This technique however utilizes a rotating frame so that it is possible to differentiate between actual spatial positions of close proximity and close proximity that is gained as a result of exchange. In this experiment NOE that is a result of exchangeable protons will be in the opposite phase of NOE that is solely the result of close proximity. Of course before one can begin to assign spatial data, the specific resonances must be assigned.

In a system such as *Hst*-8, the assignment of individual resonances is

made substantially more difficult as a result of overlap of signals. This is due in large part to the fact that the environments are so similar. The best examples of this are the 4 histidine residues and the 2 lysine residues that are present in the peptide. Are the protons at the alpha position on the peptide backbone going to be substantially dissimilar let alone those protons on the imidazolyl motifs of the histidine residues? In order to differentiate these very similar proton environments from one another, other techniques are employed. Total correlation spectroscopy (TOCSY) is a technique that tracks spin information through proton-proton *J* type couplings. In this way spin systems can be isolated investigated and quantified. This particular experiment is very well suited for peptide investigation as there is no inter-residue couplings because there are no protons on the amide carbon. However, because resonance systems are not part of aliphatic spin systems, one cannot for example see correlation in the TOCSY from the alpha proton of histidine into the imidazolyl motif. Figure 4.1.5 illustrates the TOCSY signals observed. Note that the amino terminus does not have a correlation with the alpha proton. In solution the protein is in its zwitterionic form, so the amino-terminus is actually an ammonium terminus. In this form these acidic protons can engage in exchange with other acidic protons, basic sites, or perhaps solvent. As proton exchange is a very fast chemical process the relatively slower process of NOE spin exchange (ms) cannot be observed. Also the protons on the delta and epsilon carbons do not have observable correlations due to exchange of the imidazolyl attachment that arises from

the protonation state of the two nitrogen atoms in the motif. Though TOCSY works very well for amino acids that have only aliphatic carbons, one must use other techniques to probe amino acids with aromatic residues. NOESY then can aid us in assigning these systems. Additionally, though TOSCY can aid in making intra-residue assignments, NOESY can be used to make inter-residue assignments.

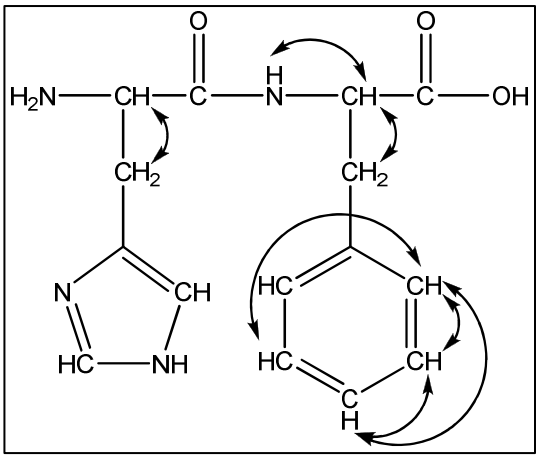

Figure 4.1.5. TOCSY correlations in a His-Phe dipeptide.

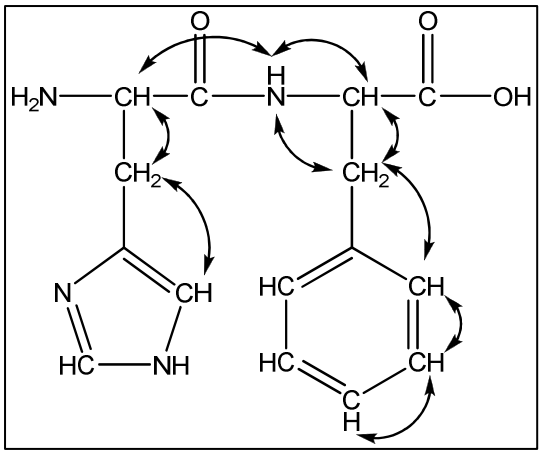

Figure 4.1.6. NOESY correlations in a His-Phe dipeptide.

Figure 4.1.6 illustrates some of the more important NOESY correlations for assignment of resonances. Notice the correlation of the beta protons into their respective resonance systems on both the His and Phe. Also the alpha proton on the His has a correlation to the amide proton on the Phe. Of course additional NOESY correlations are possible, however, the figure merely provides hypothetical correlations as an illustration of principle.

A final major technique that is useful in residue assignments is the heteronuclear single quantum coherence (HSQC). Here the connectivity of

different atomic nuclei is investigated across one bond. Figure 4.1.7 illustrates correlations observed in a ^{1}H-^{13}C HSQC experiment. 1H-15N HSQC experiments are also possible and they will be explored in a later chapter for purposes of metal ion binding studies.

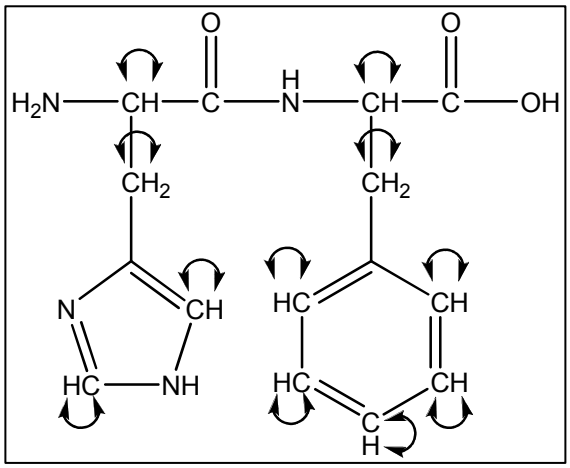

Figure 4.1.7. ^{1}H-^{13}C HSQC correlations in a His-Phe dipeptide.

Once the residue assignments have been made then the next step is determination of the spatial relationship of those now assignable protons to each other. The assignments that are the most important at this point are the inter-residue correlations, particularly those of side chain interactions. After the assignments have been made the peak intensity data is obtained. As aforementioned the spatial proximity and amount of time spent in spatial proximity have a direct effect of the intensity of correlation in NOESY and ROESY experiments. MARDIGRAS, which stands for matrix analysis of relaxation for discerning the geometry of an aqueous structure, is a program that was developed at the University of California San Francisco that will

generate distance constraints using a computer model and NOESY intensity data. Another program that was used for generating spatial restraint data and eventually outputting a molecular dynamic generated structure is crystallography and NMR system (CNS or CNSsolve), which was developed at Yale., CNS has the option of utilizing internally generated restraint data from NOESY correlations or they can be generated from MARDIGRAS and used in CNS MD simulations. Regardless of the method used the lowest energy conformation of the structure is output from CNS using the restraint data input.

4.2: Assignment of Proton Resonances *Hst*-8 in DMSO d_6

The first major undertaking in assigning the proton resonances of the various 2D spectra that were collected stem from the amide-alpha proton interaction section. Comparison of the TOCSY spectrum to the NOESY spectrum allows for identification of inter-residue NOESY interactions which are critical to the technique of NOESY jumping. The NOESY jump enables easy identification of residue order. One thing that made identification easier for our analysis was that prior studies had already assigned many of the proton resonances albeit under different solvent and pH conditions as aforementioned in the introduction to this chapter. So overlay of the TOCSY spectrum on the NOESY spectrum identified which peaks in the NOESY amide region were inter-residual. Figure 4.2.1 is part of the NOESY spectrum of *Hst*-8 in DMSO illustrating amide alpha and amide beta interactions. We

can clearly observe large poorly resolved peaks in the 7.8 ppm, 8.1 ppm, 8.9 ppm, and 9.3 ppm regions.

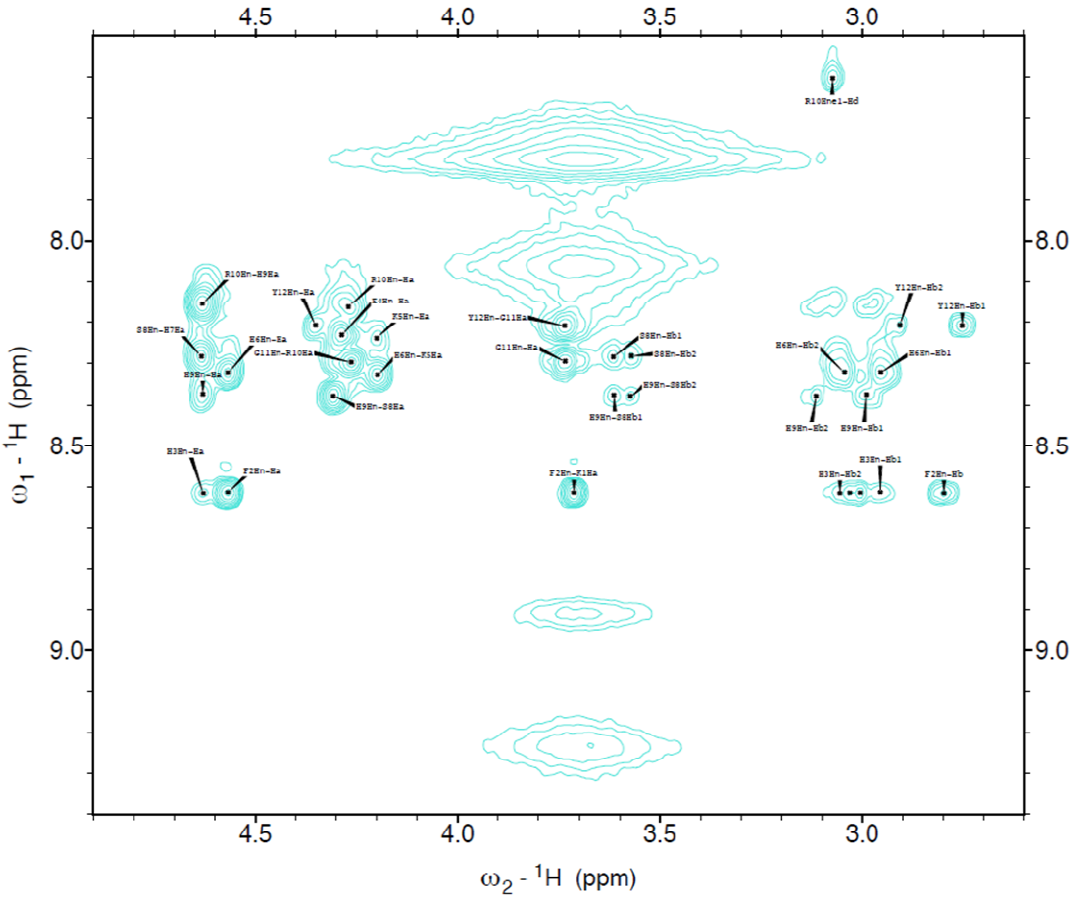

Figure 4.2.1. Part of the NOESY spectrum of *Hst*-8 in DMSO illustrating amide alpha and amide beta interactions.

Figure 4.2.2 is part of the ROESY spectrum of *Hst*-8 in DMSO illustrating amide alpha and amide beta interactions. We clearly observed that those are exchanging proton peaks as they are not present in the ROESY spectrum. Also it was expected given the peak broadness. To further the point of exchange we observe that they are absent in figure 4.2.3, part of the TOCSY spectrum of *Hst*-8 in DMSO, which illustrates the same region.

The place at which an exchangeable proton would be observed in the alpha region of the NOESY spectrum of *Hst*-8 in DMSO (figure 4.2.1) would be the proton exchanging on the amino terminus of the K1 with the $K1H_{\alpha}$. As the *N*-terminal lysine only has one inter-residual correlation, that of the $K1H_{\alpha}$ to $F2H_N$ the correlation peak at 3.71 ppm and 8.62 was fairly easily identifiable. Further evidence for the assignment of the $K1H_{\alpha}$ resonance would be that $K1H_{\beta}$ protons would have no amide correlation. This is illustrated in figures 4.2.7, 4.2.8, and 4.2.9 which are the NOESY, ROESY, and TOCSY spectra of *Hst*-8 in DMSO respectively. A final factor was the upfield chemical shift of the $K1H_{\alpha}$, as a consequence of not being next to an amide motif. Returning to the spectra illustrated in figures 4.2.1, 4.2.2, and 4.2.3, we then move along the $F2H_N$ axis to the $F2H_{\alpha}$-$F2H_N$ peak at 4.57 ppm and 8.62 ppm. We should have then moved to the $F2H_{\alpha}$-$H3H_N$ peak, however, there was no such peak to identify in the NOESY or ROESY spectra. We made the identification of the $H3H_N$ resonance using the TOCSY spectrum, figure 4.2.3 as the full NOESY spectrum.

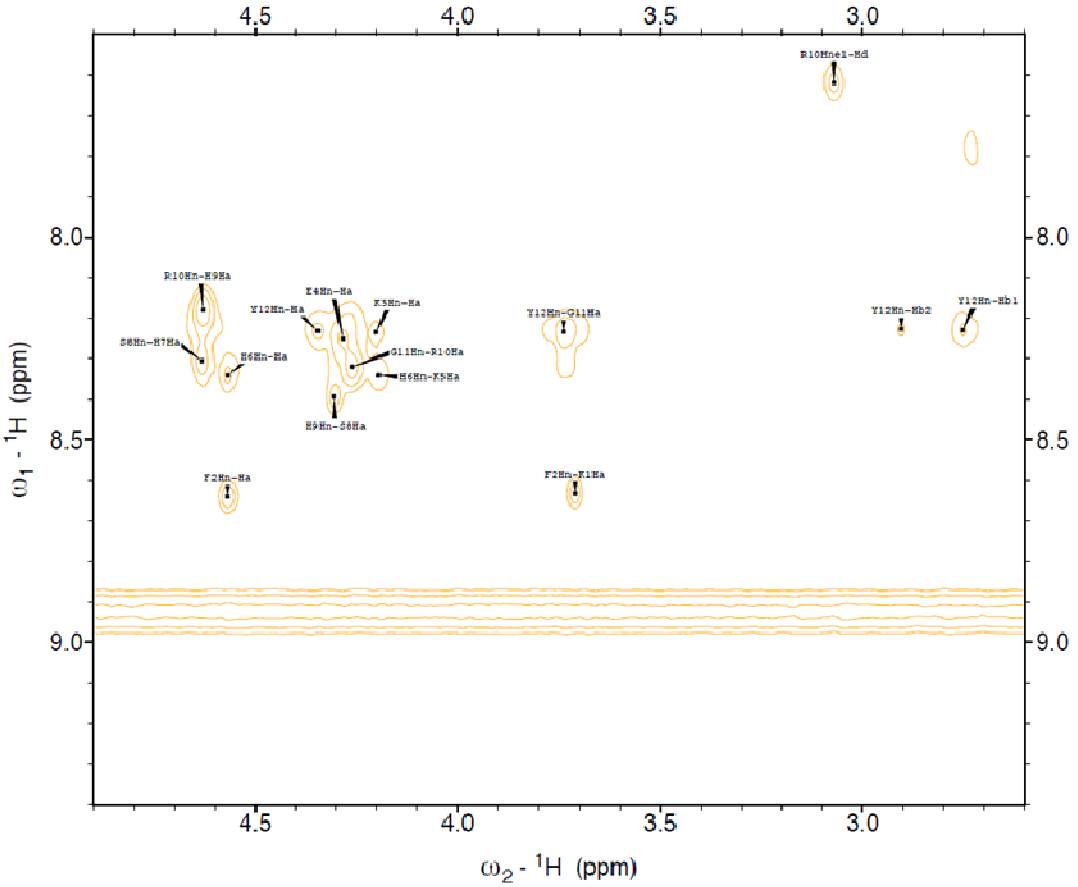

Figure 4.2.2. Part of the ROESY spectrum of *Hst*-8 in DMSO illustrating amide alpha and amide beta interactions.

The TOCSY spectrum, figure 4.2.3, illustrates the $H3H_N$–$H3H_\alpha$, $H3H_N$-$H3H_{\beta1}$, and $H3H_N$-$H3H_{\beta2}$ peaks. To confirm that these were histidine beta protons we used NOESY data (not shown), which illustrated the imidazolyl protons correlating to the beta protons. The position was confirmed by performing a NOESY jump to the $E4H_N$ from the $H3H_\alpha$ illustrated in figure 4.2.1 and obviously from there to the $E4H_N$-$E4H_\alpha$ peak. This was confirmed by the ROESY spectrum, figure 4.2.2; however, the intense peaks in the TOCSY spectrum (figure 4.2.3) of the tyrosine and arginine amide alpha

correlations obscured the glutamate amide alpha peak. The carboxylate unit of the glutamate residue allowed for easy identification in the TOCSY as illustrated in figure 4.2.7, which shows the correlation of $E4H_{\gamma}$ to $E4H_{\alpha}$. So this combined evidence confirms the assignment of the $E4H_N$-$E4H_{\alpha}$. We were unable to NOESY hop from the $E4H_{\alpha}$ to the $K5H_N$ as the region in the area was filled with other peaks. So the $K5H_N$-$K5H_{\alpha}$ correlation was confirmed using other spectra, back correlating to either the $K5H_N$ or the $K5H_{\alpha}$. This was fairly easy to accomplish as few residues had extended aliphatic chains, those of K1, K5, and R10. Figure 4.2.7 and 4.2.9 the NOESY and TOCSY spectra of *Hst*-8 in DMSO respectively, clearly illustrated the H_{α}-H_{β} and H_{α}-H_{δ} correlations of the lysine in the fifth position. We then comparing the data of the NOESY and TOCSY spectra (figures 4.2.1 and 4.2.3), NOESY jumped from the K5 to the H6. This allowed for easy identification of the $H6H_N$-$H6H_{\alpha}$. The H7 was unfortunately completely obscured by the H6. So at this point we worked backward from the tyrosine to reach the H7 resonances. Gratifyingly, we could easily NOESY jump all the way back to the H7 from the Y12 using only the NOESY and TOCSY spectra (figures 4.2.1 and 4.2.3). Now the entire backbone of the peptide was assigned (as well as a few other resonances). Using the horizontal lines from the alpha amide correlations, one could then assign the beta amide correlations in figures 4.2.1, 4.2.2, and 4.2.3 the NOESY, ROESY, and TOCSY spectra respectively of *Hst*-8 in DMSO.

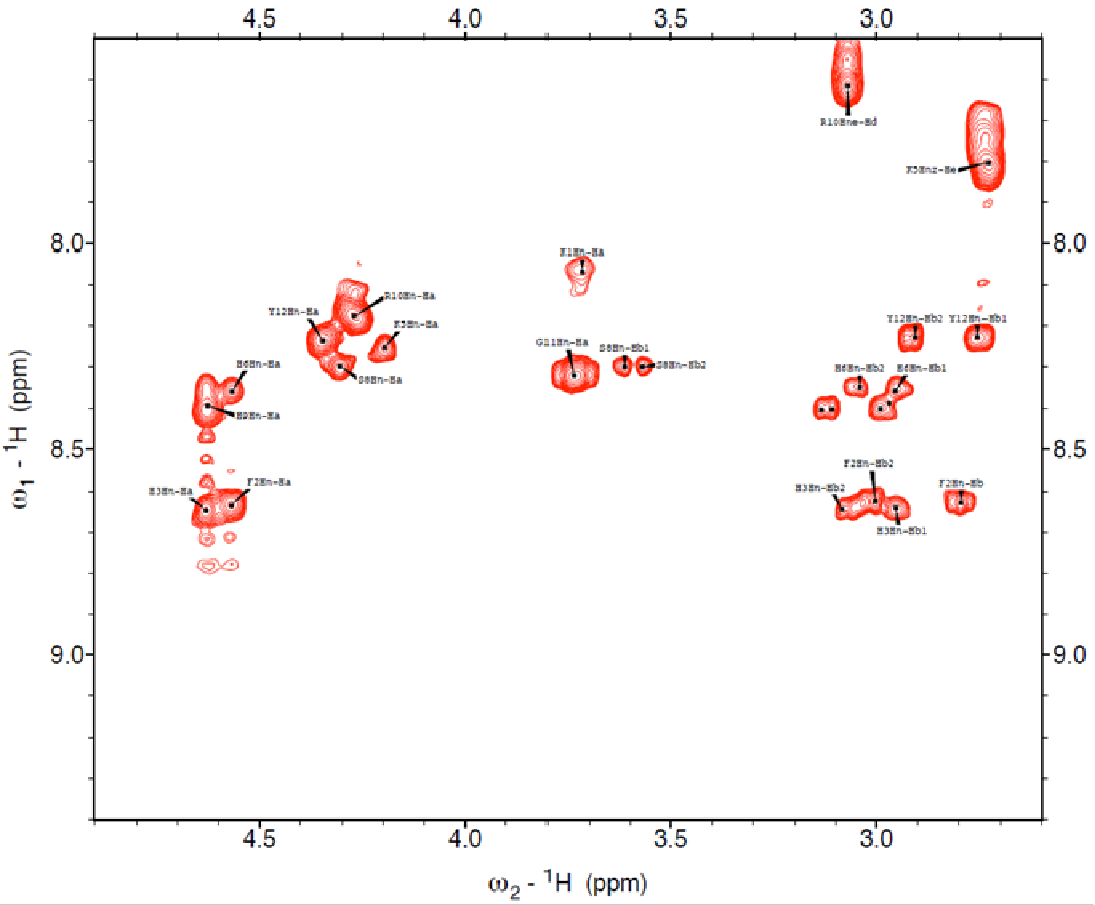

Figure 4.2.3. Part of the TOCSY spectrum of *Hst*-8 in DMSO illustrating amide alpha and amide beta interactions.

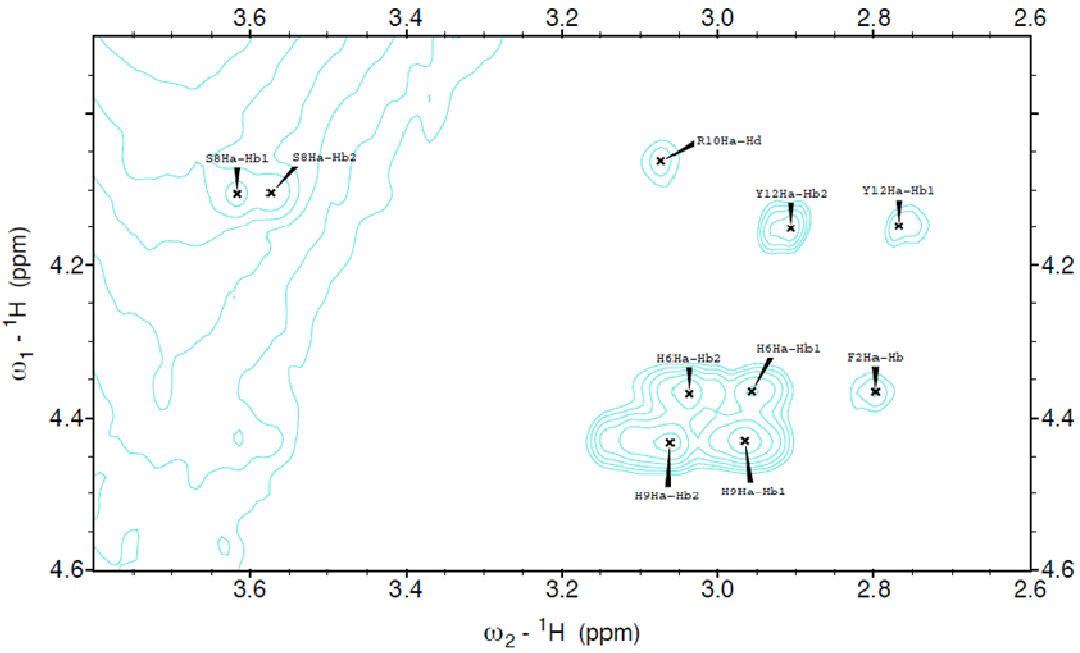

Figure 4.2.4. Part of the NOESY spectrum of *Hst*-8 in DMSO illustrating alpha beta proton interactions.

Figures 4.2.4, 4.2.5, and 4.2.6, which are the NOESY, ROESY, and TOCSY spectra respectively of *Hst*-8 in DMSO illustrate the area where some alpha-beta correlations occur. These assignments were made by laying vertical lines in the area illustrated in figures 4.2.1, 4.2.2, and 4.2.3 which are again the NOESY, ROESY, and TOCSY spectra respectively of *Hst*-8 in DMSO, which illustrate the alpha and beta protons correlating with amide protons. In addition horizontal lines were drawn from the areas that represent the reciprocal correlations of the areas illustrated in figures 4.2.1, 4.2.2, and 4.2.3. At the intersections of these lines then assignments are made at clear peaks. Thus the alpha-beta correlations are assigned.

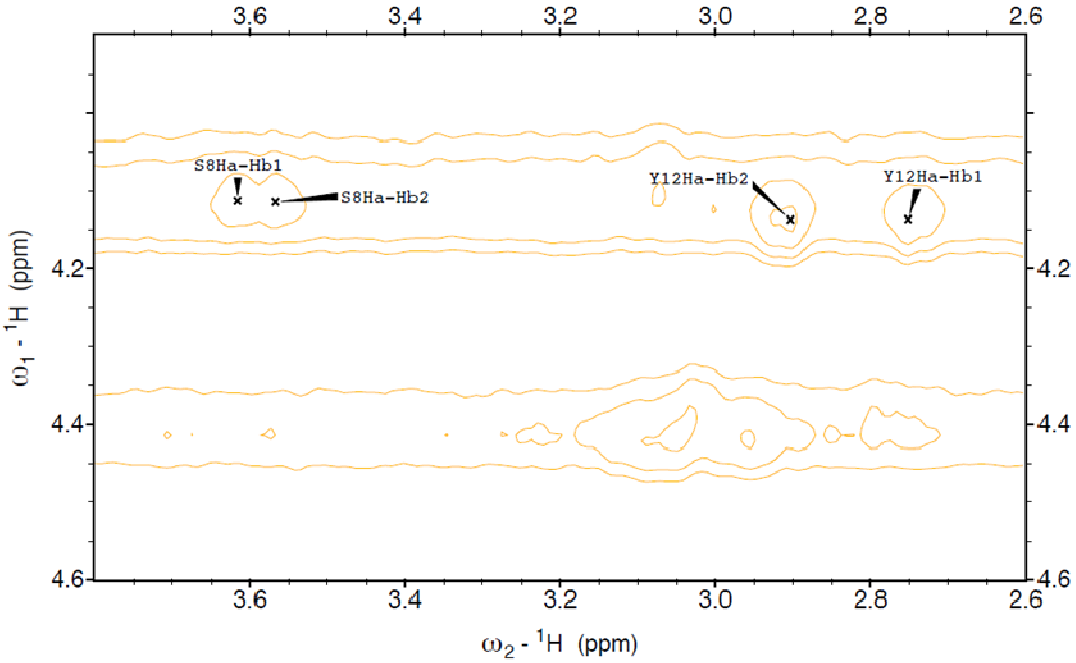

Figure 4.2.5. Part of the ROESY spectrum of *Hst*-8 in DMSO illustrating alpha beta proton interactions.

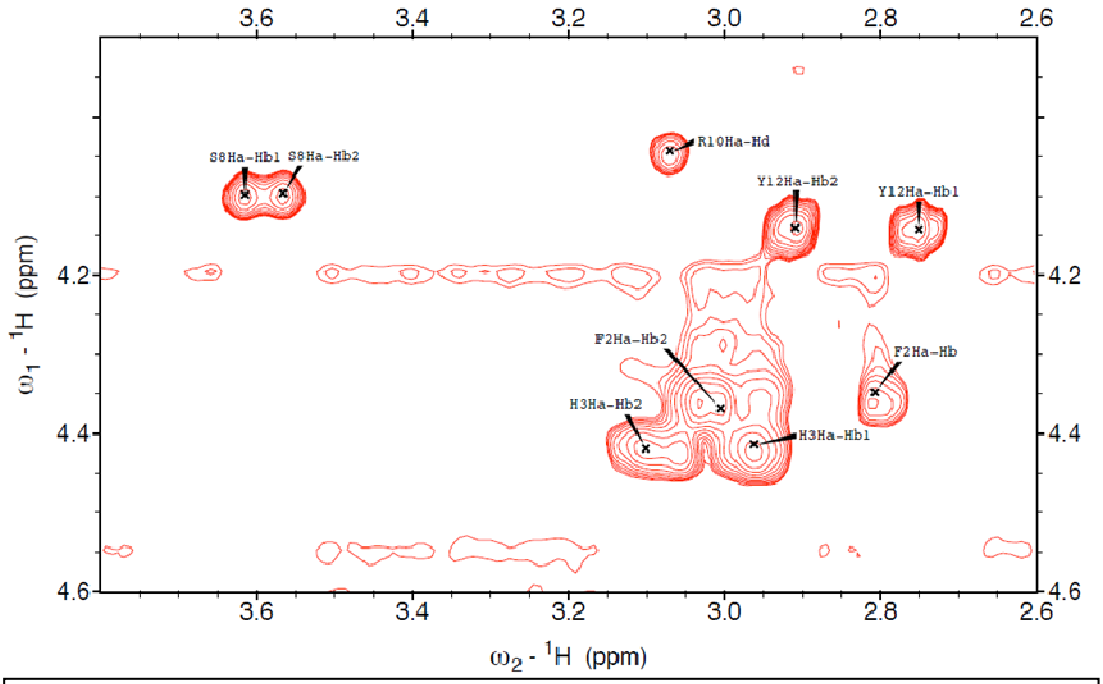

Figure 4.2.6. Part of the TOCSY spectrum of *Hst*-8 in DMSO illustrating alpha beta proton interactions.

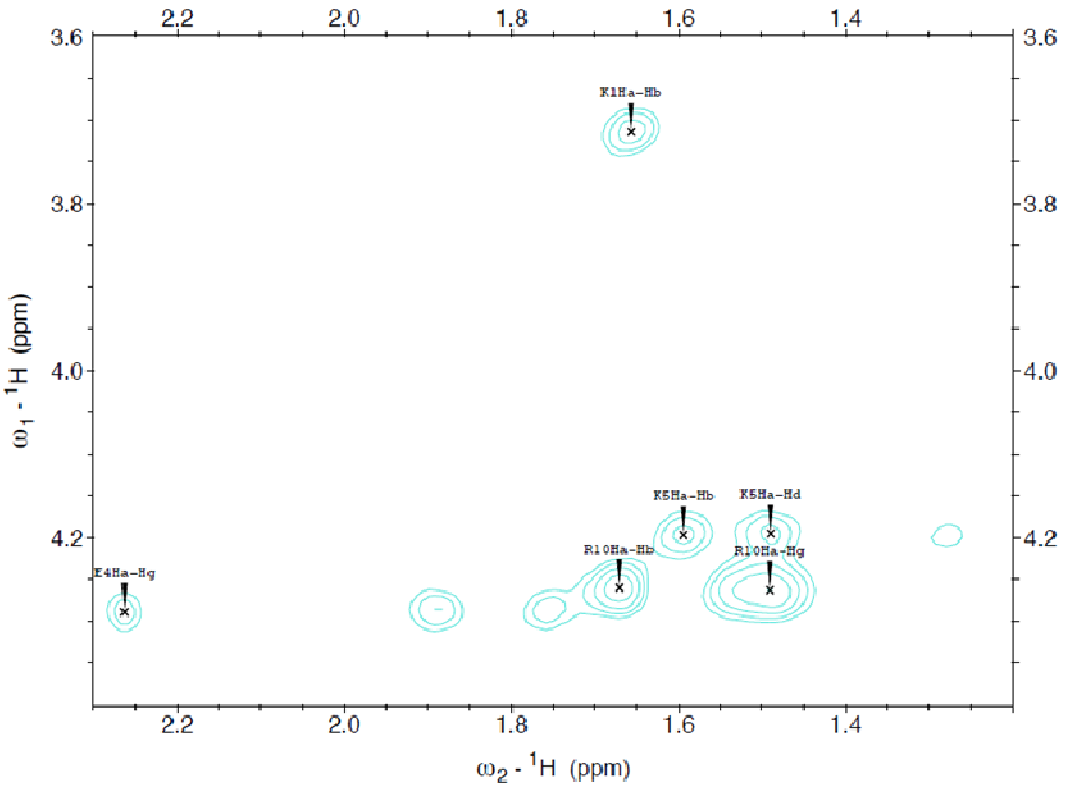

Figure 4.2.7. Part of the NOESY spectrum illustrating alpha beta and alpha other interactions of *Hst*-8 in DMSO.

Figures 4.2.7, 4.2.8, and 4.2.9 are the NOESY, ROESY, and TOCSY spectra respectively of *Hst*-8 in DMSO, which illustrate the alpha protons of aliphatic residues K1, K5, and R10 correlating to various resonances in the residue. These correlations were already discussed at length earlier in the section.

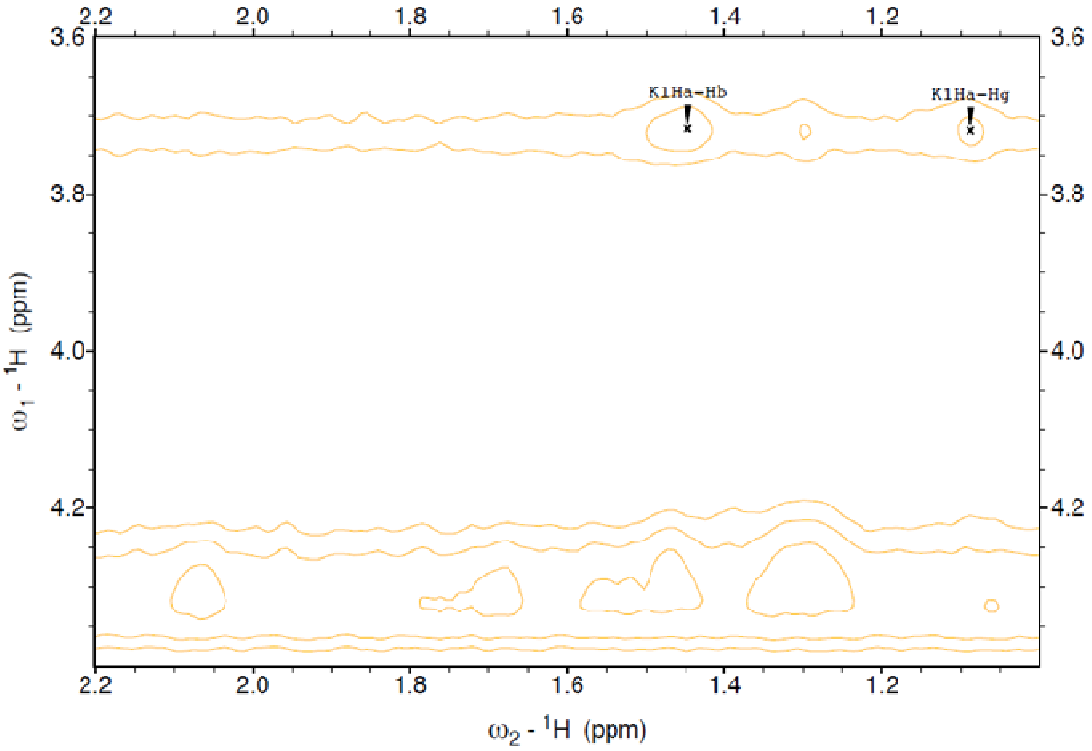

Figure 4.2.8. Part of the ROESY spectrum illustrating alpha beta and alpha other interactions of *Hst*-8 in DMSO.

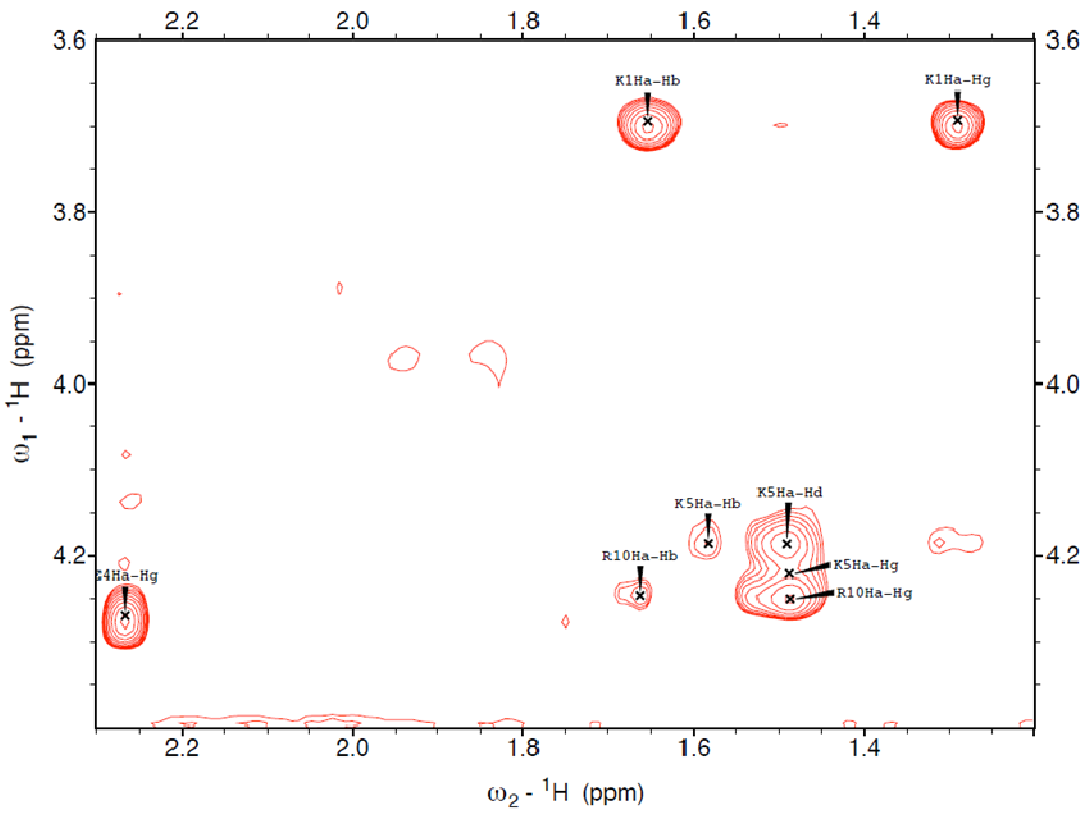

Figure 4.2.9. Part of the TOCSY spectrum illustrating alpha beta and alpha other interactions of *Hst*-8 in DMSO.

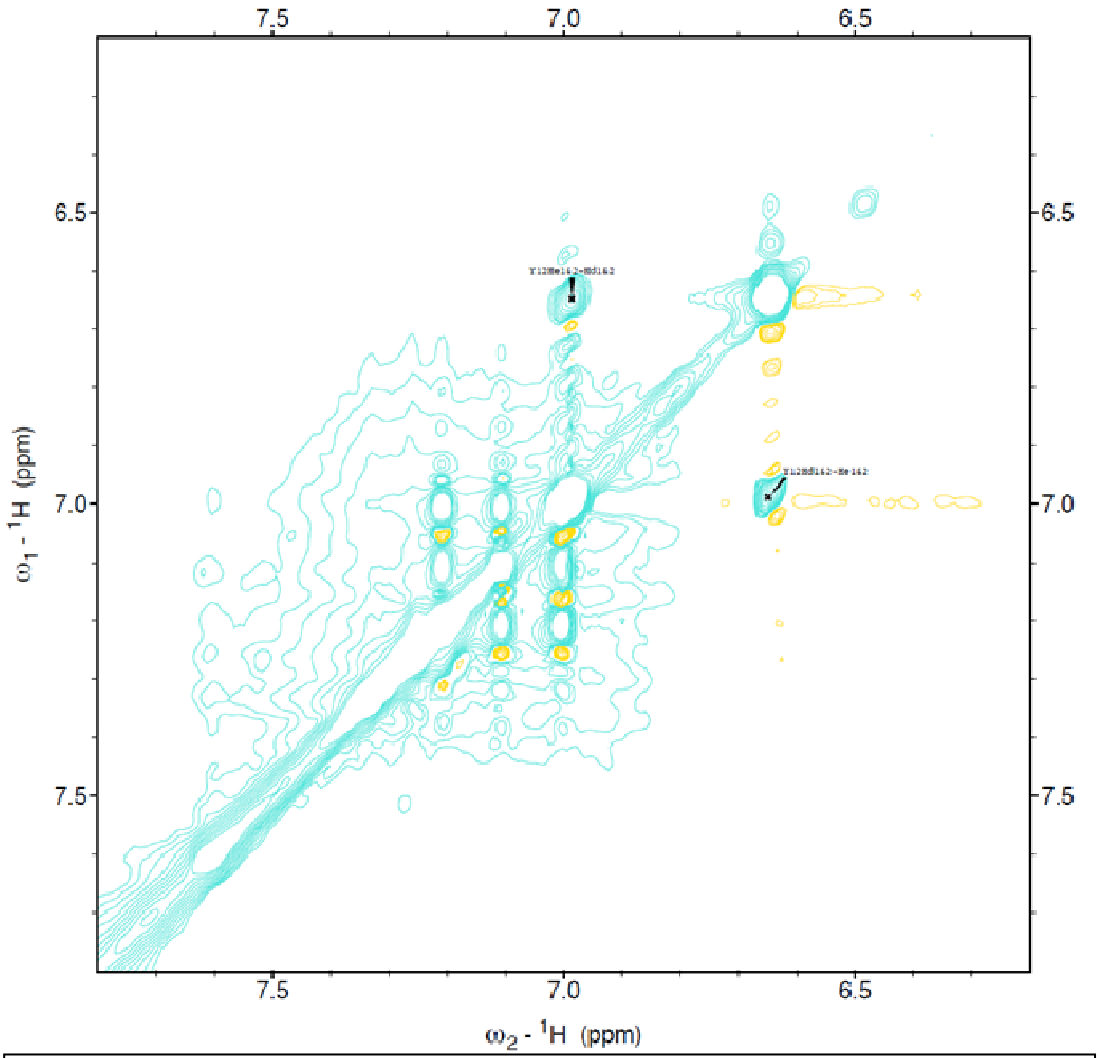

Figure 4.2.10. Part of the NOESY spectrum illustrating aromatic proton interactions of *Hst*-8 in DMSO.

Figures 4.2.10, 4.2.11, and 4.2.12 are NOESY, ROESY, and TOCSY spectra respectively of *Hst*-8 in DMSO illustrating the aromatic proton region. The correlation that is clearly identifiable is the Y12H_δ-Y12H_ε peak. Not only is this clearly identifiable by its characteristic shift, but we also confirmed this assignment by observing NOESY correlations of the Y12H_δ to the Y12H_β and Y12H_α protons (data not shown). Unfortunately the phenylalanine

correlations in the region of 7.2 ppm (illustrated in the previous chapter in figures 3.3.6, which was a ^{1}H-^{13}C-HSQC spectrum of *Hst*-8 in DMSO) are obscured by the exchange of protons on the various imidazolyl motifs. The exchange is clearly illustrated in figure 4.2.11, the ROESY spectrum of *Hst*-8 in DMSO that illustrates the aromatic region. Clearly the three bands in the 7.0 ppm, 7.1 ppm, and 7.2 ppm regions are the opposite phase of the real correlation peak the Y12H_{δ}-Y12H_{ε}. The band at 7.2 ppm could certainly obscure the phenylalanine peaks.

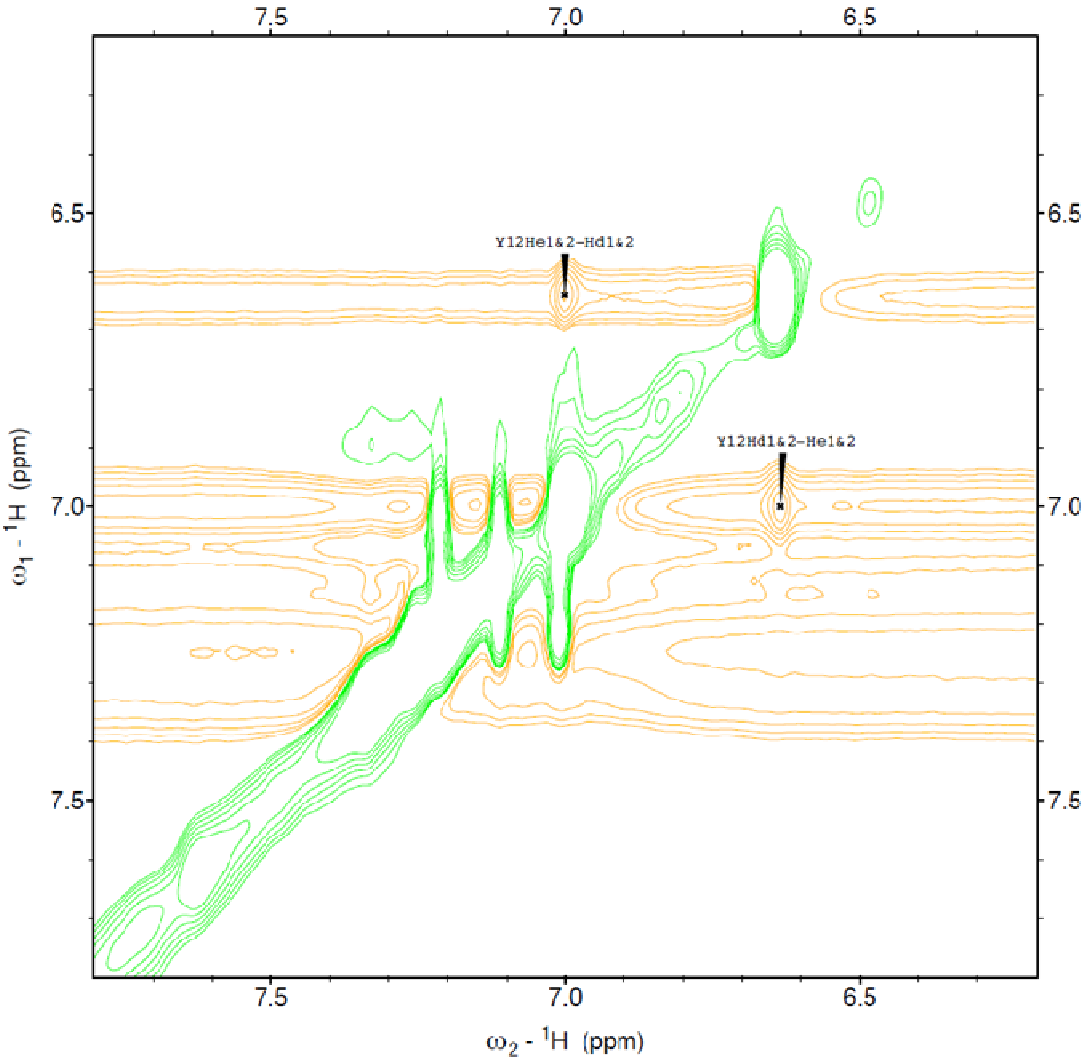

Figure 4.2.11. Part of the ROESY spectrum illustrating aromatic proton interactions of *Hst*-8 in DMSO.

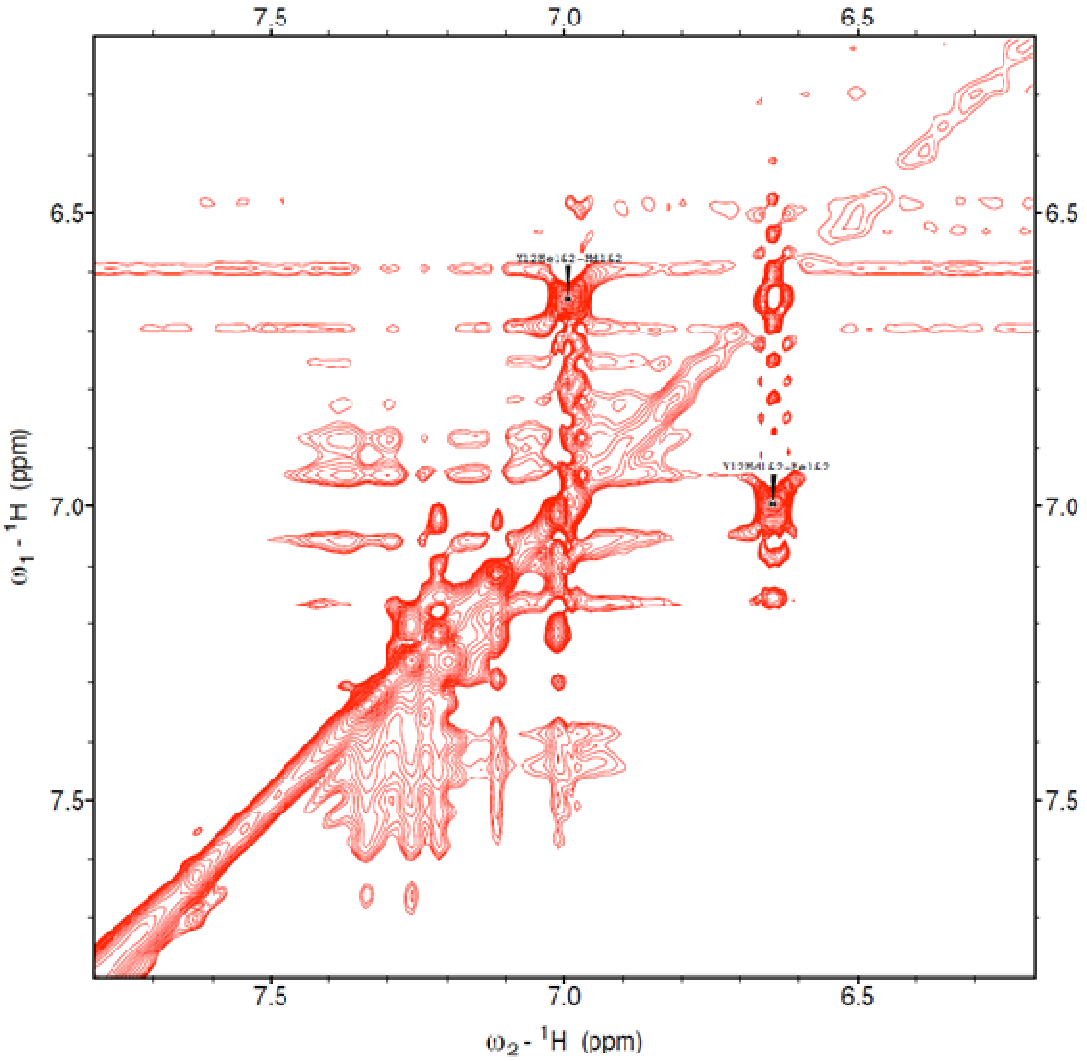

Figure 4.2.12. Part of the TOCSY spectrum illustrating aromatic proton interactions of *Hst*-8 in DMSO.

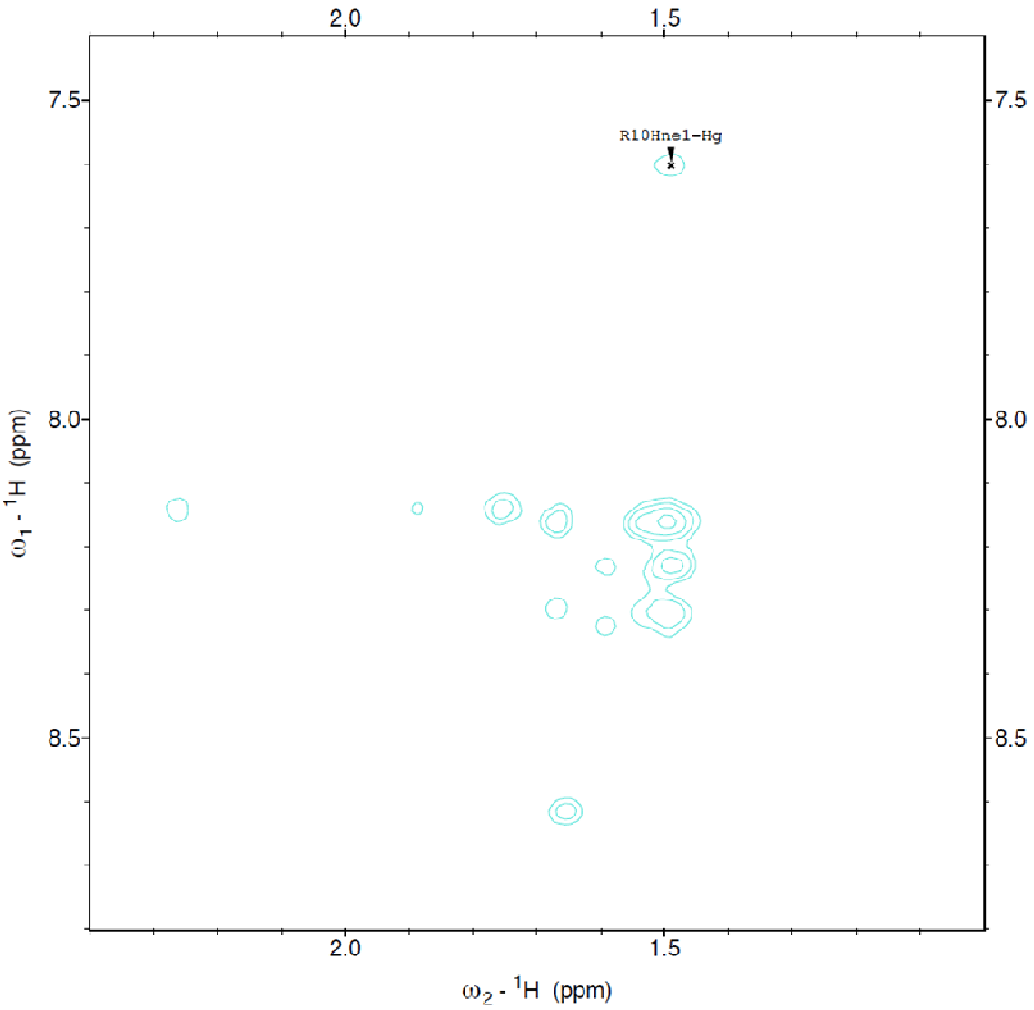

Figure 4.2.13. Part of the NOESY spectrum illustrating miscellaneous proton interactions of *Hst*-8 in DMSO.

Figure 4.2.13 is a section of the NOESY spectrum of *Hst*-8 in DMSO illustrating some miscellaneous proton interactions. The peaks are not able to be definitively assigned as they result from the imidazolyl units interacting with various beta protons. As shown in figure 4.2.14, a ROESY spectrum of *Hst*-8 in DMSO that illustrates the same region, they are absent as a result of their proton exchange and resulting isomerization.

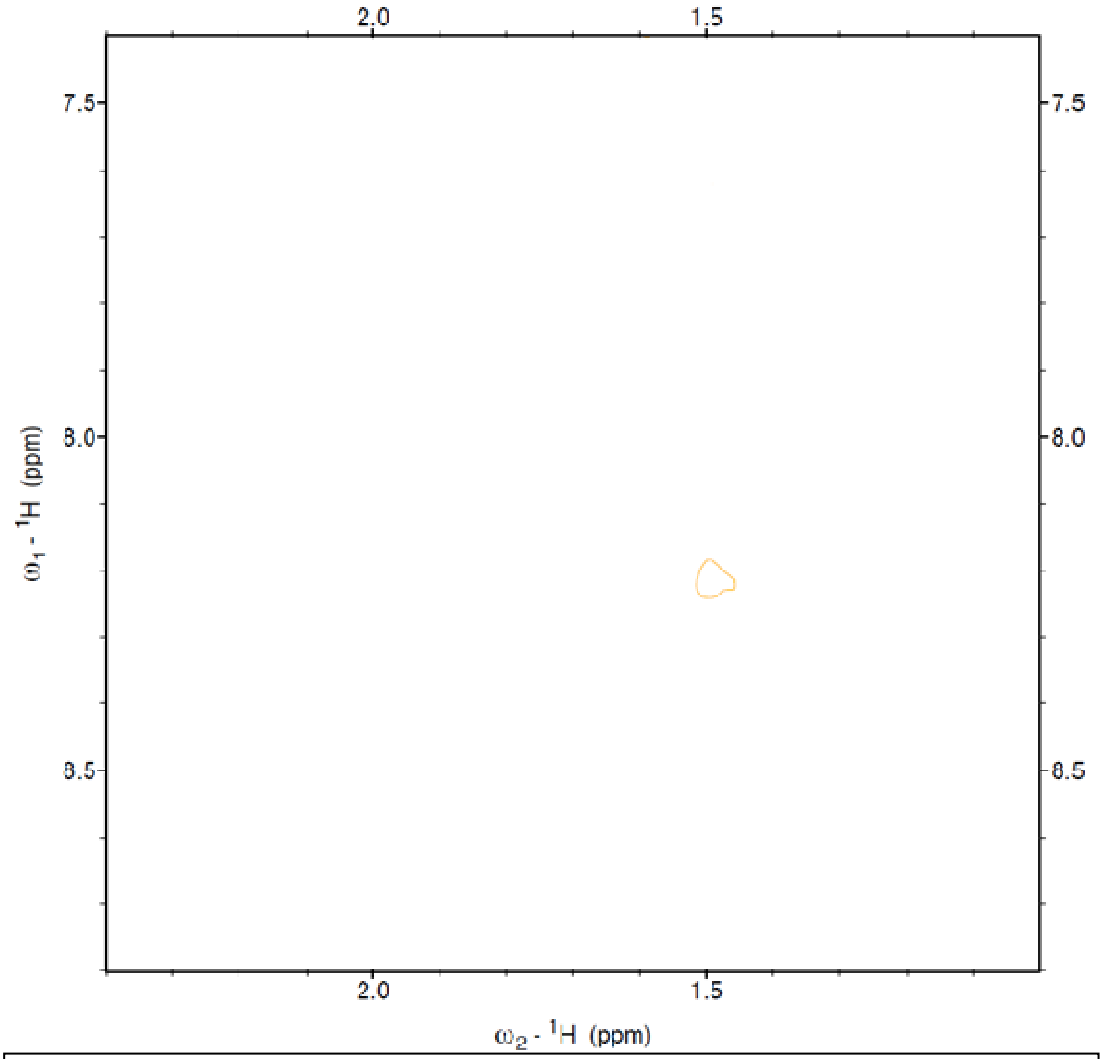

Figure 4.2.14. Part of the ROESY spectrum illustrating miscellaneous proton interactions of *Hst*-8 in DMSO.

Figure 4.2.15 is the TOCSY spectrum of *Hst*-8 in DMSO illustrating the same region as figures 4.2.13 and 4.2.14. In this we can see some of the protons attached to nitrogen atoms of various residues interacting with aliphatic protons.

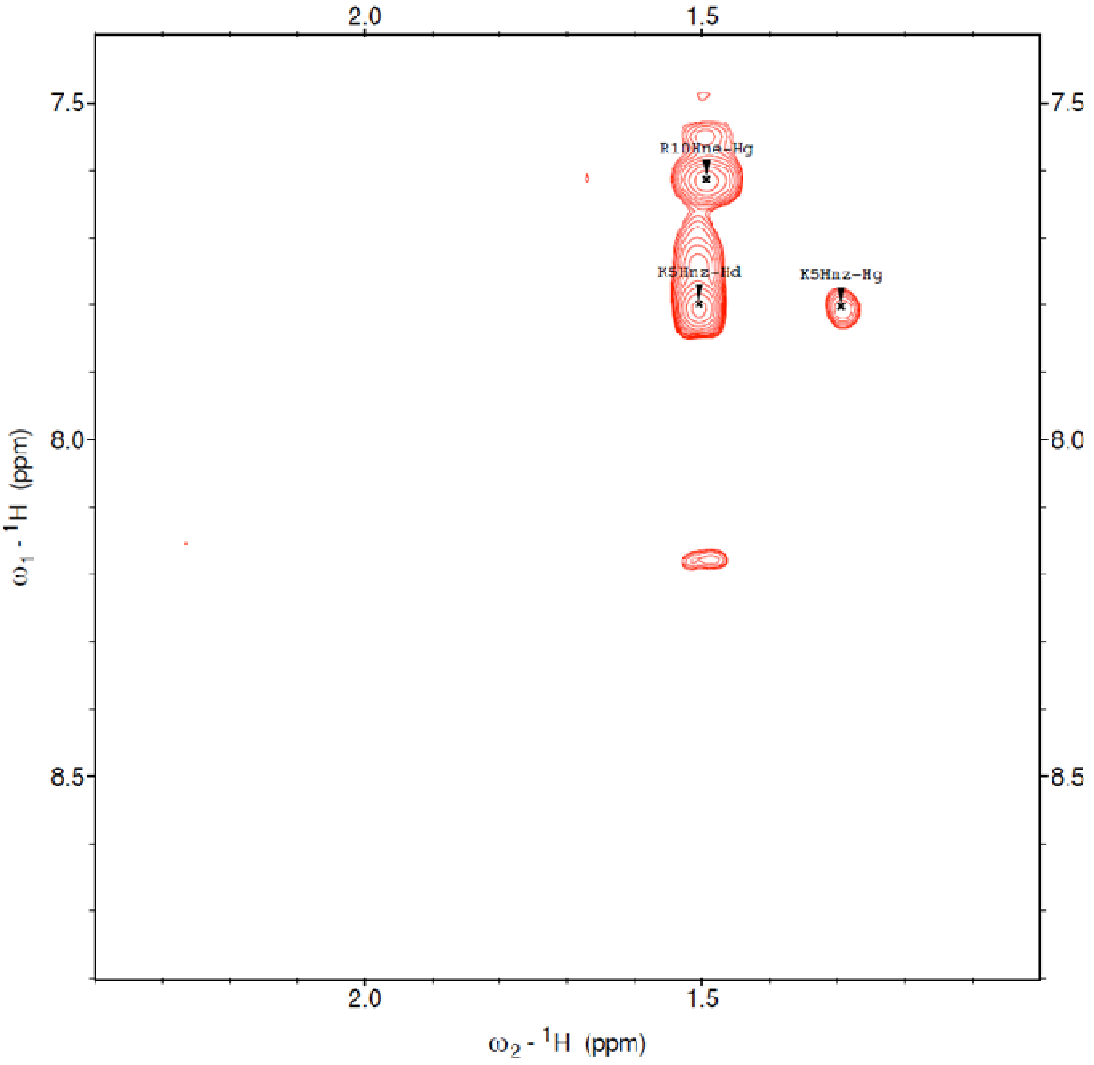

Figure 4.2.15. Part of the TOCSY spectrum illustrating miscellaneous proton interactions of *Hst*-8 in DMSO.

Table 4.2.1. Summary of the individual resonances identified in *Hst*-8 in DMSO (this study) as well as a summary of previously published work of *Hst*-8 in a variety of solvents[79].

		This study	pH 4.0 DMSO[79]	pH4.0 water[79]	40% HFA[79]
K1	N				
	α	3.71	3.74	3.96	4.00
	β	1.65	1.69	1.85	1.87
	γ	1.29	1.33	1.39	1.43
	δ	1.46	1.56	1.68	1.73
	ε	2.73	2.77	2.98	3.05
F2	N	8.62	8.64	8.46	8.07
	α	4.57	4.61	4.56	4.57
	β1	2.80	3.07	3.01	3.12
	β2	3.01	2.84	3.09	
	2,6H		7.29	7.23	7.27
	3,5H			7.33	7.36
H3	N	8.63	8.63	8.46	8.07
	α	4.63	4.65	4.50	4.59
	β1	2.96	3.06	3.05	3.11
	β2	3.06	3.00	3.18	3.28
	4H		7.62		7.23
E4	N	8.22	8.18	8.52	8.04
	α	4.29	4.32	4.18	4.41
	β1	1.75	1.81	1.93	2.04
	β2	1.89	1.94	2.07	2.16
	γ	2.26	2.31	2.30	2.54
K5	N	8.24	8.29	8.12	8.16
	α	4.20	4.25	4.09	4.40
	β1	1.59	1.65	1.73	1.85
	β2			1.80	1.96
	γ		1.34	1.40	1.51
	δ	1.50	1.54	1.68	1.74
	ε	2.74	2.77	2.98	3.04
	εNH2			6.85	7.50
H6	N	8.33	8.34	7.15	8.72
	α	4.57	4.58		4.52

	β1	2.95	3.10	3.06	3.39
	β2	3.04	3.00	3.18	
	4H	7.33	7.31		7.43
H7	N	8.32	8.34	7.15	8.72
	α	4.63	4.58		4.52
	β1	2.95	3.10	3.06	3.39
	β2	3.06	3.00	3.18	
	4H		7.31		7.43
S8	N	8.29	8.33	8.81	8.42
	α	4.30	4.35	4.41	4.53
	β1	3.61	3.65	3.83	3.90
	β2	3.56			3.94
H9	N	8.39	8.40	8.74	8.45
	α	4.63	4.65	4.66	4.77
	β1	2.98	3.15	3.11	3.20
	β2	3.11	3.02	3.20	3.33
	4H		7.34		7.31
R10	N	8.16	8.19	8.48	8.23
	α	4.26	4.29	4.26	4.36
	β1	1.67	1.72	1.70	1.79
	β2			1.74	1.85
	γ1	1.49	1.52	1.46	1.64
	γ2		1.56		
	δ	3.07	3.11	3.06	3.19
	NH1		7.61	6.98	6.96
G11	N	8.31	8.35	8.52	8.13
	α1	3.73	3.78	3.81	3.92
	α2			3.96	4.00
Y12	N	8.22	8.23	7.60	7.70
	α	4.35	4.39	4.36	4.67
	β1	2.75	2.79	2.89	3.02
	β2	2.90	2.95	3.06	3.16
	2,6H	6.99	7.03	7.03	7.13
	3,5H	6.64	6.67		6.85

Table 4.2.1 summarizes my work in identifying unique chemical resonances of *Hst*-8 in DMSO and compares it with previously published

work.[79] There is fairly good agreement between the data I was able to obtain and interpret from my *Hst* DMSO sample and the previously published work which was *Hst*-8 pH adjusted to 4.0 and dissolved in DMSO. However, I was unable to definitively assign the 4H of histidine residues 3, 7, and 9. I was also unable to definitively assign two resonances at 7.26 ppm and 7.27 ppm to either the 2,6H or 3,5H of phenylalanine. We were unable to observe a NOE correlation of the 2,6H to the beta protons of the phenylalanine. One last assignment that I was unable to make was the H_γ of the fifth lysine, which may be the result of overlap of the H_γ of the first lysine or that of another resonance. Nonetheless the assignment was fairly complete and certainly included the important backbone resonances. These backbone resonances are perhaps the most critical in determining if secondary structural elements are present.

4.3: Assignment of Proton Resonances of *Hst*-8 with Cu(I) in DMSO d_6

With the free *Hst*-8 resonances assigned the next phase was to add Cu(I) and then look at its effect upon the various NMR spectra and by extension the conformation of the peptide. One equivalent of $Cu(CH_3CN)_4PF_6$ was then added to the *Hst*-8 in DMSO sample. This was kept under a nitrogen atmosphere to prevent oxidation of the copper to the paramagnetic Cu(II). Illustrated in figures 4.3.1, 4.3.2, and 4.3.3 are the NOESY, ROESY, and TOSCY NMR spectra of *Hst*-8 and Cu(I) in DMSO illustrating amide alpha and amide beta interactions. Once again we go

through the same process as before. However, it is quite apparent at first glance comparing figure 4.2.1 to figure 4.3.1 that the addition of copper has had a pronounced effect upon the NOESY spectrum. Namely, we observe a broadening or eliminating peaks throughout the spectrum particularly in the central region of residues, H3-H7.

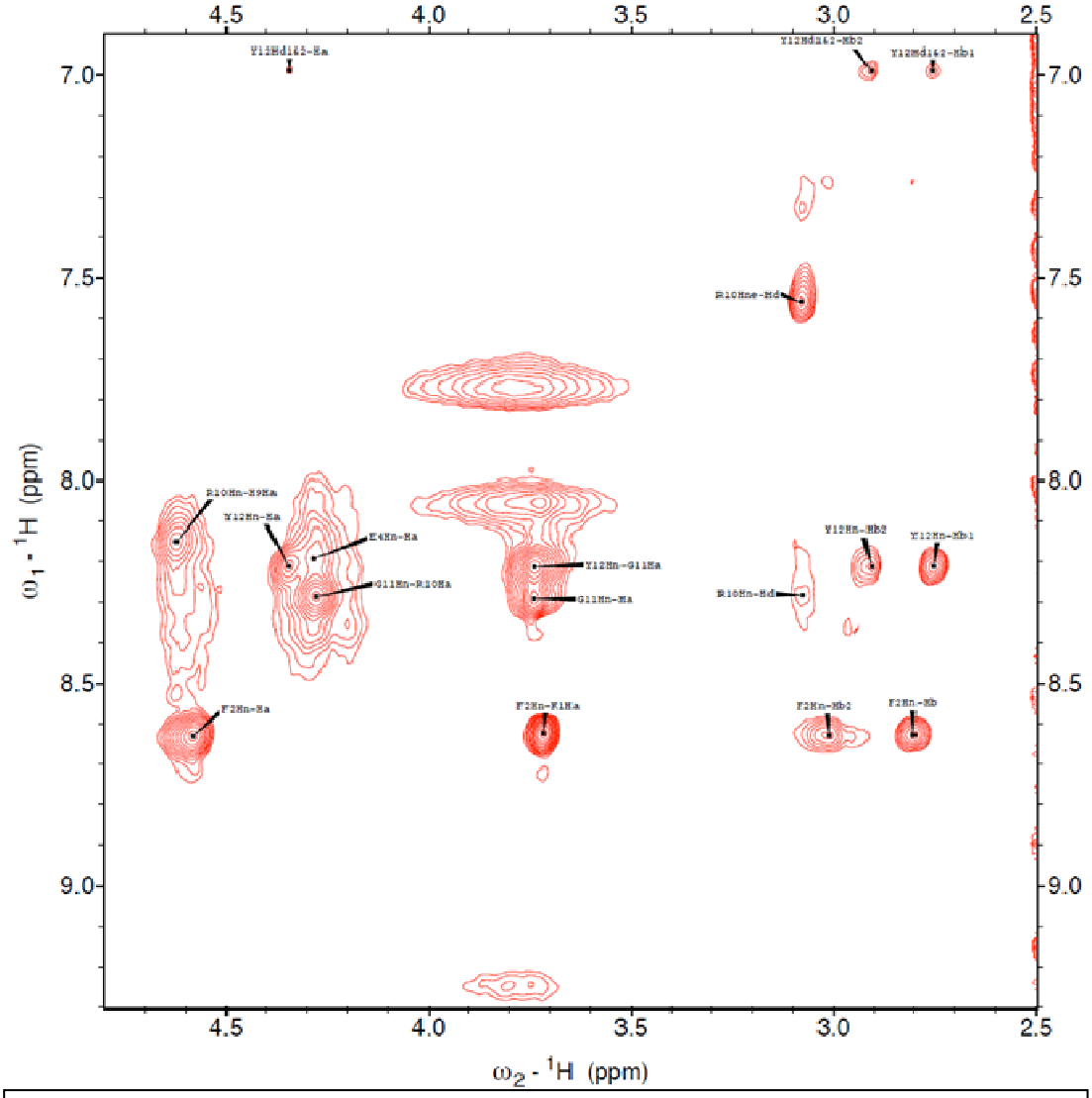

Figure 4.3.1. Part of the NOESY spectrum of *Hst*-8 and Cu(I) in DMSO illustrating amide alpha and amide beta interactions.

The correlation peak for the $F2H_N$-$K1H_\alpha$ remains in the same place as the metal free series. Further the beta protons of the phenylalanine are in the same place. These assignments were for the most part very easy. In fact that is the major trend observed throughout the study of the *Hst*-8 with Cu(I) in DMSO. This trend is apparent in table 4.3.1, a summary of resonances of protons in *Hst*-8 with 1 eq. $Cu(CH_3CN)_4PF_6$ in DMSO compared to *Hst*-8 in DMSO. One of the major things we observed in figure 4.3.1 was that not only do we not observe the peaks correlating the alpha protons to amide protons from neighboring residues in the region from the H3 to the H9, but we also do not observe the intra-residue correlations of the alpha and amide protons. Further, these correlations are also absent in the ROESY and TOCSY spectra illustrated in figures 4.3.2 and 4.3.3 respectively.

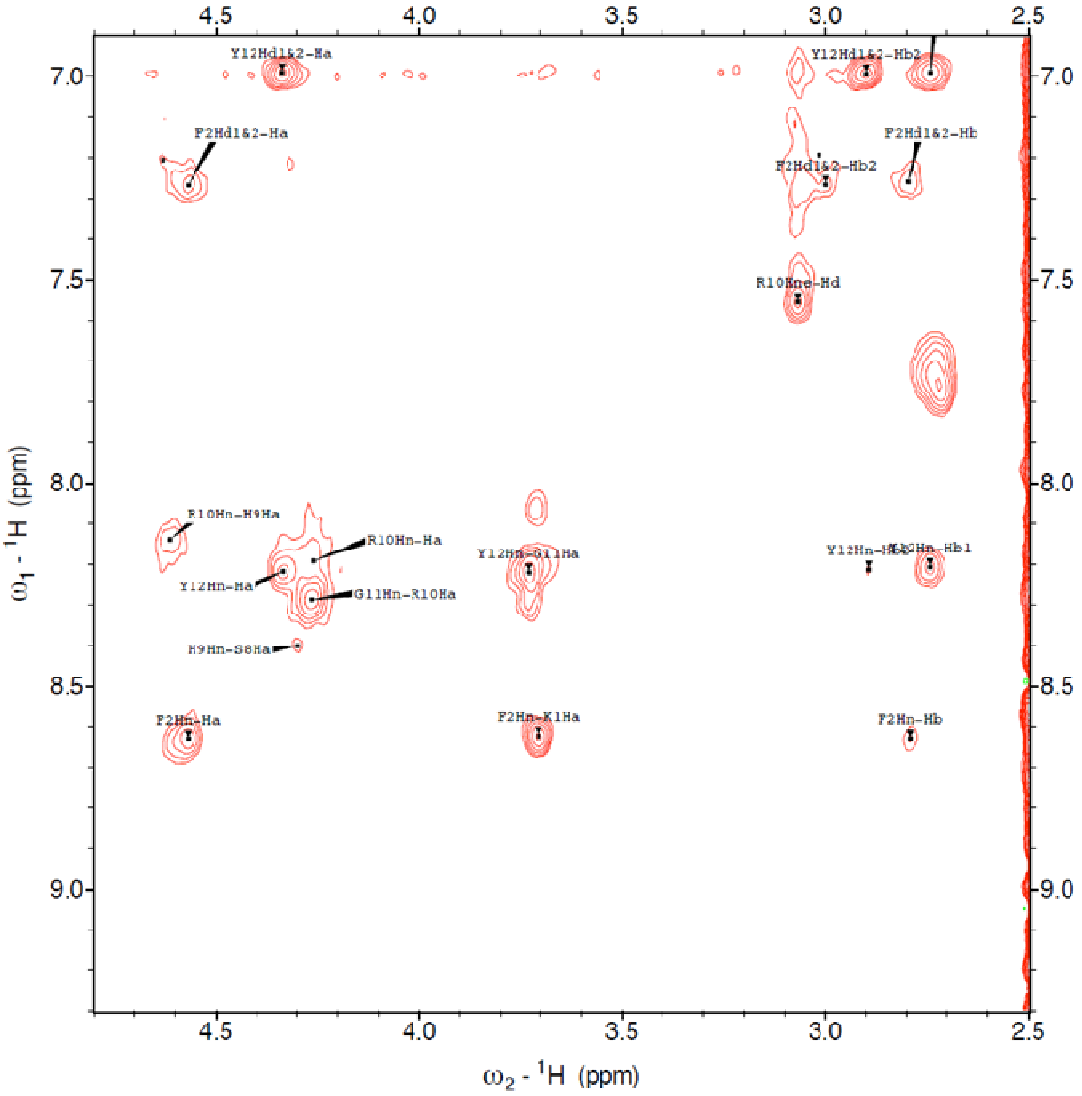

Figure 4.3.2. Part of the ROESY spectrum of *Hst*-8 and Cu(I) in DMSO illustrating amide alpha and amide beta interactions.

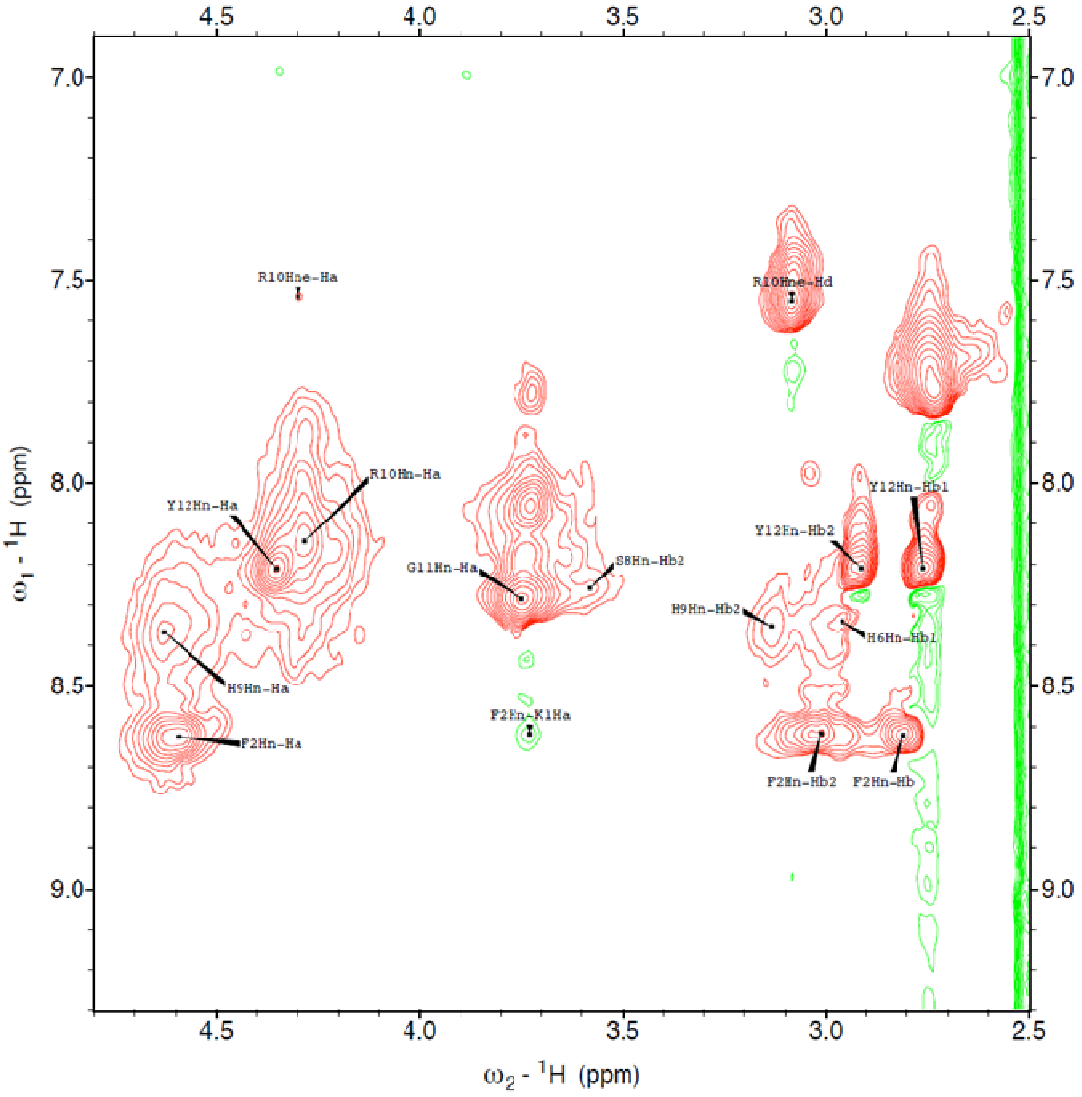

Figure 4.3.3. Part of the TOCSY spectrum of *Hst*-8 and Cu(I) in DMSO illustrating amide alpha and amide beta interactions.

Given what was observed in the previous chapter discussing the coordination of the *Hst*-8 peptide to the metal, the data combined speaks to a coordination that is not very tight and is undergoing dynamic exchange. Unfortunately, isothermal calorimetry studies have not been performed on

Hst-8 to evaluate either Cu(I) or Cu(II) binding. The closest approximation that we have is the values given for the binding of Cu(II) by *Hst*-5.[71] Using a single site model the binding constant was found to be $2.6x10^7$. However, as aforementioned there are actually three distinct moieties that often engage in metal ion binding; the ACTUN motif and two His-X-Y-Z-His motifs. Using a multisite model the researchers determined the binding constants to be $3.8x10^5$, $1.2x10^4$, and $5.2x10^4$. However, they made no comment as to which site correlated to which binding constant. Of course, copper (II) is not copper (I) Cu(I) prefers tetrahedral geometry and is softer and larger than Cu(II), which prefers square planer geometry.

The loose binding causes residues H3, H6, and H7 to be exchanging on and off the metal. This in turn results in a loss of NMR signal as the ligand exchange occurs more quickly than the millisecond timescale on which these NMR experiments are preformed. The loss of signal can result from one or a combination of several conditions. Firstly metal binding can cause nearby proton residues to shift. An averaging can then result moving the signal to unexpected places. Also the averaging causes signal broadening. If the shift then is large enough the peak then can be averaged over such a large range that it is indistinguishable from noise. Also one should consider that metal binding, particularly dynamic metal binding could result in a conformation whereby the interresidual correlations are unable to be observed simply by the fact that those alpha and amide protons are not in close proximity. Lastly of course, remains the possibility remains that protons, particularly amide

protons, are not observed as a result of ACTUN like binding interactions with the metal. Though we feel that this is unlikely given our observation of the phenylalanine amide proton, we would be remiss if we did not mention the possibility. One of the strongest indications we are dealing with an exchange phenomenon of the conformation involving the H3 residue is that no distinct alpha amide proton correlation is observed in figure 4.3.3, the TOCSY spectrum of *Hst*-8 with Cu(I) in DMSO. Further, we observe large amorphous areas in the region where we had expected to observe many of our missing correlations. As TOCSY relies on *J* couplings to transfer spin information, a change in coupling conditions by means of dynamic conformation could give rise to broadened peaks.

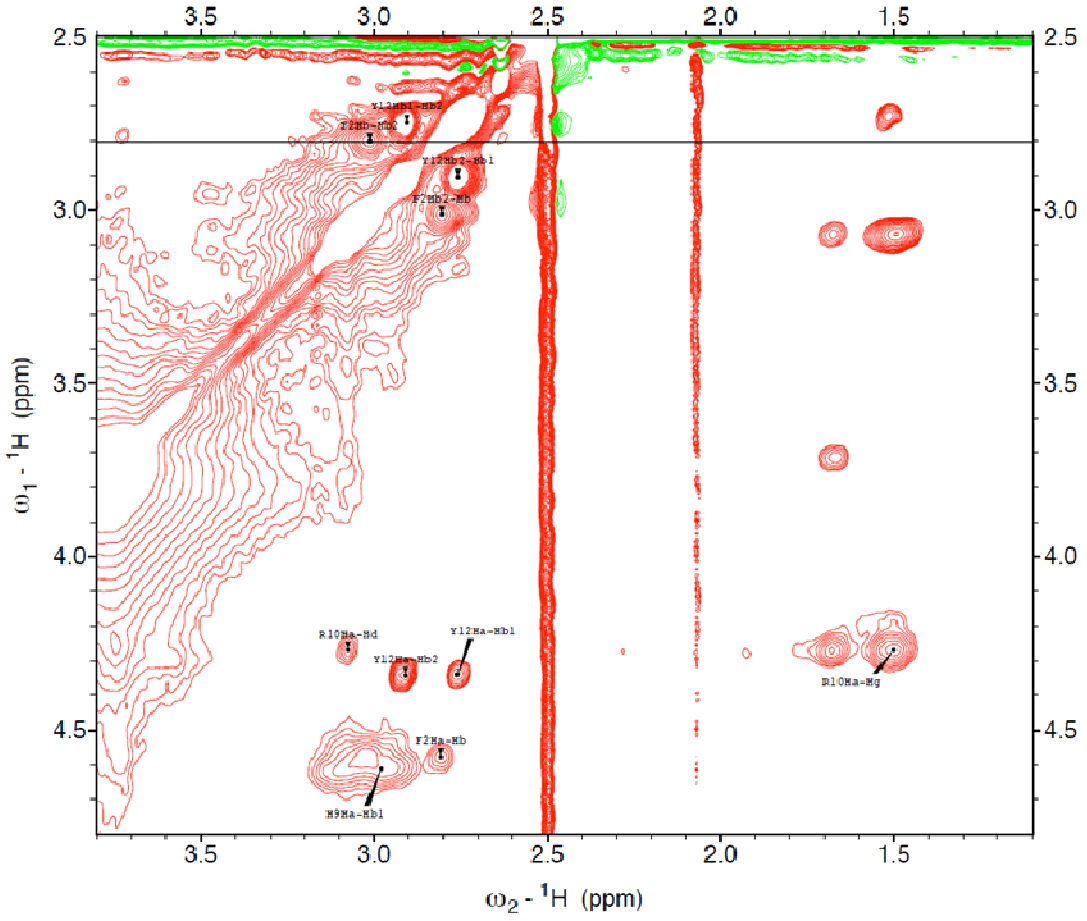

Figure 4.3.4. Part of the NOESY spectrum of *Hst*-8 and Cu(I) in DMSO illustrating alpha/beta and other proton interactions.

Figures 4.3.4, 4.3.5, and 4.3.6 are the NOESY, ROESY, and TOCSY spectra, respectively, of *Hst*-8 and Cu(I) in DMSO illustrating alpha beta and other proton interactions. As before lines were drawn from those resonances that had been definitively assigned in the alpha amide and beta amide region. At the intersections of those lines drawn from alpha and beta resonances the peaks were definitively assigned.

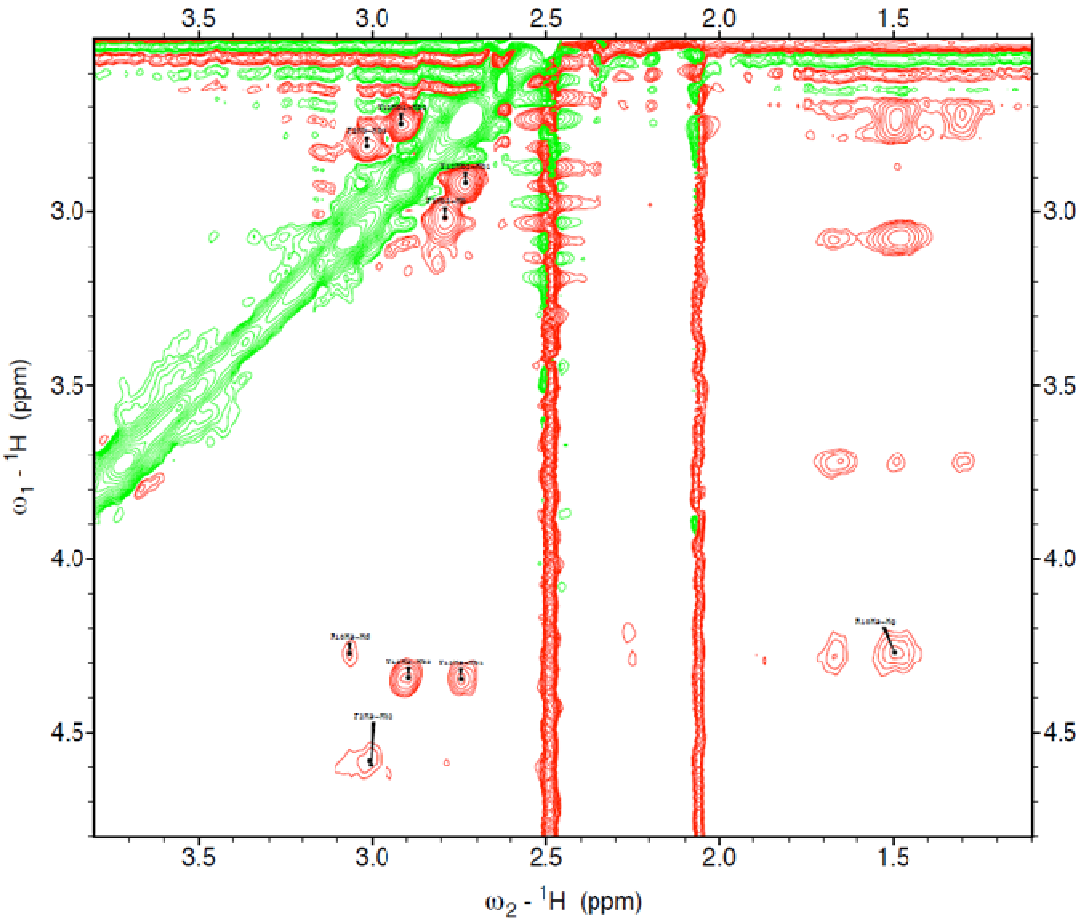

Figure 4.3.5. Part of the ROESY spectrum of *Hst*-8 and Cu(I) in DMSO illustrating alpha beta and other proton interactions.

Although we suspected the assignments of the unassigned correlations in figures 4.3.4, 4.3.5, and 4.3.6, we were regrettably unable to definitively assign them. Definitive assignment of the correlation peaks in the 2.0 ppm to 1.5 ppm range of the ω_2 axis to either the K1 or K5 was impossible. This was because without the alpha and amide peaks of K5 the rest of the residue's resonances are impossible to trace. However, these aliphatic resonances have little to do with being able to construct a picture of the global conformation of the *Hst*-8 peptide upon metal binding, particularly

those observed in figure 4.3.6, the TOCSY spectrum of *Hst*-8 and Cu(I) in DMSO, which contains no spatial information.

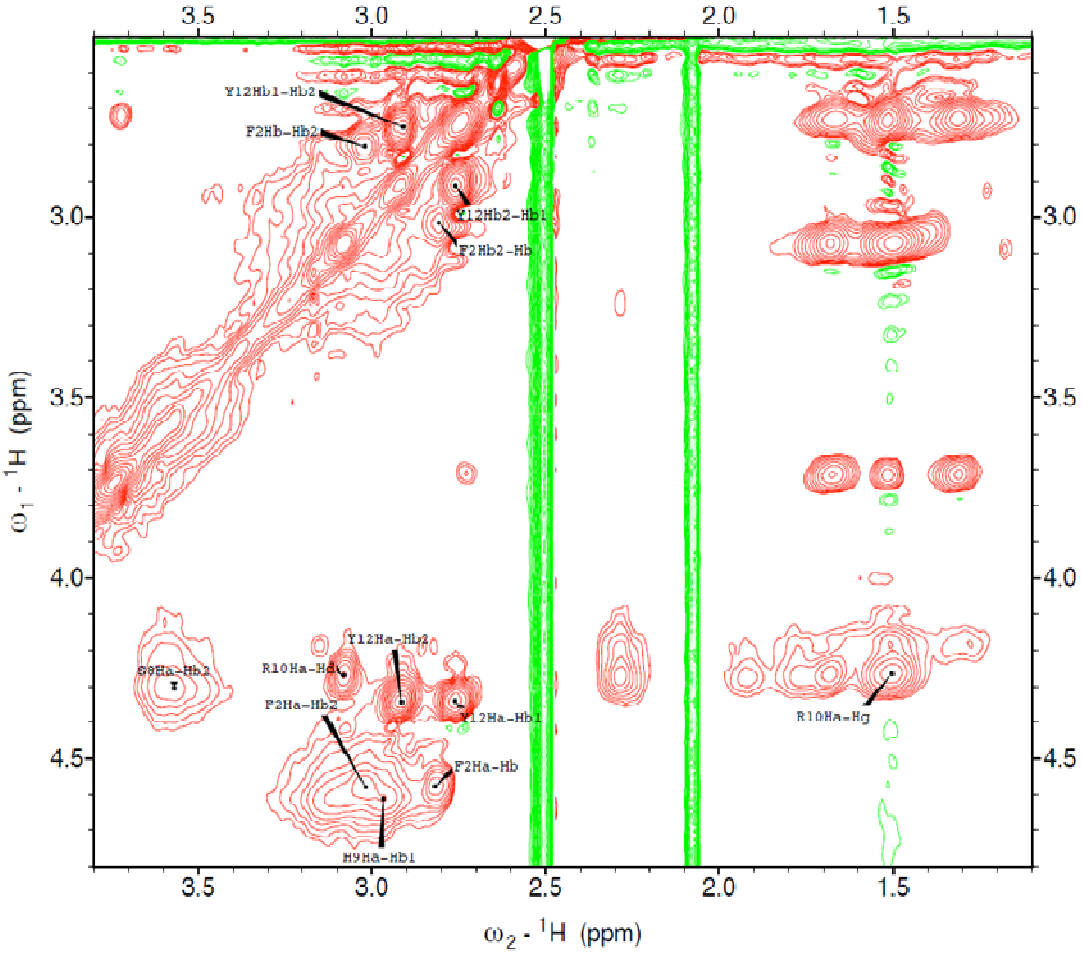

Figure 4.3.6. Part of the TOCSY spectrum of *Hst*-8 and Cu(I) in DMSO illustrating alpha beta and other proton interactions.

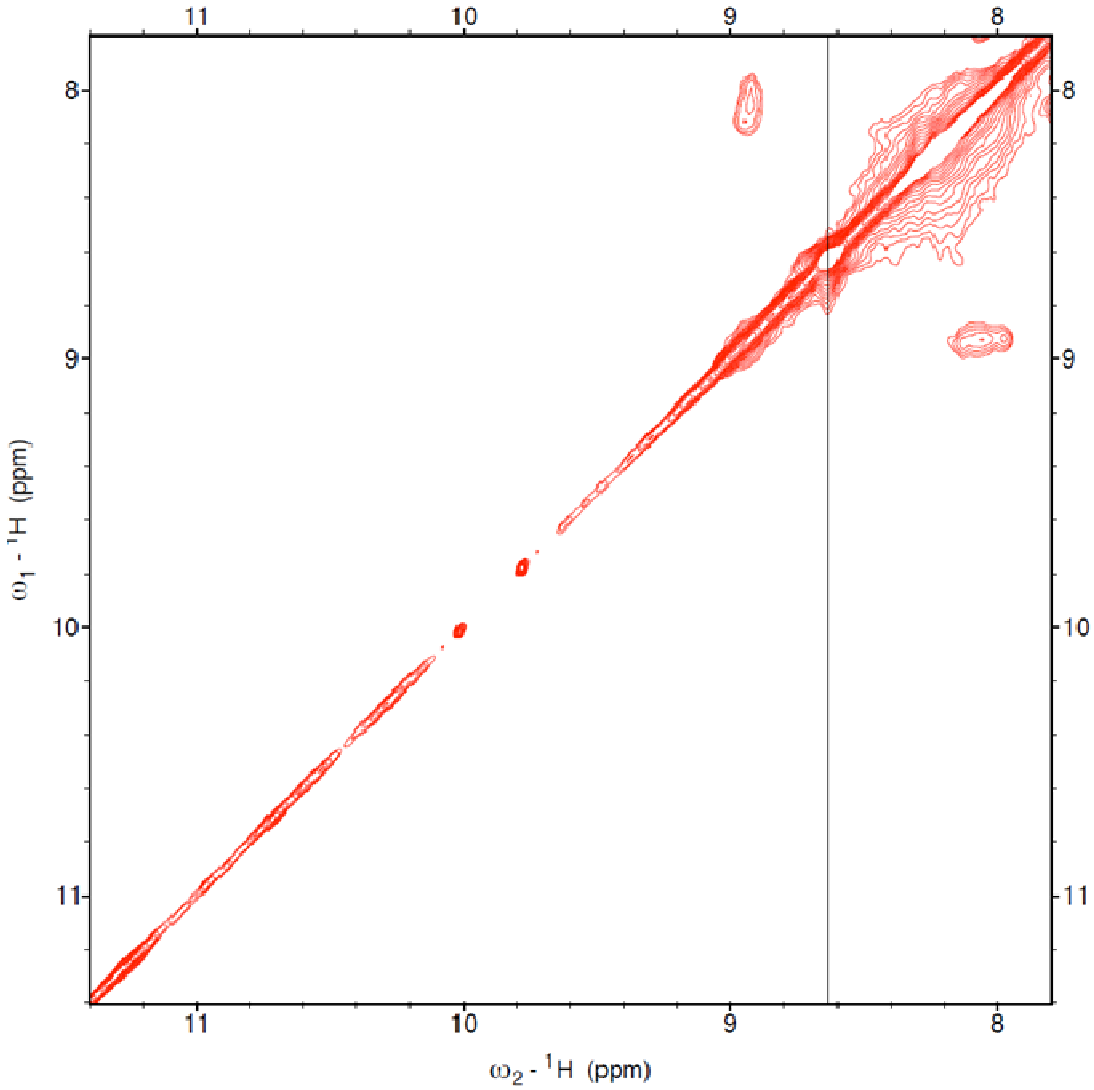

Figure 4.3.7. Part of the NOESY spectrum of *Hst*-8 and Cu(I) in DMSO illustrating histidine exchange.

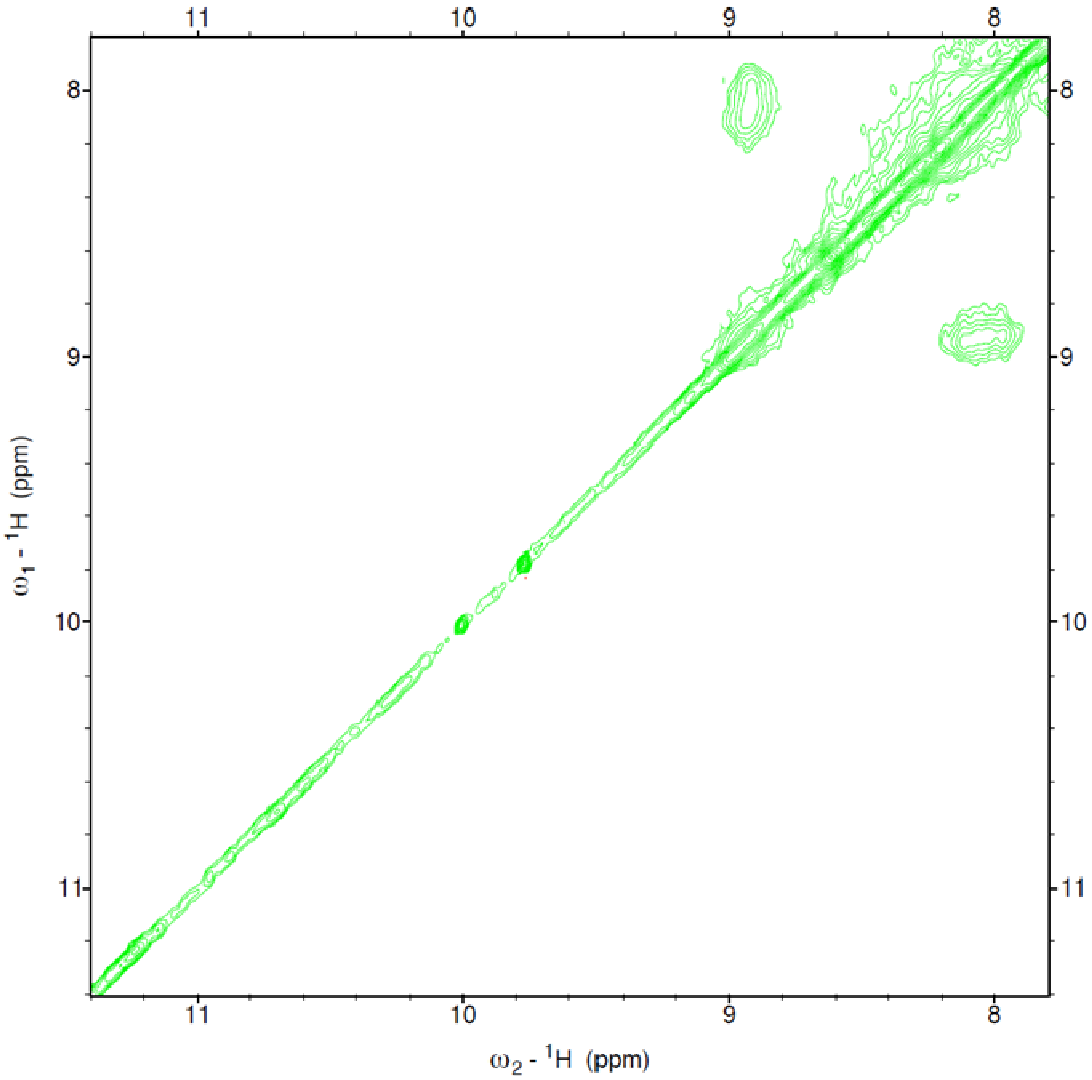

Figure 4.3.8. Part of the ROESY spectrum of *Hst*-8 and Cu(I) in DMSO illustrating histidine exchange.

Figures 4.3.7, 4.3.8, and 4.3.9 illustrate the NOESY, ROESY, and TOCSY spectra, respectively, of *Hst*-8 and Cu(I) in DMSO suggesting histidine exchange. Figure 4.3.8, the ROESY spectrum, is the best illustration of this as it clearly shows the peak to be in the opposite phase and thus arises from a situation that has exchange involved. This fits into the larger

picture that the imidazolyl units of the various histidine residues are not statically bound to the copper ion on the NMR timescale.

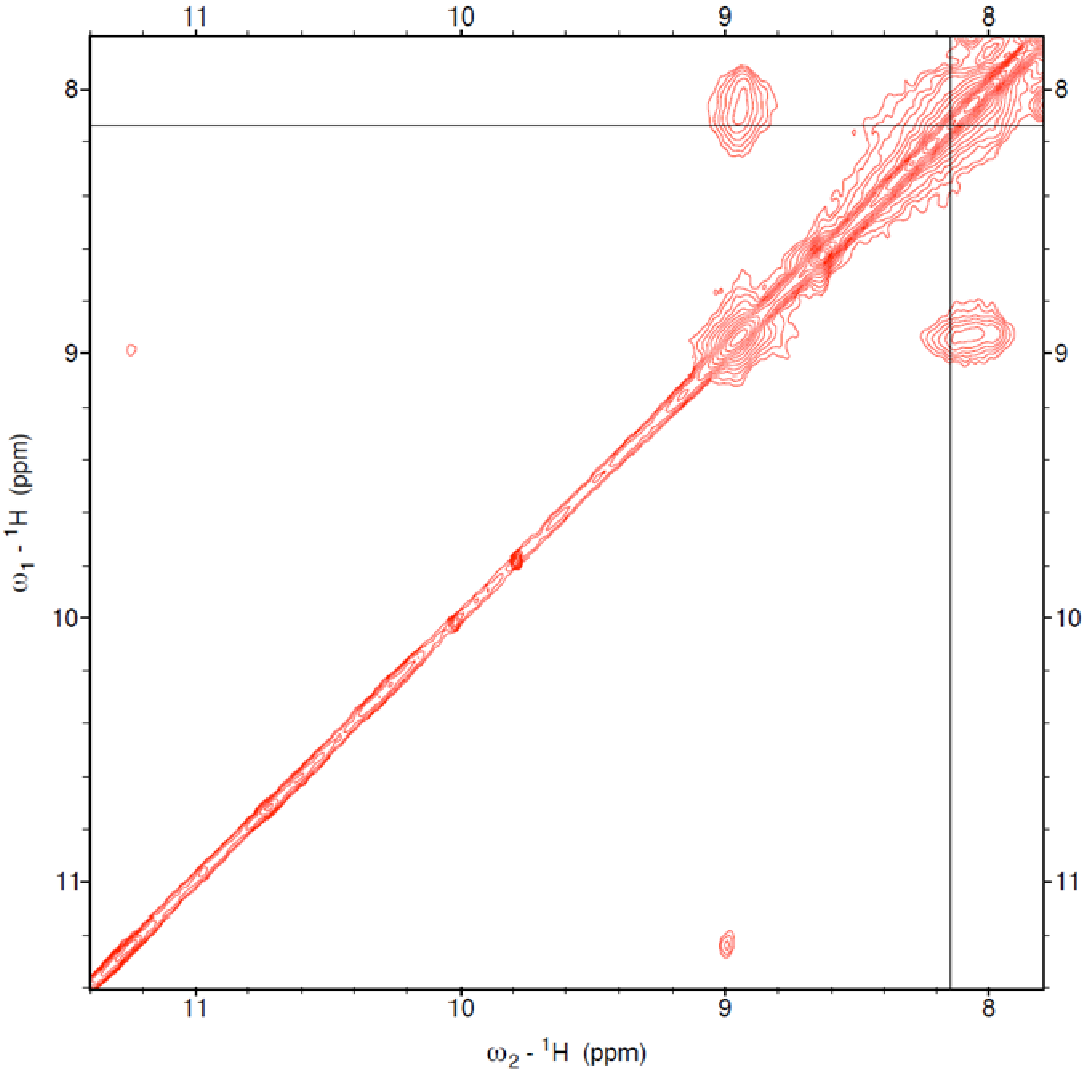

Figure 4.3.9. Part of the TOCSY spectrum of *Hst*-8 and Cu(I) in DMSO illustrating histidine exchange.

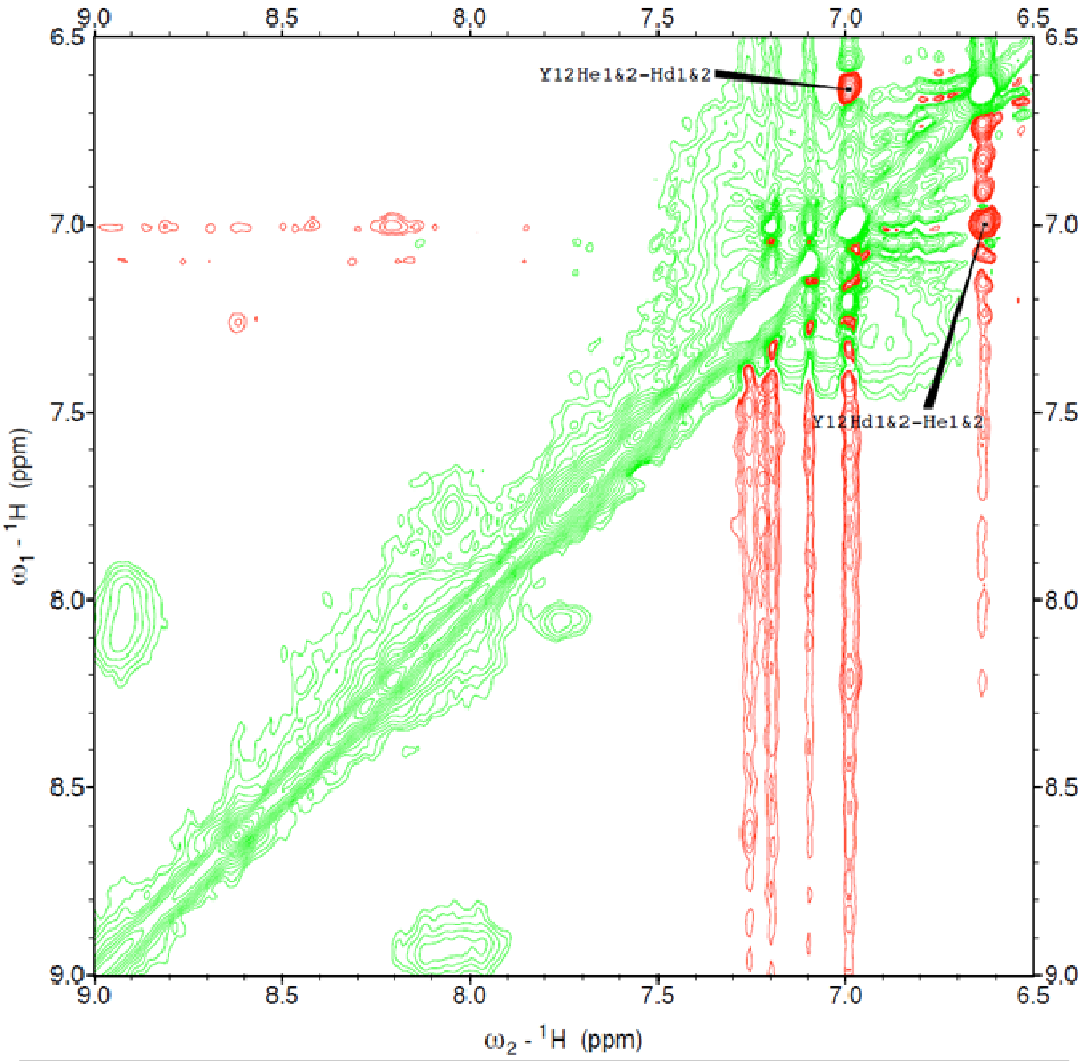

Figure 4.3.10. Part of the ROESY spectrum of *Hst*-8 and Cu(I) in DMSO illustrating the aromatic region.

Figure 4.3.10 is part of the ROESY spectrum of *Hst*-8 and Cu(I) in DMSO illustrating the aromatic region. It again illustrates the histidine exchange observed in figure 4.3.8. Exchanging protons or protons on an exchanging motif like the C_2 protons on histidine are found in the negative phase of ROESY spectra. Alternatively they can also disappear from the spectrum. We observe evidence of histidine exchange in two places, first the

correlation peak in the negative phase at 8.0 ppm and 8.9 ppm as well as the negative phase region from 6.7 ppm to 7.4 ppm that obscures the phenylalanine Hδ and Hε correlation. However, we are able to observe in both figure 4.3.10 and figure 4.3.11, part of the TOCSY spectrum of *Hst*-8 and Cu(I) in DMSO illustrating the aromatic region, including the aromatic protons of the tyrosine.

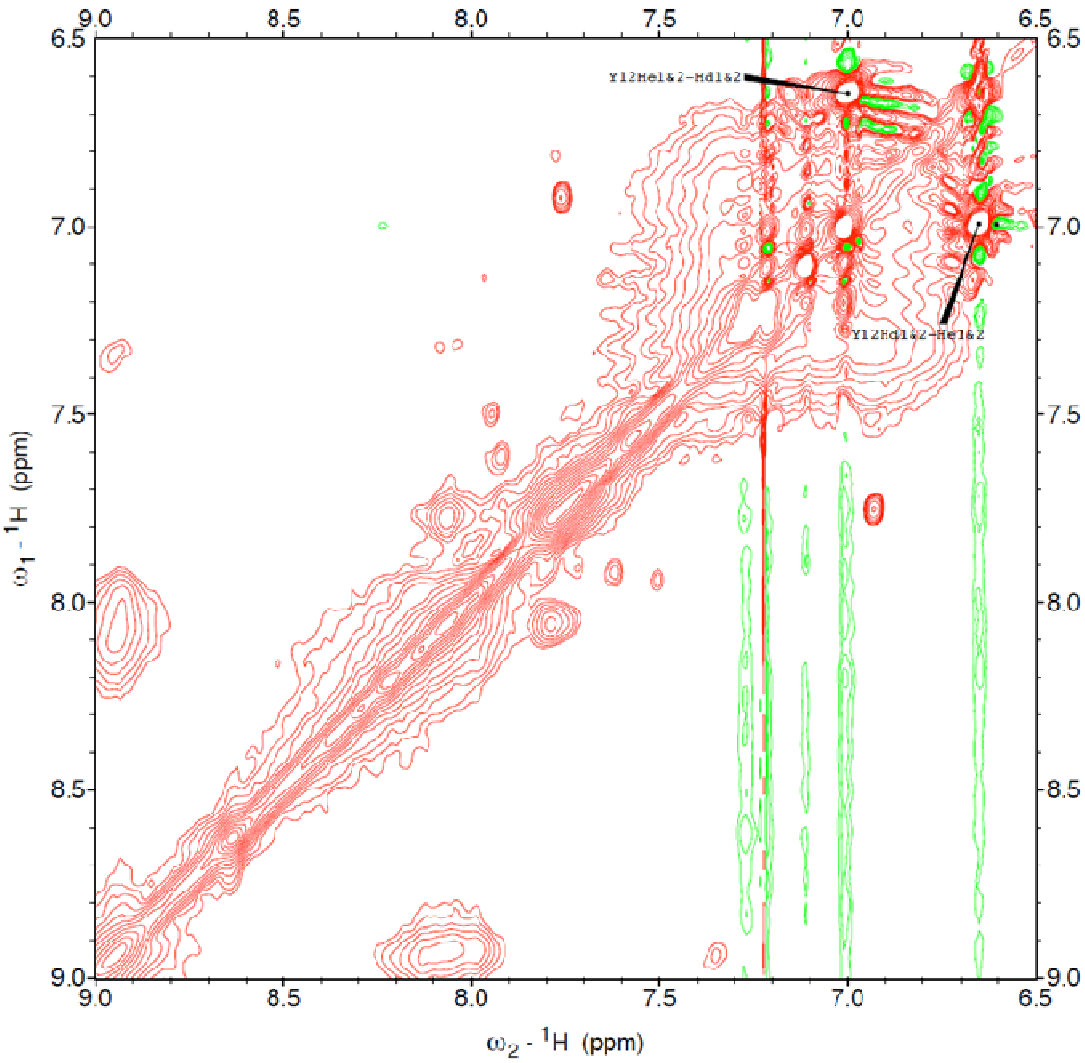

Figure 4.3.11. Part of the TOCSY spectrum of *Hst*-8 and Cu(I) in DMSO illustrating the aromatic region.

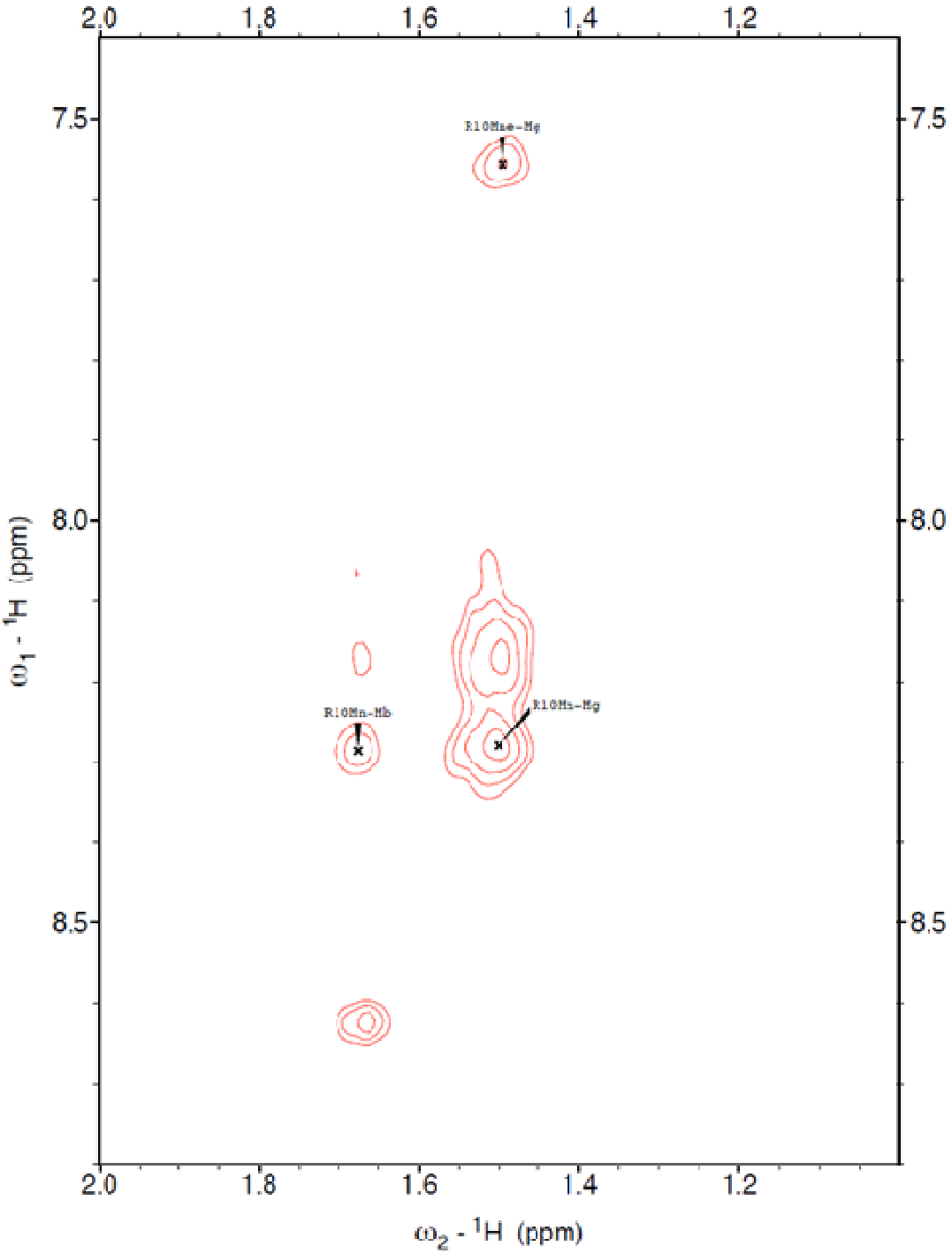

Figure 4.3.12. Part of the NOESY spectrum of *Hst*-8 and Cu(I) in DMSO illustrating miscellaneous proton interactions.

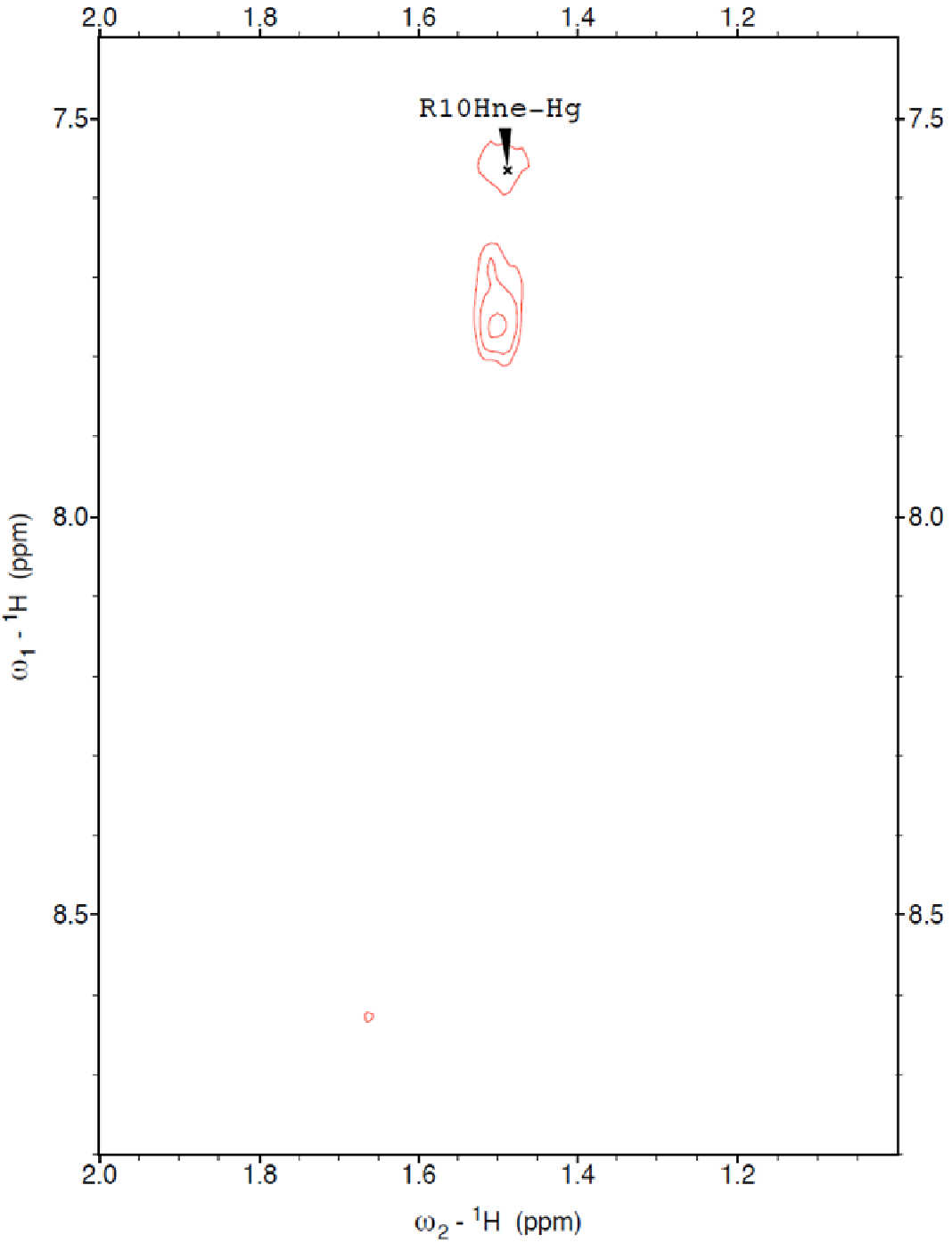

Figure 4.3.13. Part of the ROESY spectrum of *Hst*-8 and Cu(I) in DMSO illustrating miscellaneous proton interactions.

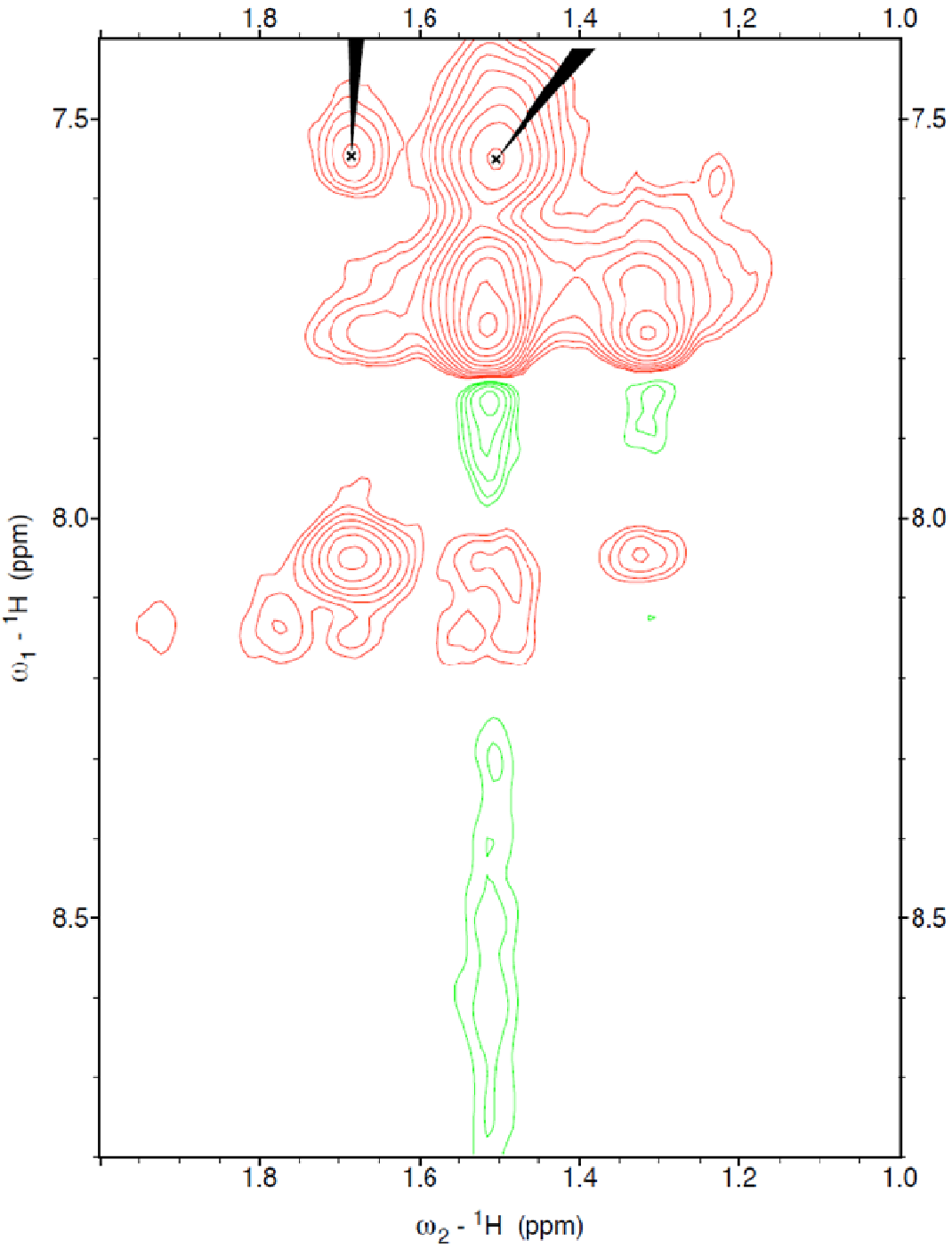

Figure 4.3.14. Part of the TOCSY spectrum of *Hst*-8 and Cu(I) in DMSO illustrating miscellaneous proton interactions.

Figures 4.3.12, 4.3.13, and 4.3.14 are the NOESY, ROESY, and TOCSY spectra of *Hst*-8 and Cu(I) in DMSO illustrating miscellaneous proton interactions. From the data obtained in the ROESY spectrum illustrating histidine exchange and the aromatic region, figures 4.3.10 and 4.3.8 respectively, we believe that the unassigned correlation peaks are those of imidazolyl units of histidines correlating to beta protons of their respective residues. However, because we were unable to assign alpha amide correlations of H3, H6, and H7, we were ultimately unable to definitively assign the beta protons either. However, here again, assigning these at this point was of no consequence, because there would be no effect on the global conformation if restrictions were not assigned to these as the connectivity of the imidazolyl unit to the beta carbon is set by consequence of the carbon connectivity.

Table 4.3.1. Summary of resonances of protons in *Hst*-8 with 1 eq. $Cu(CH_3CN)_4PF_6$ in DMSO compared to *Hst*-8 in DMSO. (N.M. - not meaningful; Am. – ambiguous; N.P. - not present)

Group	Proton	Shift for 1 eq. Cu(I)	Shift for 0 eq. Cu(I)	difference
K1	α	3.72	3.71	-0.01
K1	β	Am.	1.65	N.M.
K1	γ	Am.	1.46	N.M.
K1	δ	Am.	2.73	N.M.
K1	ε	Am	1.29	N.M.
F2	N	8.63	8.62	0.00
F2	α	4.58	4.57	-0.02

F2	β1	2.80	2.80	-0.01
F2	β2	3.01	3.01	0.00
F2	2,6H	7.27		N.M.
H3	N	N.P.	8.63	N.M.
H3	α	N.P.	4.63	N.M.
H3	β1	Am.	2.96	N.M.
H3	β2	Am.	3.06	N.M.
E4	N	8.19	8.22	0.03
E4	α	4.28	4.29	0.00
E4	β1	1.75	1.75	0.00
E4	β2	1.89	1.89	0.00
E4	γ	2.26	2.26	0.00
K5	N	N.P.	8.24	N.M.
K5	α	N.P.	4.20	N.M.
K5	β1	Am.	1.59	N.M.
K5	δ	Am.	1.50	N.M.
K5	ε	N.P.	2.74	N.M.
H6	N	8.34	8.33	-0.01
H6	α	N.P.	4.57	N.M.
H6	β1	2.96	2.95	-0.01
H6	β2	Am.	3.04	N.M.
H6	4H	Am.	7.33	N.M.
H7	N	N.P.	8.32	N.M.
H7	α	N.P.	4.63	N.M.
H7	β1	N.P.	2.95	N.M.
H7	β2	N.P.	3.06	N.M.
S8	N	8.26	8.29	0.03
S8	α	4.31	4.30	0.00
S8	β1	N.P.	3.61	N.M.
S8	β2	3.57	3.56	-0.02
H9	N	8.38	8.39	0.01
H9	α	4.62	4.63	0.01
H9	β1	2.97	2.98	0.02
H9	β2	3.10	3.11	0.01
R10	N	8.19	8.16	-0.02
R10	α	4.27	4.26	-0.01

R10	β1	1.68	1.67	-0.01
R10	β2	3.07	3.07	0.00
R10	γ	1.50	1.49	-0.01
R10	NH1	7.56	7.61	0.06
G11	N	8.29	8.31	0.02
G11	α	3.74	3.73	0.00
Y12	N	8.21	8.22	0.00
Y12	α	4.34	4.35	0.00
Y12	β1	2.75	2.75	0.00
Y12	β2	2.91	2.90	0.00
Y12	2,6H	6.99	6.99	0.00
Y12	3,5H	6.64	6.64	0.00

Table 4.3.1 was drawn from the conformational studies of *Hst*-8 by NOESY, ROESY, and TOCSY. It contains data, which is important not only in the conformational analysis but also in the metal binding studies as discussed earlier. As discussed in the prior chapter, one can notice that we observe a resonance for the phenylalanine amide proton (F2 N) in the *Hst*-8 sample with the Cu(I). Such an observation necessarily precludes ACTUN like binding on the part of *Hst*-8. Other data to note is that the chemical shifts of the vast majority of *Hst*-8 are not affected very much at all as a result of metal binding. The obvious conclusion is that those particular residues that are not dramatically shifted are not involved in metal ion binding. Also those resonances that disappear are likely involved in metal ion binding. Though one would initially expect a mere downfield shift in residues involved in metal ion binding, a loss of signal points to a different conclusion. Namely that metal ion binding is not very tight and an equilibrium on and off the metal is

occurring on the NMR time frame. The data in the respect of which residues are involved in metal ion binding fit with our hypothesis as to where the metal likely binds: the histidine residues in the 3, 6, and 7 positions. The equilibrium exchange on and off the metal not only affects the chemical shifts of the imidazolyl units of the residues, but also the beta, alpha, and amide protons as a consequence of the conformational changes occurring resulting from the metal binding equilibrium. Granted this is not conclusive evidence, but the data certainly fits the hypothesis.

In terms of analysis of the remainder of the data related to the conformational analysis. The inability to locate the amide peak for the lysine of the fifth position affected our ability to definitively assign the aliphatic chains that correlated together to either the lysine in the first position or the fifth position. This was really the only major obstacle encountered that resulted in the inability to assign a great number of peaks. The reason for our inability to observe the amido proton of the K5 results from the dynamic conformation of the backbone starting at the H3 and ending at the H7. The dynamic conformation is a result of the weak interaction of the H3, H6, and H7 with the metal ion.

4.4: Use of MARDIGRAS for Creation of Spatial Constraints

After obtaining the raw spatial information of *Hst*-8 in DMSO and that of the *Hst*-8 and Cu(I) in DMSO in the form of NOESY and ROESY spectra, we then sought to perform a conformational analysis. First we needed to

generate boundary restraint data from the raw NOESY and ROESY peak intensities. We used MARDIGRAS and its suite of helper programs to generate boundary restraint data.[134-138] One initially begins with a model. We choose to utilize two models as starting points. Our first model was *Hst*-8 in an alpha helix and the second model was *Hst*-8 as a beta strand. From there MARDIGRAS output boundary restraint data. MARDIGRAS is a program that takes NOESY intensity data and translates it to spatial restraint data. First a model is input and MARDIGRAS makes initial measurements of distances between protons with identified NOESY correlations. It then weights the intensity data from most to least intense. Finally, it generates spatial restraint data such that the intense correlations have minimal distances and the weaker correlations have comparatively longer restraint distances. It does this by using the starting model and then performing minimizations according to the weighted restraint data. The final data are output in the following format. The first and third columns are specific proton locations on residues identified in the second and fourth columns. The distance between the two protons in a row is defined by the lower and upper boundaries identified in the fifth and sixth columns respectively. The width is the distance between the lower and upper boundaries.

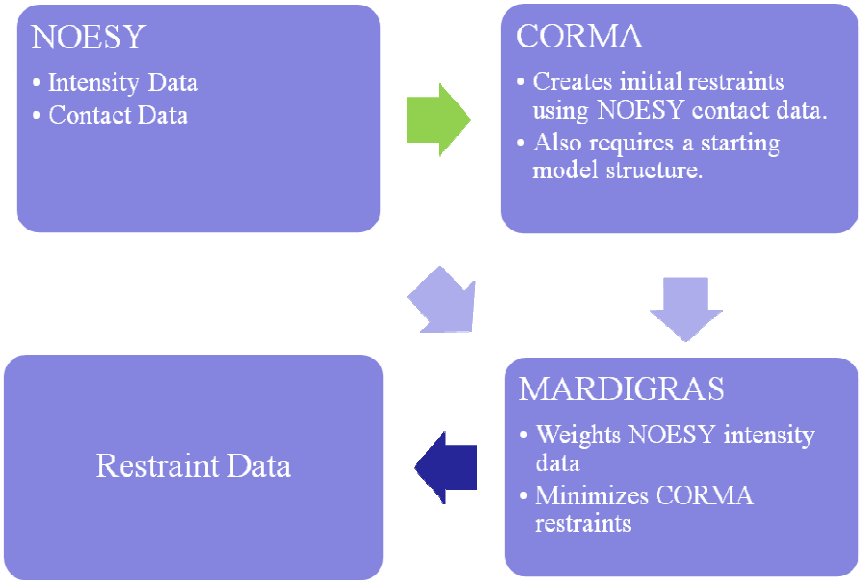

Figure 4.4.1. A graphical illustration of the information flow and processing done to generate restraint data from NOESY data using MARDIGRAS and its helper program, CORMA.

Figure 4.4.1 is a graphical illustration of the process described in detail above. The raw NOESY data contains two pieces of information the specific contacts between protons and the intensity of that contact correlation. CORMA (complete relaxation matrix analysis) has a model structure input into it. It then creates restraint information by measuring the distance between protons identified by the contact data from the NOESY spectrum (light green arrow). This initial structure with its identified restraints is then fed into MARDIGRAS along with the intensities of all the proton correlations identified in the NOESY spectrum (light blue arrows). MARDIGRAS then weights the NOESY data according to intensity and minimizes the restraints in the CORMA processed structure according to the weighting. MARDIGRAS then outputs restraint data (dark blue arrow). Both the restraints that

MARDIGRAS has determined to be ideal, as well as an upper and lower boundary for those restraints are output. Tables 4.4.1 and 4.4.2 summarize the upper and lower boundaries obtained for *Hst*-8 in DMSO. Table 4.4.1 is that obtained when CORMA had an initial model of *Hst*-8 in an alpha helix input and Table 4.4.2 is data obtained when a beta strand conformation of *Hst*-8 was input into CORMA.

Table 4.4.1. Summary of boundary data from MARDIGRAS using the peak intensity data from *Hst*-8 in DMSO using an alpha helix as a starting model. Note that Q is a variable that substitutes for methylene and R is a variable indicating its position on a ring.

ATOM_i		ATOM_j		LOW_BNDS	UP_BNDS	WIDTH
QB	K1	HA	K1	4.341	5.543	1.202
H	F2	HA	K1	4	4.713	0.713
HA	F2	H	F2	3.419	3.926	0.507
HB1	F2	H	F2	3.94	5.035	1.096
HB2	F2	H	F2	3.694	4.267	0.573
HB2	F2	HA	F2	1.911	1.962	0.051
HA	H3	H	H3	2.711	2.822	0.111
HB1	H3	H	H3	2.91	3.196	0.287
HB1	H3	HA	H3	2.326	2.352	0.026
HB2	H3	HA	H3	2.247	2.27	0.023
HA	E4	H	E4	2.272	2.301	0.03
HB1	E4	HA	E4	2.015	2.08	0.065
QG	E4	HB1	E4	4.231	5.548	1.317
QG	E4	HB2	E4	3.924	4.873	0.95
HA	K5	H	K5	1.678	1.701	0.023
QD	K5	HA	K5	2.398	2.482	0.084
H	H6	HA	K5	1.589	1.621	0.031
HA	H6	H	H6	1.808	1.836	0.028
HB1	H7	H	H7	2.047	2.121	0.074
H	S8	HA	H7	2.098	2.117	0.019
HB1	S8	H	S8	2.117	2.16	0.043
H	H9	HA	S8	1.948	1.965	0.017
H	H9	HB2	S8	3.042	3.336	0.294
HA	H9	H	H9	2.052	2.085	0.033
HB1	H9	H	H9	1.939	1.997	0.058
HB1	H9	HA	H9	2.291	2.32	0.029
HB2	H9	HA	H9	2.196	2.245	0.049
H	R10	HA	H9	3.214	3.498	0.283
H	R10	HB1	H9	2.949	3.132	0.183
H	R10	HB2	H9	2.828	2.971	0.143
HA	R10	H	R10	2.299	2.328	0.03
QB	R10	HA	R10	2.621	2.687	0.066
QG	R10	HA	R10	3.041	3.135	0.094

QD	R10	HA	R10	4.429	6.997	2.568
QD	R10	QG	R10	5.005	5.646	0.641
HE	R10	QD	R10	4.307	5.696	1.389
H	G11	HA	R10	2.372	2.407	0.035
HA	Y12	H	Y12	1.896	1.921	0.026
HB1	Y12	HA	Y12	3.008	3.527	0.52
HB2	Y12	H	Y12	1.873	1.933	0.06
RD	Y12	HB1	Y12	4.028	4.87	0.842
RE	Y12	RD	Y12	4.161	5.061	0.9

Table 4.4.2. Summary of boundary data from MARDIGRAS using the peak intensity data from *Hst*-8 in DMSO using a beta sheet as a starting model. Note that Q is a variable that substitutes for methylene and R is a variable indicating its position on a ring.

ATOM_i		ATOM_j		LOW_BNDS	UP_BNDS	WIDTH
QB	K1	HA	K1	4.273	5.432	1.158
H	F2	HA	K1	3.641	4.302	0.661
HA	F2	H	F2	3.449	3.941	0.492
HB1	F2	H	F2	3.938	5.001	1.063
HB2	F2	H	F2	3.426	3.962	0.537
HB2	F2	HA	F2	1.94	1.993	0.053
HA	H3	H	H3	2.723	2.838	0.116
HB1	H3	H	H3	2.956	3.257	0.302
HB1	H3	HA	H3	2.284	2.309	0.025
HB2	H3	HA	H3	2.225	2.248	0.023
HA	E4	H	E4	2.289	2.318	0.029
HB1	E4	HA	E4	1.995	2.056	0.061
QG	E4	HB1	E4	4.303	5.489	1.186
QG	E4	HB2	E4	4.134	5.063	0.929
HA	K5	H	K5	1.838	1.855	0.017
QD	K5	HA	K5	2.487	2.574	0.086
H	H6	HA	K5	1.754	1.77	0.016
HA	H6	H	H6	1.849	1.865	0.016
HB1	H7	H	H7	2.089	2.133	0.045
H	S8	HA	H7	2.106	2.124	0.017
HB1	S8	H	S8	2.134	2.178	0.044
H	H9	HA	S8	1.956	1.972	0.015
H	H9	HB2	S8	3.012	3.282	0.27

HA	H9	H	H9	2.075	2.104	0.029
HB1	H9	H	H9	1.955	2.004	0.049
HB1	H9	HA	H9	2.309	2.337	0.028
HB2	H9	HA	H9	2.223	2.264	0.041
H	R10	HA	H9	3.193	3.464	0.271
H	R10	HB1	H9	2.954	3.131	0.177
H	R10	HB2	H9	2.842	2.983	0.141
HA	R10	H	R10	2.286	2.312	0.026
QB	R10	HA	R10	2.624	2.701	0.077
QG	R10	HA	R10	3.197	3.293	0.096
QD	R10	QG	R10	4.15	4.672	0.522
HE	R10	QD	R10	4.33	5.648	1.318
H	G11	HA	R10	2.316	2.354	0.038
HA	Y12	H	Y12	1.905	1.922	0.017
HB1	Y12	HA	Y12	3.01	3.578	0.568
HB2	Y12	H	Y12	1.913	1.964	0.051
RD	Y12	HB1	Y12	4.764	5.781	1.016
RE	Y12	RD	Y12	4.125	4.976	0.85

The differences in the boundary widths between the two models used were not that great, usually varying by one to two hundredths of an angstrom (data not shown). So although differences were slight, the starting point for the MARDIGRAS analysis makes a difference. MARDIGRAS also outputs the distances between the correlated protons in both its minimized structure and that of the starting point of the model (data not shown). This data was not used in subsequent CNS MD simulations, it merely compares the start points and end points of inter-proton distances. It is not a full structural model.

We then performed the same MARDIGRAS analysis of the NOESY intensity data from the *Hst*-8 with 1 eq. $Cu(CH_3CN)_4PF_6$ in DMSO data. Again we used two different starting models, an alpha helix and a beta sheet.

The boundary restriction data for the alpha helix model is given in table 4.4.3. The boundary restriction data for the beta sheet model is given in table 4.4.4. As before, we noted that there was little difference between the data obtained using an alpha helix or beta sheet as a starting point. MARDIGRAS merely uses the initial model as a starting point and generates a final proton map based on the connectivity of the initial model and the intensity data that it weights to generate boundary restriction data.

Table 4.4.3. Summary of boundary data from MARDIGRAS using the peak intensity data from *Hst*-8 with 1 eq. $Cu(CH_3CN)_4PF_6$ in DMSO using an alpha helix as a starting model. Note that Q is a variable that substitutes for methylene.

ATOM_	i	ATOM_	j	LOW_BNDS	UP_BNDS	WIDTH
H	2	HA	1	3.271	3.541	0.27
HA	2	H	2	2.963	3.111	0.148
HB1	2	H	2	3.684	4.176	0.492
HB1	2	HA	2	2.317	2.344	0.027
HB2	2	H	2	3.182	3.442	0.26
HB2	2	HA	2	2.398	2.431	0.034
RD	2	HB2	2	3.024	3.306	0.282
HA	4	H	4	2.162	2.182	0.02
HB1	9	HA	9	2.267	2.293	0.027
HB2	9	HA	9	2.272	2.299	0.027
H	10	HA	9	2.327	2.361	0.034
HA	10	H	10	2.163	2.189	0.025
QG	10	H	10	2.764	2.854	0.09
QG	10	HA	10	3.201	3.332	0.131
QD	10	H	10	3.09	3.252	0.162
HE	10	QG	10	4.271	5.059	0.788
HE	10	QD	10	3.772	4.216	0.443
H	11	HA	10	2.157	2.181	0.024
QA	11	H	11	2.009	2.017	0.007
H	12	QA	11	2.282	2.294	0.012
HA	12	H	12	1.946	1.957	0.011
HB1	12	H	12	3.443	3.922	0.479
HB1	12	HA	12	3.7	4.258	0.559
HB2	12	H	12	3.09	3.392	0.302
HB2	12	HA	12	3.263	3.582	0.319
RD	12	HB1	12	4.037	5.882	1.845
RD	12	HB2	12	4.335	5.75	1.415
RE	12	RD	12	3.6	3.848	0.248

Table 4.4.4. Summary of boundary data from MARDIGRAS using the peak intensity data from *Hst*-8 with 1 eq. $Cu(CH_3CN)_4PF_6$ in DMSO using a beta sheet as a starting model. Note that Q is a variable that substitutes for methylene.

ATOM_	i	ATOM_	j	LOW_BNDS	UP_BNDS	WIDTH
H	2	HA	1	3.2	3.5	0.3
HA	2	H	2	3	3.1	0.1
HB1	2	H	2	3.7	4.2	0.5
HB1	2	HA	2	2.3	2.3	0
HB2	2	H	2	3.2	3.4	0.3
HB2	2	HA	2	2.5	2.5	0
RD	2	HB2	2	3.1	3.4	0.3
HA	4	H	4	2.2	2.2	0
HB1	9	HA	9	2.3	2.3	0
HB2	9	HA	9	2.3	2.3	0
H	10	HA	9	2.4	2.4	0
HA	10	H	10	2.2	2.2	0
QG	10	H	10	2.8	2.8	0.1
QG	10	HA	10	3.8	4	0.2
QD	10	H	10	3	3.2	0.2
HE	10	QG	10	4.2	5	0.8
HE	10	QD	10	3.7	4.1	0.4
H	11	HA	10	2.1	2.1	0
QA	11	H	11	1.9	1.9	0
H	12	QA	11	2.3	2.4	0
HA	12	H	12	2	2	0
HB1	12	H	12	3.5	4	0.5
HB1	12	HA	12	3.7	4.2	0.6
HB2	12	H	12	3.2	3.5	0.3
HB2	12	HA	12	3.2	3.6	0.3
RD	12	HB1	12	4.5	6.4	1.9
RD	12	HB2	12	4	5.4	1.4
RE	12	RD	12	3.6	3.9	0.2

One can clearly see from the data that the boundaries computed by MARDIGRAS for our system are very tight in the case of our starting from a

beta sheet model. This is likely a function of there being much fewer data points available to work with rather than simply that the beta sheet secondary structure is the conformation adopted by *Hst*-8 when Cu(I) is present.

4.5: Use of CNS for MD Studies

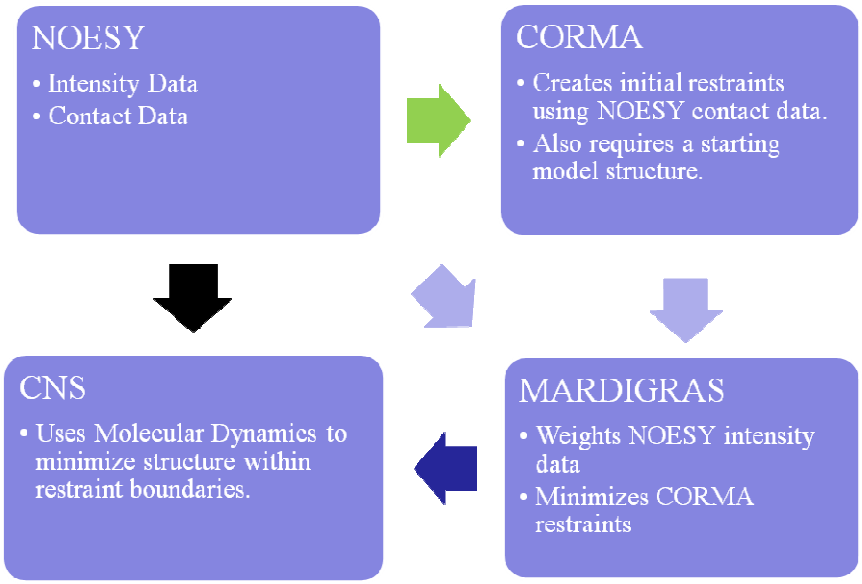

Figure 4.5.1. A graphical illustration of the information flow and processing done to generate a structure from NOESY data using MARDIGRAS using CNS.

CNS is a program that grew out of the XPLOR program.[139] It can be used for molecular dynamic studies using structural and boundary restraint data. We ran two separate simulations using CNS. Figure 4.5.1 illustrates the information flow and processing done to generate a structure from the NOESY data using CNS. First we ran a simulation using the boundary restraint data obtained from MARDIGRAS. The first step as discussed in the previous section utilized an initial starting model and the contact data from

the NOESY spectrum input into CORMA (light green arrow). Next the CORMA processed data as well as the intensity data for the proton correlations was input into MARDIGRAS (light blue arrows). MARDIGRAS output upper and lower restraint boundaries, which were both input into CNS (dark blue arrow). CNS then uses an internally generated structure along with the MARDIGRAS generated restraint data to perform a molecular dynamics simulation to output a structure. Alternatively the black arrow represents a pathway whereby we used the NOESY contact data and generic restraints as input into CNS. CNS then performed the same molecular dynamics simulation with the generic restraint data and its internally generated structure.

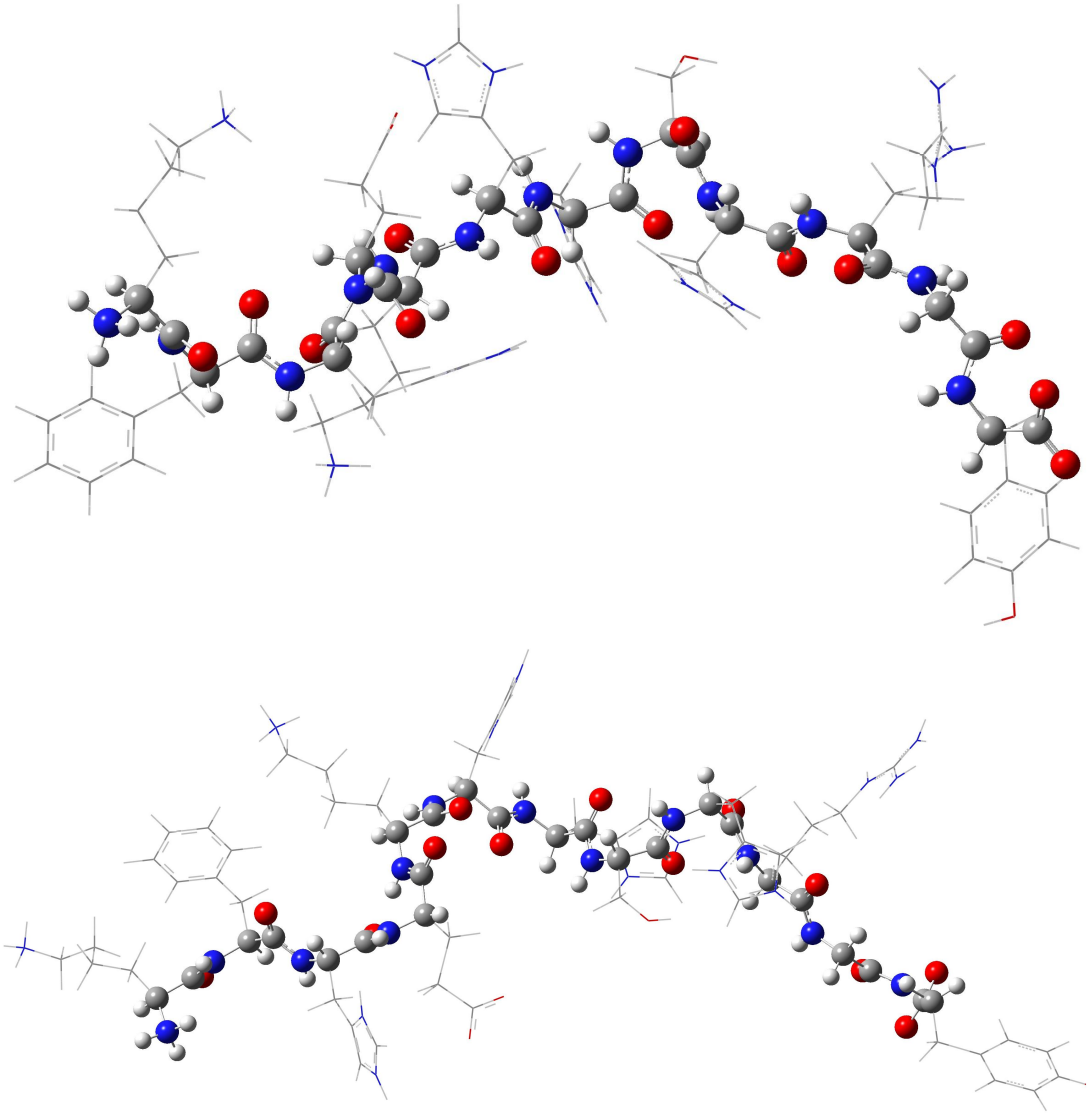

Figure 4.5.2. Two views of an *Hst*-8 structure generated as CNS output of a MD simulation using MARDIGRAS generated restraint data from contacts identified in *Hst*-8 in DMSO NOESY data. The back bone has been put in ball and stick, the side chains are wireframe. (Colorcode: white – hydrogen, gray – carbon, blue – nitrogen, and red – oxygen)

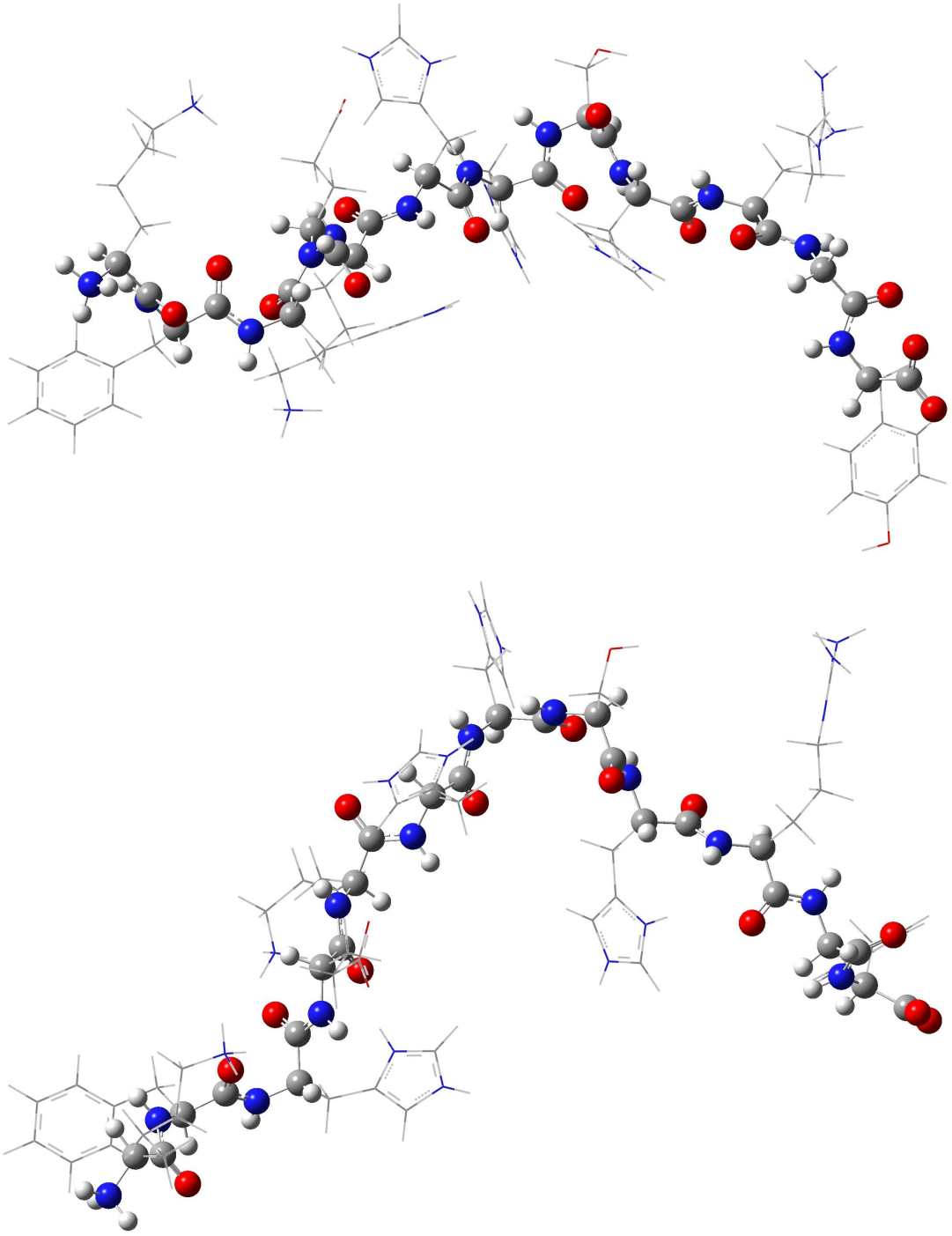

Figure 4.5.3. Two views of an *Hst*-8 structure generated as CNS output of a MD simulation using generic restraint data from contacts identified in *Hst*-8 in DMSO NOESY data. The back bone has been put in ball and stick, the side chains are wireframe. (Colorcode: white – hydrogen, gray – carbon, blue – nitrogen, and red – oxygen)

As illustrated in figures 4.5.2 and 4.5.3 both structures generated from the CNS MD minimization of the NOESY restraint data resulted in structures that contained no elements of secondary structure. One can see elements of a helical twist on the backbone of both structures; however, it is most certainly not an alpha helical twist. A sharp turn in both of the structures occurs at the H7 and is again, not a part of any secondary structural feature. This differs from the previously published literature[79] on the conformation of *Hst*-8 in DMSO. However, it should be noted that they adjusted their *Hst*-8 sample to pH 4.0 prior to dissolving it in DMSO. This may result in more histidine residues being protonated and thus electrostatically repelled. The beta strand is a very effective structure at maximizing the distance between residue side chains. Residues alternate sides along the peptide backbone which is completely extended with φ and ψ angles of 180º. This could then explain why the beta strand exists in their system. When we calculated the structure of *Hst*-8 in its completely protonated form at AM1, PM3, and PM3MM levels of theory, we clearly observed beta strand elements in the structure (figures 3.2.23 and 3.2.24). With at most one histidine residue protonated, our sample of *Hst*-8 is freer to adopt a greater array of conformations. Also one should consider that molecular dynamics simulations are not particularly sophisticated simulations. The difference between a beta sheet and random coil is not all that significant. It only takes a few degrees of divergence at each individual φ and ψ angle along the amide backbone to go from beta strand to lacking of any secondary structural

characteristics. Thus it could merely be that the computer programs that were used for their MD simulations weighted beta strand formation more than degrees of freedom. Our finding of a lack of alpha helical or beta strand secondary structural characteristics of *Hst*-8 in DMSO is similar to the lack of alpha helical and beta strand secondary structural elements observed for *Hst*-5 in an aqueous solution[78] and a lack of such secondary structural elements observed for many of the cationic antimicrobial peptides.[140, 141] As discussed in the introductory chapter these secondary structural is critical to the function of many of the short antimicrobial peptides.

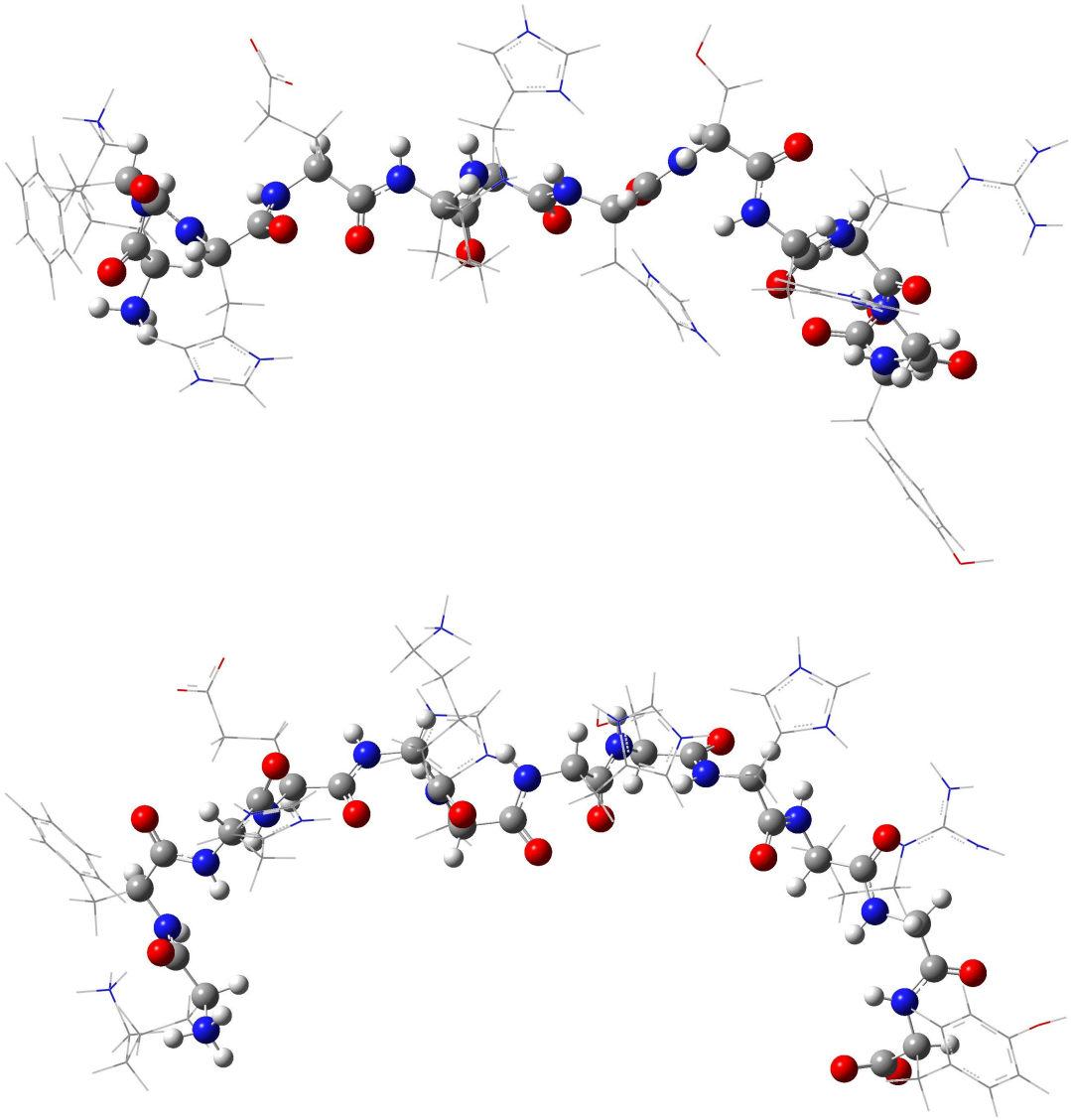

Figure 4.5.4. Two views of an *Hst*-8 structure generated as CNS output of a MD simulation using generic restraint data from contacts identified in *Hst*-8 with Cu(I) in DMSO NOESY data. The back bone has been put in ball and stick, the side chains are wireframe. (Colorcode: white – hydrogen, gray – carbon, blue – nitrogen, and red – oxygen)

Figure 4.5.3 illustrates the structure of *Hst*-8 generated by CNS using generic restraint data from contacts identified in NOESY data of the sample *Hst*-8 with Cu(I) in DMSO. Here again, we observe that the structure that

results from our MD simulation is lacking of alpha helical or beta strand secondary structural elements. The MD simulation took into account only the NOESY data, as it was incapable of handling metal binding restrictions. Nonetheless the structure obtained for *Hst*-8 plus Cu(I) in DMSO is certainly in line with our expectations given the results of our metal binding studies and our previous MD simulations (figures 4.5.1 and 4.5.2). Attempts to utilize the boundary restriction data calculated by MARDIGRAS for use in CNS MD studies failed. Both of the simulations using either the alpha helix model and beta sheet failed to reach a convergence. This is likely due to the fact that MARDIGRAS output such tight boundaries. This then resulted in CNS being unable to adopt any other conformations except that which was highly unstable and was minimized to initially using the distance restraints. This conclusion follows because when the boundary restrictions were replaced with generic contacts we were able to obtain a minimized structure.

Although this is the structure of *Hst*-8 plus Cu(I) in DMSO as determined from the simulations on the data available, I am ultimately not altogether confident in the results. This stems from the fact that there are many fewer NOESY contacts utilized in the analysis of the metal containing system than the sample, which contained no metal. Also consider that as all evidence points to a dynamic structure in the presence of copper(I), a structure arrived at by molecular dynamics minimization hardly fits all of the evidence. So ultimately while this does give us insight into the structure of *Hst*-8 plus Cu(I) in DMSO the output structure hardly tells the whole story.

Again the same hypotheses that were raised in the metal binding chapter could be tested. If utilization of stronger ligands enabled the visualization of more NOESY peaks in those samples containing Cu(I) then more contacts could be input into both MARDIGRAS and CNS. Another experimental series that would also aid in our understanding both of the free and copper bound *Hst*-8 would be to conduct the NOESY and ROESY experiments over an array of mixing times, both longer and shorter than the 150 ms we used. From this we may be able to generate even more contacts using the longer mixing times and the closest most important NOESY contacts could be confirmed using the shorter mixing times. These suggestions could generate data that when utilized in conjunction with our existing data could lead to conclusions that have a higher confidence level.

4.7: Experimental Procedures

4.7.1: General NMR Procedure, Materials, and Methods

A Varian Unity/Inova 400 MHz system upgraded to VNMRS with an auto-tunable Dual Broadband ^{15}N-^{31}P $\{^{1}H\}$ PFG probe utilizing the VNMRJ software suite for collection and processing or a Varian VXR 500 MHz system upgraded to VNMRS with a triplet resonance $^{1}H\{^{13}C/^{15}N\}$ PFG probe utilizing VNMRJ software suite for collection and processing was employed. Samples were maintained at 20ºC for the duration of the experiment. Prior to collection of 2D homonuclear or heteronuclear experiments each sample had

its 90º pulsewidth (PW90) determined, which then was input as a parameter into subsequent experiments.

For experiments involving air and moisture sensitive copper(I) species, samples were placed in a J. Young NMR tube (600 MHz glass, Wilmad Labglass). This allowed the sample to be maintained under inert atmospheric conditions (either argon or nitrogen). Also manipulation of $Cu(CH_3CN)_4PF_6$ was done in a glovebox (VAC model MO-M).

Histatin-8 was purchased as a crude solid phase preparation product (55-60% purity depending on batch) from the Molecular Biology Proteomics Facility of the University of Oklahoma Health Sciences Center. It was isolated and purified by HPLC by dissolving the sample in a small volume of 0.1% TFA/water and injection onto a C18 RP-Prep-HPLC column (Biorad BioLogic). Elution with a linear solvent gradient from 100% water (0.1% TFA) to 60% H_2O (0.1% TFA) / 40% 4:1 acetonitrile:H_2O (0.1%TFA) (4 mL/min) over 74 min afforded *Hst*-8 with a typical retention time of 9 min. The *Hst*-8 fraction was determined by ESI-MS.

Tetrakis(acetonitrile)copper(I)hexafluorophosphate, was obtained from Aldrich. Dimethylsulfoxide-D6 (D 99.9%) was obtained from Cambridge Isotope Laboratories.

4.7.2: General NOESY Parameters

Here the experimentally collected PW90 parameter was input and the mixing time for the sample was 150 ms. All other parameters were standard parameters.

4.7.3: General ROESY Parameters

Here the experimentally collected PW90 parameter was input and the mixing time for the sample was 150 ms. All other parameters were standard parameters.

4.7.4: General TOCSY Parameters

Here the experimentally collected PW90 parameter was input. All other parameters were standard parameters.

4.7.5: General ^{1}H-^{13}C HSQC Parameters

Here the experimentally collected PW90 parameter was input. All other parameters were standard parameters.

4.7.6: Analysis of Combined Collected NMR Spectra

Analysis of collected NMR data was done simultaneously by SPARKY 3, which is a very useful piece of software that handles assignment, integration, and exporting of data. It was written by T. D. Goddard and D. G.

Kneller at the University of California San Francisco. It is available free of charge at http://www.cgl.ucsf.edu/home/sparky/.

4.7.7: MARDIGRAS Analysis

MARDIGRAS and its suite of programs ultimately produce boundary restraint data from NOESY intensity data.[134-138] First models in .pdb format are processed by CORMA. A list of NOESY correlations and intensities are then also processed by CORMA. Then MARDIGRAS is run using the processed model and processed intensity files. One need only input the mixing time and the frequency of the protons in the magnetic field used and the data is output.

4.7.8: CNS Molecular Dynamics Simulations

CNS was used according to standard protocols.[139] Generally this involved generation of a .pdb file by CNS from user input sequence. Then NOESY restraint data was input into a space separated table. When MARDIGRAS restraint was used the data was input as output by MARDIGRAS using the calculated distance and the upper boundary and lower boundary limits. When generic restraint data was used the distance used was 4.0 Å, a lower boundary of 1.8 Å and an upper boundary of 5.5 Å. At this point the annealing script is run and a structure is obtained. The final structure output is an average of 5-15 structures minimized by the CNS algorithm.

4.7.9: Computational Chemistry Methods

ArgusLab (ArgusLab 4.0.1 written by Mark A. Thompson of Planaria Software LLC, Seattle, WA (http://www.arguslab.com)) was used for molecular mechanics calculations, PM3 calculations that involved metals, and AM1 calculations that involved metals.

For PM3 and AM1 calculations, as well as PM3MM and higher levels of theory Gaussian 03 was used.[129]

Results from both computational suites were visualized and exported to JPEG files using Gaussview (Gaussian, Inc., Wallingford CT http://www.gaussian.com) and ArgusLab.

Chapter 5: Project Summary

5.1: Conclusions

We have sought to add to the knowledge base of the antimicrobial *Hst* peptides in terms of meeting several project objectives. First, since there is still debate whether ROS are involved in the antimicrobial activity of the *Hst*, we sought to investigate the possibility in an *in vitro* system. In this way all external variables and possible side reactions would be eliminated and there would be definitive and quantifiable evidence for ROS production by *Hst* systems. We have clearly succeeded in meeting this major objective. Our published findings reveal that *Hst*-5 and *Hst*-8 systems in pH 7.4 MOPS buffer are capable of ROS production at levels comparable to free copper itself. As MOPS is a buffering agent that does not engage in complexation with copper we are assured that ROS production is the result of peptide metal complexes. In addition as a result of our spin trapping studies, we have observed that the specific ROS produced by an *Hst*-8 copper complex is superoxide. This is in contrast to the spin trapping studies done with only free copper where only hydroxyl radical adducts are observed.

Another major gap identified in the literature is that there has not yet been a definitive study on the metal binding environment of the peptides themselves. Many peptide analogues have been made and their metal binding activity studied. However as most of them delete histidine residues, and are very short in length, a comprehensive understanding of the metal

binding environment has yet to be investigated. Our efforts to investigate metal binding activity of *Hst*-8 to copper ions met with limited success. Ultimately we were able to observe fundamental changes in the NMR spectra we collected. Further, we could rationalize these changes based on exchange of the imidazolyl residues on and off the metal as a result of weak binding. The residues we believe are primarily involved in metal binding are the H3, H6, and H7 residues. Unfortunately, we are not able prove this, as resonances disappeared from the spectra rather than simply become downfield shifted as a result of metal ion binding. This broadening of peaks extended to the alpha amide region of the NOESY, ROESY, and TOCSY spectra, which impeded our efforts to assign the precise residues. Other efforts to investigate the ligand environment of the copper, such as EPR also met with failure.

Our final investigation dealt with uncovering the conformation of *Hst*-8 after metal ion binding. Many studies have already been done both on *Hst* conformation in the free state and *Hst* metal binding activity, however, there had not yet been a study that has integrated both metal binding and global conformation of the peptide until this work. We did have success in this endeavor. Using NMR NOESY and ROESY data we were able to obtain distance restraint data. The data, when input into a molecular dynamics simulator, resulted in a structure that was in line with expectations, namely that such a short peptide would exist largely unstructured. In fact in aqueous solution *Hst*-5 was found to be unstructured.[78, 80, 81] Moreover, it was

observed that chain length greatly influence the ability of *Hst*-5 and derivatives of *Hst*-5 to adopt secondary structure in non-aqueous environments.[80, 81] Although, a previous study had found the structure to be a beta sheet in DMSO, ultimately their conditions were different. As aforementioned this likely resulted in an *Hst*-8 species of different protonation state than our sample. The resulting electrostatic repulsion could favor the adaptation of a regular secondary structure due to the loss of favorable conformations.

5.2: Future Work

There is of course plenty of room for additional work. First and foremost it remains that there were a few resonances that were unable to be definitively assigned in the *Hst*-8 in the absence of the metal and several more in the presence of the metal. Using a higher field instrument to collect the NMR spectra combined with an increase in resolution could potentially be of benefit in assigning these resonances. Also collecting the NOESY and ROESY experiments with variable mixing times may have given more distant spatial contacts with longer mixing and eliminated all but those most close contacts for short mixing times. This could have aided in the confirmation of the boundary restrictions we obtained and added other more distant contacts.

Next we could expand the metal binding and global conformation study upon metal binding to include *Hst*-5. *Hst*-5 is comparatively a much

larger peptide, essentially twice as large as *Hst*-8. It also contains a true ACTUN type site that could potentially compete for metal binding interaction with copper. Also it contains two copper binding sites with the sequence His-X-Y-Z-His. These of course could potentially engage in an equilibrium binding, which would necessarily complicate the data collection and interpretation.

I foresee a major experimental undertaking to clarify some of the interpretations and hypotheses regarding the metal binding sites and the conformation. First to clarify as to whether or not the metal binding of the Cu(I) species to the *Hst*-8 isothermal calorimetry could be performed. Data is already available for Cu(II), but no data exists for the *Hst* and Cu(I). Ultimately one would also expand such work to include the model complexes and *Hst*-5. Also one could follow up on the possibility that utilization of stronger ligands with copper(I) could allow for the visualization of the imidazolyl motifs and perhaps the remainder of the histidine residues. ^{63}Cu NMR as a rule generally requires very tight binding on the part of the metal ligand complex. So if ITC studies indicated tight enough binding, one could consider attempting such experiments.

Further experiments that would be more focused on the conformation of the peptide and peptide metal systems could also be done in addition to seeing if perhaps ligands greatly affected the NMR. Obviously, a CD experiment could be performed on *Hst*-8 both in the presence and absence of copper (I) or (II). This would give definitive data as to if there were an

alpha helix adopted by *Hst*-8 upon metal binding. Though our studies suggest this is not the case, additional evidence is always welcome to support the case. A major issue here though is that a different solvent would have to be used as DMSO absorbs strongly in that region, so another study should accompany this particular investigation.

One should also consider using ^{15}N and ^{13}C labeled peptide; this would make NMR experiments much shorter. Also one could identify with much greater ease residues involved in binding as ^{15}N-^{13}C connectivity data could be obtained. Also using a fully isotopic ally enriched peptide, one could perform 3D NMR experiments involving a ^{15}N-^{13}C HSQC as the initial experiment. These additional NMR experiments could give connectivity data of the specific imidazolyl units to the alpha or amide protons more quickly and reliably than relying on NOESY experiments to connect the imidazolyl units to the backbone alpha and amide protons. Further, one could investigate the ^{15}N shifts directly without having to use indirect detection experiments like HSQC and HMBC experiments. These are much faster experiments and thus could give much more information.

Finally, as a last point to the metal binding studies, one could also add ascorbic acid that has been pH adjusted to 9, and then dried and added to the *Hst*-8 which had been adjusted to pH 9 and dried prior to addition of Cu(I) in DMSO system. This would just be a point to balance the experiment that we did in which we added ascorbic acid to the *Hst*-8, which had been pH

adjusted to 9 and then dried prior to addition of Cu(I) in DMSO. The ascorbic acid obviously added a proton equivalent, which undoubtedly altered the pH.

References

1. Kavanagh, K.; Dowd, S., Histatins: antimicrobial peptides with therapeutic potential. *Journal of Pharmacy and Pharmacology* **2004,** 56, (3), 285-289.

2. Helmerhorst, E. J.; VantHof, W.; Veerman, E. C. I.; SimoonsSmit, I.; Amerongen, A. V. N., Synthetic histatin analogues with broad-spectrum antimicrobial activity. *Biochemical Journal* **1997,** 326, 39-45.

3. Edgerton, M.; Koshlukova, S. E.; Lo, T. E.; Chrzan, B. G.; Straubinger, R. M.; Raj, P. A., Candidacidal activity of salivary histatins - Identification of a histatin 5-binding protein on Candida albicans. *Journal of Biological Chemistry* **1998,** 273, (32), 20438-20447.

4. Jensen, J. L.; Xu, T.; Lamkin, M. S.; Brodin, P.; Aars, H.; Berg, T.; Oppenheim, E. G., Physiological Regulation of the Secretion of Histatins and Statherins in Human Parotid Saliva. *Journal of Dental Research* **1994,** 73, (12), 1811-1817.

5. Johnson, D. A.; Yeh, C. K.; Dodds, M. W. J., Effect of donor age on the concentrations of histatins in human parotid and submandibular/sublingual saliva. *Archives of Oral Biology* **2000,** 45, (9), 731-740.

6. Sabatini, L. M.; Azen, E. A., Histatins, a Family of Salivary Histidine-Rich Proteins, Are Encoded by at Least 2 Loci (His1 and His2). *Biochemical and Biophysical Research Communications* **1989,** 160, (2), 495-502.

7. Vanderspek, J. C.; Wyandt, H. E.; Skare, J. C.; Milunsky, A.; Oppenheim, F. G.; Troxler, R. F., Localization of the Genes for Histatins to Human Chromosome-4q13 and Tissue Distribution of the Messenger-Rnas. *American Journal of Human Genetics* **1989,** 45, (3), 381-387.

8. Ahmad, M.; Piludu, M.; Oppenheim, F. G.; Helmerhorst, E. J.; Hand, A. R., Immunocytochemical localization of histatins in human salivary glands. *Journal of Histochemistry & Cytochemistry* **2004,** 52, (3), 361-370.

9. Sabatini, L. M.; Warner, T. F.; Saitoh, E.; Azen, E. A., Tissue Distribution of Rnas for Cystatins, Histatins, Statherin, and Proline-Rich Salivary Proteins in Humans and Macaques. *Journal of Dental Research* **1989,** 68, (7), 1138-1145.

10. VanderSpek, J. C.; Offner, G. D.; Troxler, R. F.; Oppenheim, F. G., Molecular cloning of human submandibular histatins. *Archives of Oral Biology* **1990,** 35, (2), 137-143.

11. Cabras, T.; Fanali, C.; Monteiro, J. A.; Amado, F.; Inzitari, R.; Desiderio, C.; Scarano, E.; Giardina, B.; Castagnola, M.; Messana, I., Tyrosine polysulfation of human salivary histatin 1. A post-translational modification specific of the submandibular gland. *J Proteome Res* **2007,** 6, (7), 2472-80.

12. Messana, I.; Cabras, T.; Pisano, E.; Sanna, M. T.; Olianas, A.; Manconi, B.; Pellegrini, M.; Paludetti, G.; Scarano, E.; Fiorita, A.; Agostino, S.; Contucci, A. M.; Calo, L.; Picciotti, P. M.; Manni, A.; Bennick, A.; Vitali, A.; Fanali, C.; Inzitari, R.; Castagnola, M., Trafficking and postsecretory events responsible for the formation of secreted human salivary peptides: A proteomics approach. *Molecular & Cellular Proteomics* **2008,** 7, (5), 911-926.

13. Xu, T.; Telser, E.; Troxler, R. F.; Oppenheim, F. G., Primary Structure and Anticandidal Activity of the Major Histatin from Parotid Secretion of the Subhuman Primate, Macaca-Fascicularis. *Journal of Dental Research* **1990,** 69, (11), 1717-1723.

14. Fitzgerald, D. H.; Coleman, D. C.; O'Connell, B. C., Susceptibility of Candida dubliniensis to salivary histatin 3. *Antimicrobial Agents and Chemotherapy* **2003,** 47, (1), 70-76.

15. Murakami, Y.; Xu, T.; Helmerhorst, E. J.; Ori, G.; Troxler, R. F.; Lally, E. T.; Oppenheim, F. G., Inhibitory effect of synthetic histatin 5 on leukotoxin from Actinobacillus actinomycetemcomitans. *Oral Microbiology and Immunology* **2002,** 17, (3), 143-149.

16. Li, X. W. S.; Reddy, M. S.; Baev, D.; Edgerton, M., Candida albicans Ssa1/2p is the cell envelope binding protein for human salivary histatin 5. *Journal of Biological Chemistry* **2003,** 278, (31), 28553-28561.

17. Li, X. W. S.; Sun, J. N. N.; Okamoto-Shibayama, K.; Edgerton, M., Candida albicans cell wall Ssa proteins bind and facilitate import of salivary histatin 5 required for toxicity. *Journal of Biological Chemistry* **2006,** 281, (32), 22453-22463.

18. Zhu, J. S.; Luther, P. W.; Leng, Q. X.; Mixson, A. J., Synthetic histidine-rich peptides inhibit Candida species and other fungi in vitro: Role of endocytosis and treatment implications. *Antimicrobial Agents and Chemotherapy* **2006,** 50, (8), 2797-2805.

19. Koshlukova, S. E.; Lloyd, T. L.; Araujo, M. W. B.; Edgerton, M., Salivary histatin 5 induces non-lytic release of ATP from Candida albicans leading to cell death. *Journal of Biological Chemistry* **1999,** 274, (27), 18872-18879.

20. Veerman, E. C. I.; Nazmi, K.; van Hof, W.; Bolscher, J. G. M.; den Hertog, A. L.; Amerongen, A. V. N., Reactive oxygen species play no role in the candidacidal activity of the salivary antimicrobial peptide histatin 5. *Biochemical Journal* **2004,** 381, 447-452.

21. Baev, D.; Rivetta, A.; Vylkova, S.; Sun, J. N. N.; Zeng, G. F.; Slayman, C. L.; Edgerton, M., The TRK1 potassium transporter is the critical effector for killing of Candida albicans by the cationic protein, Histatin 5. *Journal of Biological Chemistry* **2004,** 279, (53), 55060-55072.

22. Kuroda, T.; Bihler, H.; Bashi, E.; Slayman, C. L.; Rivetta, A., Chloride channel function in the yeast TRK-potassium transporters. *Journal of Membrane Biology* **2004,** 198, (3), 177-192.

23. Vylkova, S.; Li, X. S.; Berner, J. C.; Edgerton, M., Distinct antifungal mechanisms: beta-defensins require Candida albicans Ssa1 protein, while Trk1p mediates activity of cysteine-free cationic peptides. *Antimicrobial Agents and Chemotherapy* **2006,** 50, (1), 324-331.

24. den Hertog, A. L.; Sang, H. W. W. F.; Kraayenhof, R.; Bolscher, J. G. M.; Van't Hof, W.; Veerman, E. C. I.; Amerongen, A. V. N., Interactions of histatin 5 and histatin 5-derived peptides with liposome membranes: surface effects, translocation and permeabilization. *Biochemical Journal* **2004,** 379, 665-672.

25. Melino, S.; Rufini, S.; Sette, M.; Morero, R.; Grottesi, A.; Paci, M.; Petruzzelli, R., Zn2+ ions selectively induce antimicrobial salivary peptide histatin-5 to fuse negatively charged vesicles. Identification and characterization of a zinc-binding motif present in the functional domain. *Biochemistry* **1999,** 38, (30), 9626-9633.

26. Isola, R.; Isola, M.; Conti, G.; Lantini, M. S.; Riva, A., Histatin-induced alterations in Candida albicans: A microscopic and submicroscopic comparison. *Microscopy Research and Technique* **2007,** 70, (7), 607-616.

27. Diaz, G.; Polonelli, L.; Conti, S.; Messana, I.; Cabras, T.; Putzolu, M.; Falchi, A. M.; Fadda, M. E.; Cosentino, S.; Isola, R., Mitochondrial alterations and autofluorescent conversion of Candida albicans induced by histatins. *Microscopy Research and Technique* **2005,** 66, (5), 219-228.

28. den Hertog, A. L.; van Marle, J.; van Veen, H. A.; van't Hof, W.; Bolscher, J. G. M.; Veerman, E. C. I.; Amerongen, A. V. N., Candidacidal effects of two antimicrobial peptides: histatin 5 causes small membrane defects, but LL-37 causes massive disruption of the cell membrane. *Biochemical Journal* **2005,** 388, 689-695.

29. Helmerhorst, E. J.; Breeuwer, P.; van `t Hof, W.; Walgreen-Weterings, E.; Oomen, L. C. J. M.; Veerman, E. C. I.; Amerongen, A. V. N.; Abee, T., The Cellular Target of Histatin 5 on Candida albicans Is the Energized Mitochondrion. *J. Biol. Chem.* **1999,** 274, (11), 7286-7291.

30. Helmerhorst, E. J.; Troxler, R. F.; Oppenheim, F. G., The human salivary peptide histatin 5 exerts its antifungal activity through the formation of reactive oxygen species. *Proceedings of the National Academy of Sciences of the United States of America* **2001,** 98, (25), 14637-14642.

31. Petruzzelli, R.; Clementi, M. E.; Marini, S.; Coletta, M.; Di Stasio, E.; Giardina, B.; Misiti, F., Respiratory inhibition of isolated mammalian mitochondria by salivary antifungal peptide histatin-5. *Biochemical and Biophysical Research Communications* **2003,** 311, (4), 1034-1040.

32. Wunder, D.; Dong, J.; Baev, D.; Edgerton, M., Human salivary histatin 5 fungicidal action does not induce programmed cell death pathways in Candida albicans. *Antimicrobial Agents and Chemotherapy* **2004,** 48, (1), 110-115.

33. Baev, D.; Li, X. W. S.; Dong, J.; Keng, P.; Edgerton, M., Human salivary histatin 5 causes disordered volume regulation and cell cycle arrest in Candida albicans. *Infection and Immunity* **2002,** 70, (9), 4777-4784.

34. Vylkova, S.; Jang, W. S.; Li, W. S.; Nayyar, N.; Edgerton, M., Histatin 5 initiates osmotic stress response in Candida albicans via activation of the Hog1 mitogen-activated protein kinase pathway. *Eukaryotic Cell* **2007,** 6, (10), 1876-1888.

35. Krantz, M.; Nordlander, B.; Valadi, H.; Johansson, M.; Gustafsson, L.; Hohmann, S., Anaerobicity Prepares Saccharomyces cerevisiae Cells for Faster Adaptation to Osmotic Shock. *Eukaryotic Cell* **2004,** 3, (6), 1381-1390.

36. Tang, C. C.; Davalian, D.; Huang, P.; Breslow, R., Models for Metal-Binding Sites in Zinc Enzymes - Syntheses of Tris[4(5)-Imidazolyl]Carbinol (4-Tic), Tris(2-Imidazolyl)Carbinol (2-Tic), and Related Ligands, and Studies on Metal-Complex Binding Constants and Spectra. *Journal of the American Chemical Society* **1978,** 100, (12), 3918-3922.

37. Grogan, J.; McKnight, C. J.; Troxler, R. F.; Oppenheim, F. G., Zinc and copper bind to unique sites of histatin 5. *Febs Letters* **2001,** 491, (1-2), 76-80.

38. Brewer, D.; Lajoie, G., Evaluation of the metal binding properties of the histidine-rich antimicrobial peptides histatin 3 and 5 by electrospray ionization mass spectrometry. *Rapid Communications in Mass Spectrometry* **2000,** 14, (19), 1736-1745.

39. Rachmilovich-Calis, S.; Masarwa, A.; Meyerstein, N.; Meyerstein, D., The Fenton reaction in aerated aqueous solutions revisited. *European Journal of Inorganic Chemistry* **2005**, (14), 2875-2880.

40. Lynch, T.; Cherny, R. A.; Bush, A. I., Oxidative processes in Alzheimer's disease: the role of A beta-metal interactions. *Experimental Gerontology* **2000,** 35, (4), 445-451.

41. Valko, M.; Morris, H.; Cronin, M. T. D., Metals, toxicity and oxidative stress. *Current Medicinal Chemistry* **2005,** 12, (10), 1161-1208.

42. Brewer, G. J., Iron and copper toxicity in diseases of aging, particularly atherosclerosis and Alzheimer's disease. *Experimental Biology and Medicine* **2007,** 232, (2), 323-335.

43. Harper, M. E.; Bevilacqua, L.; Hagopian, K.; Weindruch, R.; Ramsey, J. J., Ageing, oxidative stress, and mitochondrial uncoupling. *Acta Physiologica Scandinavica* **2004,** 182, (4), 321-331.

44. Vina, J.; Lloret, A.; Orti, R.; Alonso, D., Frontiers in Neurodegenerative Disorders and Aging: Fundamental Aspects, Clinical Perspectives and New Insights. In *NATO Science Series, Series I: Life and Behavioural Sciences*, Ozben, T.; Checion, M., Eds. IOS Press: Amsterdam, 2004; Vol. 358, pp 182-188.

45. Aslan, M.; Ozben, T., Frontiers in Neurodegenerative Disorders and Aging: Fundamental Aspects, Clinical Perspectives and New Insights. In *NATO Science Series, Series I: Life and Behavioural Sciences*, Ozben, T.; Chevion, M., Eds. IOS Press: Amsterdam, 2004; Vol. 358, pp 158-169.

46. Patel, M., Mitochondrial dysfunction and oxidative stress: cause and consequence of epileptic seizures. *Free Radical Biology and Medicine* **2004,** 37, (12), 1951-1962.

47. Leonard, S. S.; Harris, G. K.; Shi, X., Metal-induced oxidative stress and signal transduction. *Free Radical Biology and Medicine* **2004,** 37, (12), 1921-1942.

48. Burkitt, M. J., A critical overview of the chemistry of copper-dependent low density lipoprotein oxidation: Roles of lipid hydroperoxides, alpha-tocopherol, thiols, and ceruloplasmin. *Archives of Biochemistry and Biophysics* **2001,** 394, (1), 117-135.

49. Lassegue, B.; Griendling, K. K., Reactive oxygen species in hypertension - An update. *American Journal of Hypertension* **2004,** 17, (9), 852-860.

50. Lovstad, R. A., A kinetic study on the copper-albumin catalyzed oxidation of ascorbate. *Biometals* **2002,** 15, (4), 351-355.

51. Bar-Or, D.; Rael, L. T.; Lau, E. P.; Rao, N. K. R.; Thomas, G. W.; Winkler, J. V.; Yukl, R. L.; Kingston, R. G.; Curtis, C. G., An analog of the human albumin N-terminus (Asp-Ala-His-Lys) prevents formation of copper-induced reactive oxygen species. *Biochemical and Biophysical Research Communications* **2001,** 284, (3), 856-862.

52. Jin, Y.; Cowan, J. A., DNA cleavage by copper-ATCUN complexes. Factors influencing cleavage mechanism and linearization of dsDNA. *Journal of the American Chemical Society* **2005,** 127, (23), 8408-8415.

53. Verkhovsky, M. I.; Morgan, J. E.; Wikstrom, M., Redox transitions between oxygen intermediates in cytochrome-c oxidase. *Proceedings of the National Academy of Sciences of the United States of America* **1996,** 93, (22), 12235-12239.

54. Yim, M. B.; Chock, P. B.; Stadtman, E. R., Copper, Zinc Superoxide-Dismutase Catalyzes Hydroxyl Radical Production from Hydrogen-Peroxide. *Proceedings of the National Academy of Sciences of the United States of America* **1990,** 87, (13), 5006-5010.

55. Misra, H. P., Generation of Superoxide Free-Radical during Autoxidation of Thiols. *Journal of Biological Chemistry* **1974,** 249, (7), 2151-2155.

56. Nyberg, G. K.; Granberg, G. P. D.; Carlsson, J., Bovine Superoxide-Dismutase and Copper Ions Potentiate the Bactericidal Effect of Autoxidizing Cysteine. *Applied and Environmental Microbiology* **1979,** 38, (1), 29-34.

57. Rowley, D. A.; Halliwell, B., Superoxide-Dependent Formation of Hydroxyl Radicals in the Presence of Thiol Compounds. *Febs Letters* **1982,** 138, (1), 33-36.

58. Schoeneich, C., Selective Cu2+/ascorbate-dependent oxidation of Alzheimer's disease β-amyloid peptides. *Annals of the New York Academy of Sciences* **2004,** 1012, 164-170.

59. Uchida, K.; Kawakishi, S., Site-Specific Oxidation of Angiotensin-I by Copper(Ii) and L-Ascorbate - Conversion of Histidine-Residues to 2-Imidazolones. *Archives of Biochemistry and Biophysics* **1990,** 283, (1), 20-26.

60. Hlavaty, J. J.; Benner, J. S.; Hornstra, L. J.; Schildkraut, I., Identification of the metal-binding sites of restriction endonucleases by Fe2+-mediated oxidative cleavage. *Biochemistry* **2000,** 39, (11), 3097-3105.

61. Bridgewater, J. D.; Lim, J.; Vachet, R. W., Transition metal-peptide binding studied by metal-catalyzed oxidation reactions and mass spectrometry. *Analytical Chemistry* **2006,** 78, (7), 2432-2438.

62. Lim, J.; Vachet, R. W., Development of a methodology based on metal-catalyzed oxidation reactions and mass spectrometry to determine the metal binding sites in copper metalloproteins. *Analytical Chemistry* **2003,** 75, (5), 1164-1172.

63. Riley, D. P., Functional mimics of superoxide dismutase enzymes as therapeutic agents. *Chemical Reviews* **1999,** 99, (9), 2573-2587.

64. Ueda, J.; Sudo, A.; Mori, A.; Ozawa, T., Generation of Hydroxyl Radicals during Dismutation of Superoxide by Sod Model Compounds. *Archives of Biochemistry and Biophysics* **1994,** 315, (1), 185-189.

65. Cabelli, D. E.; Riley, D.; Rodriguez, J. A.; Valentine, J. S.; Zhu, H., In *Biomimetic Oxidations Catalyzed by Transition Metal Complexes*, Meunier, B., Ed. Imperial College Press: London, 2000; pp 461-508.

66. Cobine, P. A.; Ojeda, L. D.; Rigby, K. M.; Winge, D. R., Yeast contain a non-proteinaceous pool of copper in the mitochondrial matrix. *Journal of Biological Chemistry* **2004,** 279, (14), 14447-14455.

67. Doolittle, R. F., Redundancies in Protein Sequences. In *Prediction of Protein Sequence and the Principles of Protein Conformation*, Fasman, G. D., Ed. Plenum: New York, 1989; pp 599-624.

68. Mozier, N. M.; Walsh, M. P.; Pearson, J. D., Characterization of a Novel Zinc-Binding Site of Protein-Kinase-C Inhibitor-1. *Febs Letters* **1991,** 279, (1), 14-18.

69. Peters, T., Interaction of One Mole of Copper with the Alpha-Amino Group of Bovine Serum Albumin. *Biochimica Et Biophysica Acta* **1960,** 39, (3), 546-547.

70. Houghton, E. A.; Nicholas, K. M., In vitro reactive oxygen species production by histatins and copper(I,II). *Journal of Biological Inorganic Chemistry* **2009,** 14, (2), 243-251.

71. Gusman, H.; Lendenmann, U.; Grogan, J.; Troxler, R. F.; Oppenheim, F. G., Is salivary histatin 5 a metallopeptide? *Biochimica Et Biophysica Acta-Protein Structure and Molecular Enzymology* **2001,** 1545, (1-2), 86-95.

72. Sutton, H. C.; Winterbourn, C. C., On the Participation of Higher Oxidation-States of Iron and Copper in Fenton Reactions. *Free Radical Biology and Medicine* **1989,** 6, (1), 53-60.

73. Urbanski, N. K.; Beresewicz, A., Generation of (OH)-O-. initiated by interaction of Fe2+ and Cu+ with dioxygen; comparison with the Fenton chemistry. *Acta Biochimica Polonica* **2000,** 47, (4), 951-962.

74. Sheldon, R. A.; Kochi, J. K., In *Metal Catalyzed Oxidations of Organic Compounds*, Academic Press: New York, 1981.

75. Castagnola, M.; Inzitari, R.; Rossetti, D. V.; Olmi, C.; Cabras, T.; Piras, V.; Nicolussi, P.; Sanna, M. T.; Pellegrini, M.; Giardina, B.; Messana, I., A cascade of 24 histatins (histatin 3 fragments) in human saliva - Suggestions for a pre-secretory sequential cleavage pathway. *Journal of Biological Chemistry* **2004,** 279, (40), 41436-41443.

76. Cabras, T.; Patamia, M.; Melino, S.; Inzitari, R.; Messana, I.; Castagnola, M.; Petruzzelli, R., Pro-oxidant activity of histatin 5 related Cu(II)-model peptide probed by mass spectrometry. *Biochemical and Biophysical Research Communications* **2007,** 358, (1), 277-284.

77. Bal, W.; Lukszo, J.; Kasprzak, K. S., Mediation of oxidative DNA damage by nickel(II) and copper(II) complexes with the N-terminal sequence of human protamine HP2. *Chemical Research in Toxicology* **1997,** 10, (8), 915-921.

78. Raj, P. A.; Marcus, E.; Sukumaran, D. K., Structure of human salivary histatin 5 in aqueous and nonaqueous solutions. *Biopolymers* **1998,** 45, (1), 51-67.

79. Tauro, S.; Coutinho, E.; Srivastava, S., Conformation of the peptide antibiotic - histatin 8 in aqueous and non aqueous media. *Letters in Peptide Science* **2001,** 8, (6), 295-307.

80. Raj, P. A.; Edgerton, M.; Levine, M. J., Salivary Histatin-5 - Dependence of Sequence, Chain-Length, and Helical Conformation for Candidacidal Activity. *Journal of Biological Chemistry* **1990,** 265, (7), 3898-3905.

81. Raj, P. A.; Soni, S. D.; Levine, M. J., Membrane-Induced Helical Conformation of an Active Candidacidal Fragment of Salivary Histatins. *Journal of Biological Chemistry* **1994,** 269, (13), 9610-9619.

82. Helmerhorst, E. J.; van't Hof, W.; Breeuwer, P.; Veerman, E. C. I.; Abee, T.; Troxler, R. F.; Amerongen, A. V. N.; Oppenheim, F. G., Characterization of histatin 5 with respect to amphipathicity, hydrophobicity, and effects on cell and mitochondrial membrane integrity excludes a candidacidal mechanism of pore formation. *Journal of Biological Chemistry* **2001,** 276, (8), 5643-5649.

83. Ramamoorthy, S.; Manning, P. G., Equilibrium studies of metal-ion complexes of interest to natural waters -- V Simple and mixed complexes of Cu(II) involving organic primary ligands and orthophosphate, pyrophosphate and sulphate as secondary ligands. *Journal of Inorganic and Nuclear Chemistry* **1973,** 35, (4), 1279-1283.

84. Good, N. E.; Izawa, S.; Anthony San, P., [3] Hydrogen ion buffers. In *Methods in Enzymology*, Academic Press: 1972; Vol. Volume 24, pp 53-68.

85. VanDyke, B. R.; Clopton, D. A.; Saltman, P., Buffer-induced anomalies in the Fenton chemistry of iron and copper. *Inorganica Chimica Acta* **1996,** 242, (1-2), 57-61.

86. Yu, Q.; Kandegedara, A.; Xu, Y.; Rorabacher, D. B., Avoiding Interferences from Good's Buffers: A Contiguous Series of Noncomplexing Tertiary Amine Buffers Covering the Entire Range of pH 3-11. *Analytical Biochemistry* **1997,** 253, (1), 50-56.

87. Magyar, J. S.; Godwin, H. A., Spectropotentiometric analysis of metal binding to structural zinc-binding sites: accounting quantitatively for pH and metal ion buffering effects. *Analytical Biochemistry* **2003,** 320, (1), 39-54.

88. Held, P., Quantitation of hydrogen peroxide using a multidetection microplate reader. *American Biotechnology Laboratory* **2002,** 20, (13), 18-19.

89. Pastor, I.; Esquembre, R.; Micol, V.; Mallavia, R.; Mateo, C. R., A ready-to-use fluorimetric biosensor for superoxide radical using superoxide dismutase and peroxidase immobilized in sol-gel glasses. *Analytical Biochemistry* **2004,** 334, (2), 335-343.

90. Vetrano, A. M.; Heck, D. E.; Mariano, T. M.; Mishin, V.; Laskin, D. L.; Laskin, J. D., Characterization of the oxidase activity in mammalian catalase. *Journal of Biological Chemistry* **2005,** 280, (42), 35372-35381.

91. Jameson, R. F.; Blackburn, N. J., Role of Cu-Cu Dinuclear Complexes in Oxidation of Ascorbic-Acid by O2 - Model for Copper-Oxidase Activity. *Journal of Inorganic & Nuclear Chemistry* **1975,** 37, (3), 809-814.

92. Davies, M. B., Reactions of L-Ascorbic-Acid with Transition-Metal Complexes. *Polyhedron* **1992,** 11, (3), 285-321.

93. Dikalov, S. I.; Vitek, M. P.; Mason, R. P., Cupric-amyloid beta peptide complex stimulates oxidation of ascorbate and generation of hydroxyl radical. *Free Radical Biology and Medicine* **2004,** 36, (3), 340-347.

94. Scarpa, M.; Stevanato, R.; Viglino, P.; Rigo, A., Superoxide ion as active intermediate in the autoxidation of ascorbate by molecular oxygen. Effect of superoxide dismutase. *J. Biol. Chem.* **1983,** 258, (11), 6695-6697.

95. Scarpa, M.; Vianello, F.; Signor, L.; Zennaro, L.; Rigo, A., Ascorbate oxidation catalyzed by bis(histidine)copper(II). *Inorganic Chemistry* **1996,** 35, (18), 5201-5206.

96. Shapiro, M. P.; Setlow, B.; Setlow, P., Killing of Bacillus subtilis spores by a modified Fenton reagent containing CuCl2 and ascorbic acid. *Applied and Environmental Microbiology* **2004,** 70, (4), 2535-2539.

97. Lloyd, D. R.; Carmichael, P. L.; Phillips, D. H., Comparison of the formation of 8-hydroxy-2 '-deoxyguanosine and single- and double-strand breaks in DNA mediated by Fenton reactions. *Chemical Research in Toxicology* **1998,** 11, (5), 420-427.

98. Strlič, M.; Kolar, J.; Šelih, V.-S.; Kočar, D.; Pihlar, B., A comparative study of several transition metals in Fenton-like reaction systems at circum-neutral pH. *Acta Chimica Slovenica* **2003,** 50, (4), 619-632.

99. Khossravi, M.; Borchardt, R. T., Chemical Pathways of Peptide Degradation: IX. Metal-Catalyzed Oxidation of Histidine in Model Peptides. *Pharmaceutical Research* **1998,** 15, 1096-1102.

100. Winterbourn, C. C.; Peskin, A. V.; Parsons-Mair, H. N., Thiol oxidase activity of copper,zinc superoxide dismutase. *Journal of Biological Chemistry* **2002,** 277, (3), 1906-1911.

101. Yoon, S. J.; Koh, Y. H.; Floyd, R. A.; Park, J. W., Copper, zinc superoxide dismutase enhances DNA damage and mutagenicity induced by cysteine/iron. *Mutation Research-Fundamental and Molecular Mechanisms of Mutagenesis* **2000,** 448, (1), 97-104.

102. Oroskar, A. A.; Lambert, C.; Peak, M. J., Effects of hydroxyl radical scavengers on relaxation of supercoiled DNA by aminomethyl-trimethyl-psoralen and monochromatic UVA photons. *Free Radical Biology and Medicine* **1996,** 20, (5), 751-756.

103. Farhataziz; Ross, A. B., Selected specific rates of reactions of transients from water in aqueous solution. III. Hydroxyl radical and perhydroxyl radical and their radical ions. *National Standard Reference Data Series (United States, National Bureau of Standards)* **1977,** 59.

104. Hodgson, E. K.; Fridovich, I., Interaction of Bovine Erythrocyte Superoxide-Dismutase with Hydrogen-Peroxide - Inactivation of Enzyme. *Biochemistry* **1975,** 14, (24), 5294-5299.

105. Barik, A.; Mishra, B.; Shen, L.; Mohan, H.; Kadam, R. M.; Dutta, S.; Zhang, H. Y.; Priyadarsini, K. I., Evaluation of a new copper(II)-curcumin complex as superoxide dismutase mimic and its free radical reactions. *Free Radical Biology and Medicine* **2005,** 39, (6), 811-822.

106. Fisher, A. E. O.; Lau, G. K. K.; Naughton, D. P., Lipophilic ionophore complexes as superoxide dismutase mimetics. *Biochemical and Biophysical Research Communications* **2005,** 329, (3), 930-933.

107. Weng, M.; Zhang, M. H.; Shen, T., Electron transfer interaction between hypocrellin A and biological substrates and quantitative analysis of superoxide anion radicals. *Journal of the Chemical Society-Perkin Transactions 2* **1997**, (11), 2393-2397.

108. Petyaev, I. M.; Hunt, J. V., Micellar acceleration of oxygen-dependent reactions and its potential use in the study of human low density lipoprotein. *Biochimica et Biophysica Acta (BBA) - Lipids and Lipid Metabolism* **1997,** 1345, (3), 293-305.

109. Weng, M.; Zhang, M.-H.; Shen, T., Interaction between hypocrellin A and some biological substrates with emphasis on an electron transfer mechanism. *Journal of Photochemistry and Photobiology A: Chemistry* **1997,** 108, (2-3), 169-173.

110. Maccarrone, M.; Rossi, A.; Dandrea, G.; Amicosante, G.; Avigliano, L., Electrophoretic Detection of Ascorbate Oxidase Activity by Photoreduction of Nitroblue Tetrazolium. *Analytical Biochemistry* **1990,** 188, (1), 101-104.

111. Bacic, G.; Spasojevic, I.; Secerov, B.; Mojovic, M., Spin-trapping of oxygen free radicals in chemical and biological systems: New traps, radicals and possibilities. *Spectrochimica Acta Part a-Molecular and Biomolecular Spectroscopy* **2008,** 69, (5), 1354-1366.

112. Kamibayashi, M.; Oowada, S.; Kameda, H.; Okada, T.; Inanami, O.; Ohta, S.; Ozawa, T.; Makino, K.; Kotake, Y., Synthesis and characterization of a practically better DEPMPO-type spin trap, 5-(2,2-dimethyl-1,3-propoxy cyclophosphoryl)-5-methyl-1-pyrroline N-oxide (CYPMPO). *Free Radical Research* **2006,** 40, (11), 1166-1172.

113. Stolze, K.; Udilova, N.; Nohl, H., Spin trapping of lipid radicals with DEPMPO-derived spin traps: Detection of superoxide, alkyl and alkoxyl radicals in aqueous and lipid phase. *Free Radical Biology and Medicine* **2000,** 29, (10), 1005-1014.

114. Tuccio, B.; Lauricella, R.; Frejaville, C.; Bouteiller, J. C.; Tordo, P., Decay of the Hydroperoxyl Spin Adduct of 5-Diethoxyphosphoryl-5-Methyl-1-Pyrroline N-

Oxide - an Epr Kinetic-Study. *Journal of the Chemical Society-Perkin Transactions 2* **1995**, (2), 295-298.

115. Sato, H.; Tani, A.; Ikeya, M., Electron spin resonance of ascorbyl (vitamin C) radicals in synthetic CaCO3 by UV irradiation. *Japanese Journal of Applied Physics Part 1-Regular Papers Short Notes & Review Papers* **2003,** 42, (2A), 428-433.

116. Flora, B.; Gusman, H.; Helmerhorst, E. J.; Troxler, R. F.; Oppenheim, F. G., A new method for the isolation of histatins 1, 3, and 5 from parotid secretion using zinc precipitation. *Protein Expression and Purification* **2001,** 23, (1), 198-206.

117. Damblon, C.; Prosperi, C.; Lian, L. Y.; Barsukov, I.; Soto, R. P.; Galleni, M.; Frere, J. M.; Roberts, G. C. K., H-1-N-15 HMQC for the identification of metal-bound histidines in Cd-113-substituted Bacillus cereus zinc beta-lactamase. *Journal of the American Chemical Society* **1999,** 121, (49), 11575-11576.

118. Scrofani, S. D. B.; Wright, P. E.; Dyson, H. J., The identification of metal-binding ligand residues in metalloproteins using nuclear magnetic resonance spectroscopy. *Protein Science* **1998,** 7, (11), 2476-2479.

119. Gaggelli, E.; Bernardi, F.; Molteni, E.; Pogni, R.; Valensin, D.; Valensin, G.; Remelli, M.; Luczkowski, M.; Kozlowski, H., Interaction of the human prion PrP(106-126) sequence with copper(II), manganese(II), and zinc(11): NMR and EPR studies. *Journal of the American Chemical Society* **2005,** 127, (3), 996-1006.

120. Kulon, K.; Valensin, D.; Kamysz, W.; Valensin, G.; Nadolski, P.; Porciatti, E.; Gaggelli, E.; Koztowski, H., The His-His sequence of the antimicrobial peptide demegen P-113 makes it very attractive ligand for Cu2+. *Journal of Inorganic Biochemistry* **2008,** 102, (4), 960-972.

121. Abajian, C.; Yatsunyk, L. A.; Ramirez, B. E.; Rosenzweig, A. C., Yeast Cox17 solution structure and copper(I) binding. *Journal of Biological Chemistry* **2004,** 279, (51), 53584-53592.

122. Coles, M. P.; Hitchcock, P. B., Synthesis and X-ray crystal structure of polymeric and dimeric copper(I) cyanide complexes incorporating a bicyclic guanidine ligand. *Polyhedron* **2001,** 20, (24-25), 3027-3032.

123. Kittleson, J. T.; Loftin, I. R.; Hausrath, A. C.; Engelhardt, K. P.; Rensing, C.; McEvoy, M. M., Periplasmic metal-resistance protein CusF exhibits high affinity and specificity for both Cu-I and Ag-I. *Biochemistry* **2006,** 45, (37), 11096-11102.

124. Kujime, M.; Kurahashi, T.; Tomura, M.; Fujii, H., 63Cu NMR Spectroscopy of Copper(I) Complexes with Various Tridentate Ligands: CO as a Useful 63Cu NMR Probe for Sharpening 63Cu NMR Signals and Analyzing the Electronic Donor Effect of a Ligand. *Inorganic Chemistry* **2006,** 46, (2), 541-551.

125. Molecular Biology Resource Facility University of Oklahoma Health Science Center (Oklahoma City, OK) Peptide Synthesis Report for Hst-8.

126. Utschig, L. M.; Poluektov, O.; Tiede, D. M.; Thurnauer, M. C., EPR investigation of Cu2+-substituted photosynthetic bacterial reaction centers: Evidence for histidine ligation at the surface metal site. *Biochemistry* **2000,** 39, (11), 2961-2969.

127. Valko, M.; Morris, H.; Mazur, M.; Telser, J.; McInnes, E. J. L.; Mabbs, F. E., High-affinity binding site for copper(II) in human and dog serum albumins (an EPR study). *Journal of Physical Chemistry B* **1999,** 103, (26), 5591-5597.

128. Volkman, J.; Nicholas, K. M., Efficient Synthesis of Tris(4-imidazolyl)methanol Derivatives. *Organic Letters* **2004,** 6, (23), 4301-4302.

129. Frisch, M. J.; Trucks, G. W.; Schlegel, H. B.; Scuseria, G. E.; Robb, M. A.; Cheeseman, J. R.; Montgomery, J., J. A.; Vreven, T.; Kudin, K. N.; Burant, J. C.; Millam, J. M.; Iyengar, S. S.; Tomasi, J.; Barone, V.; Mennucci, B.; Cossi, M.; Scalmani, G.; Rega, N.; Petersson, G. A.; Nakatsuji, H.; Hada, M.; Ehara, M.; Toyota, K.; Fukuda, R.; Hasegawa, J.; Ishida, M.; Nakajima, T.; Honda, Y.; Kitao, O.; Nakai, H.; Klene, M.; Li, X.; Knox, J. E.; Hratchian, H. P.; Cross, J. B.; Bakken, V.; Adamo, C.; Jaramillo, J.; Gomperts, R.; Stratmann, R. E.; Yazyev, O.; Austin, A. J.; Cammi, R.; Pomelli, C.; Ochterski, J. W.; Ayala, P. Y.; Morokuma, K.; Voth, G. A.; Salvador, P.; Dannenberg, J. J.; Zakrzewski, V. G.; Dapprich, S.; Daniels, A. D.; Strain, M. C.; Farkas, O.; Malick, D. K.; Rabuck, A. D.; Raghavachari, K.; Foresman, J. B.; Ortiz, J. V.; Cui, Q.; Baboul, A. G.; Clifford, S.; Cioslowski, J.; Stefanov, B. B.; Liu, G.; Liashenko, A.; Piskorz, P.; Komaromi, I.; Martin, R. L.; Fox, D. J.; Keith, T.; Al-Laham, M. A.; Peng, C. Y.; Nanayakkara, A.; Challacombe, M.; Gill, P. M. W.; Johnson, B.; Chen, W.; Wong, M. W.; Gonzalez, C.; Pople, J. A. *Gaussian 03*, Gaussian, Inc.: Wallingford CT, 2004.

130. Tsai, H. Y.; Raj, P. A.; Bobek, L. A., Candidacidal activity of recombinant human salivary histatin-5 and variants. *Infection and Immunity* **1996,** 64, (12), 5000-5007.

131. Chan, R. K., Dielectric properties of hexafluoroacetone and hexachloroacetone. *Canadian Journal of Chemistry* **1969,** 47, (12), 2253–2256.

132. Lemal, D. M., Perspective on Fluorocarbon Chemistry. *The Journal of Organic Chemistry* **2004,** 69, (1), 1-11.

133. Bermejo, G. A.; Llinas, M., Deuterated protein folds obtained directly from unassigned nuclear overhauser effect data. *Journal of the American Chemical Society* **2008,** 130, (12), 3797-3805.

134. Borgias, B. A.; Gochin, M.; Kerwood, D. J.; James, T. L., Relaxation matrix analysis of 2D NMR data. *Progress in Nuclear Magnetic Resonance Spectroscopy* **1990,** 22, (1), 83-100.

135. Borgias, B. A.; James, T. L., MARDIGRAS-A procedure for matrix analysis of relaxation for discerning geometry of an aqueous structure. *Journal of Magnetic Resonance (1969)* **1990,** 87, (3), 475-487.

136. Borgias, B. A.; James, T. L.; Norman, J. O.; Thomas, L. J., [9] Two-dimensional nuclear Overhauser effect: Complete relaxation matrix analysis. In *Methods in Enzymology*, Academic Press: 1989; Vol. Volume 176, pp 169-183.

137. James, T. L., Relaxation matrix analysis of two-dimensional nuclear Overhauser effect spectra. *Current Opinion in Structural Biology* **1991,** 1, (6), 1042-1053.

138. Thomas, P. D.; Basus, V. J.; James, T. L., Protein solution structure determination using distances from two-dimensional nuclear Overhauser effect experiments: effect of approximations on the accuracy of derived structures. *Proceedings of the National Academy of Sciences of the United States of America* **1991,** 88, (4), 1237-1241.

139. Brunger, A. T.; Adams, P. D.; Clore, G. M.; DeLano, W. L.; Gros, P.; Grosse-Kunstleve, R. W.; Jiang, J.-S.; Kuszewski, J.; Nilges, M.; Pannu, N. S.; Read, R. J.; Rice, L. M.; Simonson, T.; Warren, G. L., Crystallography & NMR System: A New Software Suite for Macromolecular Structure Determination. *Acta Crystallographica Section D* **1998,** 54, (5), 905-921.

140. Boman, H. G., Antibacterial peptides: basic facts and emerging concepts. *J Intern Med* **2003,** 254, (3), 197-215.

141. Brewer, D.; Lajoie, G., Structure-based design of potent histatin analogues. *Biochemistry* **2002,** 41, (17), 5526-5536.

List of Equations

List of Abbreviations

Hst	Histatin
ROS	reactive oxygen species
mol	mole
hr	hour
AR	Amplex Red
SOD	superoxide dismutase
EPR	electron paramagnetic resonance
CYPMPO	5-(2,2-dimethyl-1,3-propoxy cyclophosphoryl)-5-methyl-1-pyrroline N-oxide
NMR	nuclear magnetic resonance
HMBC	heteronuclear multiple bond correlation
HSQC	heteronuclear single quantum correlation
DMSO	dimethylsulfoxide
NOE	nuclear Overhauser effect
TOCSY	total correlation spectroscopy
MD	molecular dynamics
mRNA	messenger ribonucleic acid
ATP	adenosine triphosphate
NADH	nicotinamide adenine dinucleotide (reduced form)
TEM	transmission electron microscopy
HRSEM	high resolution scanning electron microscopy
FITC	fluorescein isothiocyanate

H_2-DCFDA	2',7'-dichlorodihydrofluorescein diacetate
DHF	dihydrofluorescein diacetate
TMRM	tetramethylrhodamine methylester
HEt	Dihydroethidium
DNA	deoxyribonucleic acid
TEMPO	2,2,6,6,-tetramethylpiperidine-1-oxyl
SDS-PAGE	sodium dodecylsulfate polyacrylamide gel electrophoresis
DIDS	diisothiocyanatostilbene-2,2’-disulfonic acid
CAT	catalase
redox	reduction/oxidation
BLAST	basic local alignment search tool
ITC	isothermal calorimetry
ESI-MS	electrospray ionization mass spectrometry
MS	mass spectrometry
ACTUN	amino terminal copper nickel binding motif
HFA	hexafluoroacetone
GSH	glutathione
SET	single electron transfer
MOPS	morpholino-*N*-propylsulfate
MD	molecular dynamics
CD	circular dichroism
FTIR	fourier transformed infrared
MM	molecular mechanics

AM1	Austin Method 1
PM3	Parameterized Model 3
PM3MM	Parameterized Model 3 with molecular mechanical treatment of amide bonds
DFT	density functional theory
TON	turnover number
HRP	horseradish peroxidase
EDTA	ethylenediaminetetraacetic acid
NTB	nitrotetrazolium blue chloride (nitro blue tetrazolium)
DEPMPO	5-(diethoxyphosphoryl)-5-methyl-1-pyrroline N-oxide
DMPO	5-dimethyl-1-pyrroline N-oxide
DD	double distilled
DI	deionized
UV/Vis	ultraviolet / visible
RP	reverse phase
HPLC	high performance liquid chromatography
TFA	trifluoroacetic acid
Kdal	kilodalton
2-TMIC	2-tris(N-methylimidazolyl)carbinol
TMS	tetramethylsilane
4-TIC	4-trisimidazolylcarbinol
CPMG	Carr-Purcell-Meiboom-Gill
ROESY	rotating frame Overhauser spectroscopy